MODIFIED IRON-BASED NANOPARTICLES FOR THE REMOVAL OF DYES AND HEXAVALENT CHROMIUM FROM WATER

Thesis submitted to the University of Calicut
in partial fulfilment of the requirements
for the award of the Degree of

Doctor of Philosophy
in
Chemistry

By

ANJU ROSE PUTHUKKARA P

Under the guidance of

Dr. Sunil Jose T

RESEARCH AND POSTGRADUATE DEPARTMENT OF CHEMISTRY
ST. THOMAS COLLEGE (AUTONOMOUS)
(UNIVERSITY OF CALICUT)
THRISSUR, KERALA – 680001
March 2022

Research and PG Department of Chemistry
ST.THOMAS COLLEGE *(Autonomous)*
THRISSUR - 680 001, KERALA, INDIA
Estd. 1889
(Affiliated to University of Calicut, NAAC with 'A' Grade and College with Potential for Excellence)
Web:- http://stthomas.ac.in Email:- stcthrissur@gmail.com
Phone:- +91 487 2420435 Fax:- +91 487 2421510

15-09-2022

CERTIFICATE

I hereby certify that, this is the revised version of the thesis entitled ***"Modified iron-based nanoparticles for the removal of dyes and hexavalent chromium from water"*** *submitted by* ***Ms. Anju Rose Puthukkara P*** *under my guidance after incorporating the necessary corrections/suggestions made by the adjudicators.*

Dr. Sunil Jose T

(Research Guide)

Research and PG Department of Chemistry
ST.THOMAS COLLEGE (Autonomous)
THRISSUR - 680 001, KERALA, INDIA
Estd. 1889
(Affiliated to University of Calicut, NAAC with 'A' Grade and College with Potential for Excellence)
Web:- http://stthomas.ac.in Email:- stcthrissur@gmail.com
Phone:- +91 487 2420435 Fax:- +91 487 2421510

11-03-2022

CERTIFICATE

This is to certify that the thesis entitled ***"Modified iron-based nanoparticles for the removal of dyes and hexavalent chromium from water"*** *is an authentic record of research work carried out by* ***Ms. Anju Rose Puthukkara P*** *under my supervision in partial fulfillment of the requirements for the degree of Doctor of Philosophy in Chemistry of University of Calicut and further that no part thereof has been presented before for any other degree.*

Dr. Sunil Jose T

(Research Guide)

DECLARATION

I hereby declare that the thesis entitled ***"Modified iron-based nanoparticles for the removal of dyes and hexavalent chromium from water"****, submitted to the University of Calicut in partial fulfillment of the requirement for the award of the Degree of Doctor of Philosophy in Chemistry is a bonafied research work done by me under the supervision and guidance of* ***Dr. Sunil Jose T****, Assistant Professor, Research and PG Department of Chemistry, St. Thomas College (Autonomous), Thrissur*

I further declare that this thesis has not previously formed the basis of any degree, diploma or any other similar title.

Anjurose

11-03-2022 **ANJU ROSE PUTHUKKARA P**

Acknowledgement

First and above all, I thank God Almighty for providing me with the opportunity and granting me the capability to proceed with my research work successfully. This thesis appears in its current form due to the assistance and guidance of several people. I would therefore like to offer my sincere thanks to all of them. I take the privilege to express my utmost gratitude to my guide Dr. Sunil Jose T, Assistant Professor, Department of Chemistry, St. Thomas College, Thrissur, for his care, patience, thoughtful guidance, critical comments and warm encouragement.

I wish to express my sincere gratitude to the current principal Rev. Fr. Dr. Martin Kolambrath and the former principals of St. Thomas College Dr. P O Jenson, Dr. Ignatious Antony and Dr. Joy K L for providing all the infrastructure and laboratory facilities during the whole of the research period. I would also like to thank Rev.Fr. Biju Panengadan, BURSAR of our institution, who is always approachable and exceptionally helpful. My deepest thanks and gratitude to Dr. Joshy C L, Head of the Chemistry Department, St. Thomas College, for his attention and support for the completion of my Ph. D work. I acknowledge my indebtedness and sincere thanks to the former Head of the Department Dr. Joby Thomas K for his constant support, care and the right and needful advices for the very long period during my Ph D work.

I take immense pleasure in expressing my sincere thanks to Dr. Chacko V M, Research co-ordinator. St Thomas College for his valuable guidance and suggestions while completing my Ph D course. Special thanks to Mr. Sanjo Jose, Librarian, for his generous help with library services and providing information to improve academic writing skills. I would also like to thank the college office staff for their support and help with fellowship related works and other documentation processes.

I would also like to express my extensive gratitude and thanks to faculty members of the department of chemistry Dr. Paulson Mathew, Dr. Jency Thomas K, Dr. Jinish Antony M, Dr. Reeja Johnson, Dr. Joseph Joly V L, Dr.Sr.Jisha Joseph, and Prof. Aji C V and for their consistent encouragement during my Ph D course. I am thankful to lab assistants in the department for their help and service for my labwork. Special thanks to lab assistants Mr. Andrews and Mr. Pauljo for lending their help, especially whenever technical support is needed.

I sincerely thank senior researchers and fellow labmates Dr. Vinod P Raphael, Dr. Nimmy Kuriakose, Dr. Drishya Sashidharan, Dr. Sini Varghese, Dr. Binsi M Paulson, Mr. Ramesh N, Ms. Siji T B, Dr. Ragi K, Dr. Dinoop Lal S, Ms. Vidhya Thomas, Ms. Swathy T S, Ms. Raji, Ms. Memsy

C K, Ms. Savitha Unnikrishnan K, Mr. Martin Francis, Ms. Rohini Das K, Ms. Nithya, Ms. Neera, Ms. Cinu and Ms. Akhila for their unfailing encouragement and friendliness. I again thank my co-researcher Dr. Dinoop Lal S for his warm backup in times of need. The research related discussions with him were always highly interactive and informative and I will always be indebted to him for all the knowledge he shared with me.

I gratefully acknowledge Kerala State Council for Science Technology and Environment (KSCSTE) for selecting me as a KSCSTE research fellow and providing their fellowship fund that I could utilise for my Ph .D work.

I always remain thankful to various institutions for providing me facilities to do my work and undertake various analysis. I acknowledge CLF-KVASU, Mannuthy, STIC-CUSAT, Department of Physics, CUSAT, M G University, MES Keveeyam College Valanchery, Christ College, Irinjalakuda, IISC Bangalore and NIIST Trivandrum for allocating their instrumental facilities for my research work. I sincerely thank all the CHMK library staff, University of Calicut, and especially thank Dr. Vinod V M, Assistant Librarian, CHMK library, for conducting the plagiarism check of my thesis. I am also thankful to the Educare printing press, Thrissur, for their kind co-operation and help in many printing and documentation work during my research period.

It is impossible to extend enough thanks to my family members, especially my parents, mother-in-law, husband, son and brothers, who gave me much care, support and encouragement that I needed throughout the process. They all kept me going with strength and courage during the years of my research career. My special thanks to my friends in college and outside the college, who were always there when I needed a shoulder to lean on. I would also like to genuinely thank Late Prof. P.T. Manoharan, Dr. Unnikrishnan V and Ms Bindhu S for encouraging me to pursue my dreams. I place my sincere thanks to all other persons who offered me help directly or indirectly at different stages of my research career.

With heartfelt gratitude

ANJU ROSE PUTHUKKARA P

Dedication

To my parents
For raising me to believe that anything is possible

To my husband
For encouraging me to achieve everything possible

To my child
For always being the loving and understanding son

PREFACE

Water pollution is one of the major environmental problems faced by the world, drastically influenced by population stress and industrialisation. Iron-based nanoparticles have a significant role in the remediation of water pollutants as a cost-effective material. Among the iron-based nanoparticles, zero valent iron (Fe^0) particles have had a remarkable position in wastewater treatment for the last few years due to their environmental compatibility, high reactivity, fast kinetics and magnetic property. However, rapid oxidation and agglomeration are the significant drawbacks of Fe^0 nanoparticles. The thesis reports the studies conducted to develop stable and efficient Fe^0 based nanoparticles by incorporating different materials. The efficiency of prepared materials was evaluated by analysing the removal efficiency of organic dyes and hexavalent chromium (Cr(VI)) from water. The factors influencing the removal of Cr(VI) and malachite green dye were also discussed in the thesis.

The whole thesis is divided into eight chapters. A general introduction along with the literature review of properties, synthesis methods, modification routes and application of Fe^0 nanoparticles are discussed in chapter 1. Chapter 2 includes the materials and instruments used for the synthesis, characterisation and application of the studies. In addition, the general method followed for the Cr(VI) and dye removal studies were also discussed here.

In chapter 3, Fe^0 and the second metal (Cu, Ni and Zn) loaded Fe^0 nanoparticles were prepared by the liquid-phase reduction method. The establishment of the second metal on Fe^0 and characteristics of the prepared nanoparticles were studied by HRTEM, XRD and EDAX. This chapter compares the efficiency of Fe^0 and bimetallic iron nanoparticles to remove hexavalent chromium and organic dyes from water. Various techniques were used to confirm the removal mechanism of Cr(VI) and malachite green dye from water.

The application of biopolymer chitosan, as a stabilising agent of Fe^0 and Fe/Ni nanoparticles were discussed in chapter 4. The characteristics of chitosan stabilised Fe nanoparticles were studied by the HRTEM, XPS and FTIR techniques. The prepared nanoparticles were applied to remove Cr(VI) and triphenylmethane dyes and the removal efficiency was evaluated. The influence of chitosan and nickel loading on Fe^0 for removing malachite green dye was also discussed.

Chapter 5 of the thesis mainly focuses on the preparation of novel TiO_2-zeolite composites with different percentages of TiO_2 and their application for Fe^0 stabilisation. The TiO_2-zeolite composite was prepared by sonication of ingredients followed by the hydrothermal method. The incorporation of Fe nanoparticles into TiO_2-zeolite composite was done using wet impregnation method followed by the liquid-phase reduction. For comparative study with TiO_2-zeolite-Fe nanoparticles, TiO_2-Fe and zeolite-Fe nanoparticles were also prepared. The characterisation of TiO_2 and zeolite modified Fe nanoparticles were done by XRD, HRTEM, EDAX, FTIR and UV-visible spectroscopy. The study evaluated the efficiency of prepared TiO_2-Fe, zeolite-Fe and TiO_2-zeolite-Fe nanoparticles to remove Cr(VI) and malachite green dye from water. GC-MS/MS was done to identify the malachite green degradation products using TiO_2-zeolite-Fe nanoparticles.

Chapter 6 deals with the preparation of Fe nanoparticles using two novel plant extracts from *Abrus precatorius* (AP) and *Strychnos nux-vomica* (SN). GC-MS/MS analysis has been done to identify the volatile bioactive components present in the plant extracts. The iron nanoparticles were synthesised by simple mixing of iron salt solution and plant extracts and the characterisation of Fe nanoparticles were done by UV-visible spectroscopy, FTIR, HRTEM and EDAX. The efficiency of AP-Fe and SN-Fe nanoparticles for removing Cr(VI) and malachite green dye from water was also analysed.

The preparation of plant extract from *Triphala* (TP), an ayurvedic composition and synthesis of Fe nanoparticles from it were discussed in chapter 7. Fe nanoparticles using *Terminalia chebula, Terminalia belerica* and *Phyllanthus emblica* were also synthesised for comparative study. GC-MS/MS analysis has been done to identify bioactive components in *Triphala* extract. The UV-visible spectroscopy, FTIR, HRTEM and EDAX techniques were used to characterise the prepared Fe nanoparticles. The Cr(VI) and malachite green dye removal efficiency of prepared nanoparticles are also analysed.

Chapter 8 includes the brief conclusion of all the previous chapters and it also contains the practical significance of the work and the future scope of our investigation.

LIST OF ABBREVIATIONS

Fe^0	Zero valent iron
UV	Ultraviolet
HRTEM	High-resolution transmission electron microscopy
FTIR	Fourier-transform infrared spectroscopy
EDAX	Energy-dispersive X-ray spectroscopy
XRD	X-ray powder diffraction
XPS	X-ray photoelectron spectroscopy
GC-MS/MS	Gas chromatography coupled with triple quadrupole tandem mass spectrometry
LC-MS/MS	Liquid chromatography coupled with triple quadrupole tandem mass spectrometry
MG	Malachite green
MB	Methyl blue
MO	Methyl orange
MLB	Methylene blue
Cr(VI)	Hexavalent Chromium
Cr(III)	Trivalent Chromium
CS	Chitosan
T-Z	TiO_2-zeolite
AP	*Abrus precatorius*
SN	*Strychnos nux-vomica*
TP	*Triphala*
TB	*Terminalia belerica*
PE	*Phyllanthus emblica*
TC	*Terminalia chebula*

ABSTRACT

Industrialisation and urbanisation led to the contamination of groundwater and surface water to a large extent. Zero valent iron nanoparticle (Fe^0) is a promising material for water contaminants remediation due to its large surface area to volume ratio coupled with greater reactivity. However, the Fe^0 rapidly reacts with air and water and results in reduced reactivity due to oxidation and agglomeration. Our work aims to prepare modified iron-based nanoparticles with improved reactivity, stability and dispersibility without much secondary pollution. The reactivity of modified iron-based nanoparticles was evaluated by measuring the removal efficiency of hexavalent chromium and malachite green dye from water. Iron nanoparticle modification was done by depositing catalytic metal to the Fe^0 surface, encapsulating it with polymer and depositing Fe^0 on solid support. Green synthesis of Fe nanoparticles was done using plant extracts, which neither requires additional energy nor produces any hazardous by-products.

The specific objectives of our work include (1) synthesise Fe^0 and bimetallic Fe based nanoparticles using the chemical reduction method, (2) prepare chitosan stabilised Fe^0 and Fe/Ni nanoparticles, (3) develop zeolite and TiO_2 based novel composites as supporting and stabilising material for Fe^0 nanoparticles, (4) prepare Fe nanoparticles using plant extracts as green reducing agents, (5) evaluate the efficiency of synthesised nanoparticles in the removal of toxic hexavalent chromium and toxic dyes under different reaction conditions such as initial pollutant concentration, nanoparticle dosage, contact time and solution pH.

The synthesis of modified iron nanoparticles was carried out under an inert atmosphere and the collected samples were lyophilised. The characterisation of prepared nanoparticles was performed using UV-visible spectroscopy, HRTEM, EDAX, FTIR, XRD and XPS. UV-visible spectroscopy was used to analyse the remaining concentration of the pollutant after treating with Cr(VI) and toxic dyes. The degradation product of malachite green was analysed by LC-MS/MS and GC-MS/MS. The various modifications done on iron nanoparticles in our study improved the reactivity and stability of the iron nanoparticles.

LIST OF CONTENTS

TITLE | **PAGE NO.**

CHAPTER 1
Introduction and Literature Review

CHAPTER 2
Materials and Methods

CHAPTER 3
Comparative study on the reactivity of zero valent iron nanoparticles (Fe^0) and bimetallic iron-based nanoparticles for the removal of Cr(VI) and dyes from water

CHAPTER 4

Synthesis of polymer-stabilised Fe^0 and Fe/Ni bimetallic nanoparticles for the removal of Cr(VI) and triphenylmethane dyes from water

CHAPTER 5

TiO$_2$-zeolite composite modified Fe^0 nanoparticles for the removal of Cr(VI) and malachite green dye from water

CHAPTER 6

Green synthesis of iron nanoparticles using plant extracts of *Abrus precatorius* and *Strychnos nux-vomica* for the removal of Cr(VI) and malachite green dye from water

CHAPTER 7

Green synthesis of iron nanoparticles using ayurvedic composition *Triphala* and its constituents for the removal of Cr(VI) and malachite green dye from water

CHAPTER 8

Summary and Conclusion

List of Publications and Conference presentations

LIST OF FIGURES

CHAPTER 4

Synthesis of polymer-stabilised Fe^0 and Fe/Ni bimetallic nanoparticles for the removal of Cr(VI) and triphenylmethane dyes from water

CHAPTER 5

TiO_2-zeolite composite modified Fe^0 nanoparticles for the removal of Cr(VI) and malachite green dye from water

CHAPTER 6

Green synthesis of iron nanoparticles using plant extracts of *Abrus precatorius* and *Strychnos nux-vomica* for the removal of Cr(VI) and malachite green dye from water

CHAPTER 7

Green synthesis of iron nanoparticles using ayurvedic composition *Triphala* and its constituents for the removal of Cr(VI) and malachite green dye from water

LIST OF TABLES

CHAPTER 1

Introduction and Literature Review

Chapter 1

Introduction and Literature Review

1.1. Water pollution: causes, effects and solutions

Water treatment is an ever-growing research area since pure and clean water is essential for human well being. Industrialisation, urbanisation, growing population and natural phenomena cause water pollution worldwide. According to UN reports, over 2 billion people live in a water-scarce area. Water treatment becomes essential due to the uneven and insufficient distribution of freshwater resources for the ever-expanding water requirements of the increasing world population. Providing safe drinking water is a fundamental human right and a responsibility towards future generations. Drinking potable water should be free from any physical, chemical and biological pollutants which otherwise cause water-borne diseases to human beings.

Every year, thousands of people die or become diseased by water-borne diseases such as cholera, diarrhoea, typhoid and dysentery by consuming contaminated water. Water treatment can only provide safe drinking water because preventing contamination of source water is not always possible due to the mixing of untreated industrial and sewage water and poor hygienic practices in developing and underdeveloped countries. Based on the nature of the contaminant, they are classified into physical, chemical and biological. The contaminants imparting odour, colour and turbidity to the drinking water are considered physical contaminants. The presence of sediments and organic compounds could adversely affect the aesthetic beauty of water, which is unacceptable for human consumption. Chemical and biological contaminants can also affect the colour and odour of water. Chemical contaminants consist of organic contaminants such as dyes, pesticides and inorganic contaminants are mainly heavy metals and radioactive elements. Sewage water and industrial effluents are significant sources of chemical contaminants. Biological contamination mainly happens due to the microorganisms like viruses, bacteria and parasites.

Different techniques or materials are used to inactivate or eliminate the different contaminants present in the source water in water treatment. Emerging pollutants and radioactive components act as barriers to the water treatment system. Generally, coarse particles and turbidity can be removed from raw water through coagulation, pre-filtration and sedimentation techniques. Other common techniques employed in removing water contaminants include filtration, using a disinfecting agent, irradiation by UV and visible light, reverse osmosis, adsorption, electrolysis, electrodialysis, oxidation, ion exchange, precipitation, aerobic and anaerobic treatments. High operational cost and sophisticated operational systems make these techniques unappealing. Moreover, chemicals like chlorine compounds used in water treatment cause additional contamination in water. The untreated wastewater carrying rivers and channels cause groundwater pollution in the nearby areas. So it is essential to develop simple, environmentally compactable treatment techniques to treat raw water with low cost and more efficiency[1,2].

1.2. Nanotechnology: a small answer to bigger questions

The word "nanotechnology" infers the use and application of particles and materials in nanosize. In 1959, Richard Feynman, father of modern nanotechnology, proposed the idea "There's Plenty of Room at the Bottom". The idea of manipulating matter to atomic or molecular level traverse over the conventional subjects in science like physics, chemistry, biology and engineering[3,4]. Over the last few decades, the revolution in multidisciplinary nanotechnology has led to the invention of limitless engineered nanomaterials in diverse fields such as catalysis, electronics, drug delivery, monitoring and treatment of environmental pollution[5–12]. These applications were achieved by the distinctive chemical, magnetic, optical, mechanical, catalytic and electronic properties of nanomaterials with an extremely small size, surface and quantum effect[6,7].

Nowadays, nanomaterials demonstrate significant role in environmental protection by (i) pollution prevention, (ii) pollution detection and (iii) treatment/remediation of the pollutant[13]. Nanotechnology has an essential role in pollution prevention as it reduces/eliminates waste production and improves the effective use of resources like energy, raw materials and water. Nanocatalysts show high capability for the production of desired products in chemical engineering. For example, the high capacity and cycling constancy of Li-O_2 batteries can be attained by IrO_2 nanoparticles attached to N and Co co-doped reduced graphene oxide (Co-N-rGO)[14]. In another study, biodiesel was produced from waste cooking oil and methanol using calcium oxide (CaO) nanocatalyst[15]. Detection of pollutants has been done using nanomaterials that give more sensitive results at a low cost. For example, gold nanoparticles were used to detect endosulfan pesticide in mg/L level[15] and Bi modified reduced graphene oxide was applied to detect Cd^{2+}, Pb^{2+}, Zn^{2+} and Cu^{2+} ions in water[16].

The most researched area of nanotechnology in environmental protection is the treatment of pollutants and the purification of contaminated air, water and soil. Nanomaterials can remove toxic gases in the air; for example, carbon nanotubes were used for the adsorption of dioxins, NO_x and CO_2 from the air. Porous structure and surface functional groups present in carbon nanotubes through chemical and thermal treatment are the reasons behind the specific properties of carbon nanotubes in pollutant adsorption[13]. Adsorption, filtration through nanomembranes, oxidative and reductive catalysis are the general mechanisms for removing air pollutants through nanomaterials. Different nanomaterials are used for different purposes, such as calcium-based nanomaterials used for CO_2 adsorption, TiO_2 nanomaterials used for Hg^0 removal and α-Fe_2O_3 nanocubical catalyst for the conversion of CO to CO_2 at low temperature[17].

1.3. Nanotechnology in water treatment

The non-availability of clean drinking water is a critical environmental problem facing several countries[18]. Nanotechnology introduced novel methods for pollutant treatment which also improves the efficiency of conventional water treatment methods. High efficiency, small size, multifunctionality and high selectivity for specific contaminants make nanomaterials more attractive, along with the cost-effectiveness and simple instrumental setup involved[2]. The physical and chemical properties of nanomaterials vary with size, shape and composition. The nanoparticles interact more effectively with the contaminants compared to bulky composites. Nanomaterials have a large surface area, so a substantial fraction of atoms present on the surface will increase nanoparticle reactivity. The small particle size of nanoparticles also causes quantum confinement effect and localised surface plasmon resonance. Due to this, the search for more sustainable, efficient, affordable nanomaterials is a continual process in nanotechnology. Till now, different types of nanomaterials has been used for the remediation of water contaminants. They can be broadly classified into nanosorbents, nanofilters, nanomembranes, nano-based disinfectants, nanocatalysts and nanoparticles for reduction purposes. Furthermore, these nanomaterials are in various morphological forms like nanoparticles, nanotubes and nanosheets.

1.3.1. Nanosorbents

Adsorption is a surface phenomenon in which the adsorbate comes into contact with the adsorbent and accumulates on the surface of the adsorbent due to intermolecular forces of attraction. Depending on the nature of attraction between adsorbate and adsorbent, the adsorption process is broadly categorised into physisorption and chemisorption[19]. Chemisorption is more selective than physisorption due to the electron transfer occurred in the chemical process. Different types of nanomaterials such as carbon-based nanomaterials, metal and metal oxide based nanomaterials, nanopolymers and zeolites have been used for the adsorption of water contaminants

Carbon-based nanomaterials: Traditionally, activated carbon is used for the adsorption of heavy metals and dyes due to the large surface area and high porosity. Activated carbon has a low cost since it is prepared from readily available materials like coal, wood, coconut shells and agricultural waste. Even though activated carbon possesses a weak acidic ion-exchange character, they show difficulty to remove pollutants at parts per billion level. This drawback of activated carbon has been overcome by a new era of nanomaterials like carbon nanotubes, graphene and fullerenes. The unique chemical, structural, mechanical and physical properties of carbon nanotubes make them helpful in removing dyes and heavy metals. The functionalisation of carbon nanotubes with hydroxyl and carbonyl groups increases pristine carbon nanotubes' effectiveness for dye removal[19]. According to Gao et al., the carbon nanotubes show good efficiency for the adsorption of multiple metal ions (nickel, copper, zinc and cadmium) from an aqueous solution. The surface features, ion exchange process and electrochemical potential controlled the adsorption mechanisms[20].

Another nanomaterial used for the adsorption of water contaminants is graphene, a two-dimensional sheet material consisting of a single layer of carbon atoms. Graphene-based nanomaterials include graphene, graphene oxide, reduced graphene oxide and their modifications. Generally, graphene sheets have a hydrophobic surface and exhibit a strong adsorption capacity for organic pollutants. Different functional groups such as epoxides, alcohols and carboxylic acids in graphene oxide nanomaterials make them suitable adsorbents for organic and inorganic pollutants. Modifying with hydroxyl, carboxyl, sulfonate functional groups and incorporating other nanomaterials to pristine graphene-based nanomaterials improved its adsorption capacity[21]. The mechanism suggested for the adsorption of pollutants by pristine graphene are p–p interaction and hydrophobic forces and that for graphene oxide are electrostatic, hydrogen and Lewis acid-base interactions[2].

Metal and metal oxide nanoparticles: These are common sorbents due to their high surface area, stability and reusability. Surface complexation, intraparticle diffusion and micropore active site interactions are the main forces behind the adsorption mechanism. Prevalent metal and metal oxide nanoparticles used for the adsorption process are Fe^0, Fe_3O_4, MnO, TiO_2, ZnO, SiO_2 and Al_2O_3[2,18,22]. Fe^0 is an excellent adsorbent for heavy metals and organic pollutants due to its high surface area, low cost, high reactivity, magnetic properties and environmental compatibility[2]. Recently Hasan et al. effectively used biocharcoal supported nanoscale Fe^0 to treat synthetic stormwater containing high concentrations of heavy metals (Cu, Cd and Zn)[23]. In another study, Abbas et al. synthesised surfactant modified maghemite nanoparticles and effectively removed different cationic dyes, including brilliant cresyl blue, thionine and janus green b from aqueous media[24].

Surface functionalisation of SiO_2 nanoparticles gives high effectiveness for the adsorption of dyes and heavy metals[2]. Rachel et al. successfully synthesised glycine functionalised SiO_2 nanoparticles and used them for effective absorption of malachite green dye from aqueous solution[25]. The γ-Al_2O_3 shows remarkable thermal stability and adsorption capacity and interacts with various chemical species such as heavy metals and dyes, using reactive sites[26]. Defluoridation of aqueous solutions have been studied by Sareh et al. using Al_2O_3 nanoparticles. The proposed mechanism of defluoridation is the complexation of Al_2O_3 nanoparticles with fluoride ions[27]. TiO_2 nanoparticles are significant in removing organic and inorganic pollutants due to their photocatalytic and adsorption mechanisms[2]. TiO_2 and TiO_2-based materials are widely used to remove inorganic and organic arsenic species in water. The factors influencing the adsorption capacity of TiO_2 are specific surface area, degree of crystallinity and surface modification. The surface of TiO_2-based materials makes inner-sphere complexes with inorganic and organic arsenic from water[28]. Another photocatalyst, ZnO also used for the adsorption of dyes and heavy metals[29]. Fan et al. studied the adsorptive removal of cationic and anionic dyes using ZnO nanoparticles and these nanoparticles show high adsorption capacity, good selectivity and reusability for removing malachite green, acid fuchsin and congo red dyes. Chemical precipitation, electrostatic attraction and hydrogen bonds are the adsorptive mechanisms for dye removal[30].

1.3.2. Nanocatalysts and nanoparticles for reduction

The particle size of the catalyst has a significant impact on their activity in contaminant remediation. Materials with catalytic properties and at least one of the dimensions in the nanoscale are called nanocatalysts. Typically, nanocatalyst has high activity due to its high surface to volume ratio so that more pollutants can interact with the surface of the catalyst[31,32]. Different types of nanomaterials such as noble metal nanoparticles, nano-based photocatalysts, nano-based Fenton-like catalysts and transition metal nanoparticles are employed in the catalytic degradation of water pollutants[22].

Nanomaterials for the catalytic oxidation of pollutants: Nanomaterials like TiO_2 and ZnO act as photocatalysts for the oxidation via degradation of organic pollutants to nontoxic materials. The significant advantages of these materials are high photoconductivity, high photostability, low toxicity, low cost and easy availability. In photocatalysis, the charge transfer from the valence band to the conduction band results in the formation of hydroxyl radicals and these highly reactive radicals cause the oxidation of pollutants[22]. Recently, Krishnamoorthy et al. synthesised TiO_2 nanoparticles for the photocatalytic degradation of methylene blue and congo red dyes under UV–visible light. Their studies show that alkaline condition is favourable for methylene blue degradation and acidic condition for congo red degradation[33]. The modified entities of TiO_2 and ZnO photosensitive nanoparticles have also been studied for contaminant degradation[13].

Iron-based nanomaterials were used as Fenton-like catalysts in the presence of hydrogen peroxide to degrade organic pollutants by redox reactions, dehydrogenation and electrophilic addition. The hydroxyl radicals produced by the Fenton reaction result in the degradation of organic pollutants[21]. Kuang et al. reported the mineralisation of monochlorobenzene through oxidation using green synthesised iron nanoparticles as heterogeneous Fenton-like catalysts[34]. Irradiating UV-visible radiation with the Fenton system can improve the reaction process, known as the photo-Fenton reaction. Guadalupe et al. used Fe^0 nanoparticles to degrade the 2-chlorophenol through the photo-Fenton reaction[35]. The efficiency of the Fenton system can be improved by ultrasonication. In the degradation of bisphenol A by Ruixiong et al., ultrasonication reduces the reaction's pH dependence and increases the degradation of bisphenol A[36]. Another important category of Fenton reaction is the Electro-Fenton reaction, in which continuous electrogeneration of hydrogen peroxide occurs from the reduction of oxygen on a carbonaceous cathode.

Sebastian et al. studied the degradation of antibiotic nafcillin using bimetallic Fe/Cu nanoparticles. Their studies show that Fe/Cu bimetallic nanoparticles completely removed the drug at a lower duration of electrolysis than using individual Fe and Cu nanoparticles. The reaction intermediates and by-products of the drug degradation are oxalic, oxamic, formic and acetic acids. Electrocatalytic oxidation processes are a newly emerging technology for the degradation of organic pollutants through oxidation. In this method, reactive oxygen species were generated in situ at the anode surface at high current and these reactive species degraded the organic pollutant to mineralised form[37]. Electrocatalytic degradation of tetracycline in wastewater has been done by Wenhao et al., using electrospun iron/cobalt alloy nanoparticles on carbon nanofibers. This nanocomposite shows outstanding stability, recyclability and reusability and it also completely degrade the tetracycline into CO_2 and H_2O[38].

Nanomaterials for the catalytic reduction of pollutants: Metal nanoparticles were used for the catalytic reduction of organic and inorganic pollutants. Palladium based nanomaterials were used for the reduction of hexavalent chromium from water. Weixia et al. studied the reduction of Cr(VI) using two types of Pd based nanoparticles, PVP-stabilized Pd colloidal nanoparticles and the Pd–Fe_3O_4 magnetic catalyst. PVP acts as stabilising and capping agent for Pd nanoparticles, increasing the nanoparticle's Cr(VI) reduction capacity. The incorporation of Fe_3O_4 to Pd nanoparticles improved the nanoparticle's efficiency and recyclability due to their magnetic activity[39]. The catalytic degradation of nitrophenols and dyes was investigated by Soha et al., using two silver-based nanocomposites. The first was supported on cellulose acetate filter paper and the second was impregnated into titanium dioxide. In the presence of $NaBH_4$, these silver-based nanoparticles show high degradation efficiency for 4-nitrophenol, 2-nitrophenol, 2-nitroaniline, trinitrophenol, rhodamine B dye and methyl orange dye[40]. Metallic Ni and Cu nanoparticles embedded carbon sheets are useful for the $NaBH_4$-mediated reduction of 4-nitrophenol, methyl orange and methylene blue[41]. In another study, formic acid was used as a reducing precursor and Pd/Ag alloy nanoparticles supported on amine-functionalised SiO_2 were used as a catalyst for reducing nitrate in water[42].

Nanoparticles as reducing agents: Nanoscale zero valent metals were used to reduce water contaminants due to their strong chemical reducibility, high efficiency and large specific surface area[7,43]. The reactivity, mobility, longevity and toxicity of the zero valent metals are significant for selecting appropriate nanoparticles for water pollution remediation[6]. The most investigated nano zero valent metal as a reducing agent is Fe^0 due to its low cost and high reduction potential. Fe^0 can be used to reduce halogenated organic compounds, inorganic anions and heavy metals[44]. Hocheol et al. studied the reduction of eight chlorinated ethanes using Fe^0 nanoparticles. They found that reductive β-elimination was the major pathway and reductive α-elimination and hydrogenolysis were concurrent pathways to form fewer chlorinated ethanes using Fe^0 nanoparticles[45]. Other metals such as zero valent zinc and copper can also substitute Fe^0 nanoparticles to remove contaminants. However, the toxic effect of zinc and copper at higher concentrations makes them less attractive for contaminant remediation[7]. Mario et al. compared the Cr(VI) reduction efficiency of Fe^0 and zero valent copper nanoparticles and found that Fe^0 nanoparticles are more effective than Cu^0 nanoparticles[46].

1.3.3. Nanofiltration and Nanomembranes

Nanofiltration filters out the unwanted ions, organic molecules and heavy metals from water using pressure as a driving force with low energy input. Nowadays, it is one of the best methods for drinking water purification due to its high selectivity and availability of various nanomembranes[13]. These membranes are flexible, profitable and easy to prepare. Different types of membranes have a variety of properties. Ceramic membranes show good chemical, mechanical and thermal properties. Polymeric membranes show high water flux but have a high fouling rate and less chemical resistance[47]. The properties of nanomembranes have been improved through interfacial polymerisation, incorporating NPs, electron beam irradiation, UV grafting/photografting, plasma treatment and layer-by-layer modification[21]. Incorporating functional nanoparticles into the membrane makes them multifunctional materials for water treatment. For example, Hem et al. synthesised a stable silver-doped fly ash/polyurethane (Ag-FA/PU) nanocomposite multifunctional membrane with less bio-fouling. These membranes' specialities were spider-web-like nano-neeting for nanoparticles separation, enhanced absorption capacity to remove carcinogenic arsenic and toxic organic dyes and antibacterial properties[48].

1.3.4. Nano based disinfectants

Antimicrobial nanotechnology is one of the emerging research areas in nanotechnology and different nanomaterials follow various mechanisms for antimicrobial activity. Chitosan nanoparticles inhibit the enzyme activity and DNA synthesis of bacteria[49,50]. Silver nanoparticles show different mechanisms such as i) they can penetrate in the bacterial cell wall, change the cell membrane texture leading to cell death, ii) the reactive oxygen species produced from Ag nanoparticles cause oxidative stress in the microorganism and Ag ions interrupt the replication of DNA[51]. The reactive oxygen species produced from photocatalysts like TiO_2 will damage the cell components of microorganisms. According to Sunanda et al., the photokilling of TiO_2 nanoparticles have two steps; in the first step, the outer membrane has disordered, which will ease the penetration of reactive species into the inner membrane and in the second step, the cytoplasmic membrane gets disordered and cause the death of bacteria[52].

Carbon nanotubes can also kill the bacteria and the reported mechanism for the destruction of bacteria are i) physical piercing, ii) oxidative stress, iii) length-dependent wrapping, iv) cell membrane damage by direct contact, v) penetration of the bacterial lipid membrane and vi) laser photothermal ablation[53]. The antibacterial activity of fullerene nanoparticles differs in gram-positive bacteria and gram-negative bacteria. In gram-negative bacteria, the proportion of unsaturated fatty acids decreases and the proportion of cyclopropane fatty acids increase in the bacterial cell wall and this will cause the inactivation of the bacteria. In gram-positive bacteria, the alterations in the phospholipid structure, increased permeability of the cell membrane and cell wall destruction causes the death of bacteria[54]. In water treatment systems, iron-based nanomaterials have a significant position compared to other nanomaterials mediated techniques due to their capacity for reduction, oxidation, complexation and adsorption of water contaminants.

1.4. Iron-based nanomaterials

Iron is a reactive metal and the fourth most abundant metal in the earth's crust[55]. Generally, iron exists as Fe^{2+} and Fe^{3+} in the earth's lithosphere. Fe^0, bimetallic/trimetallic iron-based compounds and iron oxides are the major iron-based nanomaterials[56–58]. Fe^0 symbolises iron in zero oxidation state or elemental state. Iron oxide is the common name used to denote the oxides, hydroxides and oxy-hydroxides of Fe^{2+} and Fe^{3+} cations with O^{2-} and OH^- anions. Fe_2O_3, Fe_3O_4, FeO, FeO(OH), $Fe(OH)_3$, $Fe(OH)_2$ and $Fe_5HO_8.4H_2O$ are the common iron oxides seen in the earth's crust. Most iron oxides have the Fe^{3+} oxidation state and low solubility[59]. Along with high reactivity, small particle size and large surface area, the iron nanomaterials also possess less toxicity, biodegradability, magnetic susceptibility and dual redox properties in water. The precursors used to synthesise iron-based nanomaterials have low costs and are widely available[60]. Fe^0 becomes a benchmark term among different iron-based nanomaterials due to its unique properties[61,62].

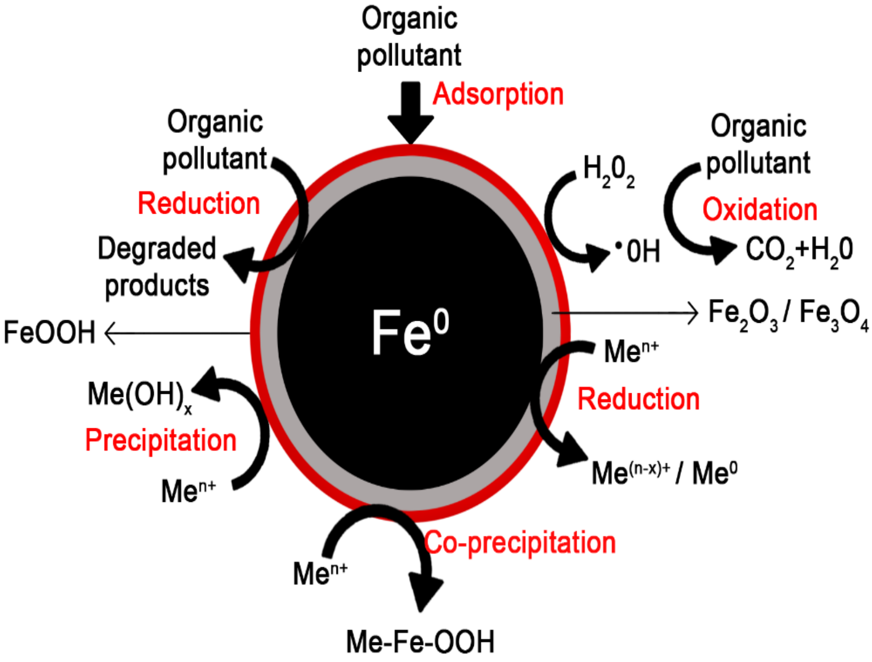

Figure 1.1 *General mechanism of zero valent iron (Fe^0) nanoparticles for pollutant removal*

1.5. Zero valent iron (Fe^0) nanoparticles and their properties

Around the last three decades, the Fe^0 or metallic iron nanoparticles were widely employed to remediate wastewater, drinking water and groundwater[63,64]. The standard electrode potential of Fe^{2+}/Fe^0 is -0.440 eV, which makes Fe^0 a strong reducing agent for oxidative pollutants. Reduction is the major mechanism carried out by the Fe^0 nanoparticles and adsorption and oxidation are the other mechanisms tailed by Fe^0 nanoparticles. The general mechanism of Fe^0 nanoparticles is shown in figure 1.1. Core-shell structure, large specific surface area and magnetic property are the three key influencing properties behind the high reactivity of Fe^0 nanoparticles[44]. Generally, Fe^0 nanoparticles have a core-shell structure with a metallic iron core and iron oxide shell. The iron oxide/hydroxide shell formation is due to the oxidation/corrosion of the metallic (Fe^0) iron core. The oxidation of iron with oxygen and water (equation 1.1 & 1.2) can be expressed as follows.

$$2Fe^0(s) + 4H^+(aq) + O_2(aq) \rightarrow 2Fe^{2+}(aq) + 2H_2O \qquad (1.1)$$

$$Fe^0(s) + 2H_2O(aq) \rightarrow Fe^{2+}(aq) + H_2(g) + 2OH^-(aq) \qquad (1.2)$$

The core-shell structure contributes to the unique properties of Fe^0. The core Fe^0 have strong reducing power for organic pollutants. The iron oxide shell can improve/impede the electron transfer from Fe^0 and/or molecular oxygen activation. The defect in the oxide shell can improve the reduction capacity of Fe^0 nanoparticles. The physical and chemical composition of the oxide shell, such as porosity and electronic conductivity, can influence the mass transfer property and reactivity of Fe^0 nanoparticles. For example, the conductive iron oxides like FeO and Fe_3O_4 allows electron transfer, but oxides like FeO(OH) inhibit the electron transfer from the iron core to the iron oxides shell. It may be due to the difference in bandgap energy of FeO(OH) and others since FeO and Fe_3O_4 have significantly less bandgap energy than FeO(OH). It is important to note that contaminant reduction was more thermodynamically favourable in oxide shell compared to iron core surface. However, it is greatly influenced by the porosity of the iron oxide. As the porosity decreases, oxide shell density increases with prolonged reaction time due to the formation of oxyhydroxides. Usually, molecular oxygen is undesirable for the reductive mechanism of Fe^0 due to the reactivity loss by unwanted reaction with molecular oxygen. Nevertheless, this molecular oxygen can produce reactive oxygen species like hydrogen peroxide, hydroxyl radical and superoxide radical by reacting with the Fe^0. Moreover, the reactive species can oxidise the contaminants to low molecular weight or complete mineralisation to CO_2. Another important thing is that the oxide shell of iron nanoparticles mainly mediates the adsorption mechanism. The pollutant adsorption to the shell of the iron nanoparticles improves the efficiency for the reduction of organic and inorganic pollutants[65]. The large specific surface area provides more reaction sites on the surface of Fe^0 nanoparticles. It will increase the reaction between the contaminant and Fe^0 nanoparticles. Along with large specific surface area, high-density reactive surface sites and greater intrinsic reactivity of surface sites contributed to the enhanced reactivity of Fe^0

nanoparticles. The magnetic property of nanoparticles accelerates the aggregation of Fe^0 nanoparticles, leading to a decrease in the reactivity of Fe^0 nanoparticles[44].

In the 1990s, wang et al. applied nanoscale iron nanoparticles to treat trichloroethylene (TCE) and Polychlorinated biphenyl (PCB)[66]. In the years that followed, Fe^0 nanoparticles were used for the degradation or removal of various water pollutants such as antibiotics[67], halogenated organic compounds[68,69], nitro compounds[70], explosives[71], pesticides[72,73], inorganic anions[74], heavy metals/metalloids[75], dyes[76–78] and radioactive elements[57]. Even though the major mechanism of Fe^0 nanoparticles for pollutant removal is considered as adsorption, oxidation via Fenton reaction and reduction, the other mechanisms like complexation and co-precipitation also occur simultaneously and sequentially[79]. The electron transfer from Fe^0 to pollutant reduces the pollutant and transforms the Fe^0 to non-toxic Fe^{2+} and Fe^{3+} species[55]. The reductive properties of Fe^0 were mainly due to the three reductive (Fe^0, Fe^{2+} and H_2) species. Gotpagar et al. proposed three mechanisms for the dehalogenation of TCE, in that the most prevalent one is reduction of TCE by direct reduction of Fe^0. Along with that, reduction by H_2 (produced during the corrosion process) and reduction by Fe^{2+} ion (produced by the corrosion process) improved the reductive dehalogenation of TCE[80]. Heavy metals or metalloids are removed by the absorption or chemical precipitation mechanism. Different heavy metals possess different mechanisms using Fe^0 nanoparticles due to their difference in standard electrode potential since the standard electrode potential of Fe^0 nanoparticle is −0.44 V. Reductive precipitation happens in metals with much higher standard electrode potential than Fe^0. Sorption and partial chemical reduction occur in metals that have slightly more positive standard electrode potential than Fe^0. Lastly, sorption/surface complexation occurs in metals with a more negative standard electrode potential than Fe^0[62]. Another application of Fe^0 nanoparticles is as a Fenton-like catalyst for the degradation of organic contaminants. Fe^0 reacts with an oxygen molecule and produces H_2O_2, which is reduced to water by accepting two more e^- from Fe^0. The resulting Fe^{2+} and H_2O_2, known as Fenton reagent and hydroxyl radicals produced during the Fenton's reaction, could act as the oxidising agent for organic compound degradation[81]. Generally, the removal/degradation mechanism by Fe^0 nanoparticles depend on various parameters, including the type of pollutant, availability of oxygen and pH[82,83].

Large scale application of Fe^0 nanoparticles is widespread in the USA compared to Europe and other countries[84]. In 2009, Namen et al. studied Cr(VI) removal in groundwater using Fe^0 filings, Fe^0 powder and Fe^0 nanoparticles and found that Fe^0 nanoparticles are more efficient for Cr(VI) removal. Fe^0 nanoparticles are also helpful for municipal wastewater treatment[85,86]. The laboratory-scale continuous flow system is tested for nitrate reduction using Fe^0 nanoparticles and found that Fe^0 nanoparticle reactivity is vulnerable to groundwater constituents[87].

Even though the Fe^0 nanoparticles are highly effective for pollutant remediation, they also face practical application difficulties, including reactivity loss due to the intrinsic passive layer, aggregation tendency, less stability, reduced mobility, narrow working pH and low working pH selectivity for contaminants[88]. The oxygen and water molecules present in the environment reacted with Fe^0 to create a passive layer on the surface of nanoparticles. The formed iron oxide layer on the surface of the Fe^0 nanoparticles showed some ability for the adsorption of pollutants even though this iron oxide layer decreases the reduction capacity of Fe^0 nanoparticles[59]. Despite the disadvantages of the Fe^0 nanoparticles, their low cost, environmental compatibility and biodegradability make them a central attraction for water pollution remediation by researchers worldwide.

1.6. Synthesis of zero valent iron (Fe^0) nanoparticles

Several methods for producing Fe^0 nanoparticles include physical, chemical, and biological methods. For example, chemical reduction methods[89], electrochemical methods[90], ultrasound-assisted methods[56] and carbothermal reduction methods[91] etc. Generally, top-down and bottom-up approaches are followed widely to synthesise Fe^0 nanoparticles. The size, shape and reactivity of the nanoparticles are influenced by the synthesis method adopted. In top-down approaches, micro/granular iron particles are crushed into nanosized particles through mechanical or chemical[92]. Ball milling, noble gas sputtering and laser ablation are the top-down methods commonly used for Fe^0 nanoparticles production.

Ball milling: In ball milling, micro iron particles are broken down to Fe^0 nanoparticles by the mechanical forces created on stainless steel beads in a high-speed rotary chamber[93]. The formed particles have an irregular shape and high surface energy to cause a strong aggregation tendency[92]. The milling process influences the size, shape and reactivity of Fe^0 nanoparticles. The conventional ball milling process uses organic solvents like mono ethylene glycol to produce flattened iron nanoparticles. Ribas et al. established that introducing fine alumina powder to the organic solvent containing ball milling system breaks the iron flakes into smaller particles[94]. Shaolin et al. verified that solvent-free Fe^0 nanoparticles with particle size below 50 nm were formed after 8 hours of precision milling using micro iron as precursors[93]. Ball milling is helpful for large scale industrial production and it does not require any toxic and expensive chemicals.

Laser ablation: In this method, the iron metal target is locally melted and vaporised by the laser pulse. When the surrounding medium cools the hot metal atoms, the metal nanoparticles are formed from it[95]. It is a small scale synthesis method and the formed nanoparticles will easily get oxidised in the presence of oxygen and water. Yosmery et al. synthesised Fe^0 nanoparticles with a mean particles size of 17 nm by laser ablation method and stabilised by surfactant sodium dodecyl sulfate. They used a medium with a high H^+ concentration during the synthesis, which reduces the oxide shell thickness[96].

The bottom-up approach synthesises Fe^0 nanoparticles from either iron oxide nanoparticles, iron-containing molecules or dissolved iron salt solution using various reducing agents. Reduction using chemical reducing agents like $NaBH_4$, carbothermal reduction, electrochemical deposition, chemical vapour deposition and reduction using biogenic compounds are bottom-up methods for Fe^0 nanoparticle production[88,95].

Liquid-phase reduction: Reduction of the iron metal salt solution using a potent reducing agent like sodium borohydride under an inert atmosphere is the most commonly practised one. After the slow addition of $NaBH_4$, the formed black precipitate was washed with water, ethanol and acetone, then vacuum filtered and stored in airtight vials[92]. Good efficiency, the requirement of a short time for synthesis, high reactivity and easy to perform reaction are the advantages of sodium borohydride mediated synthesis of nanoparticles[97]. However, this method has shown some drawbacks due to the high cost and the toxic effect of potent reducing agents and less stability of nanoparticles[98]. According to Sungjun et al., $NaBH_4$ reduces the $FeCl_3$ salt solution and disintegrates the formed Fe^0 nanoparticles to smaller particle sizes[99]. Heesoo et al. established that washing and drying conditions during the synthesis of zero valent iron nanoparticles influence the surface characteristics of Fe^0 and reactivity towards contaminants. Fe^0 nanoparticles reactivity can be improved using volatile solvents for washing and drying in anaerobic conditions[100].

Carbothermal reduction: In the carbothermal reduction method, high temperature and the presence of gas reducing agents like H_2, CO and CO_2 lead to the formation of Fe^0 nanoparticles using iron oxide nanoparticles or aqueous salt solutions of Fe^{2+} precursors[92]. These gaseous reducing agents were formed by the thermal decomposition of carbonaceous materials like biochar and carbon black[88]. Lura et al. synthesised Fe^0 on carbon black under argon atmosphere at a high temperature of 600-800°C[91].

Electrochemical deposition: Electrochemical deposition method uses electric current, electrodes (cathode and anode) and Fe^{2+}/Fe^{3+} salt solutions for the Fe^0 production through electrolysis. The atoms of iron deposited on the cathode have a high tendency for agglomeration and it can be overcome by introducing cationic surfactants and ultrasonic waves[88]. Chen et al. synthesised Fe^0 nanoparticles by combining electrochemistry and ultrasonic vibration. Fe^0 nanoparticles of 1–20 nm diameter and 25.4 m^2/g specific surface area were produced using platinum as cathode and cetylpyridinium chloride as dispersion agent[90].

Chemical vapour deposition: In this method, pyrolysis of organoiron compounds like iron pentacarbonyl in the gas phase under inert conditions will give Fe^0 nanoparticles[95]. Choi et al. synthesised Fe^0 nanoparticles through the chemical vapour deposition method using iron pentacarbonyl [$Fe(CO)_5$] as iron precursor under flowing helium atmosphere. An increase in the decomposition temperature during the reaction causes an increase in the particle size of nanoparticles. The formed spherical core-shell nanoparticles have a particle size between 5 to 13 nm[101].

Biogenic synthesis: The toxic effect of chemicals and other drawbacks of conventional methods promotes the environment-friendly production of Fe^0 nanoparticles. Biogenic materials were used for the green synthesis of nanoparticles and also it could act as both stabilising and reducing agents for nanoparticles.

The abundance and easy availability of plants make them a significant candidate for biogenic synthesis. The secondary metabolites, enzymes and other plant biomolecules are the factors behind the reducing capacity of plant biomaterials. Polyphenols, flavonoids, amino acids, terpenoids, reducing sugars, steroids, saponins, vitamins, alkaloids and organic acids are the main plant biomolecules used to reduce iron ions[102,103]. Different plant parts followed various mechanisms for reducing Fe^0 nanoparticles due to the difference in bioactive components containing them. Extracts of leaves, seeds, fruits, bark and flowers were applied to reduce Fe^0 nanoparticles. Additionally, plant extracts' stabilising and capping property decreases the aggregation and controls nanoparticles' morphology. Researchers found that the green synthesis method for the Fe^0 nanoparticles lessens the use of stabilising agents during synthesis. Low toxicity, more availability, simple and rapid synthesis route, more energy efficiency, low cost, faster reaction, good stability of nanoparticles, environmental compatibility and significant capability to control morphology, size and growth of the nanoparticles are also advantageous of plant-based synthesis Fe^0 nanoparticles. The mechanism of phytogenic Fe^0 nanoparticles for pollutant removal is almost similar to Fe^0 nanoparticles. In some cases, plant extract itself shows some capacity for pollutant removal. Even though the plant-mediated Fe^0 nanoparticles have tremendous advantages, they also have drawbacks. The significant issues are the incomplete reduction of Fe^{2+} ions to Fe^0 nanoparticles by the plant components and lower reactivity and surface energy of phytogenic Fe^0 nanoparticles compared to chemically prepared Fe0 nanoparticles[104–106].

Tea leaves are one of the most commonly used plant extracts to synthesise Fe^0 nanoparticles. The tea extract contains many polyphenols and caffeine, which acts as a reducing, capping and stabilising agent during the preparation of Fe^0 nanoparticles[34,107]. Typically, a single pot synthesis method is followed for the tea leaf extract based synthesis of Fe^0 nanoparticles. The iron precursor (ferric chloride/ferric nitrate/ferrous sulphate) was treated with the tea extract at a specific volume ratio under room temperature and eventually, dark greenish/brown/black nanoparticles were formed within a few minutes. Hoag et al. used a 2:1 ratio for 0.1 M $FeCl_3$ and 20 g/L green tea extract and produced spherical nanoparticles of 5 to 15 nm particle size[107]. Creda et al. compared the properties of green synthesised and chemically ($NaBH_4$) synthesised nanoparticles. Different kinds of iron nanoparticles such as lepidocrocite, magnetite and Fe^0 nanoparticle were produced by blueberry leaf extracts and this may be due to the presence of different phenolic compounds with different reducing and complexing capacities. Previous studies show that blueberry leaves have phenolic compounds (e.g. caffeic acid, chlorogenic acid and ferulic acid) with high reducing potential. Compared to chemically synthesised Fe^0 nanoparticles, less agglomerated and more dispersible Fe nanoparticles are formed by blueberry leaf extract[108].

Different parts of fruit such as peal, albedo, pulp and seed were used to synthesise the Fe^0 nanoparticles. Citrine fruit extracts are the most widely investigated fruit materials for producing Fe^0 nanoparticles. Machado et al. utilised the juice industry waste of citrine fruits such as orange, lime, lemon and mandarin to synthesise Fe^0 nanoparticles. The peel, albedo and pulp of these fruits were collected and its bioactive ingredients were extracted using water. The green Fe^0 nanoparticles are produced by the simple mixing of fruit extract and iron (III) solution. The fruit extract created Fe^0 nanoparticles with diverse sizes, shapes and agglomeration. The concentration and chemical composition of the extract, temperature and reaction time are the parameters that influenced the size and shape of the Fe^0 nanoparticles. The majority of the Fe^0 nanoparticles except the orange pulp and albedo did not show any settlement, making stable dispersions in the aqueous medium. The authors professed that citrine fruits extracts could be used to synthesise Fe^0 nanoparticles[109]. The unique chemical properties of flowers made them an appropriate material for generating various nanoparticles. Sravanthi et al. suggested a novel green method for preparing Fe^0 nanoparticles using *Calotropis gigantea* (CG) flower extract as a reducing and capping agent and the *Pithecellobium dulce* seeds and chitosan as green stabilising agent and template. *Calotropis gigantea* flower extracts were prepared by boiling in an aqueous medium and it was mixed with $Fe(NO_3)_3.9H_2O$ in a 1:1 ratio. The formed nanoparticles were mixed with chitosan and Pithecellobium dulce seed powder. A large number of polyphenols present in the flower extract helps the reduction of iron precursors. More phenolic groups provide more anti-radical capacity consecutively more antioxidant ability. Post grafting of iron nanoparticles using biomaterials and chitosan helped to prevent the oxidation and agglomeration of iron nanoparticles. The particle size of nanoparticles prepared by flower extract is between 50-90 nm and polydisperse[110].

The synthesis of Fe^0 nanoparticles using root extract is rare. Green Fe^0 nanoparticles were produced through the root extracts of *Ferula persica* as a reducing agent and $FeSO_4 \cdot 7H_2O$ as an iron precursor. *F. persica* is an essential medicinal plant since it contains a broad range of bioactive agents. Root extract was prepared by mixing the root tissue powder of *F. persica* with water and tailed by heating at 90°C for 1 hour. During the synthesis of green Fe^0 nanoparticles (G-Fe^0), the root extract was mixed with the iron sulphate solution for 2 hours at pH 8. The formed black precipitate was collected through centrifugation, washed with deionised water, and dried. These prepared nanoparticles showed the tendency for oxidation due to the high reactivity of Fe^0. To overcome this problem, β-cyclodextrin (βCD) was applied as a stabilising and capping agent for iron nanoparticles. The primary antioxidant constituent of *F. persica* is ferulic acid and coumarins, forming the resonance-stabilised phenoxy radicals. The reduction of metal ions through *F. persica* was assigned to the resonance stabilisation and ferulic acid/coumarin dimer formation[111].

1.7. Modification on Fe^0 nanoparticles

Fe^0 nanoparticles have a few drawbacks despite several advantages due to high surface energy and intrinsic magnetic interaction, which will cause chains like aggregation, rapid surface oxidation and microscale iron particle formation[112]. In order to reduce the aggregation and to improve the effectiveness and stability of the Fe^0 nanoparticles, several modifications are implemented eventually during the synthesis. They are (i) encapsulation of Fe^0 nanoparticles in a matrix/support like silica and activated carbon[83,113], (ii) emulsification of Fe^0 nanoparticles using oils[114], (iii) doping the Fe^0 nanoparticles with other catalytic metals such as Cu, Ag and Ni[115–117], (iv) coating the surface Fe^0 nanoparticles with polymers[118], surfactants[119] and natural products[120]. The selection of stabilisation techniques depends on the intended application of Fe^0 nanoparticles since the stabilising material influence the chemical and physical properties and morphology of the prepared nanoparticles. The nanoparticle production expense is related to the cost of reducing agents and stabilising agents. Some of the modification/stabilisation methods for the Fe^0 nanoparticles are shown in figure 1.2.

1.7.1. Doping with catalytic metal

Bimetallic iron nanoparticles were synthesised by depositing a less active second catalytic metal onto the surface of the iron nanoparticle, improving the reactivity and functionality of Fe^0 nanoparticles. Even though bimetallic nanoparticles are widely used to enhance the reactivity of Fe^0 nanoparticles, the mechanism behind the enhanced reactivity is still not clear. One possible mechanism is that bimetallic nanoparticles act as a galvanic cell in which Fe^0 act as an anode and the second metal (Pd, Ni, Cu, or Zn) acts as a cathode. Iron gets oxidised and the second metal remains unchanged. The electron transfer from Fe^0 core to contaminant were permitted through doped catalytic metal. This will lead to the enhancement in reactivity of Fe^0 nanoparticles[112]. Various bimetallic combinations such as Fe/Cu, Fe/Pd, Fe/Ni, Fe/Pt, Fe/Au, Fe/Al and Fe/Ag were prepared and applied for environmental remediation studies[116,117,121–124]. Tao et al. synthesised Pd/Fe nanoparticles and used them for dechlorination reaction. Doping of Fe^0 with noble metal

Pd enhances the dechlorination reaction by utilising H_2 produced through iron corrosion with Pd as the cathode to allow electron transfer from Fe^0 core to contaminant[125]. Markova et al. reported novel air-stable bimetallic Fe/Ag nanoparticles with high antimicrobial efficiency and phosphorous removal potential. These nanoparticles were prepared by direct reduction of Ag^+ ions by commercially prepared Fe^0 nanoparticles. Silver nanoparticles were formed with particle sizes between 10-30 nm depending on the initial concentration of the $AgNO_3$ solution[117].

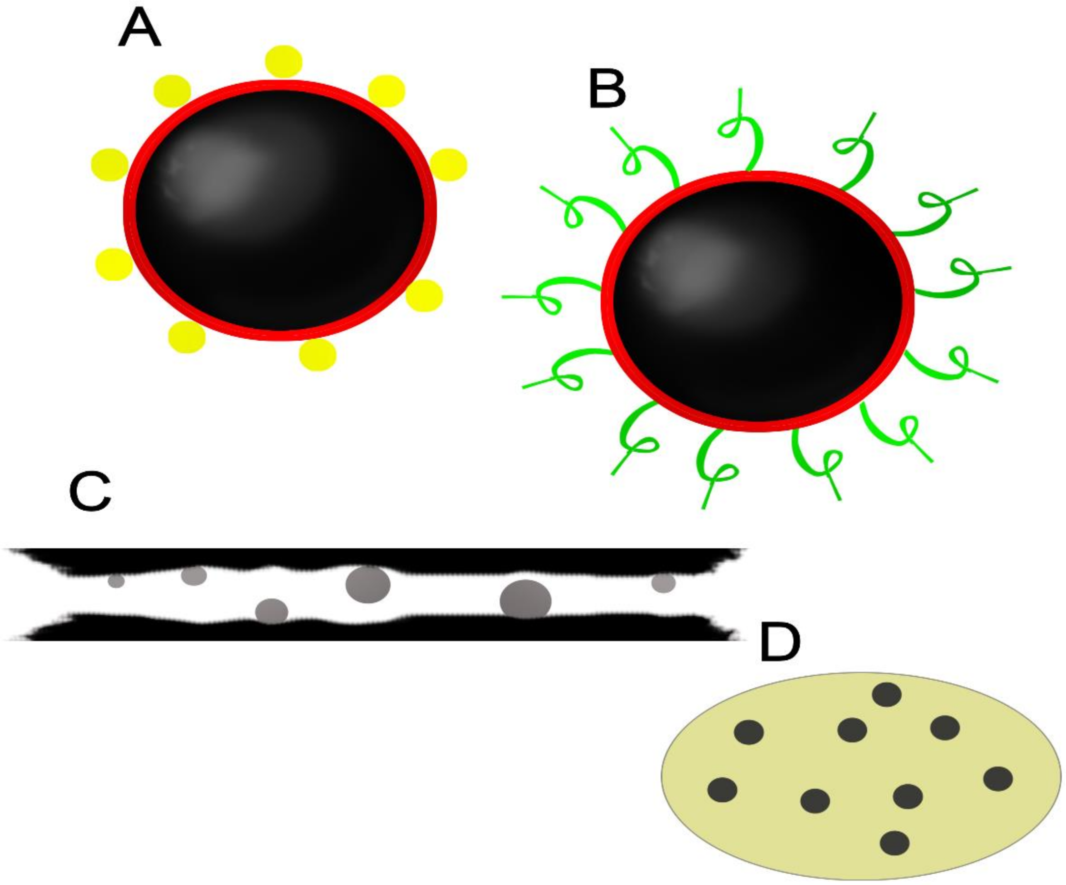

Figure 1.2 *Modification of Fe^0 nanoparticles A) doping with catalytic metal, B) surface modification using polymers/surfactants, C) immobilisation onto a solid support and D) emulsification*

1.7.2. Surface modification/coating

Surface modified Fe^0 nanoparticles were synthesised by coating a surface modifier on the Fe^0 nanoparticles surface to prevent aggregation and rapid oxidation. Proper surface modification of the nanoparticles improved the dispersibility in aqueous media and mobility in porous media. Through surface modification, the surface charge of the Fe^0 nanoparticles gets changed, which reduces the electrostatic attraction between Fe^0

nanoparticles and leads to the formation of nanoparticles with less particle size and less aggregation. Some surface modifiers use steric hinders to separate the Fe^0 nanoparticles through steric repulsion. An ideal surface modifier should have the capacity to get coated on the surface of Fe^0 nanoparticles and become stable with the changes in the surrounding environment. Low cost and less toxicity are the additional requirements for the ideal surface modifier[88,112]. Different types of monomers, polymers, surfactants and polysaccharides are used for the surface modification of Fe^0 nanoparticles and some of them are given below.

Polymers: Claudio et al. synthesised air-stable Fe^0 nanoparticles coated with ethylene glycol at standard atmospheric conditions. Functionalisation with a short polymer chain like ethylene glycol gives high dispersibility to the Fe^0 nanoparticles through steric repulsion between the grafted polymers[126]. Innocuous polymers like carboxymethyl cellulose (CMC) are commonly used to stabilise the Fe^0 nanoparticles and reduce agglomeration. Feng et al. established that particle size and dispersibility of the Fe^0 nanoparticles were manipulated using different types of carboxymethyl cellulose stabilisers. The size of the nanoparticles decreases with the increase in the CMC/Fe^{2+} molar ratio, degree of substitution to CMC and lowering the synthesising temperature. According to them, CMC accelerated the nucleation of Fe atoms during Fe^0 nanoparticles formation and formed a negatively charged layer on the surface of Fe^0 via sorption. This layer induces the electrosteric stabilisation of Fe^0 nanoparticles[127]. Mohammad et al. reported that starch stabilised Fe^0 nanoparticles show more capability to remove As(III, V) than CMC-Fe^0 and bare Fe^0[128]. Lin et al. studied the characteristics of polyacrylic acid stabilised zero valent iron nanoparticles (PNZVI) and carboxymethyl cellulose stabilised zero valent iron nanoparticles (CNZVI). The average particle size of PNZVI was 12 nm. In CNZVI nanoparticles, tens of nanoparticles with particle size 1–3 nm aggregate together to form a secondary particle. Through chemisorption, the two polymers adsorbed onto the Fe^0 surface. Steric stabilisation by the polymers played a vital role in the dispersion of the synthesised nanoparticles[129]. Polyvinyl pyrrolidone (PVP) coated Fe/Cu bimetallic nanoparticles were synthesised by et al. to prevent the agglomeration of Fe^0 nanoparticles. These nanoparticles show high dispersibility, confirmed by the high zeta potential value of 38.7 mV in distilled water at neutral pH. The result indicates that the static repellence of nanoparticles was the reason for high dispersibility and stability[130]. A detailed study on the stabilisation of Fe^0 nanoparticles using natural hydrocolloid gum karaya (GK) has been done by Vinod et al. In this study, the activated Fe^0 nanoparticles were mixed with purified Gum Karaya to generate nanoparticles suspensions of Fe^0-GK. The SEM images revealed the fibrous structure of the GK, which helped the Fe^0 nanoparticles bound inside the GK scaffolds, leading to the formation of homogeneous dispersions of Fe^0 nanoparticles. The GK's significant advantages are the presence of functional groups such as -OH, >CO, CH_3CO– and –COOH and its inherent high viscosity. The steric hindrance and negative surface charge of GK molecule through functional groups provided stability to the GK-Fe^0 nanoparticles. Also the formation of gel networks and bidentate bridging between GK and Fe^0 reduced the aggregation of nanoparticles. The GK exhibited several mechanisms (e.g. chemisorption, physisorption, ion- exchange and surface precipitation) to absorb the toxic heavy metals[120].

Surfactants: Surfactants are amphiphilic organic compounds that contain hydrophobic tails and hydrophilic heads. The surface of the Fe^0 nanoparticles absorb the hydrophobic tail and the hydrophilic head hinders the aggregation of nanoparticles using steric or electrostatic repulsion forces. Anionic, cationic and nonionic surfactants were used to stabilise Fe^0 nanoparticles[112]. Xiangyu et al. used three anionic surfactants such as methyl ester sulfonate (MES), anionic polyacrylamide (APAM) and sodium dodecylbenzene sulfonate (SDBS) to stabilise Fe^0 nanoparticles. The surface coating of surfactant reduces the particle size and surface oxidation of the Fe^0 nanoparticles. The presence of surfactant also increases the dispersibility and reactivity of Fe^0 nanoparticles compared to pristine Fe^0[131]. Peng et al. used polyacrylic acid (PAA) and three non-ionic surfactants (Tween 20, Tween 40 and Tween 60) to modify the Fe^0 surface. Even though all modifiers show good dispersing ability, PAA based Fe^0 nanoparticles exhibit more stability than surfactant-based Fe^0 nanoparticles. In all surfactants, Tween 20 show better reactivity, better stability and better mobility through porous media[132].

1.7.3. Immobilisation onto supports

Immobilised Fe^0 nanoparticles were synthesised to overcome the Fe^0 nanoparticle's separation difficulty from the water after purification. Different materials such as clay, silica, activated carbon, zeolites, resins, membranes and metal oxides were used to synthesise immobilised/supported nanoparticles. The Fe^0 nanoparticles get trapped on the pores or fixed on the surface of the supporting materials and these immobilisations affect the physicochemical properties of Fe^0 nanoparticles[88]. Incorporation of a support control growth reduce the aggregation and improve the reactivity of the Fe^0 nanoparticles. Additionally, the supported Fe^0 nanoparticles have a specific capacity to adsorb contaminants before degradation[112]. Augmented particle dispersion and applicability in a continuous flow system can be attained through solid support[133]. Some of the solid supports used to stabilise Fe^0 nanoparticles are given below.

Clays and zeolites: Clays and zeolites are widely used to remove heavy metal ions through ion exchange and adsorption properties. Low cost, wide availability and high porosity are the additional advantages of clay minerals. Different clay minerals and zeolites are used to stabilise the Fe^0 nanoparticles. Muath et al. prepared Fe^0 nanoparticles with different iron/clinoptilolite ratios. Clinoptilolite is a natural zeolite with a large surface area, structural, chemical and thermal stability. Clinoptilolite crystals form physical barriers between the dispersed chains of iron nanoparticles, reducing the agglomeration of Fe^0 nanoparticles[134]. Besides clinoptilolite, minerals like rectorite, sepiolite and kaolin have also stabilised the Fe^0 nanoparticles[135–137].

Carbon-based materials: Carbon-based materials such as activated carbon[138], biochar[139], graphene-based compounds[140], carbon nanotubes[141] and carbon black[91] are used to stabilize the Fe^0 nanoparticles. Due to the porous structure and mechanical strength, the carbon-based materials act as good supporting materials for Fe^0 nanoparticles. Mahsa et al. prepared a novel nanoadsorbent based on the combination of zero valent iron, graphene oxide and active carbon and ultrasonication used to improve the physical properties of nanoparticles. Incorporation of the graphene oxide reduces the particle size and the crystallinity of the Fe^0 nanoparticles. With respect to active carbon, the space between the graphene oxide becomes higher and more space is available for Fe^0 nanoparticles accommodation at low graphene oxide concentration. The prepared nanocomposite show more Fe^0 stability and graphene coupling improves reactivity through electron transfer and protects Fe^0 from surface passivation[142].

Metal oxides: Metal oxides like $Mg(OH)_2$ and TiO_2 were used to stabilise the Fe^0 nanoparticles. Minghui et al. synthesised novel $Mg(OH)_2$ supported Fe^0 nanoparticles and applied them for Pb(II) removal. The synthesised Fe^0 nanoparticles uniformly immobilised on the surface of flower-like petals of $Mg(OH)_2$ which reduced the aggregation of the nanoparticles. The reducing capacity of the Fe^0 nanoparticles is enhanced by the hydroxides provided by $Mg(OH)_2$[143]. The efficiency of Fe^0 nanoparticles can also be enhanced by supporting them into a TiO_2 matrix. The porous TiO_2 matrix increase dispersibility and stability and decrease oxidation and agglomeration of Fe^0 nanoparticles[144].

1.7.4. Emulsification

Emulsified Fe^0 nanoparticles consist of food-grade surfactant, vegetable oil, Fe^0 nanoparticles and water. During emulsification, the Fe^0 nanoparticles were surrounded by an oil-liquid membrane. Emulsified Fe^0 nanoparticles mainly focussed on the remediation of groundwater polluted by organic solvents. Fe^0 nanoparticles degraded the contaminants in the solution sequestrated by oil molecules. Enhanced stability due to the oil layer that results in limited oxidation and better mobility through porous media are the advantages of emulsified Fe^0 nanoparticles. Jun et al. studied the degradation of nitrobenzene using emulsified Fe^0 nanoparticles and found that adsorption and reductive reaction cause the removal of nitrobenzene. Usually, 1 % and 2 % oil concentrations are preferred to modify Fe^0 nanoparticles for better performance[145]. Tao et al. used gum arabic to stabilise Fe^0 nanoparticles in a soybean oil-in-water emulsion. Emulsification not only increases the shelf life of Fe^0 nanoparticles but also limits the oxidation of Fe^0 by water and non-target solutes during application[114].

1.8. Applications of zero valent iron-based nanomaterials

Implementation of appropriate methods/materials for water treatment is a difficult task. The selected method should fulfil the standard water quality parameters in the respective countries and be efficient, cost-effective and environmentally friendly. Simple treatment methods/materials and reusability of the materials made it economical in water treatment. Even though numerous materials are available, iron-based nanomaterials are widely investigated nowadays. Iron-based nanoparticles are extensively used for drinking and wastewater treatment and are also used for groundwater treatment. The ability of zero valent iron nanoparticles for environmental water treatment was established through laboratory and field-scale tests. The application of iron-based nanoparticles can be categorised based on the type of pollutant they remove since different mechanisms are followed during the removal of specific pollutants. The applications of Fe^0 are shown in figure 1.3.

1.8.1. Removal of heavy metals/metalloids:

Industrial wastewater from electroplating, steel plants and tanning industries contains a large amount of toxic heavy metals such as Cr(VI), Pb(II), Hg(II), Cd(II), As(III), Ni(II) and Cu(II), wherein Cr(VI) is the most widely studied heavy metal for removal purposes. Usually, chromium is present in the environment in two oxidation states, Cr(III) and Cr(VI), in which Cr(VI) is more toxic compared to Cr(III). Conventional methods find it difficult for Cr(VI) precipitation since they are typically found as oxyanions (CrO_4^{2-} and $Cr_2O_7^{2-}$). Surprisingly, the Fe^0 nanoparticles gave a new solution to this problem due to their large surface area and high reactivity. In recent years, treatment of Cr(VI) has been accomplished with Fe^0 nanoparticles. The Cr(VI) removal process involves three major mechanisms: adsorption, reduction and co-precipitation[146]. Typically, the Cr(VI) concentration has been analysed through UV-visible spectroscopy using the 1,5-diphenylcarbazide method. During the Cr(VI) removal, the hexavalent chromium was reduced into Cr(III) along with the oxidation of Fe^0 to Fe^{2+} and Fe^{3+}. According to researchers, the initial pH of the solution is the major influencing factor for the removal of the Cr(VI). Even though the optimum pH range showed some differences, the Cr(VI) removal preferred the acidic pH. The predominant Cr(VI) form at pH in between 2-6 was $HCrO_4^-$ and the major Cr(VI) form at pH > 6 was CrO_4^{2-}. The $HCrO_4^-$ formed was more susceptible to adsorption compared to CrO_4^{2-} form[147]. In acidic pH, iron corrosion was accelerated by H^+ ions which increases the removal rate of Cr(VI). The H^+ ions also helped to maintain the reactivity of the iron nanoparticles by removing the passive oxide layer on the iron surface. At a higher pH range, surface passive layer formation prevents the electron transfer from Fe^0 to Cr(VI)[148]. At $pH<pH_{zpc}$, the primary mechanisms for Cr(VI) removal was redox reaction and electrostatic attraction, but at $pH>pH_{zpc}$, redox reaction and ion exchange reaction were the predominant mechanisms, even though at higher pH, redox reaction was not preferred. In the ion-exchange mechanism, -OH was substituted by chromate anions[147]. While evaluating the other parameters influencing the Cr(VI) removal, it is evident that the percentage of removal was directly proportional to the contact time and amount of adsorbent and inversely proportional to the initial concentration of Cr(VI) solution[149–151].

Vinod et al. stabilised the chemically synthesised Fe^0 nanoparticles by Gum karaya (GK) and examined them to remove chromium completely. They discovered that the reduction of Cr(VI) to Cr(III) by Fe^0–GK and followed adsorption of the remaining Cr(III) onto gum karaya were the possible mechanism behind the Cr(IV) removal. This leads to the total removal of Cr(VI) from the contaminated water[120]. According to Quian et al., the major and final product of Cr(VI) reduction by carboxymethyl cellulose-stabilised Fe^0 nanoparticles was iron hydroxide and chromium hydroxide since the precipitation of $Cr(OH)_3$ and mixed Cr(III)/Fe(III) hydroxides onto the iron surface was confirmed through spectroscopic data[152]. Jiao et al. compare the Cr(VI) removal capacity of agar stabilised Fe^0 nanoparticles with bare Fe^0 nanoparticles and found that agar stabilised Fe^0 nanoparticles have outstanding Cr(VI) removal capacity in various conditions. 100 % removal efficiency of 50 mg/L Cr(VI) was attained within 2 hours using Cr(VI)/agar-Fe^0 nanoparticles at a molar ratio of 0.025 and optimum pH 3[153]. Dong et al. synthesised biochar and modified biochar supported Fe^0 and analysed their capacity to remove Cr(VI). They found that acid-treated biochar based Fe^0 has the highest Cr(VI) removal efficiency. They also noticed that low biochar to Fe^0 ratio causes the aggregation of iron nanoparticles and high biochar to Fe^0 ratio blocks the active sites of the Fe^0 nanoparticles[154]. In another study, Soroosh et al. inferred that activated carbon stabilised Fe^0 has a 33 times higher adsorption capacity and a greater affinity for Cr(VI) than activated carbon[155]. According to Xiao et al., temperature and pH are the variables that strongly affect the Cr(VI) removal and some anions such as CO_3^{2-} and HCO_3^- can also influence it[146]. According to Xiangyu et al., the effect of temperature on Cr(VI) removal was complex due to various factors. With increased temperature, the adsorption capacity increases upto a certain point whereas the surface complexation and electrostatic interaction may decrease after an optimum temperature[131]. The stabilising agent of Fe^0 has an important role in the Cr(VI) removal. For example, amino-functionalised vermiculite-supported nanoscale zero-valent iron showed high efficiency and reusability for Cr(VI) removal compared to bare Fe^0. Electrostatic attraction between the negative species of Cr(VI) and protonated amino groups on the stabilising agent of Fe^0 influence the removal of Cr(VI)[156]. Feglian et al. studied the removal of Cr(VI) and Cr(III) from water using resin supported Fe^0 nanoparticles. The removal of Cr(VI) was accomplished by chemical reduction. Cr(III) removal was done by ion exchange at pH below 6.3 and precipitation at pH greater than 6.3[157]. Yaru et al. prepared the heteroaggregates of montmorillonite microparticles with nanoscale Fe^0 to study the Cr(VI) removal efficiency from water. The Cr(VI) removal followed the pseudo-second-order kinetics and Langmuir equilibrium model. The authors suggested that Cr(VI) removal was mainly by chemisorption and is spontaneous and exothermic[158]. The complete removal of 100 mg/L Cr(VI) was achieved within 30 minutes by 0.2 g/L of green nanoparticles, which was synthesised using the leaf extracts of *Rosa damascene* (RD), *Thymus vulgaris* (TV) and *Urtica dioica* (UD). The higher pore volume on the nanoparticles leads to higher Cr(VI) removal. Since the prepared nanoparticles are susceptible to agglomeration, the nanoparticles in the agglomerates show multilayer adsorption along with adsorption into the internal adsorption site of small pores[159].

The high affinity of arsenic for proteins makes them a toxic contaminant in groundwater and wastewater. As(III) is more toxic than As(V) due to the neutral character of the oxyanions (H_3AsO_3, $H_2AsO_3^-$ and $HAsO_3^{2-}$) of As (III). So, the neutral character of As(III) (Arsenite) does not prefer adsorption, but the oxyanions of As(V) can be adsorbed onto solid minerals. Hence for the effective removal of arsenic, the researchers practised the conversion of As(III) to As(V)[160,161]. The Fe^0 nanoparticles showed multiple mechanisms for removing arsenic, such as adsorption, absorption, precipitation, co-precipitation, oxidation and reduction. It may be due to the core-shell structure of iron nanoparticles in which the shell consists of iron oxides and iron hydroxides and the core consists of metallic iron[108]. The metallic iron can reduce the As(V) into As(III) and As(0) due to its fast kinetics. The oxidation and complexation of the As(III) have been done by iron oxide/hydroxide shell, formed during the oxidation of Fe^0. The removal mechanisms depend on the redox nature of the pollutant and the nature of the medium, such as pH, ionic strength and redox potential[161]. Tandon et al. synthesised Fe^0 nanoparticles supported on the montmorillonite clay particles using tea liquor as a reducing agent. The authors revealed that 99 % As(III) could be removed from the water within 30 minutes by green montmorillonite clay-Fe^0 nanoparticles. The removal efficiency depends on the amount of Fe^0 nanoparticles loaded on montmorillonite clay particles and the maximum removal efficiency was obtained at both low and high pH. It was also found that as time increased, the Fe^0 nanoparticles were agglomerated due to the expulsion of Fe^0 nanoparticles from the clay cage, leading to the decrease in the elimination of As(III)[161]. Rana et al. suggested a new mechanism for the oxidation of As(III) to As(V) using green Fe^0 nanoparticles which are synthesised using guava leaf extract. In batch experiments, 2-propanol was used as a hydroxyl radical scavenger to determine the possible reaction mechanism of As(III) oxidation via leaf extract stabilised Fe^0 nanoparticles. The decrease (70 % to 26 %) in the oxidation of As(III) at acidic pH 3 indicated that oxidation was not only mediated by the $^{\cdot}OH$ radicals produced by green Fe^0. Some oxidants originating from guava leaf extracts was also responsible for the oxidation. More than 70 % of As(III) was oxidised into As(V) using prepared nanoparticles within 10 minutes and the optimum pH for the reaction was pH 3 and pH 7[160].

The Fe^0 nanoparticles were also used to eliminate the divalent heavy metals such as Co, Pb, Hg, Ni and Cu[162,163]. Wen et al. found that Fe^0 nanoparticles are efficient for removing Zn^{2+}. Hydroxide shell on the surface of Fe^0 nanoparticles exhibits a major role in the adsorption and co-precipitation of Zn^{2+}[164]. Ye et al. used calcium alginate encapsulated Ni/Fe nanoparticles beads to remove Cu^{2+} through adsorption and reduction[165]. The elimination of Pb(II) and Hg(II) ions from the water was investigated using *Azolla filiculoides* modified Fe^0 nanoparticles. The XRD results reveal that these heavy metals were reduced into metallic forms or other possible insoluble forms. The reduction of heavy metal cations is energetically favourable due to the differences in the standard electrode potential of Fe(II)/Fe(0) (-44 eV) with Pb(II)/Pb(0) (-0.12 V) and Hg(II)/Hg(0) (+0.86 V). The metallic core in the Fe^0 nanoparticles exhibited a crucial role in the Pb(II) and Hg(II) reduction. The uptake efficiency was increased with increasing temperature and the time required for the maximum uptake was around 20 minutes[166].

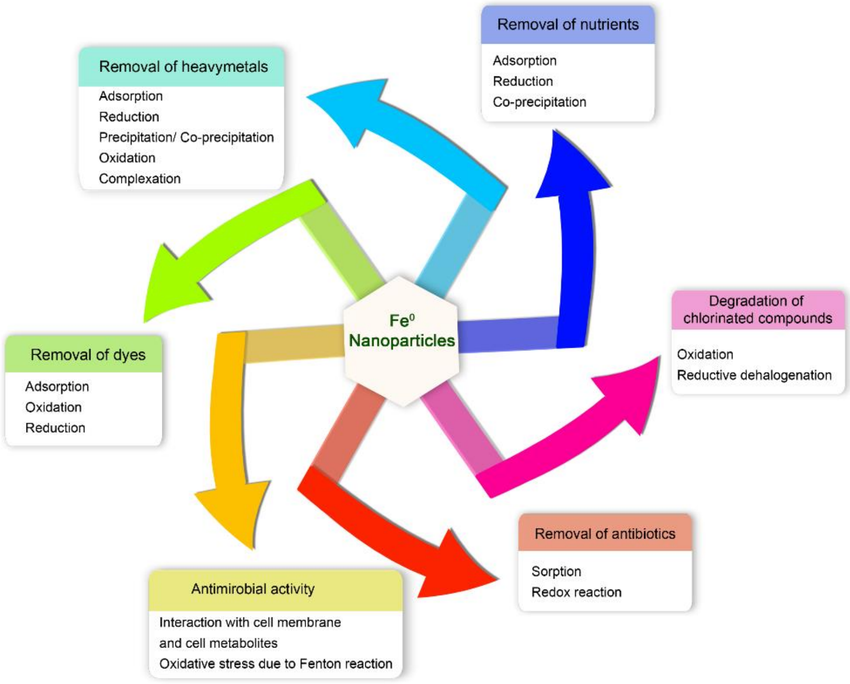

Figure 1.3 *Application of Fe^0 nanoparticles in water treatment*

1.8.2. Removal of nutrients:

Contamination due to nutrients such as nitrates and phosphates significantly affects the water bodies since they lead to eutrophication[167]. Wang et al. compared the nitrate removal efficiency from an aqueous medium using green-Fe^0 nanoparticles and chemically synthesised Fe^0 nanoparticles. Green Fe^0 nanoparticles were prepared using green tea and eucalyptus leaf extracts. The authors found that chemically synthesised nanoparticles are more efficient than green nanoparticles, but on the other hand, the green nanoparticles have high stability even after two months of air storage. The Fe^0-iron oxide/polyphenols core-shell structure of green nanoparticles favoured nitrate removal by adsorption, co-precipitation and reduction[168]. Yu-Hoon et al. established that during reaction with the Fe^0 nanoparticles, nitrate was degraded into ammonium ion followed by ammonia stripping under high pH, which reduces the nitrogen amount in the solution[169].

1.8.3. Degradation/removal of dyes:

A large amount of dye wastewater from the industries reduces the light penetration to the water bodies and leads to the formation of toxic contaminants. The significant contribution of textile dye pollution was from azo and triarylmethane dyes[110]. The Fe0 nanoparticles have been used to remove various dyes in the last few years. Reduction, adsorption and oxidation via advanced oxidation process are the major mechanisms for dye removal. In the presence of hydrogen peroxide, the Fe^0 nanoparticles acted as Fenton-like catalyst, producing hydroxyl radicals and eventually leading to the oxidation of pollutants in water. Nanoparticle size and lifespan are the limiting factors in the advanced Fenton-like reactions[170].

Yang et al. compared the efficiency of Fe^0 nanoparticles to remove three different dyes, including azo dye (Reactive brilliant red), triphenylmethane dye (Malachite green) and anthraquinone dye (Reactive brilliant blue). The results indicated that pH has a negligible effect on dye removal. They suggested that the dye decolourisation process is mainly due to the chromophore destruction and transformation of some functional groups such as amino and aromatic rings[171]. Chen et al. used kaolin stabilised Fe^0 nanoparticles to degrade triphenylmethane dye crystal violet. Crystal violet adsorbed onto the surface of the Fe^0 nanoparticles, then transformed into leuco crystal violet. Finally, reduction by Fe^0 nanoparticles caused the cleavage of the C=C bond[136]. The polyacrylic acid modified filter paper was used as a matrix to stabilise Fe^0 nanoparticles by Pingping et al. and these novel nanoparticles were applied to remove cationic methylene blue and anionic methyl blue dyes. Decolourisation of the methylene blue dye is attributed to the cleavage of -C=N- and -C=S- bonds, while the decolouration of methyl blue is attributed to the cleavage of -C=C- and -C=N- bonds by Fe^0 nanoparticles[172].

Fe^0 nanoparticles act as heterogeneous Fenton-like catalysts for the degradation of organic dyes. Degradation of the azo dye, Direct Black G, was studied by Jiajiang et al. using kaolin supported Fe^0 nanoparticles. In the degradation process, firstly, the dye molecules are adsorbed onto the surface of nanoparticles, then the azo bond is scavenged by the strong reduction of Fe^0 nanoparticles which leads to the formation of reduced product of dye molecules. H_2O_2 in the solution caused the formation of $^{\cdot}OH$ radicals by reacting with the iron nanoparticles. The $^{\cdot}OH$ radicals formed are potent oxidising agents that react with the dyes and oxidise and mineralises them into CO_2 and H_2O[173].

Fe^0 nanoparticles can perform the decolourisation of azo dyes through the oxidation of dye molecules by hydroxyl radical. Hydroxyl radicals are generated by the reaction between the excited surface electrons from the nanoparticles and dissolved oxygen molecules. Harshiny et al. compared azo dye, methyl orange (MO) removal efficiency using green Fe^0 nanoparticles synthesised using *Amaranthus dubius* leaf extract and chemically synthesised Fe^0 nanoparticles using sodium borohydride. The green synthesised Fe^0 nanoparticles (81 %) show slightly less removal efficiency than chemically synthesised ones (90 %), which may be due to the surface stabilisation of Fe^0 nanoparticles[174]. Radini et al. incorporated UV irradiation technique with green Fe^0 nanoparticles for the effective removal of MO. Iron nanoparticles are used as a photocatalyst for MO removal. The MO dye molecules are degraded into smaller molecules due to the photodegradation of dye on the reactive surface of Fe^0 nanoparticles. The hydroxyl radical produced by the UV-irradiation on iron nanoparticles is the reactive agent behind the removal of MO[175].

Huang et al. compared the malachite green (MG) dye removal using three types of iron nanoparticles synthesised by tea leaves such as green tea (GT), oolong tea (OT) and black tea (BT). The green tea stabilised Fe^0 nanoparticles showed higher removal efficiency with 81 %, following OT-Fe^0 nanoparticles (75 %) and BT-Fe^0 nanoparticles (67 %). A large amount of polyphenols/caffeine content in GT-Fe^0 nanoparticles make them a beneficial removal agent for dyes. The dye removal increased with temperature since the dye degradation process by GT- Fe^0 nanoparticles is an endothermic process. The authors proposed two possible mechanisms for MG removal using tea leaf stabilised Fe^0 nanoparticles. The first one is the reduction of contaminant using Fe^0, which involves the cleavage of the -C=C- and =C=N- bond linked to the benzene ring. The second one is the adsorption of dye molecules onto iron/iron oxide and tea extract components[176].

1.8.4. Degradation of chlorinated compounds:

The removal of volatile organic compounds such as cis-1,2-dichloroethene, perchloroethene and trichloroethene was studied by Vinod et al. They used gum karaya to stabilise the chemically synthesised Fe^0 nanoparticles for the removal of chlorinated compounds. The enhancement of surface reactivity per unit area of the Fe^0 nanoparticles and growth in the sorption area of the prepared nanoparticles were the significant advantages of gum karaya stabilised Fe^0 nanoparticles. The major mechanism for reducing chlorinated hydrocarbon using the prepared nanoparticles was β-elimination. The Fe^0 nanoparticles act as an electron donor for the reductive dehalogenation of chlorinated compounds. The chlorine number was calculated to estimate the possibility of direct removal of chlorinated compounds and the results indicated that the simultaneous degradation of all chlorinated hydrocarbons has occurred without any lower chlorinated hydrocarbon formation[120].

Kuang et al. suggested a mechanism for removing monochlorobenzene (MCB) using green Fe^0 nanoparticles synthesised from tea leaf extract (GT). GT-Fe nanoparticles were used as heterogeneous Fenton-like catalysts for the oxidation of monochlorobenzene. The authors proposed a three-step mechanism for the mineralisation of the monochlorobenzene in which the first step is the adsorption of the pollutant to the iron/iron oxide surface of the adsorbent. In the next step, the hydroxyl radicals were generated through the reaction of iron species with hydrogen peroxide. Finally, hydroxyl radicals attacked the MCB, which was mineralised into CO_2 and H_2O on the surface of iron nanoparticles. The favourable MCB removal conditions using GT-Fe nanoparticles were optimized as 0.6 g/L GT-Fe nanoparticles, 0.045 mol/L H_2O_2 and initial pH 3[34].

1.8.5. Degradation/removal of antibiotics:

Pharmaceutical products in the aquatic ecosystem have been a concern for researchers in the last few years due to their environmental and health effects. Fe^0 nanoparticles were used for the removal of pharmaceutical products. Machado et al. prepared green Fe^0

nanoparticles (gnFe^0) using oak leaf extract and studied its antibiotic amoxicillin elimination capacity. They investigated the possibility of gnFe^{0}s as a reductant and a Fenton-like catalyst to remove the amoxicillin (AMX) from soil and water. 100 % degradation of the amoxicillin was attained by gnFe^0 as a reductant after 95 min with a 1:15 AMX/gnFe^0 molar ratio in water. At the same time, 100 % removal efficiency of amoxicillin was attained by gnFe^0 as a Fenton-like catalyst in 15 minutes with a molar ratio of 1:13:1 AMX/H_2O_2/gnFe^0. The gnFe^0 degraded the amoxicillin by physical sorption, redox reactions and biological degradation methods. The application of natural extract on prepared nanoparticles has boosted the biodegradation of amoxicillin. The mechanism of amoxicillin degradation included the transformation of amoxicillin into undetectable amoxicillin penicilloic acid through the b-lactam ring-opening reaction[177].

1.8.6. Antimicrobial activity:

Fe^0 based nanoparticles show superior antimicrobial activity. Khan et al. synthesised iron nanoparticles using flower extract of *Hibiscus sabdariffa roselle* as a reducing agent. The authors studied the antifungal and antibacterial activities of bio fabricated iron nanoparticles in fungus (*Candida albicans, Candida glabrata* and *Candida tropicalis*) and bacteria (*Escherichia coli* and *Staphylococcus aureus*) through the disk diffusion method. The flower extract capped iron nanoparticles displayed a significant inhibition zone for all the pathogenic microorganisms. The mechanism of the antimicrobial activity of iron nanoparticles includes the interaction between the iron nanoparticles and cell membrane of the microbes, bonding between the iron nanoparticles and metabolites present inside the microorganisms, deformation and structural changes in the bacterial cell wall and membranes eventually, death of microorganisms[178]. Iron nanoparticle's antibacterial effect was studied on gram-positive and gram-negative bacteria by Radini et al. Antibacterial efficiency was analysed by agar well diffusion method and found that iron nanoparticles have more zone of inhibition in *Escherichia coli* (gram-negative, 16 mm) than *Staphylococcus aureus* (gram-positive, 12 mm). The interaction between iron nanoparticles and bacterial cell membranes influenced the antibacterial activity of iron nanoparticles. The differences in the cell membrane structure of the bacteria lead to different inhibition zone for different bacteria. A thick peptidoglycon layer was present in the cell wall of gram-positive bacteria, whereas a thin peptidoglycon layer was seen in gram-negative bacteria. It makes gram-negative bacteria more vulnerable to iron nanoparticles, and its growth was significantly prevented[175]. Recently vitta et al. studied the antibacterial activity through the agar diffusion method on *Bacillus subtilis*, *Escherichia coli*, *Staphylococcus aureus* and *Pseudomonas aeruginosa* using iron nanoparticles prepared by leaf extracts of *Eucalyptus robusta*. Even though the iron nanoparticles exhibit antibacterial activity, the leaf extract of *Eucalyptus robusta* boosted the capability of iron nanoparticles since the phytochemical components of the *Eucalyptus robusta* have some antibacterial activity. The authors proposed two mechanisms for the antibacterial activity of newly synthesised nanoparticles. In the first one, they suggested that the accumulation of particles in the cytoplasmic region causes the rupture of the membrane and eventually leads to the bacteria's death. The reaction between nanoparticles and biomolecules inside the bacteria caused the conformational changes in protein structure and DNA molecule, leading to bacteria-killing. In the second mechanism, the authors proposed the production of reactive oxygen species through the Fenton-like reaction, where the bacteria produces hydrogen peroxide as a metabolic product. The reactive oxygen species causes oxidative stress on bacteria, leading to bacterial death[179].

1.9. Objectives of the present study

- Synthesise Fe^0 and bimetallic Fe based nanoparticles using chemical reduction method.
- Prepare chitosan stabilised Fe^0 and Fe/Ni nanoparticles.
- Develop TiO_2 and zeolite based novel composites as supporting and stabilising material for Fe^0 nanoparticles.
- Prepare Fe nanoparticles using plant extracts as green reducing agents.
- Evaluate the efficiency of synthesised nanoparticles in the removal of toxic hexavalent chromium under different reaction conditions such as initial Cr(VI) concentration, nanoparticle dosage, contact time and solution pH.
- Study the effectiveness of synthesised nanoparticles regarding the removal of toxic dyes under various reaction conditions, including initial dye concentration, nanoparticles dosage, contact time and solution pH.

1.10. References

[1] A.B. Pandit, J.K. Kumar, Drinking Water Treatment for Developing Countries, The Royal Society of Chemistry, 2019. https://doi.org/10.1039/9781788012935.

[2] R. Das, C.D. Vecitis, A. Schulze, B. Cao, A.F. Ismail, X. Lu, J. Chen, S. Ramakrishna, Recent advances in nanomaterials for water protection and monitoring, Chem. Soc. Rev. 46 (2017) 6946–7020. https://doi.org/10.1039/c6cs00921b.

[3] J.E. Hulla, S.C. Sahu, A.W. Hayes, Nanotechnology: History and future, Hum. Exp. Toxicol. 34 (2015) 1318–1321. https://doi.org/10.1177/0960327115603588.

[4] T. Masciangioli, W.X. Zhang, Environmental technologies at the nanoscale, Environ. Sci. Technol. 37 (2003). https://doi.org/10.1021/es0323998.

[5] S. Bonaiti, B. Calderon, E. Collina, IOP Conference Series: Earth and Environmental Science Review on Nano zerovalent Iron (nZVI): From Modification to Environmental Applications Related content, IOP Conf. Ser. Earth Environ. Sci. 51 (2017). https://doi.org/10.1088/1755-1315/51/1/012004.

[6] R.A. Crane, T.B. Scott, Nanoscale zero-valent iron: Future prospects for an emerging water treatment technology, J. Hazard. Mater. 211–212 (2012) 112–125. https://doi.org/10.1016/j.jhazmat.2011.11.073.

[7] L. Li, J. Hu, X. Shi, M. Fan, J. Luo, X. Wei, Nanoscale zero-valent metals: a review of synthesis, characterization, and applications to environmental remediation, Environ. Sci. Pollut. Res. 23 (2016) 17880–17900. https://doi.org/10.1007/s11356-016-6626-0.

[8] B. Hu, Y. Ai, J. Jin, T. Hayat, A. Alsaedi, L. Zhuang, X. Wang, Efficient elimination of organic and inorganic pollutants by biochar and biochar-based materials, Biochar. 2 (2020) 47–64. https://doi.org/10.1007/s42773-020-00044-4.

[9] Z. Chen, S. Zhang, Y. Liu, N.S. Alharbi, S.O. Rabah, S. Wang, X. Wang, Synthesis and fabrication of g-C3N4-based materials and their application in elimination of pollutants, Sci. Total Environ. 731 (2020) 139054. https://doi.org/10.1016/j.scitotenv.2020.139054.

[10] X. Liu, R. Ma, L. Zhuang, B. Hu, J. Chen, X. Liu, X. Wang, Recent developments of doped g-C3N4 photocatalysts for the degradation of organic pollutants, Crit. Rev. Environ. Sci. Technol. 0 (2020) 1–40. https://doi.org/10.1080/10643389.2020.1734433.

[11] N.S. Alharbi, B. Hu, T. Hayat, S.O. Rabah, A. Alsaedi, L. Zhuang, X. Wang, Efficient elimination of environmental pollutants through sorption-reduction and photocatalytic degradation using nanomaterials, Front. Chem. Sci. Eng. (2020). https://doi.org/10.1007/s11705-020-1923-z.

[12] X. Wang, X. Li, J. Wang, H. Zhu, Recent Advances in Carbon Nitride-based Nanomaterials for the Removal of Heavy Metal Ions from Aqueous Solution, Wuji Cailiao Xuebao/Journal Inorg. Mater. 35 (2020) 260–270. https://doi.org/10.15541/jim20190436.

[13] I.S. Yunus, Harwin, A. Kurniawan, D. Adityawarman, A. Indarto, Nanotechnologies in water and air pollution treatment, Environ. Technol. Rev. 1 (2012) 136–148. https://doi.org/10.1080/21622515.2012.733966.

[14] X. Zeng, D. Dang, L. Leng, C. You, G. Wang, C. Zhu, S. Liao, Doped reduced graphene oxide mounted with IrO2 nanoparticles shows significantly enhanced performance as a cathode catalyst for Li-O2 batteries, Electrochim. Acta. 192 (2016) 431–438. https://doi.org/10.1016/j.electacta.2016.02.008.

[15] T.A. Degfie, T.T. Mamo, Y.S. Mekonnen, Optimized Biodiesel Production from Waste Cooking Oil (WCO) using Calcium Oxide (CaO) Nano-catalyst, Sci. Rep. 9 (2019). https://doi.org/10.1038/s41598-019-55403-4.

[16] Y.N. Zhang, Q. Niu, X. Gu, N. Yang, G. Zhao, Recent progress on carbon nanomaterials for the electrochemical detection and removal of environmental pollutants, Nanoscale. 11 (2019) 11992–12014. https://doi.org/10.1039/c9nr02935d.

[17] Q. Zhao, X. Li, Q. Zhou, D. Wang, H. Xu, Nanomaterials Developed for Removing Air

Pollutants, Adv. Nanomater. Pollut. Sens. Environ. Catal. (2019) 203–247. https://doi.org/10.1016/B978-0-12-814796-2.00006-X.

[18] M.M. Khin, A.S. Nair, V.J. Babu, R. Murugan, S. Ramakrishna, A review on nanomaterials for environmental remediation, Energy Environ. Sci. 5 (2012) 8075–8109. https://doi.org/10.1039/c2ee21818f.

[19] H. Sadegh, G.A.M. Ali, V.K. Gupta, A.S.H. Makhlouf, R. Shahryari-ghoshekandi, M.N. Nadagouda, M. Sillanpää, E. Megiel, The role of nanomaterials as effective adsorbents and their applications in wastewater treatment, J. Nanostructure Chem. 7 (2017) 1–14. https://doi.org/10.1007/s40097-017-0219-4.

[20] Z. Gao, T.J. Bandosz, Z. Zhao, M. Han, J. Qiu, Investigation of factors affecting adsorption of transition metals on oxidized carbon nanotubes, J. Hazard. Mater. 167 (2009) 357–365. https://doi.org/10.1016/j.jhazmat.2009.01.050.

[21] F. Lu, D. Astruc, Nanocatalysts and other nanomaterials for water remediation from organic pollutants, Coord. Chem. Rev. 408 (2020) 213180. https://doi.org/10.1016/j.ccr.2020.213180.

[22] M. Anjum, R. Miandad, M. Waqas, F. Gehany, M.A. Barakat, Remediation of wastewater using various nano- materials, Arab. J. Chem. 12 (2019) 4897–4919. https://doi.org/10.1016/j.arabjc.2016.10.004.

[23] M.S. Hasan, M. Geza, R. Vasquez, G. Chilkoor, V. Gadhamshetty, Enhanced Heavy Metal Removal from Synthetic Stormwater Using Nanoscale Zerovalent Iron–Modified Biochar, Water. Air. Soil Pollut. 231 (2020). https://doi.org/10.1007/s11270-020-04588-w.

[24] A. Afkhami, M. Saber-Tehrani, H. Bagheri, Modified maghemite nanoparticles as an efficient adsorbent for removing some cationic dyes from aqueous solution, Desalination. 263 (2010) 240–248. https://doi.org/10.1016/j.desal.2010.06.065.

[25] R.F. Mansa, C.S. Sipaut, I.A. Rahman, N.S.M. Yusof, M. Jafarzadeh, Preparation of glycine–modified silica nanoparticles for the adsorption of malachite green dye, J. Porous Mater. 23 (2016) 35–46. https://doi.org/10.1007/s10934-015-0053-3.

[26] S. Banerjee, R.K. Gautam, A. Jaiswal, M.C. Chattopadhyaya, Y.C. Sharma, Rapid scavenging of methylene blue dye from a liquid phase by adsorption on alumina nanoparticles, RSC Adv. 5 (2015) 14425–14440. https://doi.org/10.1039/c4ra12235f.

[27] S. Tangsir, L.D. Hafshejani, A. Lähde, M. Maljanen, A. Hooshmand, A.A. Naseri, H. Moazed, J. Jokiniemi, A. Bhatnagar, Water defluoridation using Al2O3 nanoparticles synthesized by flame spray pyrolysis (FSP) method, Chem. Eng. J. 288 (2016) 198–206. https://doi.org/10.1016/j.cej.2015.11.097.

[28] X. Guan, J. Du, X. Meng, Y. Sun, B. Sun, Q. Hu, Application of titanium dioxide in arsenic removal from water: A review, J. Hazard. Mater. 215–216 (2012) 1–16. https://doi.org/10.1016/j.jhazmat.2012.02.069.

[29] V. Dhiman, N. Kondal, ZnO Nanoadsorbents: A potent material for removal of heavy metal ions from wastewater, Colloids Interface Sci. Commun. 41 (2021). https://doi.org/10.1016/j.colcom.2021.100380.

[30] F. Zhang, X. Chen, F. Wu, Y. Ji, High adsorption capability and selectivity of ZnO nanoparticles for dye removal, Colloids Surfaces A Physicochem. Eng. Asp. 509 (2016) 474–483. https://doi.org/10.1016/j.colsurfa.2016.09.059.

[31] S. Dey, G.C. Dhal, Applications of Rhodium and Ruthenium Catalysts for CO Oxidation:

an Overview, Polytechnica. 3 (2020) 26–42. https://doi.org/10.1007/s41050-020-00023-5.

[32] G. Lofrano, G. Libralato, J. Brown, Nanotechnologies for Environmental Remediation, Springer International Publishing, Cham, 2017. https://doi.org/10.1007/978-3-319-53162-5.

[33] K. Sathiyan, R. Bar-Ziv, O. Mendelson, T. Zidki, Controllable synthesis of TiO2 nanoparticles and their photocatalytic activity in dye degradation, Mater. Res. Bull. 126 (2020) 110842. https://doi.org/10.1016/j.materresbull.2020.110842.

[34] Y. Kuang, Q. Wang, Z. Chen, M. Megharaj, R. Naidu, Heterogeneous Fenton-like oxidation of monochlorobenzene using green synthesis of iron nanoparticles, J. Colloid Interface Sci. 410 (2013) 67–73. https://doi.org/10.1016/j.jcis.2013.08.020.

[35] G.B. Ortiz De La Plata, O.M. Alfano, A.E. Cassano, 2-Chlorophenol degradation via photo Fenton reaction employing zero valent iron nanoparticles, J. Photochem. Photobiol. A Chem. 233 (2012) 53–59. https://doi.org/10.1016/j.jphotochem.2012.02.023.

[36] R. Huang, Z. Fang, X. Yan, W. Cheng, Heterogeneous sono-Fenton catalytic degradation of bisphenol A by Fe3O4 magnetic nanoparticles under neutral condition, Chem. Eng. J. 197 (2012) 242–249. https://doi.org/10.1016/j.cej.2012.05.035.

[37] R. Salazar, M.S. Ureta-Zañartu, C. González-Vargas, C. do N. Brito, C.A. Martinez-Huitle, Electrochemical degradation of industrial textile dye disperse yellow 3: Role of electrocatalytic material and experimental conditions on the catalytic production of oxidants and oxidation pathway, Chemosphere. 198 (2018) 21–29. https://doi.org/10.1016/j.chemosphere.2017.12.092.

[38] W. Xie, Y. Shi, Y. Wang, Y. Zheng, H. Liu, Q. Hu, S. Wei, H. Gu, Z. Guo, Electrospun iron/cobalt alloy nanoparticles on carbon nanofibers towards exhaustive electrocatalytic degradation of tetracycline in wastewater, Chem. Eng. J. 405 (2021). https://doi.org/10.1016/j.cej.2020.126585.

[39] W. Tu, K. Li, X. Shu, W.W. Yu, Reduction of hexavalent chromium with colloidal and supported palladium nanocatalysts, J. Nanoparticle Res. 15 (2013) 1593. https://doi.org/10.1007/s11051-013-1593-6.

[40] S.M. Albukhari, M. Ismail, K. Akhtar, E.Y. Danish, Catalytic reduction of nitrophenols and dyes using silver nanoparticles @ cellulose polymer paper for the resolution of waste water treatment challenges, Colloids Surfaces A Physicochem. Eng. Asp. 577 (2019) 548–561. https://doi.org/10.1016/j.colsurfa.2019.05.058.

[41] M.A. Ahsan, V. Jabbari, A.A. El-Gendy, M.L. Curry, J.C. Noveron, Ultrafast catalytic reduction of environmental pollutants in water via MOF-derived magnetic Ni and Cu nanoparticles encapsulated in porous carbon, Appl. Surf. Sci. 497 (2019). https://doi.org/10.1016/j.apsusc.2019.143608.

[42] Y. Ding, W. Sun, W. Yang, Q. Li, Formic acid as the in-situ hydrogen source for catalytic reduction of nitrate in water by PdAg alloy nanoparticles supported on amine-functionalized SiO2, Appl. Catal. B Environ. 203 (2017) 372–380. https://doi.org/10.1016/j.apcatb.2016.10.048.

[43] H.A. Maitlo, K.-H. Kim, V. Kumar, S. Kim, J.-W. Park, Nanomaterials-based treatment options for chromium in aqueous environments, Environ. Int. 130 (2019) 104748. https://doi.org/10.1016/j.envint.2019.04.020.

[44] L. Li, M. Fan, R.C. Brown, J. Van Leeuwen, J. Wang, W. Wang, Y. Song, P. Zhang,

Synthesis, properties, and environmental applications of nanoscale iron-based materials: A review, Crit. Rev. Environ. Sci. Technol. 36 (2006) 405–431. https://doi.org/10.1080/10643380600620387.

[45] H. Song, E.R. Carraway, Reduction of Chlorinated Ethanes by Nanosized Zero-Valent Iron: Kinetics, Pathways, and Effects of Reaction Conditions, Environ. Sci. Technol. 39 (2005) 6237–6245. https://doi.org/10.1021/es048262e.

[46] M. Rivero-Huguet, W.D. Marshall, Reduction of hexavalent chromium mediated by micron- and nano-scale zero-valent metallic particles, J. Environ. Monit. 11 (2009) 1072–1079. https://doi.org/10.1039/b819279k.

[47] K. Jain, A.S. Patel, V.P. Pardhi, S.J.S. Flora, Nanotechnology in Wastewater Management: A New Paradigm Towards Wastewater Treatment, Molecules. 26 (2021) 1797. https://doi.org/10.3390/molecules26061797.

[48] H.R. Pant, H.J. Kim, M.K. Joshi, B. Pant, C.H. Park, J.I. Kim, K.S. Hui, C.S. Kim, One-step fabrication of multifunctional composite polyurethane spider-web-like nanofibrous membrane for water purification, J. Hazard. Mater. 264 (2014) 25–33. https://doi.org/10.1016/j.jhazmat.2013.10.066.

[49] S. Islam, M.A.R. Bhuiyan, M.N. Islam, Chitin and Chitosan: Structure, Properties and Applications in Biomedical Engineering, J. Polym. Environ. 25 (2017) 854–866. https://doi.org/10.1007/s10924-016-0865-5.

[50] L. Qi, Z. Xu, X. Jiang, C. Hu, X. Zou, Preparation and antibacterial activity of chitosan nanoparticles, Carbohydr. Res. 339 (2004) 2693–2700. https://doi.org/10.1016/j.carres.2004.09.007.

[51] I.X. Yin, J. Zhang, I.S. Zhao, M.L. Mei, Q. Li, C.H. Chu, The antibacterial mechanism of silver nanoparticles and its application in dentistry, Int. J. Nanomedicine. 15 (2020) 2555–2562. https://doi.org/10.2147/IJN.S246764.

[52] K. Sunada, T. Watanabe, K. Hashimoto, Studies on photokilling of bacteria on TiO 2 thin film, J. Photochem. Photobiol. A Chem. 156 (2003) 227–233. https://doi.org/10.1016/S1010-6030(02)00434-3.

[53] T. Mocan, C.T. Matea, T. Pop, O. Mosteanu, A.D. Buzoianu, S. Suciu, C. Puia, C. Zdrehus, C. Iancu, L. Mocan, Carbon nanotubes as anti-bacterial agents, Cell. Mol. Life Sci. 74 (2017) 3467–3479. https://doi.org/10.1007/s00018-017-2532-y.

[54] M. Azizi-Lalabadi, H. Hashemi, J. Feng, S.M. Jafari, Carbon nanomaterials against pathogens; the antimicrobial activity of carbon nanotubes, graphene/graphene oxide, fullerenes, and their nanocomposites, Adv. Colloid Interface Sci. 284 (2020). https://doi.org/10.1016/j.cis.2020.102250.

[55] F. Fu, D.D. Dionysiou, H. Liu, The use of zero-valent iron for groundwater remediation and wastewater treatment: A review, J. Hazard. Mater. 267 (2014) 194–205. https://doi.org/10.1016/j.jhazmat.2013.12.062.

[56] M.R. Jamei, M.R. Khosravi, B. Anvaripour, A novel ultrasound assisted method in synthesis of NZVI particles, Ultrason. Sonochem. 21 (2014) 226–233. https://doi.org/10.1016/j.ultsonch.2013.04.015.

[57] T. Shubair, O. Eljamal, A.M.E. Khalil, A. Tahara, N. Matsunaga, Novel application of nanoscale zero valent iron and bimetallic nano-Fe/Cu particles for the treatment of cesium contaminated water, J. Environ. Chem. Eng. 6 (2018) 4253–4264.

https://doi.org/10.1016/j.jece.2018.06.015.

[58] S. Dadfarnia, A.M. Haji Shabani, S.E. Moradi, S. Emami, Methyl red removal from water by iron based metal-organic frameworks loaded onto iron oxide nanoparticle adsorbent, Appl. Surf. Sci. 330 (2015) 85–93. https://doi.org/10.1016/j.apsusc.2014.12.196.

[59] B.I. Kharisov, H. V. Rasika Dias, O. V. Kharissova, V. Manuel Jiménez-Pérez, B. Olvera Pérez, B. Muñoz Flores, Iron-containing nanomaterials: Synthesis, properties, and environmental applications, RSC Adv. 2 (2012) 9325–9358. https://doi.org/10.1039/c2ra20812a.

[60] D. Lopez-Tejedor, R. Benavente, J.M. Palomo, Iron nanostructured catalysts: Design and applications, Catal. Sci. Technol. 8 (2018) 1754–1776. https://doi.org/10.1039/c7cy02259j.

[61] Y. Zhou, B. Gao, A.R. Zimmerman, H. Chen, M. Zhang, X. Cao, Biochar-supported zerovalent iron for removal of various contaminants from aqueous solutions, Bioresour. Technol. 152 (2014) 538–542. https://doi.org/10.1016/j.biortech.2013.11.021.

[62] W. Yan, A.A. Herzing, C.J. Kiely, W.X. Zhang, Nanoscale zero-valent iron (nZVI): Aspects of the core-shell structure and reactions with inorganic species in water, J. Contam. Hydrol. 118 (2010) 96–104. https://doi.org/10.1016/j.jconhyd.2010.09.003.

[63] S.M. Ponder, J.G. Darab, T.E. Mallouk, Remediation of Cr(VI) and Pb(II) aqueous solutions using supported, nanoscale zero-valent iron, Environ. Sci. Technol. 34 (2000) 2564–2569. https://doi.org/10.1021/es9911420.

[64] X. Wang, P. Wang, J. Ma, H. Liu, P. Ning, Synthesis, characterization, and reactivity of cellulose modified nano zero-valent iron for dye discoloration, Appl. Surf. Sci. 345 (2015) 57–66. https://doi.org/10.1016/j.apsusc.2015.03.131.

[65] Y. Mu, F. Jia, Z. Ai, L. Zhang, Iron oxide shell mediated environmental remediation properties of nano zero-valent iron, Environ. Sci. Nano. 4 (2017) 27–45. https://doi.org/10.1039/C6EN00398B.

[66] C.B. Wang, W.X. Zhang, Synthesizing nanoscale iron particles for rapid and complete dechlorination of TCE and PCBs, Environ. Sci. Technol. 31 (1997) 2154–2156. https://doi.org/10.1021/es970039c.

[67] Z. Fang, J. Chen, X. Qiu, X. Qiu, W. Cheng, L. Zhu, Effective removal of antibiotic metronidazole from water by nanoscale zero-valent iron particles, Desalination. 268 (2011) 60–67. https://doi.org/10.1016/j.desal.2010.09.051.

[68] Y.C. Chang, S.C. Huang, K.F. Chen, Evaluation of the effects of nanoscale zero-valent iron (nZVI) dispersants on intrinsic biodegradation of trichloroethylene (TCE), Water Sci. Technol. 69 (2014) 2357–2363. https://doi.org/10.2166/wst.2014.169.

[69] H. Song, E.R. Carraway, Reduction of chlorinated methanes by nano-sized zero-valent iron. Kinetics, pathways, and effect of reaction conditions, Environ. Eng. Sci. 23 (2006) 272–284. https://doi.org/10.1089/ees.2006.23.272.

[70] K. Sravanthi, D. Ayodhya, P.Y. Swamy, Green synthesis, characterization and catalytic activity of 4-nitrophenol reduction and formation of benzimidazoles using bentonite supported zero valent iron nanoparticles, Mater. Sci. Energy Technol. 2 (2019) 298–307. https://doi.org/10.1016/j.mset.2019.02.003.

[71] G. Naja, A. Halasz, S. Thiboutot, G. Ampleman, J. Hawari, Degradation of hexahydro-1,3,5-trinitro-1,3,5-triazine (RDX) using zerovalent iron nanoparticles, Environ. Sci. Technol. 42 (2008) 4364–4370. https://doi.org/10.1021/es7028153.

[72] A.N. Bezbaruah, J.M. Thompson, B.J. Chisholm, Remediation of alachlor and atrazine contaminated water with zero-valent iron nanoparticles, J. Environ. Sci. Heal. - Part B Pestic. Food Contam. Agric. Wastes. 44 (2009) 518–524. https://doi.org/10.1080/03601230902997501.

[73] K. Šimkovič, J. Derco, M. Valičková, Removal of selected pesticides by nano zero-valent iron, Acta Chim. Slovaca. 8 (2015) 152–155. https://doi.org/10.1515/acs-2015-0026.

[74] C.A. Akinremi, N.N. Omosun, S. Adewuyi, J.O. Azeez, S.N. Olanrewaju, Preparation and Characterization of Chitosan-Humic Acid-Zerovalent Iron Nanocomposite for Nitrate Reduction in Water, J. Appl. Chem. 2016 (2016) 1–8. https://doi.org/10.1155/2016/1895854.

[75] J. Filip, J. Kolařík, E. Petala, M. Petr, O. Šráček, R. Zbořil, Nanoscale zerovalent iron particles for treatment of metalloids, 2019. https://doi.org/10.1007/978-3-319-95340-3_4.

[76] Y. Mao, Z. Xi, W. Wang, C. Ma, Q. Yue, Kinetics of solvent blue and reactive yellow removal using microwave radiation in combination with nanoscale zero-valent iron, J. Environ. Sci. (China). 30 (2015) 164–172. https://doi.org/10.1016/j.jes.2014.09.030.

[77] P. Prema, S. Thangapandian, M. Selvarani, S. Subharanjani, C. Amutha, Color removal efficiency of dyes using nanozerovalent iron treatment, Toxicol. Environ. Chem. 93 (2011) 1908–1917. https://doi.org/10.1080/02772248.2011.606613.

[78] H.Y. Shu, M.C. Chang, H.H. Yu, W.H. Chen, Reduction of an azo dye Acid Black 24 solution using synthesized nanoscale zerovalent iron particles, J. Colloid Interface Sci. 314 (2007) 89–97. https://doi.org/10.1016/j.jcis.2007.04.071.

[79] C. Noubactep, An analysis of the evolution of reactive species in Fe0/H2O systems, J. Hazard. Mater. 168 (2009) 1626–1631. https://doi.org/10.1016/j.jhazmat.2009.02.143.

[80] J. Golpagar, E. Grulke, T. Tsang, D. Bhattacharyya, Reductive dehalogenation of trichloroethylene using zero-valent iron, Environ. Prog. 16 (1997) 137–143. https://doi.org/10.1002/ep.3300160221.

[81] P. Raizada, P. Singh, A. Kumar, B. Pare, S.B. Jonnalagadda, Zero valent iron-brick grain nanocomposite for enhanced solar-Fenton removal of malachite green, Sep. Purif. Technol. 133 (2014) 429–437. https://doi.org/10.1016/j.seppur.2014.07.012.

[82] E. Xingu-Contreras, G. García-Rosales, I. García-Sosa, A. Cabral-Prieto, Degradation of methyl orange using iron nanoparticles with/without support at different conditions, Microporous Mesoporous Mater. 292 (2020) 109782. https://doi.org/10.1016/j.micromeso.2019.109782.

[83] P. Singh, P. Raizada, S. Kumari, A. Kumar, D. Pathania, P. Thakur, Solar-Fenton removal of malachite green with novel Fe0-activated carbon nanocomposite, Appl. Catal. A Gen. 476 (2014) 9–18. https://doi.org/10.1016/j.apcata.2014.02.009.

[84] N.C. Mueller, J. Braun, J. Bruns, M. Černík, P. Rissing, D. Rickerby, B. Nowack, Application of nanoscale zero valent iron (NZVI) for groundwater remediation in Europe, Environ. Sci. Pollut. Res. 19 (2012) 550–558. https://doi.org/10.1007/s11356-011-0576-3.

[85] R. Eljamal, I. Kahraman, O. Eljamal, I.P. Thompson, I. Maamoun, G. Yilmaz, Impact of nZVI on the formation of aerobic granules, bacterial growth and nutrient removal using aerobic sequencing batch reactor, Environ. Technol. Innov. 19 (2020) 100911. https://doi.org/10.1016/j.eti.2020.100911.

[86] O. Eljamal, K. Sasaki, T. Hirajima, Sorption Kinetic of Arsenate as Water Contaminant on

Zero Valent Iron, J. Water Resour. Prot. 05 (2013) 563–567. https://doi.org/10.4236/jwarp.2013.56057.

[87] A.M.E. Khalil, O. Eljamal, B.B. Saha, N. Matsunaga, Performance of nanoscale zero-valent iron in nitrate reduction from water using a laboratory-scale continuous-flow system, Chemosphere. 197 (2018) 502–512. https://doi.org/10.1016/j.chemosphere.2018.01.084.

[88] M. Stefaniuk, P. Oleszczuk, Y.S. Ok, Review on nano zerovalent iron (nZVI): From synthesis to environmental applications, Chem. Eng. J. 287 (2016) 618–632. https://doi.org/10.1016/j.cej.2015.11.046.

[89] Y.P. Sun, X. qin Li, J. Cao, W. xian Zhang, H.P. Wang, Characterization of zero-valent iron nanoparticles, Adv. Colloid Interface Sci. 120 (2006) 47–56. https://doi.org/10.1016/j.cis.2006.03.001.

[90] S.S. Chen, H. Der Hsu, C.W. Li, A new method to produce nanoscale iron for nitrate removal, J. Nanoparticle Res. 6 (2004) 639–647. https://doi.org/10.1007/s11051-004-6672-2.

[91] L.B. Hoch, E.J. Mack, B.W. Hydutsky, J.M. Hershman, J.M. Skluzacek, T.E. Mallouk, Carbothermal synthesis of carbon-supported nanoscale zero-valent iron particles for the remediation of hexavalent chromium, Environ. Sci. Technol. 42 (2008) 2600–2605. https://doi.org/10.1021/es702589u.

[92] J. Adusei-Gyamfi, V. Acha, Carriers for nano zerovalent iron (nZVI): Synthesis, application and efficiency, RSC Adv. 6 (2016) 91025–91044. https://doi.org/10.1039/c6ra16657a.

[93] S. Li, W. Yan, W.X. Zhang, Solvent-free production of nanoscale zero-valent iron (nZEVI) with precision milling, Green Chem. 11 (2009) 1618–1626. https://doi.org/10.1039/b913056j.

[94] D. Ribas, M. Cernik, V. Martí, J.A. Benito, Improvements in nanoscale zero-valent iron production by milling through the addition of alumina, J. Nanoparticle Res. 18 (2016). https://doi.org/10.1007/s11051-016-3490-2.

[95] T. Pasinszki, M. Krebsz, Synthesis and application of zero-valent iron nanoparticles in water treatment, environmental remediation, catalysis, and their biological effects, Nanomaterials. 10 (2020). https://doi.org/10.3390/nano10050917.

[96] Y. Vitta, V. Piscitelli, A. Fernandez, F. Gonzalez-Jimenez, J. Castillo, α-Fe nanoparticles produced by laser ablation: Optical and magnetic properties, Chem. Phys. Lett. 512 (2011) 96–98. https://doi.org/10.1016/j.cplett.2011.07.020.

[97] H. Pullin, R. Springell, S. Parry, T. Scott, The effect of aqueous corrosion on the structure and reactivity of zero-valent iron nanoparticles, Chem. Eng. J. 308 (2017) 568–577. https://doi.org/10.1016/j.cej.2016.09.088.

[98] S. Saif, A. Tahir, Y. Chen, Green synthesis of iron nanoparticles and their environmental applications and implications, Nanomaterials. 6 (2016). https://doi.org/10.3390/nano6110209.

[99] S. Bae, S. Gim, H. Kim, K. Hanna, Effect of NaBH4 on properties of nanoscale zero-valent iron and its catalytic activity for reduction of p-nitrophenol, Appl. Catal. B Environ. 182 (2016) 541–549. https://doi.org/10.1016/j.apcatb.2015.10.006.

[100] H. Woo, J. Park, S. Lee, S. Lee, Effects of washing solution and drying condition on reactivity of nano-scale zero valent irons (nZVIs) synthesized by borohydride reduction,

Chemosphere. 97 (2014) 146–152. https://doi.org/10.1016/j.chemosphere.2013.11.010.

[101] C.-J. Choi, X.-L. Dong, B.-K. Kim, Microstructure and Magnetic Properties of Fe Nanoparticles Synthesized by Chemical Vapor Condensation, Mater. Trans. 42 (2001) 2046–2049. https://doi.org/10.2320/matertrans.42.2046.

[102] F.E. García, A.M. Senn, J.M. Meichtry, T.B. Scott, H. Pullin, A.G. Leyva, E.B. Halac, C.P. Ramos, J. Sacanell, M. Mizrahi, F.G. Requejo, M.I. Litter, Iron-based nanoparticles prepared from yerba mate extract. Synthesis, characterization and use on chromium removal, J. Environ. Manage. 235 (2019) 1–8. https://doi.org/10.1016/j.jenvman.2019.01.002.

[103] Y. Wei, Z. Fang, L. Zheng, E.P. Tsang, Biosynthesized iron nanoparticles in aqueous extracts of Eichhornia crassipes and its mechanism in the hexavalent chromium removal, Appl. Surf. Sci. 399 (2017) 322–329. https://doi.org/10.1016/j.apsusc.2016.12.090.

[104] O.P. Bolade, A.B. Williams, N.U. Benson, Green synthesis of iron-based nanomaterials for environmental remediation: A review, Environ. Nanotechnology, Monit. Manag. 13 (2020) 100279. https://doi.org/10.1016/j.enmm.2019.100279.

[105] K.S. Siddiqi, A. ur Rahman, Tajuddin, A. Husen, Biogenic Fabrication of Iron/Iron Oxide Nanoparticles and Their Application, Nanoscale Res. Lett. 11 (2016). https://doi.org/10.1186/s11671-016-1714-0.

[106] A. Ebrahiminezhad, A. Zare-Hoseinabadi, A.K. Sarmah, S. Taghizadeh, Y. Ghasemi, A. Berenjian, Plant-Mediated Synthesis and Applications of Iron Nanoparticles, Mol. Biotechnol. 60 (2018) 154–168. https://doi.org/10.1007/s12033-017-0053-4.

[107] G.E. Hoag, J.B. Collins, J.L. Holcomb, J.R. Hoag, M.N. Nadagouda, R.S. Varma, Degradation of bromothymol blue by “greener” nano-scale zero-valent iron synthesized using tea polyphenols, J. Mater. Chem. 19 (2009) 8671–8677. https://doi.org/10.1039/b909148c.

[108] K. Manquián-Cerda, E. Cruces, M. Angélica Rubio, C. Reyes, N. Arancibia-Miranda, Preparation of nanoscale iron (oxide, oxyhydroxides and zero-valent) particles derived from blueberries: Reactivity, characterization and removal mechanism of arsenate, Ecotoxicol. Environ. Saf. 145 (2017) 69–77. https://doi.org/10.1016/j.ecoenv.2017.07.004.

[109] S. Machado, J.P. Grosso, H.P.A. Nouws, J.T. Albergaria, C. Delerue-Matos, Utilization of food industry wastes for the production of zero-valent iron nanoparticles, Sci. Total Environ. 496 (2014) 233–240. https://doi.org/10.1016/j.scitotenv.2014.07.058.

[110] K. Sravanthi, D. Ayodhya, P. Yadgiri Swamy, Green synthesis, characterization of biomaterial-supported zero-valent iron nanoparticles for contaminated water treatment, J. Anal. Sci. Technol. 9 (2018). https://doi.org/10.1186/s40543-017-0134-9.

[111] J. Nasiri, E. Motamedi, M.R. Naghavi, M. Ghafoori, Removal of crystal violet from water using B-cyclodextrin functionalized biogenic zero-valent iron nanoadsorbents synthesized via aqueous root extracts of Ferula persica, J. Hazard. Mater. 367 (2019) 325–338. https://doi.org/10.1016/j.jhazmat.2018.12.079.

[112] H.J. Lu, J.K. Wang, S. Ferguson, T. Wang, Y. Bao, H.X. Hao, Mechanism, synthesis and modification of nano zerovalent iron in water treatment, Nanoscale. 8 (2016) 9962–9975. https://doi.org/10.1039/c6nr00740f.

[113] F.S. Dos Santos, F.R. Lago, L. Yokoyama, F.V. Fonseca, Synthesis and characterization of zero-valent iron nanoparticles supported on SBA-15, J. Mater. Res. Technol. 6 (2017) 178–

183. https://doi.org/10.1016/j.jmrt.2016.11.004.

[114] T. Long, C.A. Ramsburg, Encapsulation of nZVI particles using a Gum Arabic stabilized oil-in-water emulsion, J. Hazard. Mater. 189 (2011) 801–808. https://doi.org/10.1016/j.jhazmat.2011.02.084.

[115] A.D. Bokare, R.C. Chikate, C. V. Rode, K.M. Paknikar, Iron-nickel bimetallic nanoparticles for reductive degradation of azo dye Orange G in aqueous solution, Appl. Catal. B Environ. 79 (2008) 270–278. https://doi.org/10.1016/j.apcatb.2007.10.033.

[116] Y. Li, D. Han, Y. Arai, X. Fu, X. Li, W. Huang, Kinetics and mechanisms of debromination of tetrabromobisphenol A by Cu coated nano zerovalent iron, Chem. Eng. J. 373 (2019) 95–103. https://doi.org/10.1016/j.cej.2019.04.182.

[117] Z. Marková, K.M.H. Šišková, J. Filip, J. Čuda, M. Kolář, K. Šafářová, I. Medřík, R. Zbořil, Air stable magnetic bimetallic Fe-Ag nanoparticles for advanced antimicrobial treatment and phosphorus removal, Environ. Sci. Technol. 47 (2013) 5285–5293. https://doi.org/10.1021/es304693g.

[118] I. San Román, M.L. Alonso, L. Bartolomé, A. Galdames, E. Goiti, M. Ocejo, M. Moragues, R.M. Alonso, J.L. Vilas, Relevance study of bare and coated zero valent iron nanoparticles for lindane degradation from its by-product monitorization, Chemosphere. 93 (2013) 1324–1332. https://doi.org/10.1016/j.chemosphere.2013.07.050.

[119] Y.T. Wei, S. chee Wu, S.W. Yang, C.H. Che, H.L. Lien, D.H. Huang, Biodegradable surfactant stabilized nanoscale zero-valent iron for in situ treatment of vinyl chloride and 1,2-dichloroethane, J. Hazard. Mater. 211–212 (2012) 373–380. https://doi.org/10.1016/j.jhazmat.2011.11.018.

[120] V.T. Padil Vinod, S. Wacławek, C. Senan, J. Kupčík, K. Pešková, M. Černík, H.M. Somashekarappa, Gum karaya (Sterculia urens) stabilized zero-valent iron nanoparticles: characterization and applications for the removal of chromium and volatile organic pollutants from water, RSC Adv. 7 (2017) 13997–14009. https://doi.org/10.1039/c7ra00464h.

[121] F. Fu, Z. Cheng, D.D. Dionysiou, B. Tang, Fe/Al bimetallic particles for the fast and highly efficient removal of Cr(VI) over a wide pH range: PERFORMANCE and mechanism, J. Hazard. Mater. 298 (2015) 261–269. https://doi.org/10.1016/j.jhazmat.2015.05.047.

[122] R.J. Barnes, O. Riba, M.N. Gardner, T.B. Scott, S.A. Jackman, I.P. Thompson, Optimization of nano-scale nickel/iron particles for the reduction of high concentration chlorinated aliphatic hydrocarbon solutions, Chemosphere. 79 (2010) 448–454. https://doi.org/10.1016/j.chemosphere.2010.01.044.

[123] C. ping Tso, Y. hsin Shih, The reactivity of well-dispersed zerovalent iron nanoparticles toward pentachlorophenol in water, Water Res. 72 (2015) 372–380. https://doi.org/10.1016/j.watres.2014.12.038.

[124] R. Wang, T. Tang, G. Lu, Z. Zheng, K. Huang, H. Li, X. Tao, H. Yin, Z. Shi, Z. Lin, F. Wu, Z. Dang, Mechanisms and pathways of debromination of polybrominated diphenyl ethers (PBDEs) in various nano-zerovalent iron-based bimetallic systems, Sci. Total Environ. 661 (2019) 18–26. https://doi.org/10.1016/j.scitotenv.2019.01.166.

[125] T. Zhou, Y. Li, T.T. Lim, Catalytic hydrodechlorination of chlorophenols by Pd/Fe nanoparticles: Comparisons with other bimetallic systems, kinetics and mechanism, Sep. Purif. Technol. 76 (2010) 206–214. https://doi.org/10.1016/j.seppur.2010.10.010.

[126] C.A. Ruiz-Torres, R.F. Araujo-Martínez, G.A. Martínez-Castañón, J.E. Morales-Sánchez, J.M. Guajardo-Pacheco, J. González-Hernández, T.J. Lee, H.S. Shin, Y. Hwang, F. Ruiz, Preparation of air stable nanoscale zero valent iron functionalized by ethylene glycol without inert condition, Chem. Eng. J. 336 (2018) 112–122. https://doi.org/10.1016/j.cej.2017.11.047.

[127] F. He, D. Zhao, manipulating the size and dispersibility of zerovalent iron nanoparticles by use of carboxymethyl cellulose stabilizers, Environ. Sci. Technol. 42 (2008) 3480. https://doi.org/10.1021/es8004255.

[128] M. Mosaferi, S. Nemati, A. Khataee, S. Nasseri, A.A. Hashemi, Removal of arsenic (III, V) from aqueous solution by nanoscale zero-valent iron stabilized with Starch and Carboxymethyl cellulose, J. Environ. Heal. Sci. Eng. 12 (2014) 1–11. https://doi.org/10.1186/2052-336X-12-74.

[129] Y.H. Lin, H.H. Tseng, M.Y. Wey, M. Der Lin, Characteristics of two types of stabilized nano zero-valent iron and transport in porous media, Sci. Total Environ. 408 (2010) 2260–2267. https://doi.org/10.1016/j.scitotenv.2010.01.039.

[130] R.D. Kale, P.B. Kane, Synthesis of PVP stabilized bimetallic nanoparticles for removal of azo based reactive dye from aqueous solution, Sustain. Chem. Pharm. 10 (2018) 153–162. https://doi.org/10.1016/j.scp.2018.11.002.

[131] X. Wang, L. Le, A. Wang, H. Liu, J. Ma, M. Li, Comparative study on properties, mechanisms of anionic dispersant modified nano zero-valent iron for removal of Cr(VI), J. Taiwan Inst. Chem. Eng. 66 (2016) 115–125. https://doi.org/10.1016/j.jtice.2016.05.049.

[132] Y.P. Peng, T.Y. Chen, C.Y. Wu, Y.C. Chang, K.F. Chen, Dispersant-modified iron nanoparticles for mobility enhancement and TCE degradation: a comparison study, Environ. Sci. Pollut. Res. 26 (2019) 34157–34166. https://doi.org/10.1007/s11356-018-3739-7.

[133] W. Yan, H.L. Lien, B.E. Koel, W.X. Zhang, Iron nanoparticles for environmental clean-up: Recent developments and future outlook, Environ. Sci. Process. Impacts. 15 (2013) 63–77. https://doi.org/10.1039/c2em30691c.

[134] M. Nairat, T. Shahwan, A.E. Eroğlu, H. Fuchs, Incorporation of iron nanoparticles into clinoptilolite and its application for the removal of cationic and anionic dyes, J. Ind. Eng. Chem. 21 (2015) 1143–1151. https://doi.org/10.1016/j.jiec.2014.05.027.

[135] M. Daneshkhah, H. Hossaini, M. Malakootian, Removal of metoprolol from water by sepiolite-supported nanoscale zero-valent iron, J. Environ. Chem. Eng. 5 (2017) 3490–3499. https://doi.org/10.1016/j.jece.2017.06.040.

[136] Z.X. Chen, Y. Cheng, Z. Chen, M. Megharaj, R. Naidu, Kaolin-supported nanoscale zero-valent iron for removing cationic dye-crystal violet in aqueous solution, J. Nanoparticle Res. 14 (2012). https://doi.org/10.1007/s11051-012-0899-0.

[137] N. Yuan, G. Zhang, S. Guo, Z. Wan, Enhanced ultrasound-assisted degradation of methyl orange and metronidazole by rectorite-supported nanoscale zero-valent iron, Ultrason. Sonochem. 28 (2016) 62–68. https://doi.org/10.1016/j.ultsonch.2015.06.029.

[138] S. Hu, Y. Wu, H. Yao, C. Lu, C. Zhang, Enhanced Fenton-like removal of nitrobenzene via internal microelectrolysis in nano zerovalent iron/activated carbon composite, Water Sci. Technol. 73 (2016) 153–160. https://doi.org/10.2166/wst.2015.467.

[139] L. Han, S. Xue, S. Zhao, J. Yan, L. Qian, M. Chen, Biochar supported nanoscale iron

particles for the efficient removal of methyl orange dye in aqueous solutions, PLoS One. 10 (2015) 1–15. https://doi.org/10.1371/journal.pone.0132067.

[140] H. Chen, Y. Cao, E. Wei, T. Gong, Q. Xian, Facile synthesis of graphene nano zero-valent iron composites and their efficient removal of trichloronitromethane from drinking water, Chemosphere. 146 (2016) 32–39. https://doi.org/10.1016/j.chemosphere.2015.11.095.

[141] G. Sheng, A. Alsaedi, W. Shammakh, S. Monaquel, J. Sheng, X. Wang, H. Li, Y. Huang, Enhanced sequestration of selenite in water by nanoscale zero valent iron immobilization on carbon nanotubes by a combined batch, XPS and XAFS investigation, Carbon N. Y. 99 (2016) 123–130. https://doi.org/10.1016/j.carbon.2015.12.013.

[142] M. Bagheri, S.M. Jafari, M.H. Eikani, Ultrasonic-assisted production of zero-valent iron-decorated graphene oxide/activated carbon nanocomposites: Chemical transformation and structural evolution, Mater. Sci. Eng. C. 118 (2021) 111362. https://doi.org/10.1016/j.msec.2020.111362.

[143] M. Liu, Y. Wang, L. Chen, Y. Zhang, Z. Lin, Mg(OH)2 supported nanoscale zero valent iron enhancing the removal of Pb(II) from aqueous solution, ACS Appl. Mater. Interfaces. 7 (2015) 7961–7969. https://doi.org/10.1021/am509184e.

[144] E. Petala, M. Baikousi, M.A. Karakassides, G. Zoppellaro, J. Filip, J. Tuček, K.C. Vasilopoulos, J. Pechoušek, R. Zbořil, Synthesis, physical properties and application of the zero-valent iron/titanium dioxide heterocomposite having high activity for the sustainable photocatalytic removal of hexavalent chromium in water, Phys. Chem. Chem. Phys. 18 (2016) 10637–10646. https://doi.org/10.1039/c6cp01013j.

[145] J. Dong, C. Wen, D. Liu, W. Zhang, J. Li, H. Jiang, C. Qin, M. Hong, Study on degradation of nitrobenzene in groundwater using emulsified nano-zero-valent iron, J. Nanoparticle Res. 17 (2015) 31. https://doi.org/10.1007/s11051-014-2829-9.

[146] Z. Xiao, H. Zhang, Y. Xu, M. Yuan, X. Jing, J. Huang, Q. Li, D. Sun, Ultra-efficient removal of chromium from aqueous medium by biogenic iron based nanoparticles, Sep. Purif. Technol. 174 (2017) 466–473. https://doi.org/10.1016/j.seppur.2016.10.047.

[147] Y. Liu, S.P. Sohi, S. Liu, J. Guan, J. Zhou, J. Chen, Adsorption and reductive degradation of Cr(VI) and TCE by a simply synthesized zero valent iron magnetic biochar, J. Environ. Manage. 235 (2019) 276–281. https://doi.org/10.1016/j.jenvman.2019.01.045.

[148] S.S. Poguberović, D.M. Krčmar, S.P. Maletić, Z. Kónya, D.D.T. Pilipović, D. V. Kerkez, S.D. Rončević, Removal of As(III) and Cr(VI) from aqueous solutions using “green” zero-valent iron nanoparticles produced by oak, mulberry and cherry leaf extracts, Ecol. Eng. 90 (2016) 42–49. https://doi.org/10.1016/j.ecoleng.2016.01.083.

[149] V. Madhavi, T.N.V.K.V. Prasad, A.V.B. Reddy, B. Ravindra Reddy, G. Madhavi, Application of phytogenic zerovalent iron nanoparticles in the adsorption of hexavalent chromium, Spectrochim. Acta - Part A Mol. Biomol. Spectrosc. 116 (2013) 17–25. https://doi.org/10.1016/j.saa.2013.06.045.

[150] S.S. Poguberović, D.M. Krčmar, B.D. Dalmacija, S.P. Maletić, D.D. Tomašević-Pilipović, D. V. Kerkez, S.D. Rončevic, Removal of Ni(II) and Cu(II) from aqueous solutions using “green” zero-valent iron nanoparticles produced by oak and mulberry leaf extracts, Water Sci. Technol. 74 (2016) 2115–2123. https://doi.org/10.2166/wst.2016.387.

[151] A. Soliemanzadeh, M. Fekri, The application of green tea extract to prepare bentonite-supported nanoscale zero-valent iron and its performance on removal of Cr(VI): Effect of relative parameters and soil experiments, Microporous Mesoporous Mater. 239 (2017) 60–

69. https://doi.org/10.1016/j.micromeso.2016.09.050.

[152] Q. Wang, H. Qian, Y. Yang, Z. Zhang, C. Naman, X. Xu, Reduction of hexavalent chromium by carboxymethyl cellulose-stabilized zero-valent iron nanoparticles, J. Contam. Hydrol. 114 (2010) 35–42. https://doi.org/10.1016/j.jconhyd.2010.02.006.

[153] C. Jiao, Y. Cheng, W. Fan, J. Li, Synthesis of agar-stabilized nanoscale zero-valent iron particles and removal study of hexavalent chromium, Int. J. Environ. Sci. Technol. 12 (2015) 1603–1612. https://doi.org/10.1007/s13762-014-0524-0.

[154] H. Dong, J. Deng, Y. Xie, C. Zhang, Z. Jiang, Y. Cheng, K. Hou, G. Zeng, Stabilization of nanoscale zero-valent iron (nZVI) with modified biochar for Cr(VI) removal from aqueous solution, J. Hazard. Mater. 332 (2017) 79–86. https://doi.org/10.1016/j.jhazmat.2017.03.002.

[155] S. Mortazavian, H. An, D. Chun, J. Moon, Activated carbon impregnated by zero-valent iron nanoparticles (AC/nZVI) optimized for simultaneous adsorption and reduction of aqueous hexavalent chromium: Material characterizations and kinetic studies, Chem. Eng. J. 353 (2018) 781–795. https://doi.org/10.1016/j.cej.2018.07.170.

[156] R. Zhao, Z. Zhou, X. Zhao, G. Jing, Enhanced Cr(VI) removal from simulated electroplating rinse wastewater by amino-functionalized vermiculite-supported nanoscale zero-valent iron, Elsevier Ltd, 2019. https://doi.org/10.1016/j.chemosphere.2018.11.118.

[157] F. Fu, J. Ma, L. Xie, B. Tang, W. Han, S. Lin, Chromium removal using resin supported nanoscale zero-valent iron, J. Environ. Manage. 128 (2013) 822–827. https://doi.org/10.1016/j.jenvman.2013.06.044.

[158] Y. Yin, C. Shen, X. Bi, T. Li, Removal of hexavalent chromium from aqueous solution by fabricating novel heteroaggregates of montmorillonite microparticles with nanoscale zero-valent iron, Sci. Rep. 10 (2020) 1–12. https://doi.org/10.1038/s41598-020-69244-z.

[159] M. Fazlzadeh, K. Rahmani, A. Zarei, H. Abdoallahzadeh, F. Nasiri, R. Khosravi, A novel green synthesis of zero valent iron nanoparticles (NZVI) using three plant extracts and their efficient application for removal of Cr(VI) from aqueous solutions, Adv. Powder Technol. 28 (2017) 122–130. https://doi.org/10.1016/j.apt.2016.09.003.

[160] A. Rana, N. Kumari, M. Tyagi, S. Jagadevan, Leaf-extract mediated zero-valent iron for oxidation of Arsenic (III): Preparation, characterization and kinetics, Chem. Eng. J. 347 (2018) 91–100. https://doi.org/10.1016/j.cej.2018.04.075.

[161] P.K. Tandon, R.C. Shukla, S.B. Singh, Removal of arsenic(III) from water with clay-supported zerovalent iron nanoparticles synthesized with the help of tea liquor, Ind. Eng. Chem. Res. 52 (2013) 10052–10058. https://doi.org/10.1021/ie400702k.

[162] S. Li, W. Wang, F. Liang, W.X. Zhang, Heavy metal removal using nanoscale zero-valent iron (nZVI): Theory and application, J. Hazard. Mater. 322 (2017) 163–171. https://doi.org/10.1016/j.jhazmat.2016.01.032.

[163] Z. Li, L. Wang, J. Meng, X. Liu, J. Xu, F. Wang, P. Brookes, Zeolite-supported nanoscale zero-valent iron: New findings on simultaneous adsorption of Cd(II), Pb(II), and As(III) in aqueous solution and soil, J. Hazard. Mater. 344 (2018) 1–11. https://doi.org/10.1016/j.jhazmat.2017.09.036.

[164] W. Liang, C. Dai, X. Zhou, Y. Zhang, Application of zero-valent iron nanoparticles for the removal of aqueous zinc ions under various experimental conditions, PLoS One. 9 (2014). https://doi.org/10.1371/journal.pone.0085686.

[165] Y. Kuang, J. Du, R. Zhou, Z. Chen, M. Megharaj, R. Naidu, Calcium alginate encapsulated Ni/Fe nanoparticles beads for simultaneous removal of Cu (II) and monochlorobenzene, J. Colloid Interface Sci. 447 (2015) 85–91. https://doi.org/10.1016/j.jcis.2015.01.080.

[166] M. Arshadi, M.K. Abdolmaleki, F. Mousavinia, S. Foroughifard, A. Karimzadeh, Nano modification of NZVI with an aquatic plant Azolla filiculoides to remove Pb(II) and Hg(II) from water: Aging time and mechanism study, J. Colloid Interface Sci. 486 (2017) 296–308. https://doi.org/10.1016/j.jcis.2016.10.002.

[167] L. Katata-Seru, T. Moremedi, O.S. Aremu, I. Bahadur, Green synthesis of iron nanoparticles using Moringa oleifera extracts and their applications: Removal of nitrate from water and antibacterial activity against Escherichia coli, J. Mol. Liq. 256 (2018) 296–304. https://doi.org/10.1016/j.molliq.2017.11.093.

[168] T. Wang, J. Lin, Z. Chen, M. Megharaj, R. Naidu, Green synthesized iron nanoparticles by green tea and eucalyptus leaves extracts used for removal of nitrate in aqueous solution, J. Clean. Prod. 83 (2014) 413–419. https://doi.org/10.1016/j.jclepro.2014.07.006.

[169] Y.H. Hwang, D.G. Kim, H.S. Shin, Mechanism study of nitrate reduction by nano zero valent iron, J. Hazard. Mater. 185 (2011) 1513–1521. https://doi.org/10.1016/j.jhazmat.2010.10.078.

[170] B. Desalegn, M. Megharaj, Z. Chen, R. Naidu, Green synthesis of zero valent iron nanoparticle using mango peel extract and surface characterization using XPS and GC-MS, Heliyon. 5 (2019) e01750. https://doi.org/10.1016/j.heliyon.2019.e01750.

[171] Y. He, J.F. Gao, F.Q. Feng, C. Liu, Y.Z. Peng, S.Y. Wang, The comparative study on the rapid decolorization of azo, anthraquinone and triphenylmethane dyes by zero-valent iron, Chem. Eng. J. 179 (2012) 8–18. https://doi.org/10.1016/j.cej.2011.05.107.

[172] P. Yu, H. Yu, Q. Sun, B. Ma, Filter paper supported nZVI for continuous treatment of simulated dyeing wastewater, Sci. Rep. 9 (2019) 1–8. https://doi.org/10.1038/s41598-019-47863-5.

[173] J. Lin, M. Sun, X. Liu, Z. Chen, Functional kaolin supported nanoscale zero-valent iron as a Fenton-like catalyst for the degradation of Direct Black G, Chemosphere. 184 (2017) 664–672. https://doi.org/10.1016/j.chemosphere.2017.06.038.

[174] M. Harshiny, C.N. Iswarya, M. Matheswaran, Biogenic synthesis of iron nanoparticles using Amaranthus dubius leaf extract as a reducing agent, Powder Technol. 286 (2015) 744–749. https://doi.org/10.1016/j.powtec.2015.09.021.

[175] I.A. Radini, N. Hasan, M.A. Malik, Z. Khan, Biosynthesis of iron nanoparticles using Trigonella foenum-graecum seed extract for photocatalytic methyl orange dye degradation and antibacterial applications, J. Photochem. Photobiol. B Biol. 183 (2018) 154–163. https://doi.org/10.1016/j.jphotobiol.2018.04.014.

[176] L. Huang, X. Weng, Z. Chen, M. Megharaj, R. Naidu, Green synthesis of iron nanoparticles by various tea extracts: Comparative study of the reactivity, Spectrochim. Acta - Part A Mol. Biomol. Spectrosc. 130 (2014) 295–301. https://doi.org/10.1016/j.saa.2014.04.037.

[177] S. Machado, J.G. Pacheco, H.P.A. Nouws, J.T. Albergaria, C. Delerue-Matos, Green zero-valent iron nanoparticles for the degradation of amoxicillin, Int. J. Environ. Sci. Technol. 14 (2017) 1109–1118. https://doi.org/10.1007/s13762-016-1197-7.

[178] Z. Khan, S.A. Al-Thabaiti, Green synthesis of zero-valent Fe-nanoparticles: Catalytic degradation of rhodamine B, interactions with bovine serum albumin and their enhanced

antimicrobial activities, J. Photochem. Photobiol. B Biol. 180 (2018) 259–267. https://doi.org/10.1016/j.jphotobiol.2018.02.017.

[179] Y. Vitta, M. Figueroa, M. Calderon, C. Ciangherotti, Synthesis of iron nanoparticles from aqueous extract of Eucalyptus robusta Sm and evaluation of antioxidant and antimicrobial activity, Mater. Sci. Energy Technol. 3 (2020) 97–103. https://doi.org/10.1016/j.mset.2019.10.014.

CHAPTER 2

Materials and Methods

Chapter 2

Materials and Methods

The materials and techniques used for the synthesis, applications and characterisation of iron-based nanoparticles are discussed in this chapter. Along with this, the methods used for the removal studies of Cr(VI) and dyes are also discussed.

2.1. Materials used

Chemicals	Manufacturer
Acetone	Merck, India
Copper sulphate pentahydrate	Sigma Aldrich
Chitosan	Sigma Aldrich
Demineralised water	Nice, India
Diphenylcarbazide	Sigma Aldrich
Hydrochloric acid	Merck, India
Hydrogen peroxide (30% W/V)	Merck, India
Iron(III) chloride hexahydrate	Sigma Aldrich
Malachite green	Merck, India
Methyl blue	Merck, India
Methyl orange	Merck, India
Methylene blue	Merck, India
Nickel(II) sulphate hexahydrate	Merck, India
Nitric acid	Merck, India
Potassium dichromate	Merck, India
Sodium borohydride	Sigma Aldrich
Sodium hydroxide	Sigma Aldrich
Sulphuric acid	Merck, India
Titanium dioxide (nanopowder)	Sigma Aldrich
Natural zeolite	Sigma Aldrich
Zinc nitrate hexahydrate	Sigma Aldrich

All the experiments were conducted using pure and analytical grade chemicals that were used directly without further purification. In order to remove the water content in ethanol, the rectified ethanol was refluxed in the presence of CaO and followed by a reaction with magnesium ribbon and iodine solution. Demineralised water was used in all the experiments.

Plant materials used in this study such as *Abrus precatorius* (AP), *Strychnos nux vomica* (SN), *Terminalia chebula* (TC), *Terminalia belerica* (TB) and *Phyllanthus emblica* (PE) were collected from the local market.

2.2. Application of iron-based nanoparticles

2.2.1 Cr(VI) removal studies

The dissolved Cr(VI) ion concentration in the aqueous solution was determined spectroscopically using diphenylcarbazide as the complexing agent in acidic medium. Cr(VI) stock solution was prepared by dissolving 141.4 mg of dried $K_2Cr_2O_7$ in 1000 mL deionised water (1 mL = 50 µg Cr). The complexing agent, diphenylcarbazide, was prepared by dissolving 250 mg of 1,5-diphenylcarbazide in 50 mL acetone. After reacting with Cr(VI), the diphenylcarbazide formed a red-violet complex which was measured at an absorbance of 540 nm. 5 mg/L of Cr(VI) solution was used for the batch experiments prepared by diluting 10 mL of Cr(VI) stock solution to 100 mL. To determine the unknown concentration of the Cr(VI), a standard calibration graph was constructed using a known Cr(VI) concentration. For this, 9.5 mL of different concentrations (0 to 7 mg/L) of known Cr(VI) solution were prepared by dilution and transferred to a 50 mL beaker. To this, 0.2 mL of diphenylcarbazide was added and mixed gently. Then, 10 % H_2SO_4 was added to adjust the pH of the solution to 2 and the solution was diluted to 10 mL using demineralised water. A red-violet complex was formed within a few minutes and its absorbance was measured using a UV-visible spectrophotometer at a wavelength of 540 nm. A reference solution was prepared by the same procedure, where demineralised water was used instead of Cr(VI) solution. A calibration curve was made by plotting the absorbance against the Cr(VI) concentration.

For the Cr(VI) removal study, a specific amount of iron-based nanoparticles was added into 10 mL of Cr(VI) solution of the desired concentration. After sonication for a previously determined time, the solution was centrifuged and 9.5 mL of the Cr(VI) solution was transferred into a 10 mL vial. 0.2 mL of diphenylcarbazide was added to this and mixed it gently. 10 % H_2SO_4 was added to get the solution with pH 2 and diluted to 10 mL using demineralised water. The solution was kept for 5 to 10 minutes for complete colour development. After measuring the absorbance, the mg/L of chromium present in the solution was determined using the calibration curve.

The effect of various parameters such as nanoparticle dosage, initial concentration of Cr(VI), initial pH of the solution and contact time were also studied for the removal of Cr(VI). The Cr(VI) removal efficiency was estimated using the formula,

$$Percentage\ of\ removal\ efficiency(\%) = \frac{C_0 - C_t}{C_0} * 100 \tag{2.1}$$

C_0 and C_t were the initial and final Cr(VI) concentrations in the aqueous solution.

2.2.2 Dye removal studies

The dye removal efficiency of iron-based nanoparticles was evaluated using malachite green (MG) as a model dye. MG stock solution of 500 mg/L was prepared in demineralised water. The UV-visible spectrophotometer was used to determine the concentration of MG dye at a wavelength of 617 nm. The working solutions for batch experiments were prepared by diluting the stock solution. To determine the unknown concentration of the MG dye, a standard calibration graph was constructed using a known MG concentration. For this, different concentrations of MG solution were prepared by dilution and its absorbance was measured. A calibration curve was made by plotting the absorbance against the MG concentration.

In dye removal experiments, a specific amount of iron-based nanoparticles was added to a definite concentration of MG dye. After sonication for a previously determined time, the solution was centrifuged and absorbance was determined using a UV-visible spectrophotometer. The remaining MG concentration present in the solution was determined from the calibration graph. The influence of various parameters such as initial dye concentration, nanoparticle dosage, initial pH of the dye solution and contact time were also studied regarding MG dye removal. The removal efficiency of iron-based nanoparticles for MG dye removal was calculated by the formula,

$$Percentage\ of\ removal\ efficiency(\%) = \frac{C_0 - C_t}{C_0} * 100 \tag{2.2}$$

C_0 and C_t were the initial and final concentrations of dyes in the aqueous solution.

In some chapters, the removal study of dyes methyl blue (MB), methylene blue (MLB) and methyl orange (MO) are also reported in addition to MG dye. The characteristic absorbance of MB, MLB and MO was measured at 595 nm, 668 nm and 464 nm. The procedure used for MG dye removal was followed for the other dye removal too.

2.3. Characterisation and analytical techniques used

The prepared nanoparticles were lyophilised using Operon FDU 7003 lyophiliser for the characterisation purpose. Particle size and morphology of the prepared compounds were analysed using Jeol/JEM 2100 High-resolution transmission electron microscopy (HRTEM) and FEI Inspect S50-SEM scanning electron microscopy (SEM). Binding energies of the nanoparticles were investigated via X-ray photoelectron spectroscopy (XPS, Kratos Analytical, Ultra axis). Fourier transform infrared spectra of the compounds were investigated through Spectrum Two Fourier transform infrared spectrometer (ATR-FTIR, Perkin Elmer, USA) and SHIMADZU IR Affinity-1 in the frequency range 4000 – 600 cm^{-1}. XRD data were collected using PANalytical Aeris X-ray diffractometer using Cu Kα radiation of wavelength $\lambda = 0.15406$ nm in the scan range $2\theta = 5 - 90^{o}$. The absorbance of the solution was measured using a UV-visible spectrophotometer (SHIMADZU UV 1800) and the UV absorbance of solid samples was done by UV-visible spectrometer UV-2600, Shimadzu, Japan. Elemental analysis and mapping of the compounds were done using energy dispersive X-ray analysis (EDAX) by Jeol 6390LA/OXFORD XMX N and Bruker Nano GmbH, XFlash detector 6/100.

CHAPTER 3

Comparative study on the reactivity of zero valent iron nanoparticles (Fe^0) and bimetallic iron-based nanoparticles for the removal of dyes and Cr(VI) from water

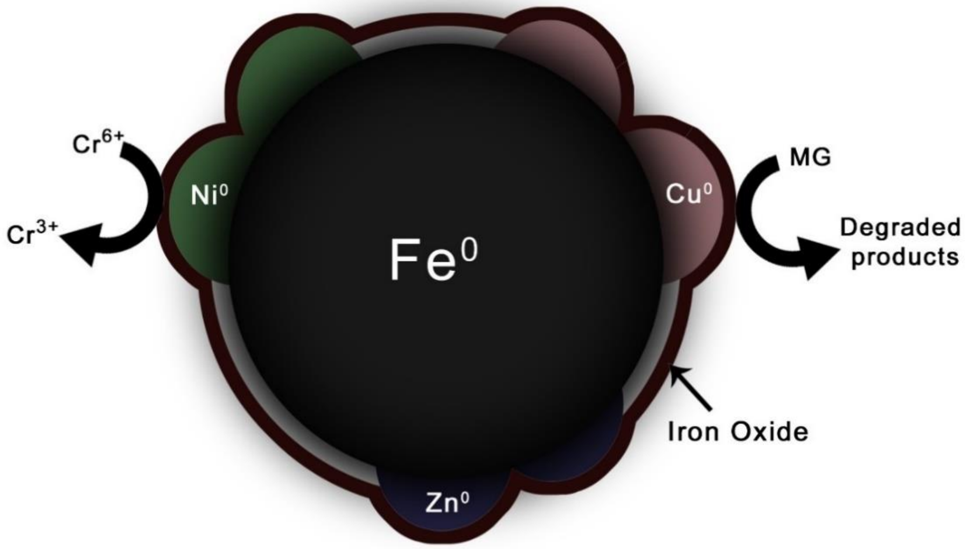

Chapter 3

Comparative study on the reactivity of zero valent iron nanoparticles (Fe^0) and bimetallic iron-based nanoparticles for the removal of Cr(VI) and dyes from water

3.1 Introduction

The high potential of Fe^0 nanoparticles for the remediation of water contaminants has been discussed thoroughly in chapter 1. Even though the Fe^0 nanoparticles show good efficiency for contaminant removal, the formation of the surface passive layer decreases the capacity of Fe^0 nanoparticles in the aqueous medium. Gradual reduction of reactivity over time, narrow pH range and low stability of the nanoparticles due to leaching are the additional drawbacks of monometallic nanoparticles. One of the efficient methods to overcome these problems and improve the efficiency of Fe^0 nanoparticles is incorporating a second metal on the surface of Fe^0 nanoparticles. The characteristics properties of bimetallic iron-based nanoparticles have differed from monometallic Fe^0 nanoparticles. The previous studies suggest that the iron-based bimetallic nanoparticles show high catalytic activity, increased selectivity, upgraded stability and less cost than monometallic Fe^0 nanoparticles. Iron-based bimetallic nanoparticles also followed adsorption, reduction, oxidation, including advanced oxidation mechanisms similar to Fe^0 nanoparticles in removing organic, inorganic and heavy metal contaminants from water and wastewater[1].

Generally, the preparation of bimetallic nanoparticles can be done through two methods - co-reduction and successive reduction of two metal salts. In the co-reduction method, two metal salts are mixed in a suitable solvent and simultaneously reduced using an appropriate reducing agent. It is similar to the preparation of monometallic nanoparticles. If the two metal ions have different redox potentials, the metal ion with the highest redox potential reduces fast, precipitates and forms the core and the second metal ion forms a shell on the core metal ion. If the two metal ions have similar redox potential, metal alloys will be formed due to simultaneous reduction. Successive reduction method is used to prepare core-shell bimetallic nanoparticles. At first, core metal nanoparticles are prepared through reduction using a potent reducing agent and then the second metal gets deposited on the surface of the core metal. This is due to the galvanic couple generated between the two metals which in turn cause the reduction of the second metal by the core metal having a more negative reduction potential[2,3].

Bimetallic combinations such as Fe/Ni, Fe/Cu, Fe/Zn, Fe/Al and Fe/Ag were already reported earlier. However, the formation and reactivity towards contaminants are not established well. Tamer et al. compared the efficiency of Fe^0 and Fe/Cu nanoparticles to treat the radioactive caesium through adsorption. The result shows that the sorption process in Fe/Cu nanoparticles was kinetically faster and more efficient than in Fe^0. It is important to note that Fe^0 and Fe/Cu nanoparticles show high selectivity towards caesium in the presence of competing cations like Na^+, K^+, Ca^{2+} and Mg^{2+}[4]. Reductive detoxification of halogenated hydrocarbons, nitroaromatics and metalloids like Cr(VI) is a unique property of Fe^0. Bimetallisation of Fe^0 improves reduction capacity and prevents the formation of toxic byproducts. Fe^0 acts as the anode in dehalogenation reaction and gets oxidised, while the second metal catalyses electron transfer and hydrogen generation[5–7]. Tee et al. studied the role of Ni/Fe nanoparticles on the degradation of trichloroethylene. They found that Ni/Fe nanoparticles rapidly degraded the trichloroethylene and ethane was the main degradation product. They also noted that the Ni/Fe nanoparticles show a higher reaction rate than Fe nanoparticles and the degradation rate increases with an increase in Ni percentage from 2 wt % to 25 wt %. With the increase in nickel percentage, due to the formation of a less-reactive nickel-rich surface layer, the extent of trichloroethylene degradation gets decreases.

The degradation of p-nitrophenol using Fe/Cu nanoparticles under aerobic and anaerobic conditions was investigated by Xiong et al. Under anaerobic conditions, the reduction capacity of Fe/Cu bimetallic nanoparticles is higher than Fe^0 since the metal additives like Cu increase the steady-state concentration of atomic hydrogen at the surface or near-surface of the iron-based reductant and improves the electron transfer from Fe^0 to the pollutant resulting in the degradation of p-nitrophenol to p-aminophenol. Under the aerobic condition, the produced atomic hydrogen is consumed by the dissolved oxygen and decrease the reduction capacity of Fe/Cu nanoparticles. However, under aerobic conditions, the dissolved oxygen could be reduced into H_2O_2 by Fe^0 and these H_2O_2 provide hydroxyl radicals by the Fenton-like reaction. The strong oxidant, hydroxyl radical, could degrade the organic pollutant into mineralised form. They suggest that for Fe/Cu bimetallic nanoparticles, the aerobic condition would be the best method to treat pollutants since the Fe/Cu bimetallic nanoparticles not only break the benzene ring and

–NO_2 group of p-nitrophenol but also mineralised most of the intermediates into CO_2 and H_2O[8].

As previously mentioned, iron-based nanoparticles were used to treat water contaminants. In this study, dyes and hexavalent chromium were selected as model pollutants to examine the effectiveness of iron-based nanoparticles. Chromium naturally exists in the environment and it has many potential health risks for living organisms. Leather tanning, electroplating, painting and metallurgy industries use various forms of Cr as raw material[9]. Among the different oxidation states (-2 to +6), Cr(III) and Cr(VI) are the most commonly occurring oxidation states[10,11]. Cr(III) is an essential component for sugar and fat metabolism. Insufficient Cr(III) intake causes symptoms similar to diabetes and cardiovascular diseases[12]. A low Cr(III) concentration in plants promotes growth and increases yield. Cr(III) is more toxic than Cr(VI) due to its high oxidising potential, high solubility and mobility across the membranes in living organisms. Cr(VI) is carcinogenic and a powerful epithelial irritant. Cr(VI) also affects humans' well-being by causing diseases such as liver damage, pulmonary congestion, vomiting, and severe diarrhoea[13]. It is also noted that Cr(VI) is toxic to aquatic organisms and plants. Usually, Cr(VI) is seen in the environment as chromate (CrO_4^{2-}), dichromate ($Cr_2O_7^{2-}$) and CrO_3, while Cr(III) is seen as oxides, hydroxides and sulphates which are less toxic, relatively insoluble in water, exhibit less mobility and shows a high tendency to bound to organic matter. Cr(III) forms hydroxide and precipitates with Fe in ground water[14]. Nevertheless, in the presence of high concentrations of oxygen or oxides of Mn, the Cr(III) can be oxidised to Cr(VI)[15].

Dyes are a noteworthy class of organic compounds used in the textile, paper, cosmetic and food industries. Many dyes and their degradation products are toxic, mutagenic and carcinogenic to living organisms. They reduce sunlight penetration, leading to the decreased photosynthetic activity of the aquatic life even at low concentrations. So, the treatment of dye-containing water is necessary before releasing them into the environment[16]. Malachite green (MG) is a basic, cationic triphenylmethane dye produced by the polymerisation of benzaldehyde and dimethylaniline in the presence of concentrated sulphuric acid. In aquaculture, MG is used as an insecticide and fungicide. It is also used as a dye in the silk, wood, cotton, leather, paper and acrylic industries due to its low cost, good efficiency, lack of suitable alternatives and easy availability. MG has a complex aromatic structure which may cause its degradation problematic. MG decreases the sunlight penetration in the water bodies, affecting the photosynthetic activity and productivity of the aquatic system. MG is environmentally persistent and shows teratogenic, mutagenic and carcinogenic effects. It may cause detrimental effects in the liver, gill, kidney, intestine and gonads in aquatic organisms. In humans, it may cause tumours by inhibiting human glutathione-S-transferase activity and irritating the gastrointestinal tract due to ingestion. Skin contact with MG causes irritation, pain and redness. The adverse effects of MG make its effective removal mandatory[17–19].

Methyl blue (MB) is an anionic triphenylmethane dye used as a biological colouring agent and pH indicator. It is also applied for leather and cotton. MB dye is harmful if swallowed and lead to skin, eye and respiratory tract irritation. As per literature, very little study has been reported about the toxicity and removal of MB from aqueous media[20,21]. Methyl orange (MO) is an anionic azo dye commonly applied in chemical, textile and paper industries. It has a mono-azo bond and the sulphonic and azo groups present in the molecular structure cannot be degraded easily, which harms the environment. It is poisonous when swallowed and causes allergic reactions like skin eczema if contacted to the skin[22–25]. Methylene blue (MLB) is a cationic thiazine dye generally used in paper, textile and dye industries. It will cause nausea, vomiting and diarrhoea when ingested through the mouth[26,27]. The detrimental effects of dyes make it a great concern from an environmental and healthy point of view.

Although many researchers investigated the effectiveness of bimetallic iron-based nanoparticles, there is a lack of information about Cr(VI) reduction and dye degradation. This study examined the most effective bimetallic combination and the optimum percentage of the second metal deposition. The objectives of this study are (i) synthesis of Fe^0 nanoparticles and bimetallic Fe based nanoparticles, (ii) characterisation of the prepared nanoparticles by HRTEM, XRD and EDAX (iii) optimisation of second catalytic metal loaded on the Fe^0 nanoparticles, (iv) determine the effectiveness of prepared nanoparticles for the decolourisation of four different dyes and hexavalent chromium (v) investigate the effect of various parameters including nanoparticle dosage, initial concentration of pollutant, solution pH and the contact time in pollutant removal (vi) to find out the MG degradation mechanism through analysing the degradation products.

3.2 Experimental details

3.2.1 Synthesis of Fe^0, Fe/Ni, Fe/Cu and Fe/Zn nanoparticles

Monometallic Fe^0 and bimetallic Fe/Ni, Fe/Cu and Fe/Zn nanoparticles were prepared by the liquid-phase reduction method under nitrogen atmosphere using sodium borohydride as the reducing agent. Ferric solution is prepared by dissolving 1 g of $FeCl_3.6H_2O$ in 10 mL ethanol-water (1:1) solution and stirred for 15 minutes under the nitrogen atmosphere. Sodium borohydride (0.5 g) was dissolved in 50 mL water and added dropwise to ferric chloride solution. The appearance of a black precipitate indicates the formation of Fe^0 nanoparticles (as shown in equation 3.1) which was then collected through vacuum filtration. After washing with ethanol, the nanoparticles were lyophilised and stored in airtight bottles. Figure 3.1 show the preparation of Fe^0 nanoparticles using $NaBH_4$.

$$2FeCl_3 + 6NaBH_4 + 18H_2O \rightarrow 2Fe^0 + 6B(OH)_3 + 6NaCl + 21H_2 \uparrow \qquad (3.1)$$

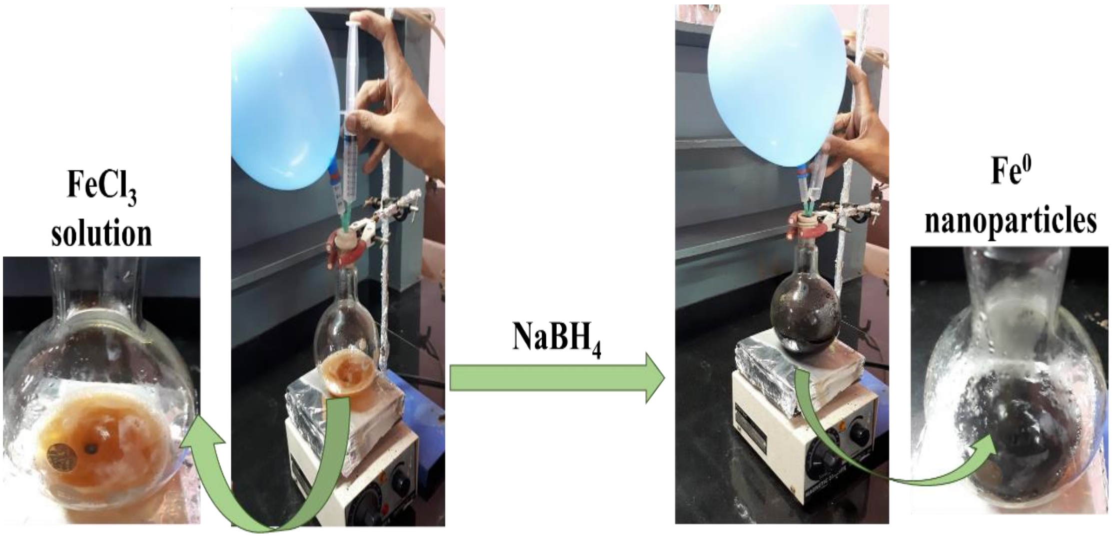

Figure 3.1 *Photographs of the preparation of Fe^0*

The method for preparing bimetallic nanoparticles was similar to the monometallic synthesis. In the preparation of Fe/Cu and Fe/Ni bimetallic nanoparticles, 10 mL metal salt solutions of either $NiSO_4.6H_2O$ or $CuSO_4.5H_2O$ of specific concentration were prepared and added dropwise to the freshly prepared iron particle suspended in absolute ethanol. The solution is rapidly stirred for 30 minutes to achieve bimetallic nanoparticles with specific second metal loading. Fe/Zn nanoparticles were prepared by the co-reduction method by mixing solutions with a specific concentration of $FeCl_3.6H_2O$ and $Zn(NO_3)_2.6H_2O$ and reducing them simultaneously under the nitrogen atmosphere. The prepared bimetallic nanoparticles were vacuum filtered, lyophilised and stored in airtight bottles. Bimetallic nanoparticles with 5, 10 and 15 weight % of second metal were prepared by changing the concentration of the second metal salt solution. The reaction of Fe^0 with $Ni^{2+}$and Cu^{2+} is shown in equations 3.2-3.3.

$$Ni^{2+} + Fe^0 \rightarrow Ni^0 + Fe^{2+} \tag{3.2}$$

$$Cu^{2+} + Fe^0 \rightarrow Cu^0 + Fe^{2+} \tag{3.3}$$

3.2.2 Batch experiments

Cr(VI) removal studies

The method followed for the batch experiments of Cr(VI) removal were already given in chapter 2. In the present study, various parameters investigated for the removal of Cr(VI) are nanoparticle dosage (1-8 g/L), initial concentration of Cr(VI) (1-7 mg/L), initial pH of the solution (4-10) and contact time (5-20 min). 1.0 M NaOH and 1.0 M H_2SO_4 were used to adjust the pH of the solution. All experiments were performed with a duplicate.

Dye removal studies

Malachite green (MG), methyl blue (MB), methylene blue (MLB) and methyl orange (MO) dye solutions were prepared by dilution of stock solution just before use. Dye removal experiments were carried out in 100 mL beakers with 20 mL of dye solution. Firstly, 0.5 g/L of nanoparticles were added to the 50 mg/L of the dye solution in a beaker and rapidly agitated using a bath sonicator. The samples were collected after 15 minutes and the absorbance was measured using a UV-visible spectrophotometer. Samples without the addition of nanoparticles have been examined under identical conditions and no significant changes were observed. The MG dye removal was investigated thoroughly by changing nanoparticles dosage (0.25–1 g/L), initial concentration of the dye (10–50 mg/L), pH (5-7) and contact time (5-30 min). To study the effect of pH, the initial pH of the dye solution was adjusted using 1.0 M NaOH and 1.0 M H_2SO_4. All experiments were performed with a duplicate.

3.2.3 Characterisation and analytical techniques used

The prepared nanoparticles were characterised by HRTEM, EDAX and XRD techniques. Details of characterisation techniques are discussed in chapter 2. Elemental analysis and mapping of the Fe^0, Fe/Ni, Fe/Cu and Fe/Zn nanoparticles were done by EDAX (Jeol 6390LA/OXFORD XMX N). EDAX analysis using Bruker Nano GmbH, XFlash detector

6/100 were done to find out the presence of chromium in Fe^0, Fe/Ni, Fe/Cu and Fe/Zn nanoparticles which is treated with the hexavalent chromium solution. The degradation products of MG dye was analysed by LC-MS/MS and GC-MS/MS. The aqueous solution of MG dye after treating with Fe^0 nanoparticles was collected, filtered through a 0.22 µm membrane filter and divided into two equal volumes. The first part is used for LC-MS/MS analysis and the second part was used for GC-MS/MS analysis.

To determine the volatile MG degradation products in the solution using GC-MS/MS, the samples were centrifuged at 5000 rpm for 15 minutes and the supernatant solution was extracted twice with ethyl acetate (10 mL). Then the extract was concentrated to 1 mL and filtered using a 0.22 µm syringe filter. Gas chromatography coupled with triple quadrupole tandem mass spectrometry (GC-MS/MS) analysis of the MG dye degradation products were carried out using TSQ 8000 GC-MS/MS. The separation of compounds has been done using the DB-5MS capillary column (30 m × 0.25 mm × 0.25 µm). The carrier gas was helium with a flow rate of 1mL/min. The column oven temperature was programmed from an initial temperature of 40ºC (hold 1 min) to 100ºC (hold 1 min) then to 150 ºC (hold 1 min) and finally to 250ºC (hold 1 min) each at 10ºC min^{-1}. The injection volume was 1 mL and the oven running time was 25 minutes. The ionisation energy applied was 70 eV. Data acquisition was started after a solvent delay of 4 minutes, with the mass spectrometer operating in full-scan mode. Compounds were identified using the National Institute of Standards and Technology (NIST) MS search 2.0 Library.

The MG dye degradation products identification was also carried out on an LC-MS/MS system. Liquid chromatography was performed using a Dionex Ultimate 3000 (Thermo) micro-LC equipped with C18, 150 x 4.6 mm, 5 µm reversed-phase column operated at 25ºC. The UV detection wavelength was 254 nm. The mobile phase consisted of water (A) and acetonitrile (B) containing 0.1 % formic acid. The gradient program was (time (min), % B): (0.00, 1); (5.00, 1); (30.00, 20); (45.00, 40); (60.00, 95); (74.00, 95); and (75.00, 1) and the flow rate was 300 µL/min. Impact HD (Bruker) ESI QTOF high-resolution mass spectrometer was used for MS/MS analysis in the positive ions mode and the mass range was 100-2000 m/z. The ESI conditions were as follows: capillary voltage, 4500 V; the nebuliser pressure, 60 psi; drying gas flow, 12 L min^{-1}; temperature, 220 °C.

3.3 Results and discussion

3.3.1 Characterisation of Fe^0, Fe/Ni, Fe/Cu and Fe/Zn nanoparticles

HRTEM

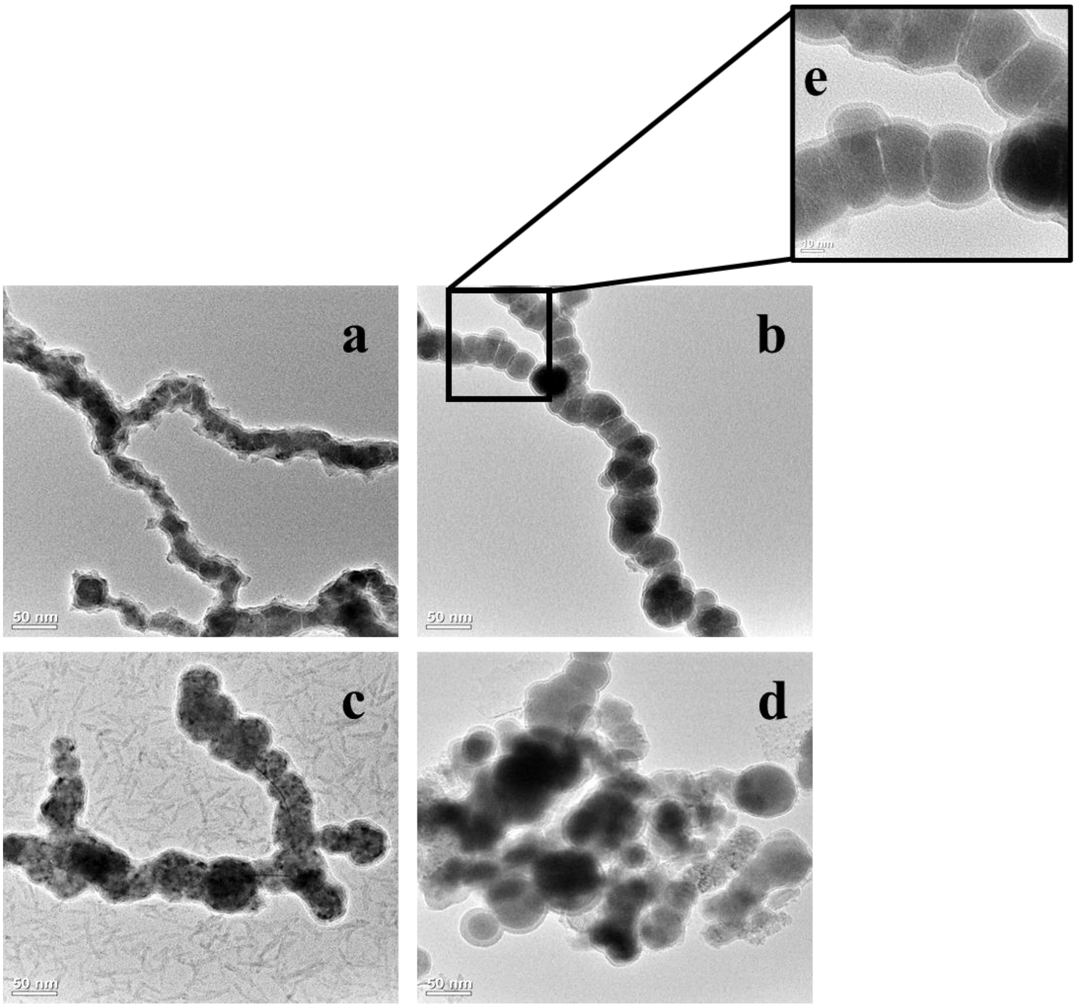

Figure 3.2 *HRTEM images of a) Fe^0 b) Fe/Cu c) Fe/Ni d) Fe/Zn nanoparticles and e) HRTEM image of Fe/Cu nanoparticles enlarged.*

Figure 3.2 shows the HRTEM images of monometallic Fe^0 nanoparticles and bimetallic Fe/Cu, Fe/Ni and Fe/Zn nanoparticles. All the prepared nanoparticles show a tendency for agglomeration, primarily as chain clusters due to the electrostatic and magnetic interactions. The dark colour in the HRTEM image indicates the heavier atomic mass/high-density particles and the bright colour indicates the lighter atomic mass/low-density particles. The results show that the major composition of the prepared nanoparticles has a core of highly dense Fe^0 particles and a shell of low dense iron oxides. The structure of bimetallic nanoparticles is complicated and varies from core-shell segregated structures to intermetallic/alloyed structures. The characteristics of the second metal do not significantly influence the morphology of the nanoparticles. Two factors influencing the bimetallic formation are the surface energies of the metals involved and the atomic radii of the metals. The element with low surface energy is deposited on those with high surface energy. The particle size distribution of prepared nanoparticles is shown in table 3.1.

Nanoparticle	Particle size range	Average particle size
Fe^0	21.9 - 45 nm	30.9 nm
Fe/Cu	14.4 – 50.2 nm	37.0 nm
Fe/Ni	17.7 - 71.0 nm	41.8 nm
Fe/Zn	19.2 - 85.7 nm	43.2 nm

Table 3.1 *Average particle size and particle size distribution of Fe^0, Fe/Ni, Fe/Cu and Fe/Zn nanoparticles*

The selected area electron diffraction (SAED) pattern of the prepared nanoparticles is shown in figure 3.3. The SAED pattern shows that the particles have crystalline and amorphous nature. The bright spots in the SAED pattern indicate the crystalline nature of Fe^0 and bimetal whereas the faded rings indicate the presence of amorphous iron oxide particles.

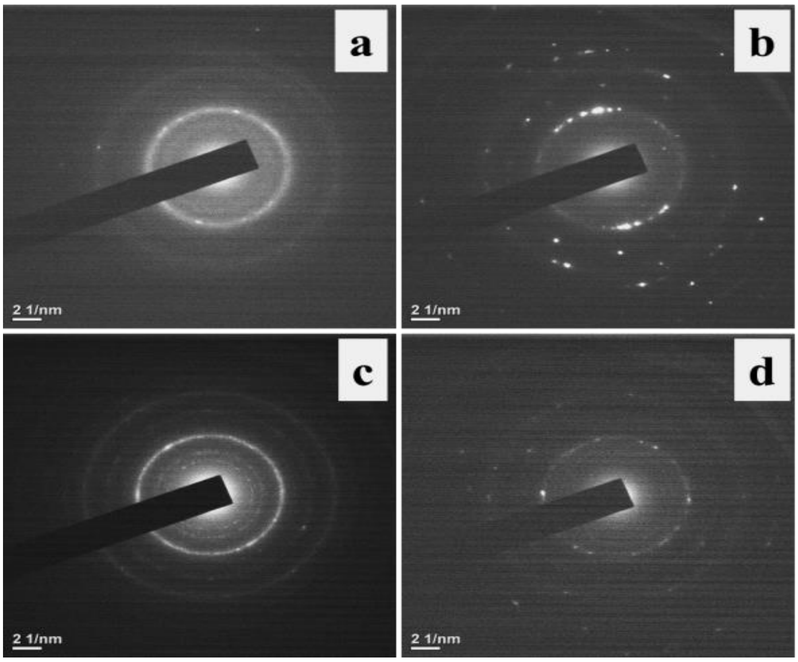

Figure 3.3 *SAED pattern of a) Fe^0 b) Fe/Cu c) Fe/Ni and d) Fe/Zn nanoparticles*

XRD

Figure 3.4 (a, b, c & d) shows the XRD pattern of Fe^0, Fe/Ni, Fe/Cu and Fe/Zn nanoparticles prepared by chemical reduction method. All the samples exhibit the characteristic peak of Fe^0 and peaks due to the formation of iron oxides. In Fe^0 nanoparticles, the peak at 44.7° corresponds to the (110) plane of Fe^0[28]. The peak at 31.51° matched with the (210) plane of γ-FeO(OH)[29] and the peak at 34.95° confirmed the presence of Fe_2O_3 ((201) plane)[30]. In the case of bimetallic nanoparticles, there was a shift in the characteristic peak of the Fe^0. The prepared Fe/Ni, Fe/Cu and Fe/Zn bimetallic nanoparticles exhibit the characteristic peak of Fe^0 at 44.9°, 45.1° and 45.2° respectively. It may be due to the stress-induced deviation due to nickel, copper or zinc deposition over the template Fe^0 nanoparticles. However, the weight percentage of the second metal loaded on the Fe^0 nanoparticles was too low to detect any characteristic peak of Cu, Ni or Zn. The peaks due to the oxidation of Fe^0 nanoparticles were seen in the XRD spectra of prepared nanoparticles. The peaks at 30.5° and 35.2° correspond to the (220) and (311) planes of Fe_3O_4[31]. In addition, impurities due to the addition of reducing agent $NaBH_4$ were causing some peaks in the XRD spectra of prepared nanoparticles.

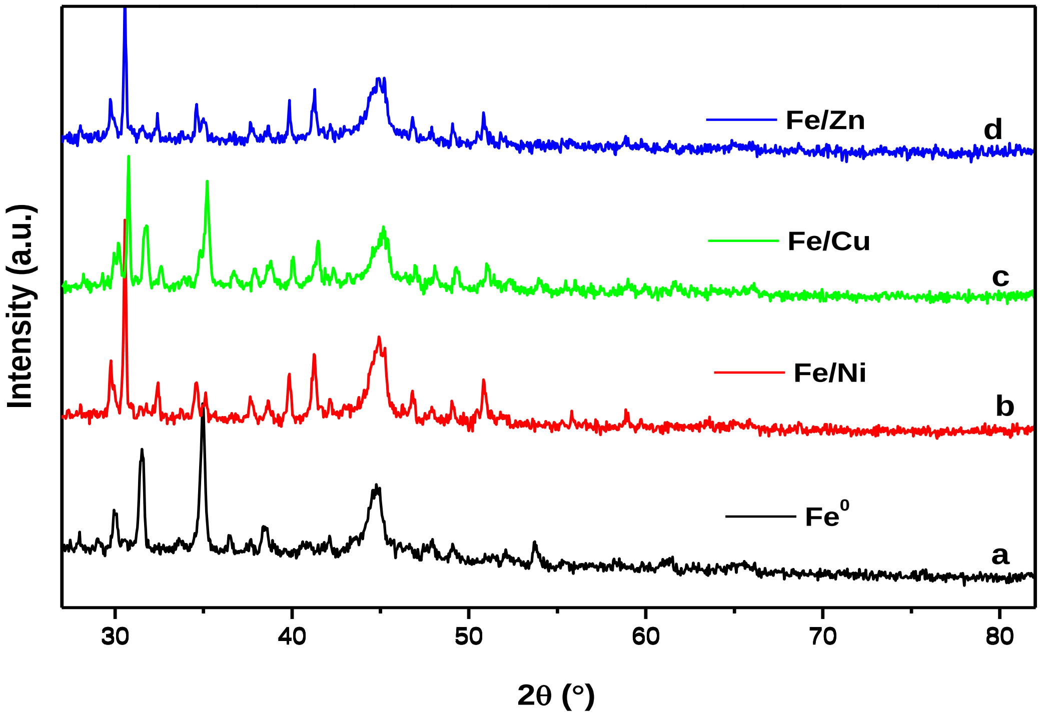

***Figure 3.4** XRD pattern of (a) Fe^0, (b) Fe/Ni, (c) Fe/Cu and (d) Fe/Zn nanoparticles*

EDAX

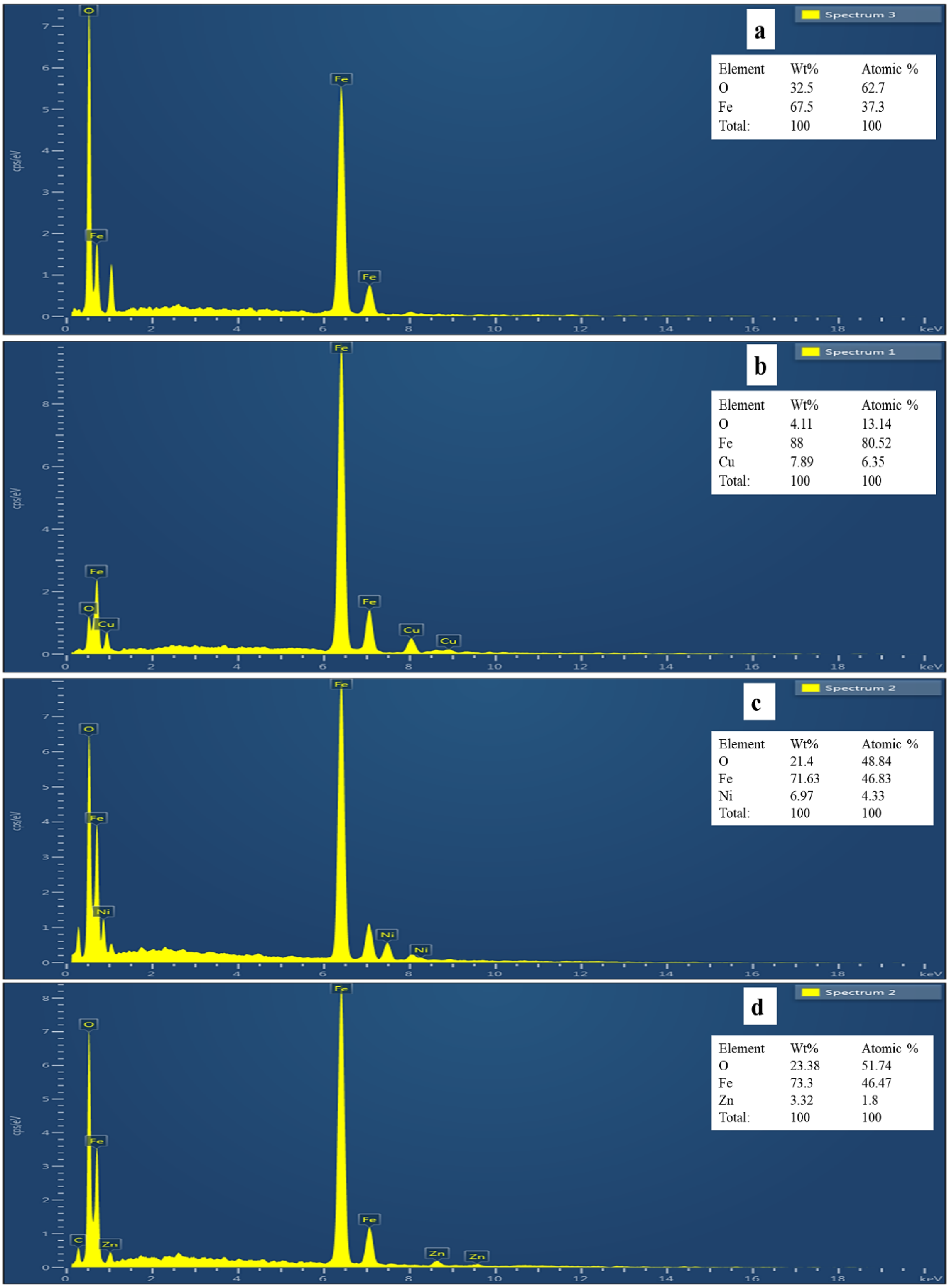

Element	Wt%	Atomic %
O	32.5	62.7
Fe	67.5	37.3
Total:	100	100

Element	Wt%	Atomic %
O	4.11	13.14
Fe	88	80.52
Cu	7.89	6.35
Total:	100	100

Element	Wt%	Atomic %
O	21.4	48.84
Fe	71.63	46.83
Ni	6.97	4.33
Total:	100	100

Element	Wt%	Atomic %
O	23.38	51.74
Fe	73.3	46.47
Zn	3.32	1.8
Total:	100	100

Figure 3.5 *EDAX spectra of (a) Fe^0, (b) Fe/Cu, (c) Fe/Ni and (d) Fe/Zn nanoparticles*

EDAX was used to analyse the elemental composition of Fe, O and second metal (Cu, Ni and Zn) in the prepared nanoparticles composition. As shown in figure 3.5, the weight percentages of 7.89 % (Cu), 6.97 % (Ni) and 3.32 % (Zn) of second metal successfully plated on the surface of the iron nanoparticles. The weight % of the second metal in Fe/Zn is less compared to other bimetallic nanoparticles. The presence of O in the nanoparticles indicates that the prepared nanoparticles tend to form metal oxide by contact with the air. Compared to monometallic nanoparticles, the weight percentage of oxygen is less in bimetallic nanoparticles. It indicates that the addition of second metal on the surface of Fe^0 reduce the rapid oxidation of Fe^0 nanoparticles.

3.3.2 Cr(VI) removal studies

Cr(VI) removal efficiency of Fe^0 and bimetallic nanoparticles has been studied using 5 mg/L Cr(VI) solution and depicted in figure 3.6. The UV-visible spectra of the removal study show that Fe/Ni nanoparticles exhibit the highest removal efficiency followed by Fe/Cu, Fe^0 and Fe/Zn nanoparticles respectively. Figure 3.7 represents the Cr(VI) removal photographs using prepared nanoparticles.

Typically Fe^0 exhibits three mechanisms for removing Cr(VI) - reduction, adsorption and co-precipitation. During the reduction process, Cr^{6+} was reduced into Cr^{3+} and precipitated as $Cr(OH)_3$ as represented by equations 3.4 and 3.5.

$$2Fe^0 + Cr_2O_7^{2-} + 8H^+ \longrightarrow 3Fe^{2+} + 2Cr(OH)_3 + H_2O \tag{3.4}$$

$$6Fe^{2+} + Cr_2O_7^{2-} + 8H^+ \longrightarrow 6Fe^{3+} + 2Cr(OH)_3 + H_2O \tag{3.5}$$

The reduced Cr^{3+} also form mixed Cr^{3+}–Fe^{3+} hydroxides by reacting with Fe^{3+} and H_2O represented in equations 3.6 and 3.7.

$$xCr^{3+} + (1-x)Fe^{3+} + 3H_2O \rightarrow Cr_xFe_{1-x}(OH)_3 + 3H^+ \tag{3.6}$$

$$xCr^{3+} + (1-x)Fe^{3+} + 2H_2O \rightarrow Cr_xFe_{1-x}OOH + 3H^+ \tag{3.7}$$

Along with this, the FeO(OH) formed by reacting the $Fe^{2+/3+}$ with water molecules acted as a suitable adsorbent for Cr(VI). The formation of the oxide/hydroxide layer of Fe along with the Cr species causes self-inhibition of electron transfer from Fe^0 to Cr(VI) and eventually leads to the shortfall in the reductive precipitation of Cr(VI)[2].

The prepared Fe/Ni and Fe/Cu bimetallic nanoparticles show better efficiency than Fe^0 and Fe/Zn. It is probably due to more reductive precipitation of Cr(VI) since bimetallisation of Fe^0 nanoparticles improves the electron transfer of Fe^0 core to the Cr(VI). During the iron corrosion of bimetallic nanoparticles, molecular hydrogen formed on the surface of catalytic metal along with ferrous iron production. Cr(VI) was adsorbed onto the surface of Fe/Ni and Fe/Cu nanoparticles and reduced by the electron transfer from Fe or second metal (Ni or Cu). The decreased efficiency of Fe/Zn nanoparticles owing to the rapid oxidation of the Zn due to their high reactivity[32].

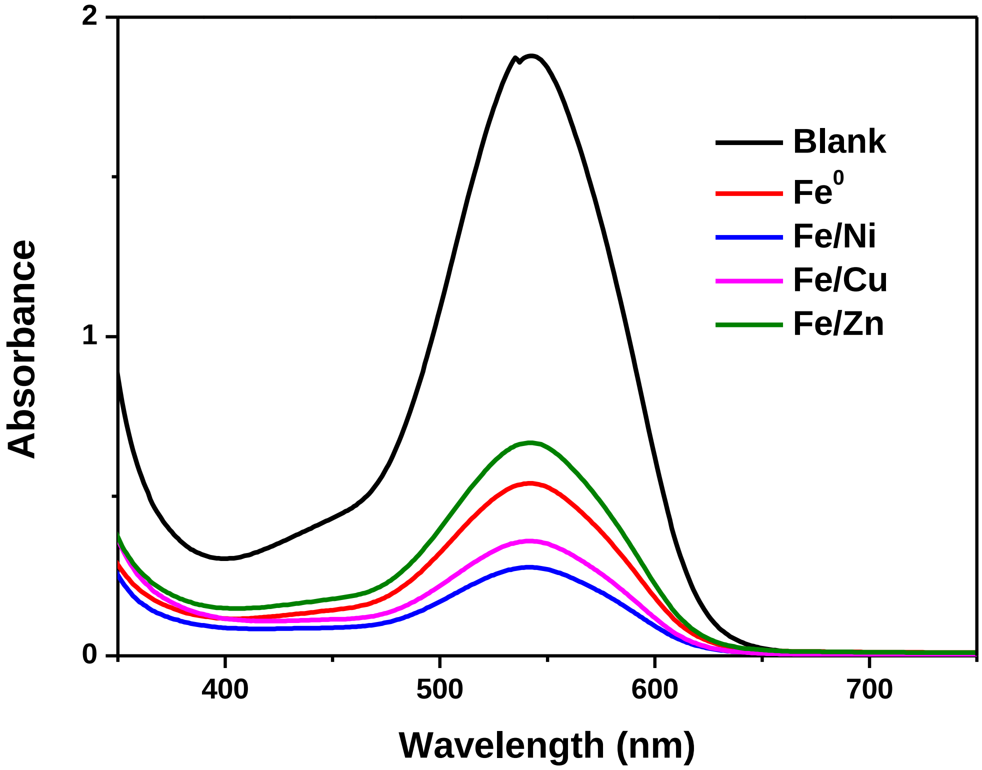

Figure 3.6 *UV-visible spectra of Cr(VI) after treating Fe^0, Fe/Ni, Fe/Cu and Fe/Zn nanoparticles*

Figure 3.7 *Photographs of Cr(VI) removal using Fe^0, Fe/Ni, Fe/Cu and Fe/Zn nanoparticles*

EDAX analysis

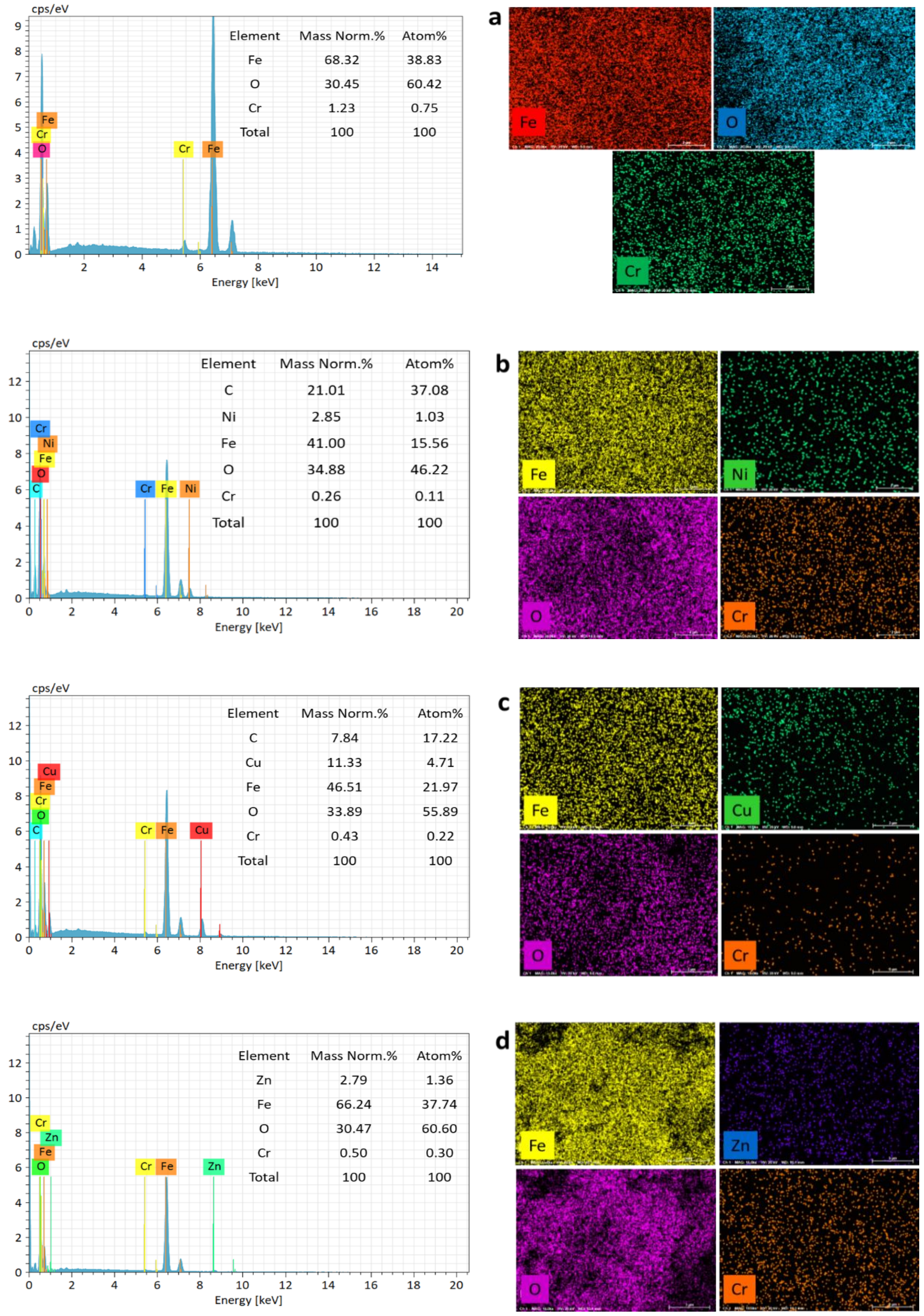

Element	Mass Norm.%	Atom%
Fe	68.32	38.83
O	30.45	60.42
Cr	1.23	0.75
Total	100	100

Element	Mass Norm.%	Atom%
C	21.01	37.08
Ni	2.85	1.03
Fe	41.00	15.56
O	34.88	46.22
Cr	0.26	0.11
Total	100	100

Element	Mass Norm.%	Atom%
C	7.84	17.22
Cu	11.33	4.71
Fe	46.51	21.97
O	33.89	55.89
Cr	0.43	0.22
Total	100	100

Element	Mass Norm.%	Atom%
Zn	2.79	1.36
Fe	66.24	37.74
O	30.47	60.60
Cr	0.50	0.30
Total	100	100

Figure 3.8 *EDAX spectra and mapping of (a) Fe^0, (b) Fe/Ni, (c) Fe/Cu and (d) Fe/Zn nanoparticles after treating with Cr(VI) solution*

The precipitation of Cr(VI) on the surface of Fe^0 and bimetallic nanoparticles were further confirmed by EDAX. Figure 3.8 shows the EDAX spectra and mapping of Fe^0, Fe/Ni, Fe/Cu and Fe/Zn nanoparticles after reacting with Cr(VI) solution. All the samples show a significant amount of Cr, which confirms the precipitation of Cr(VI) on the surface of prepared nanoparticles. It was also observed from the mapping image that all the elements are homogeneously distributed in the matrix.

Effect of the nanoparticle dosage

The influence of nanoparticle dosage on Cr(VI) removal was examined using different nanoparticles dosage (1-8 g/L), keeping the initial Cr(VI) concentration (5 mg/L) and contact time (10 min) as constant. As shown in figure 3.9a, the higher nanoparticle dosage lowers the Cr(VI) concentration in the solution. Fe/Ni nanoparticles have shown the highest removal efficiency and the lowest by Fe/Zn nanoparticles. Fe/Ni nanoparticles attained 88 % removal efficiency using a nanoparticle dosage of 2 g/L. At the same time, Fe/Cu, Fe^0 and Fe/Zn show 83 %, 73 % and 66 % Cr(VI) removal efficiency only. It is important to note that all the samples attained 100 % removal efficiency while using a nanoparticle dosage of 8 g/L. As the dosage of nanoparticles increases, there will be an increase in the number of reactive sites for Cr(VI). It will eventually lead to more reduction and adsorption[33].

Effect of the initial concentration

Figure 3.9b shows the effect of the initial concentration of Cr(VI) on the removal of Cr(VI) from water at constant contact time (10 min) and nanoparticles dosage (2 g/L). The initial Cr(VI) concentration varies from 1 to 7 mg/L. As expected, Cr(VI) removal efficiency increases with a decrease in the initial concentration of Cr(VI). All the nanoparticles show 100 % removal efficiency at 1 mg/L solution. But in the initial concentration of 7 mg/L, the nanoparticles show 71 %, 65 %, 61 % and 56 % removal efficiency for Fe/Ni, Fe/Cu, Fe^0 and Fe/Zn nanoparticles respectively. The binding sites available for Cr(VI) removal were fixed at a definite amount of nanoparticles dosage. As the concentration increases, the insufficient availability of reactive sites decreases the Cr(VI) removal. Along with that, the rapid formation of Fe^{3+}-Cr^{3+} hydroxide on the surface of nanoparticles suppresses the Cr(VI) reduction in higher Cr(VI) concentration[33].

Effect of contact time

The effect of contact time on the removal of Cr(VI) has been studied by keeping nanoparticles dosage (2 g/L) and initial concentration of Cr(VI) (5 mg/L) as constant. Fe/Ni nanoparticles completely removed Cr(VI) from the solution within 20 minutes of reaction time. As indicated in figure 3.9c, Cr(VI) removal efficiency was maximum in the first 15 minutes, which may be attributed to the presence of enormous available binding sites for Cr(VI). After 15 minutes of contact time, the nanoparticles slightly move to the equilibrium state owing to the decrease in the vacant binding sites and precipitation of Fe^{3+}-Cr^{3+} hydroxide on the surface of nanoparticles[34].

Effect of pH

One of the significant parameters influencing the effective removal of Cr(VI) is the pH of the solution. In this study, the influence of the solution pH 4, 7 and 10 has been studied (figure 3.9d) by taking other parameters such as initial Cr(VI) concentration (5 mg/L), contact time (10 min) and nanoparticle dosage (2 g/L) as constant. The results show that all the nanoparticles show 100 % removal efficiency at pH 4. When the pH of the solution increases, different nanoparticles show different Cr(VI) removal capacities. Under neutral pH, Fe/Ni nanoparticles show the highest removal efficiency followed by Fe/Cu, Fe^0 and Fe/Zn nanoparticles. Fe/Ni and Fe/Cu nanoparticles show higher removal efficiency at pH 10 than Fe^0 nanoparticles and Fe/Zn nanoparticles. Fe/Zn nanoparticles are drastically influenced by the pH of the solution and reduce its efficiency to 34 % at pH 10.

The high removal efficiency of Cr(VI) at low pH is attributed to the electrostatic attraction between negatively charged Cr(VI) anions with the positively charged nanoparticle surface. The formed passive iron oxide layer due to the oxidation is effortlessly removed at low pH. This creates more reactive sites for Cr(VI) reduction and adsorption. Along with that at acidic pH, the predominant Cr(VI) species present in the solution was $HCrO_4^-$ which is more susceptible for adsorption compared with CrO_4^{2-}. In higher pH, the prevalent Cr(VI) forms are CrO_4^{2-} and $Cr_2O_7^{2-}$. Electrostatic repulsion and competition between Cr(VI) anions and OH^- ions are the major reasons behind the less removal of Cr(VI) at higher pH[32–35].

Effect of second metal deposition on Fe^0

Effect of second metal loading on the removal of Cr(VI) has been studied (as shown in figure 3.9e) by keeping all other parameters such as initial Cr(VI) concentration (5 mg/L), nanoparticle dosage (2 g/L) and contact time (10 min) constant. The results inferred that Fe/Ni nanoparticles are highly reactive than Fe/Cu and Fe/Zn bimetallic nanoparticles. The optimum bimetal percentage for the better Cr(VI) removal was 10 %. At 15 % of bimetal concentration, the Cr(VI) removal efficiency does not significantly improve compared to 10 % second metal loading.

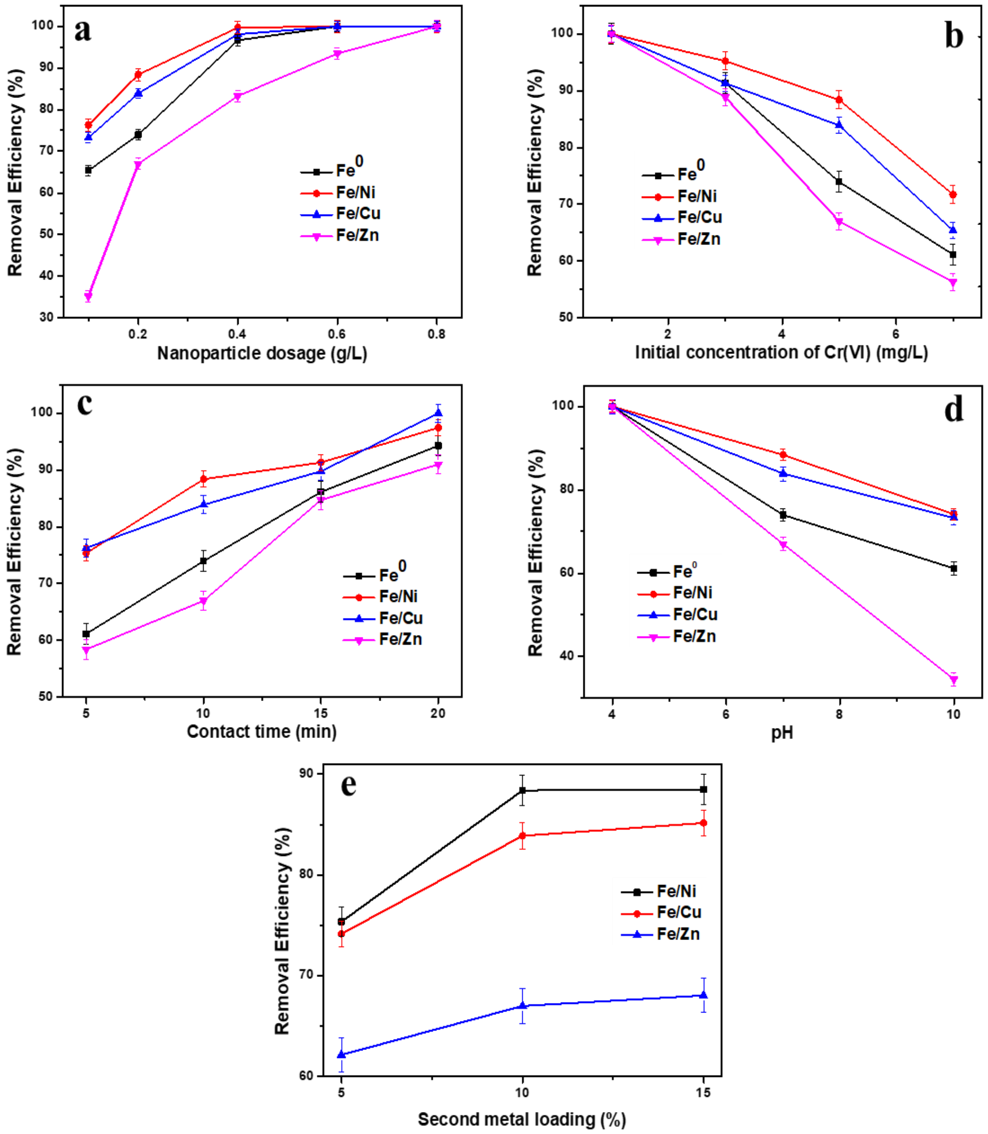

***Figure 3.9** (a) Effect of nanoparticle dosage (b) Effect of initial concentration of Cr(VI) (c) Effect of contact time (d) Effect of pH (e) Effect of second metal loading in Cr(VI) removal using Fe^0, Fe/Ni, Fe/Cu and Fe/Zn nanoparticles*

3.3.3 Dye removal studies

Effect on different dyes

As shown in figure 3.10, four commonly used organic dyes (MG, MB, MO and MLB) were used to check the reactivity of Fe^0 and three bimetallic nanoparticles (Fe/Ni, Fe/Cu and Fe/Zn). In the decolourisation experiment, the 50 mg/L of freshly prepared dye solutions were treated with 0.8 g/L of nanoparticles for 15 minutes. It was observed that Fe/Cu and Fe/Ni bimetallic nanoparticles show better removal efficiency compared to Fe^0 and Fe/Zn nanoparticles. It was noteworthy that the iron-based nanoparticles effectively removed cationic and anionic triphenylmethane dyes compared to azo or thiazine dyes. It may be due to the differences in structure and functional groups of dyes.

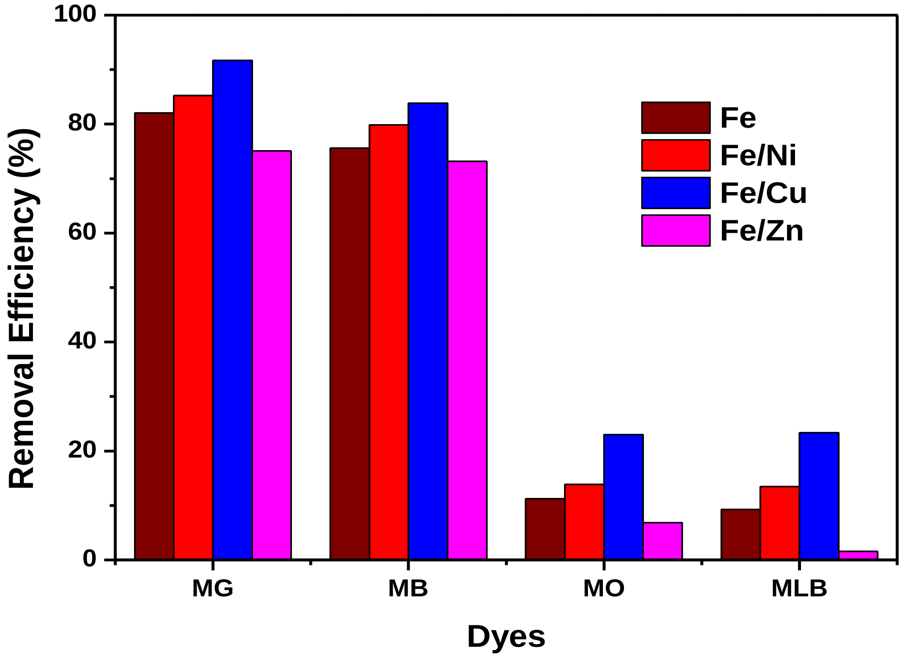

Figure 3.10 *Comparison of percentage removal of MG, MB, MO and MLB dyes using* Fe^0*, Fe/Ni, Fe/Cu and Fe/Zn nanoparticles*

MG removal using Fe^0, Fe/Ni, Fe/Cu and Fe/Zn nanoparticles

MG was selected as a model pollutant among four different dyes to study the effect of different parameters on iron-based nanoparticles. Figure 3.11 demonstrates the UV-visible spectra of MG after reacting with iron-based nanoparticles and figure 3.12 represents the corresponding reaction photographs. The characteristic peak of MG was observed at 617 nm, which corresponds to the -C-N- functional groups of MG. The absorptions observed at 424 nm, 316 nm and 248 nm are due to the conjugated framework of MG comprising of aromatic rings. After adding iron-based nanoparticles, the peaks at 617 nm, 424 nm and 316 nm were alarmingly decreased and a new peak emerged at 360 nm. The emergence of a new peak indicated the degradation of the MG dye molecule. According to Du et al, the peak at 360 nm confirms the presence of 4-dimethylamino benzophenone, a significant degradation product formed by the attack on the central carbon of MG. The peak at 248 nm corresponds to the single benzene absorption, which is enhanced after the addition of iron-based nanoparticles and it also suggests the degradation of the MG dye molecule[18]. Fe/Cu shows the highest removal efficiency among the four iron-based nanoparticles followed by Fe/Ni, Fe^0 and Fe/Zn nanoparticles. Better electron transfer and production of reactive oxygen species could be the reason for enhanced decolourisation of MG dye solution.

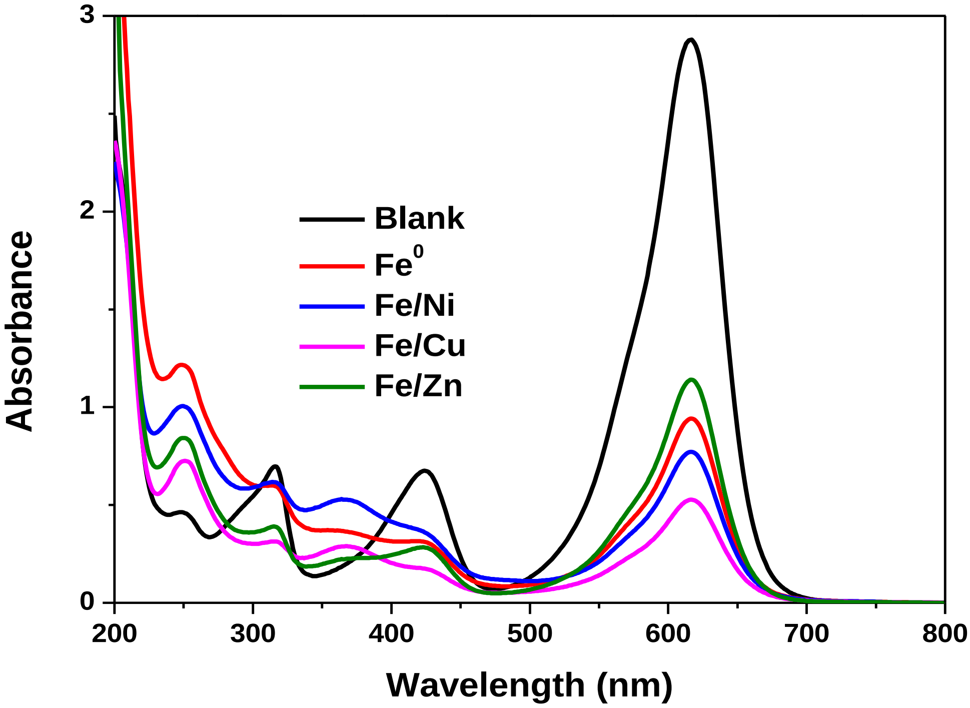

Figure 3.11 *UV-visible spectra of MG dye after treating with Fe^0, Fe/Ni, Fe/Cu and Fe/Zn nanoparticles*

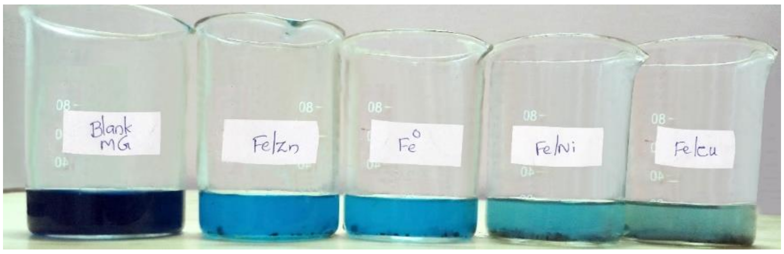

Figure 3.12 *Photographs of MG dye removal using Fe^0, Fe/Ni, Fe/Cu and Fe/Zn nanoparticles*

Effect of nanoparticle dosage

Effect of nanoparticle dosage on MG dye removal has been studied using Fe^0, Fe/Ni, Fe/Zn and Fe/Cu nanoparticles in different nanoparticle dosages varying from 0.25 g/L to 1 g/L by keeping MG concentration (50 mg/L) and contact time (15 min) as constant. As shown in figure 3.13a, the highest removal efficiency was exhibited by Fe/Cu bimetallic nanoparticles, followed by Fe/Ni, Fe^0 and Fe/Zn nanoparticles. At the dosage of 0.5 g/L, 73 %, 65 %, 59 % and 53 % of dye molecules were decolourised using Fe/Cu, Fe/Ni, Fe^0 and Fe/Zn nanoparticles respectively. With the increase in nanoparticle dosage, the availability of active reactive sites and total surface area increase, it was eventually leading to more decolourisation of dye molecules. All bimetallic nanoparticles showed the same trend. However, in the dosage of 1 g/L, there will be a decrease in the rate of dye decolourisation. It implies that at higher nanoparticle dosage, aggregation and overlapping of nanoparticles reduced the active surface area and eventually leads a decline in the decolourisation of dye molecules[36].

Effect of the initial concentration of MG

The effect of the initial concentration of MG in the dye decolourisation has been studied in 10-50 mg/L dye solutions by keeping nanoparticle dosage (0.5 g/L) and contact time (15 min) constant. As shown in figure 3.13b, 10 mg/L dye solutions were removed more efficiently than 50 mg/L dye solutions. The Fe/Cu, Fe/Ni, Fe^0 and Fe/Zn nanoparticles show 82 %, 69 %, 68 % and 59 % of removal efficiency respectively for MG dye solution. The remarkable decrease in dye removal efficiency with concentration is mainly attributed to the increased electrostatic repulsive interaction between the adsorbed cationic molecules with concentration.

Effect of contact time

The removal efficiency of nanoparticles was greatly influenced by the interaction time between nanoparticles and dye molecules. In this study, the effect of contact time on dye removal has been studied (figure 3.13c) by varying the contact time (5- 30 min) between the nanoparticles and dye molecules by keeping all other parameters constant. The result shows that the nanoparticles removal efficiency increases with increasing contact time upto a specific time and after that the percentage removal efficiency tends to an equilibrium point. Initially, the number of surface active sites was more for adsorption and degradation, leading to the rapid decolourisation of dye molecules. After some time, the surface passive layer was formed due to iron corrosion and the surface adsorptive sites were filled with dye molecules. This leads to a decrease in the decolourisation rate of dye molecules[37].

Effect of pH

The effect of pH on dye removal has been studied and shown in figure 3.13d. The results envisage that acidic pH was preferred by the iron-based nanoparticles for better removal efficiency. There is not much significant difference in removal efficiency from neutral to alkaline pH. Fe/Cu bimetallic nanoparticles show the highest removal efficiency in acidic pH. The removal efficiency of 58 %, 68 %, 74 % and 78 % were shown by Fe/Zn, Fe^0, Fe/Ni and Fe/Cu nanoparticles respectively. At acidic pH, the electron transfer and production of reactive species were enhanced causing the better degradation of MG dye molecules. However, there may be a chance for a decrease in the adsorption of dye molecules due to the electrostatic repulsion between the positively charged surface of iron nanoparticles and cationic MG dye molecules. When the pH of the solution increases, there will be a decrease in electrostatic repulsion, promoting the adsorption of the dye molecules. Nevertheless, the formation of the surface passive layer in the surface of the iron nanoparticles reduces the electron transfer from the Fe^0 core in basic pH. In this case, the high removal efficiency at acidic pH inferred that degradation is the major mechanism for dye removal compared to adsorption[36–38].

Effect of second metal deposition on Fe^0

The percentage of second metal deposition in the Fe^0 has a vital role in removing dye molecules. The effect of the second metal dosage on dye removal has been studied (figure 3.13e) by changing the second metal dosage from 5 % to 15 % by keeping all other parameters such as initial dye concentration (50 mg/L), nanoparticle dosage (0.5 g/L) and contact time (15 min) constant. The results show that 10 % bimetal loading shows better removal efficiency than 5 % and 15 % bimetal loading. This shows that 5 % bimetal loading was not sufficient to improve the property of Fe nanoparticles. When the second metal % increases, more electron transfer and formation of reactive oxygen species occur, leading to more removal efficiency. However, the excess quantity of the second metal led to increased nanoparticle agglomeration and decreased the interaction between iron nanoparticles and dye molecules. It will eventually cause a decrease in the removal efficiency[39].

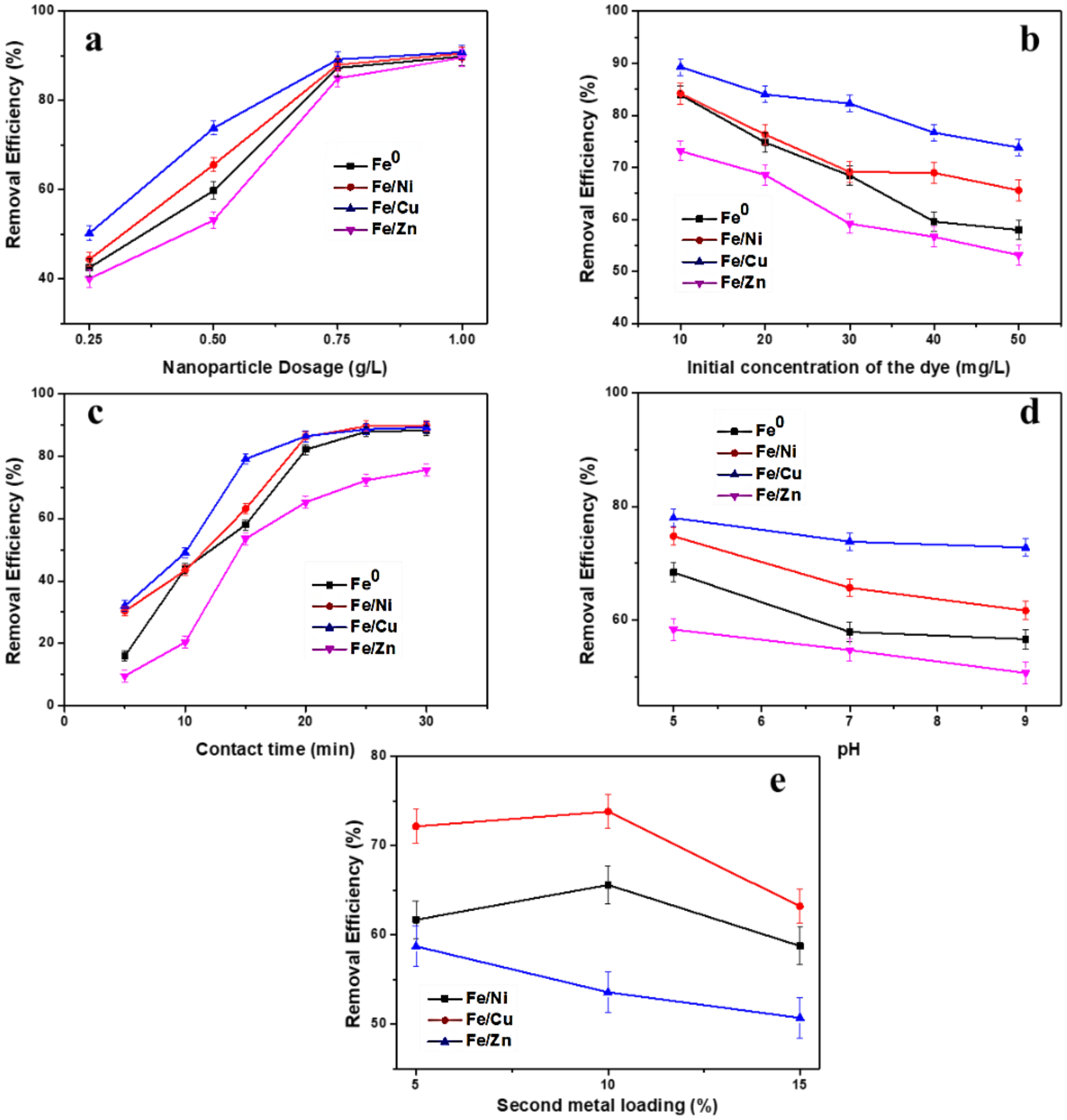

Figure 3.13 *(a) Effect of nanoparticle dosage (b) Effect of initial concentration of MG (c) Effect of contact time (d) Effect of pH (e) Effect of second metal loading in MG dye removal using* Fe^0*, Fe/Ni, Fe/Cu and Fe/Zn nanoparticles*

GC-MS/MS analysis

To determine the volatile degradation product of MG, GC-MS/MS study has been performed after complete decolourisation of dye solution using Fe^0 nanoparticles. GC-MS/MS analysis identified two possible degradation products using the NIST library. Mass spectra of the identified products are shown in figure 3.14(a&b). One possible intermediate eluted at 7.83 min was identified as cyclohexa-2,5-diene-1,4-dione (MW 108) and another degradation product eluted at 19.90 min was confirmed as diphenylmethanone (MW 182). The two degradation products indicated by GC-MS/MS could result from the destruction of the entire conjugated chromophore structure of MG. The area covered by diphenylmethanone was 4.30, implying that it was the major degradation product. The formation of these stable compounds results from the interaction of reactive oxygen species and other active species with dye molecules.

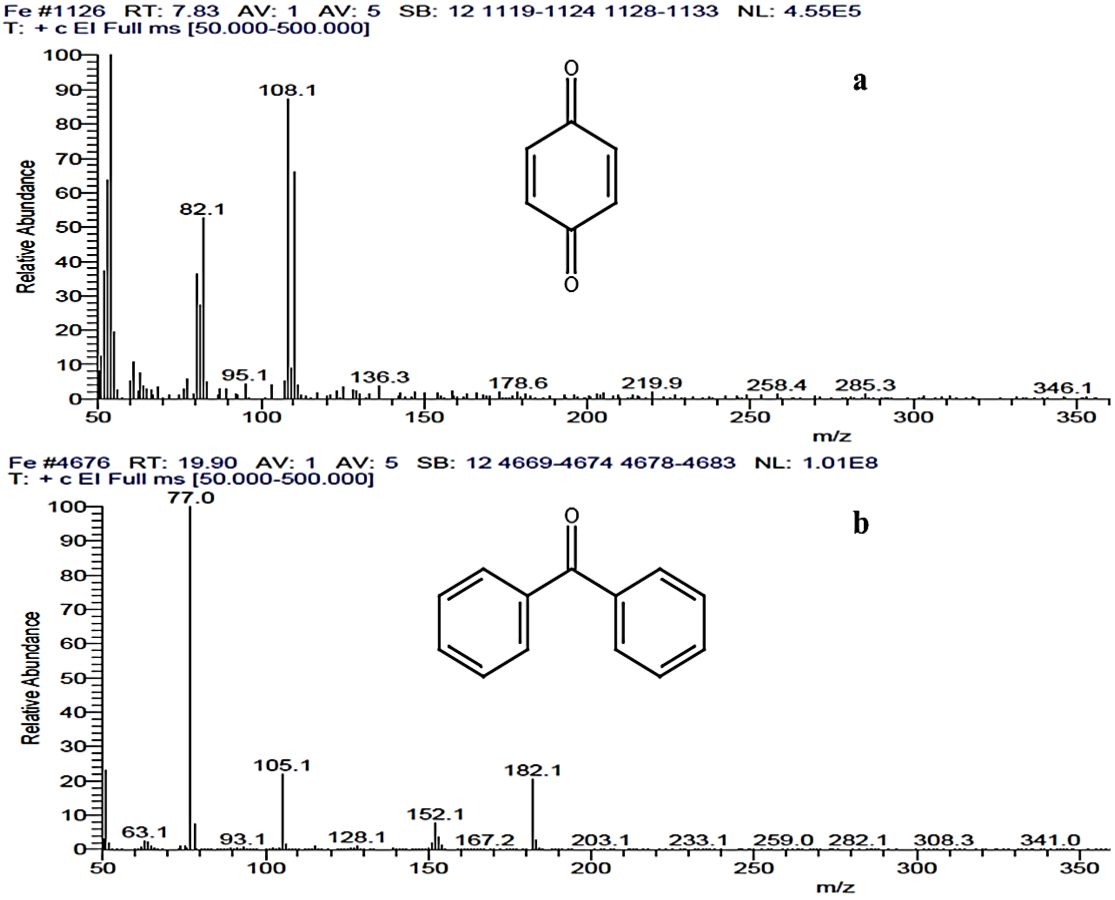

Figure 3.14 *Mass spectra of MG degradation products identified by GC-MS/MS analysis a) cyclohexa-2,5-diene-1,4-dione and b) diphenylmethanone*.

LC-MS/MS analysis

In order to provide the supportive information for the proposed degradation mechanism of MG dye molecules, LC-MS/MS study has been carried out in the solution of MG. Figure 3.15 shows the MG solution's LC-MS/MS chromatogram after being treated with Fe^0 nanoparticles. MG has been detected in retention time (Rt) 69.79 min with m/z 330. The degradation products identified and their m/z values and Rt are listed in table 3.2. All the identified compounds did not show an apparent peak in the LC-MS/MS chromatogram but were detected by mass spectrometry.

Compound	**IUPAC name**	**Rt (min)**	**m/z**
MG	4-[4-(dimethylamino)phenyl]-phenyl-methylene]cyclohexa-2,5-dien-1-ylidene]-dimethyl-ammonium	69.79	330.3359
MG-CH_2	dimethyl-[4-[[4-(methylamino)phenyl]-phenyl-methylene]cyclohexa-2,5-dien-1-ylidene]azanium	58.6	316.2841
MG-2CH_2	dimethyl-[4-[[4-(methylamino)phenyl]-phenyl-methylene]cyclohexa-2,5-dien-1-ylidene]ammonium	65.28	302.3052
MG-3CH_2	[4-[(4-aminophenyl)-phenyl-methylene]cyclohexa-2,5-dien-1-ylidene]-methylazanium	61.74	288.2888
MG-4CH_2	[[4-[(4-aminophenyl)-phenyl-methylene]cyclohexa-2,5-dien-1-ylidene]azanium	50.74	274.2735
MG-2CH_2-NH_2	4-(dimethylamino)tritylradical	56.0	287.1552
LMG	4-[[4-(dimethylamino)phenyl]-phenyl-methyl]-N,N-dimethyl-aniline	46.63	331.2081
LMG-CH_2	4-[[4-(dimethylamino)phenyl]-phenyl-methyl]-N-methyl-aniline	60.1	317.1720
LMG-3CH_2	4-[[4-(methylamino)phenyl]-phenylmethyl]aniline	33.74	289.1259
LMG-4CH_2-NH_2	4-benzhydrylaniline	57.95	260.2579
LMG-4CH_2-2NH_2	benzhydrylbenzene	60.74	245.0781
LMG+OH	4-[bis[4-(dimethylamino)phenyl]methyl]phenol	37.31	347.1304

LMG+2OH	5-[bis[4-(dimethylamino)phenyl]methyl]benzene-1,3-diol	68.90	363.3090
LMG+OH-CH$_2$-CH$_3$	N-[4-[[4-(dimethylamino)phenyl]-phenylmethyl]phenyl]hydroxylamine	69.1	319.2836
LMG+OH-4CH$_2$	4-[bis(4-aminophenyl)methyl]phenol	60.4	290.2696
DLBP	[4-(dimethylamino)phenyl]-phenylmethanone	62.6	226.1229
DLBP -CH$_2$	[4-(methylamino)phenyl]-phenylmethanone	60.05	212.1069
DLBP +OH	[4-(dimethylamino)phenyl]-(4-hydroxyphenyl)methanone	65.30	242.2841
DLBP +OH -CH$_2$	[3-hydroxy-4-(methylamino)phenyl]-phenylmethanone	63.46	228.2679
DLBP +OH -2CH$_2$	(4-aminophenyl)-(4-hydroxyphenyl)methanone	58.3	214.2528
DLBP +2OH -2CH$_2$	(4-aminophenyl)-(2,4-dihydroxyphenyl)methanone	52.3	230.2467
$C_8H_{11}N$	N,N-dimethylaniline	70.07	122.0965
$C_9H_{11}O_2N$	4-(dimethylamino)benzoic acid	51.8	166.0866

Table 3.2 *Products identified by LC-MS/MS*

Compared to GC-MS/MS analysis, more degradation products were identified by LC-MS/MS analysis since several volatile degradation products are too low to be eluted under the gas chromatographic conditions used. Mass spectra of some degradation products are shown in figure 3.16.

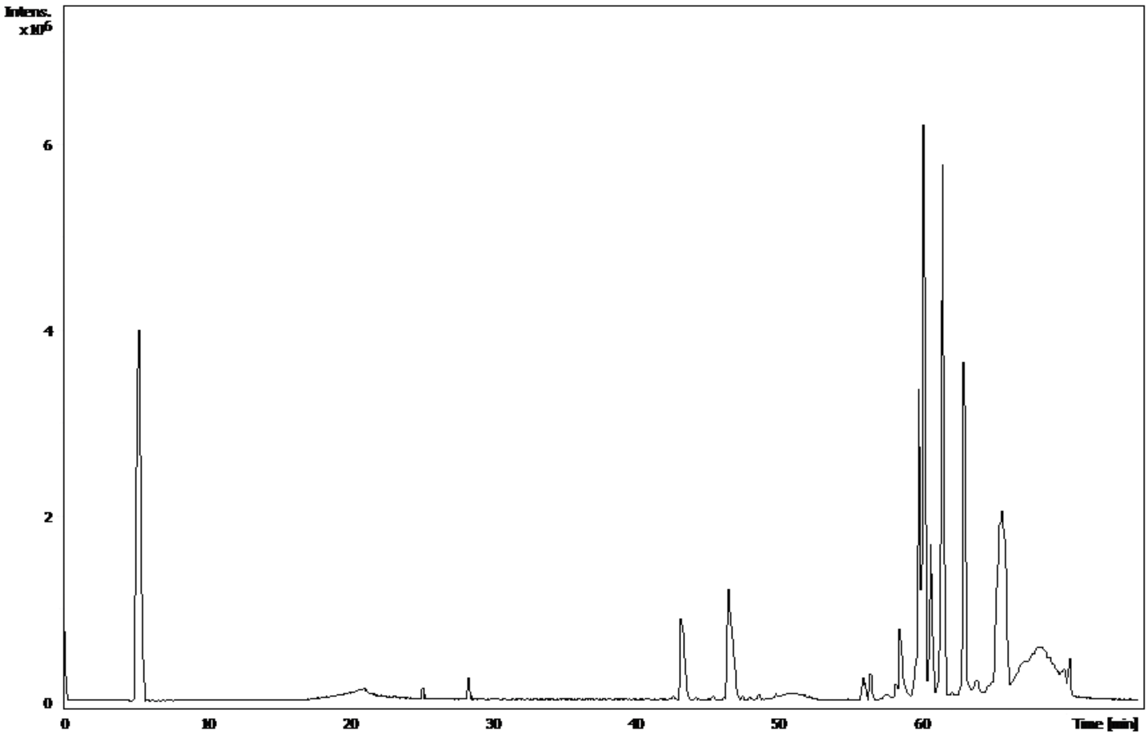

Figure 3.15 *LC-MS/MS of MG degradation products after treating with Fe^0 nanoparticles*

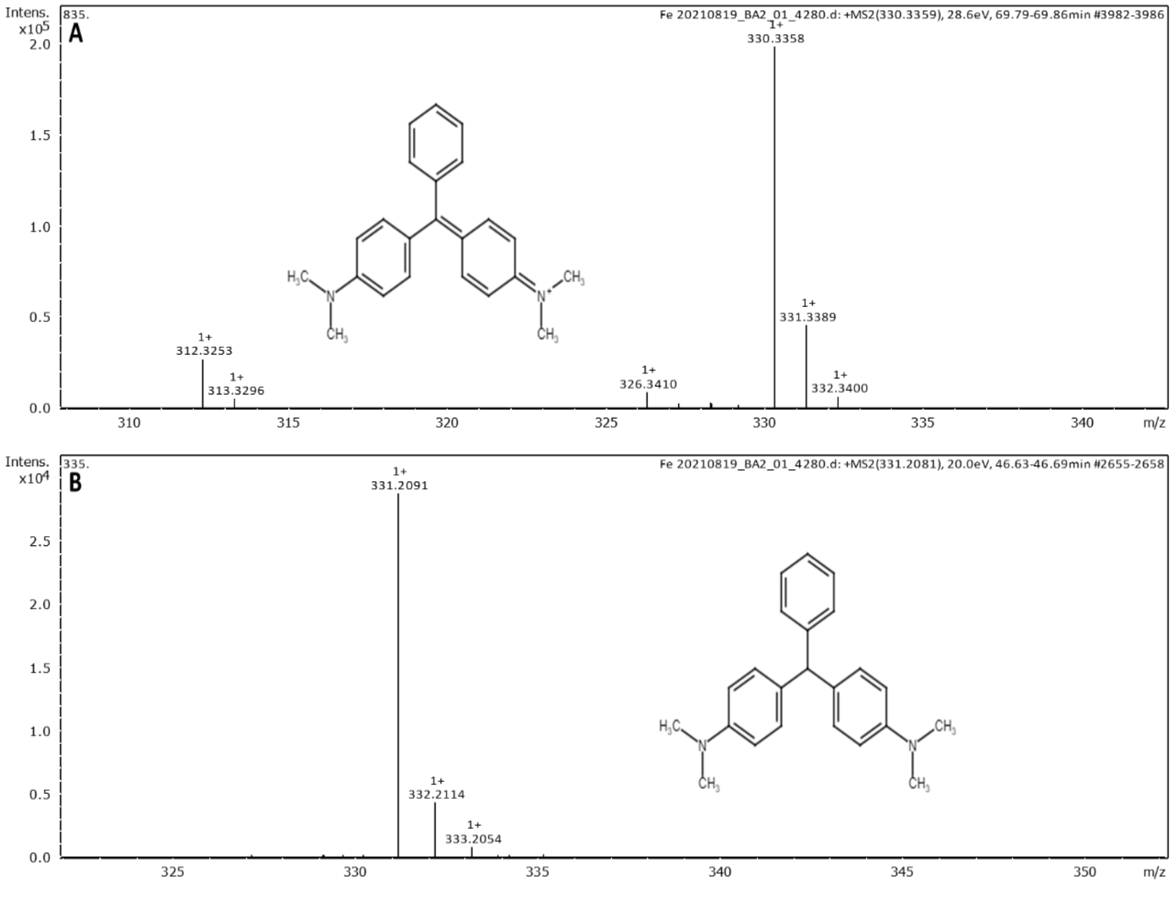

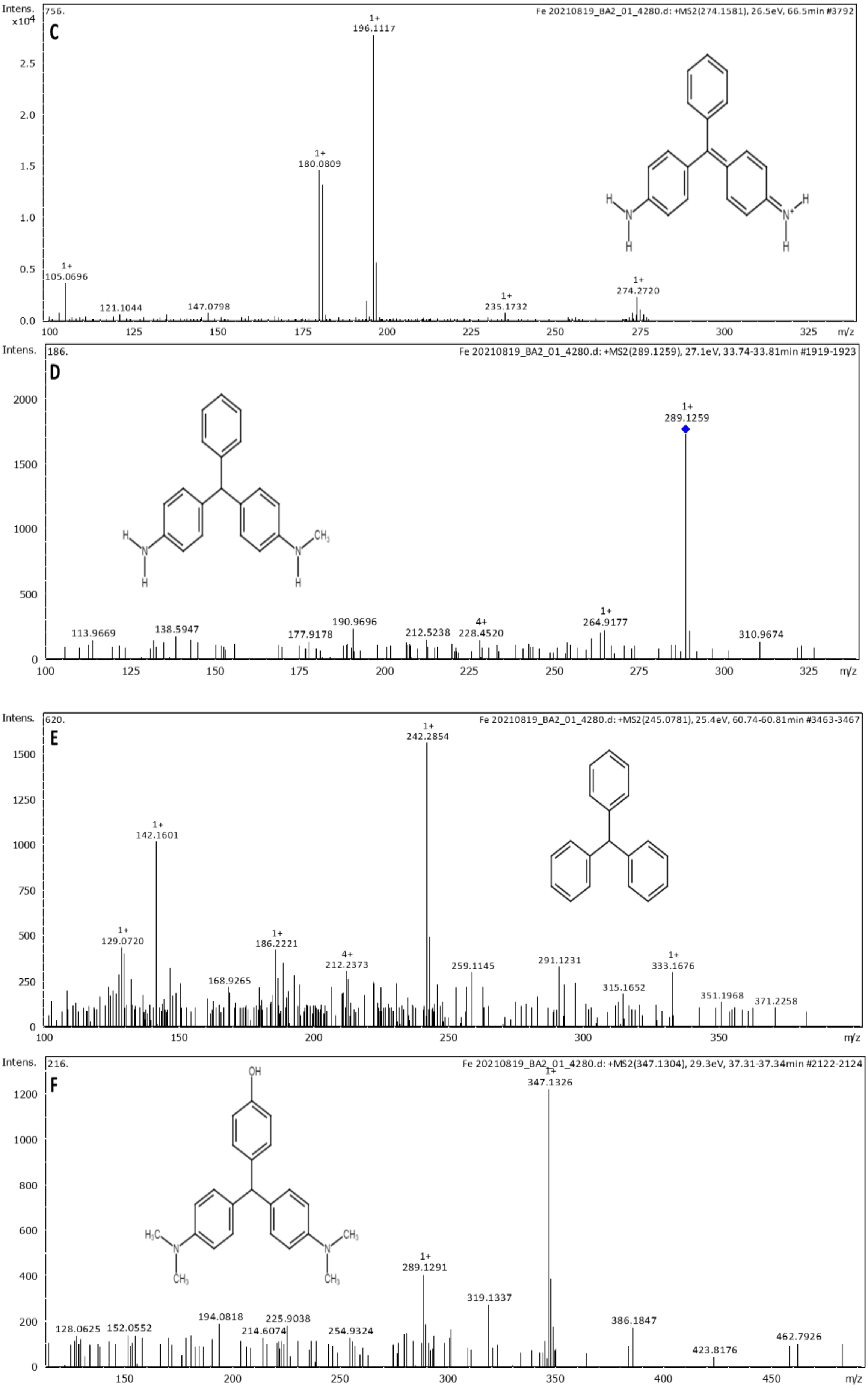
Intens.
x10^4
756.
C
Fe 20210819_BA2_01_4280.d: +MS2(274.1581), 26.5eV, 66.5min #3792
2.5
2.0
1.5
1.0
0.5
0.0
1+
196.1117
1+
180.0809
1+
105.0696
121.1044
147.0798
1+
235.1732
1+
274.2720
H
N
H
N+
H
H
100
125
150
175
200
225
250
275
300
325
m/z
Intens.
186.
D
Fe 20210819_BA2_01_4280.d: +MS2(289.1259), 27.1eV, 33.74-33.81min #1919-1923
2000
1500
1000
500
0
1+
289.1259
H
N
H
N
CH3
H
113.9669
138.5947
177.9178
190.9696
212.5238
4+
228.4520
1+
264.9177
310.9674
100
125
150
175
200
225
250
275
300
325
m/z
Intens.
620.
E
Fe 20210819_BA2_01_4280.d: +MS2(245.0781), 25.4eV, 60.74-60.81min #3463-3467
1500
1250
1000
750
500
250
0
1+
242.2854
1+
142.1601
1+
129.0720
1+
186.2221
4+
212.2373
168.9265
259.1145
291.1231
1+
333.1676
315.1652
351.1968
371.2258
100
150
200
250
300
350
m/z
Intens.
216.
F
Fe 20210819_BA2_01_4280.d: +MS2(347.1304), 29.3eV, 37.31-37.34min #2122-2124
1200
1000
800
600
400
200
0
OH
H3C
N
CH3
N
CH3
CH3
1+
347.1326
1+
289.1291
319.1337
128.0625
152.0552
194.0818
225.9038
214.6074
254.9324
386.1847
423.8176
462.7926
150
200
250
300
350
400
450
m/z

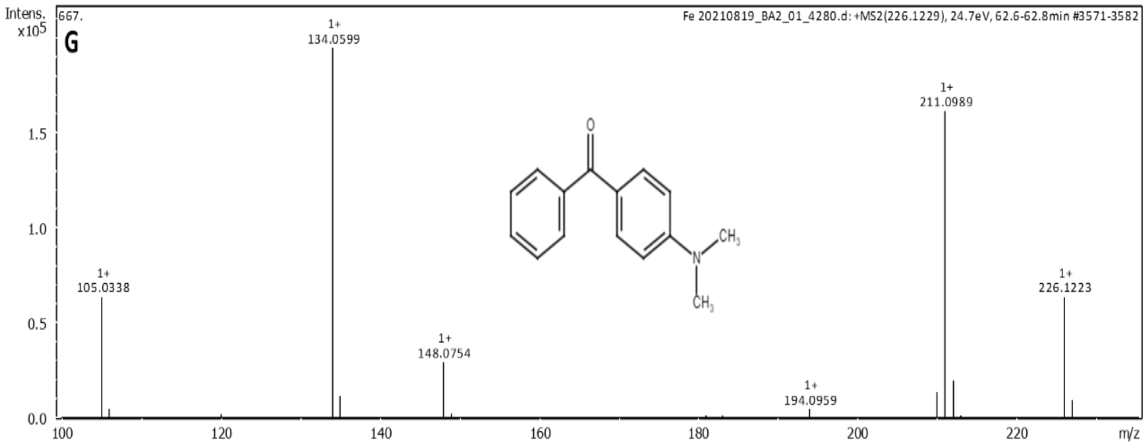
Intens. x10^5
667.
G
Fe 20210819_BA2_01_4280.d: +MS2(226.1229), 24.7eV, 62.6-62.8min #3571-3582
1+ 134.0599
1+ 211.0989
1+ 105.0338
1+ 226.1223
1+ 148.0754
1+ 194.0959
0.0
0.5
1.0
1.5
100
120
140
160
180
200
220
m/z
O
N
CH3
CH3

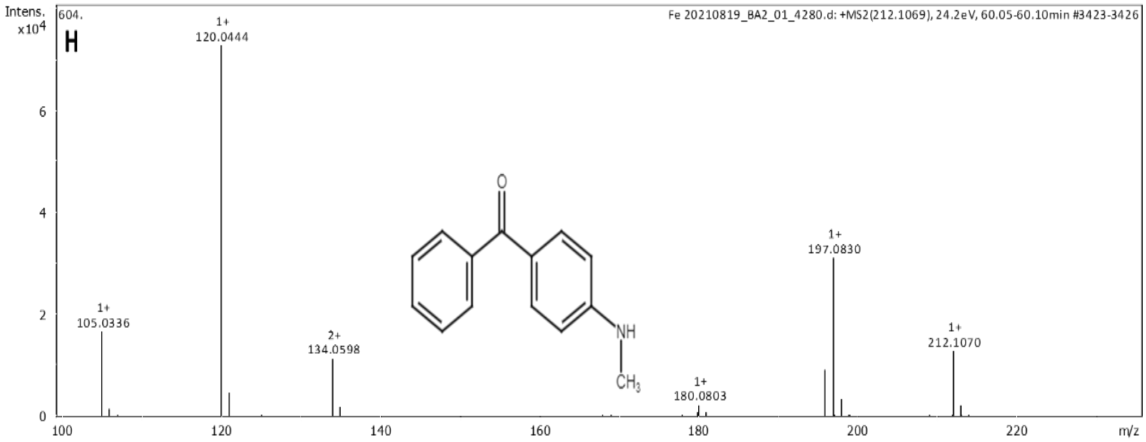
Intens. x10^4
604.
H
Fe 20210819_BA2_01_4280.d: +MS2(212.1069), 24.2eV, 60.05-60.10min #3423-3426
1+ 120.0444
1+ 197.0830
1+ 105.0336
2+ 134.0598
1+ 212.1070
1+ 180.0803
0
2
4
6
100
120
140
160
180
200
220
m/z
O
NH
CH3

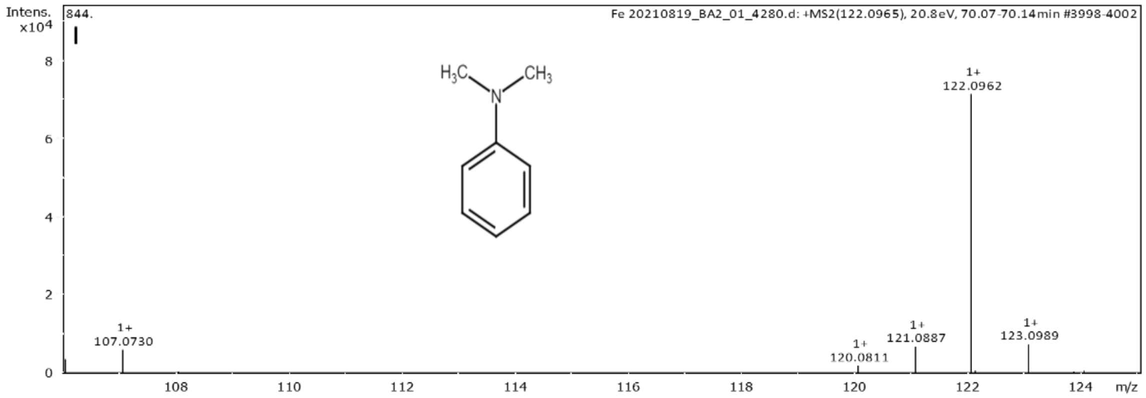
Intens. x10^4
844.
I
Fe 20210819_BA2_01_4280.d: +MS2(122.0965), 20.8eV, 70.07-70.14min #3998-4002
H3C
N
CH3
1+ 122.0962
1+ 107.0730
1+ 120.0811
1+ 121.0887
1+ 123.0989
0
2
4
6
8
108
110
112
114
116
118
120
122
124
m/z

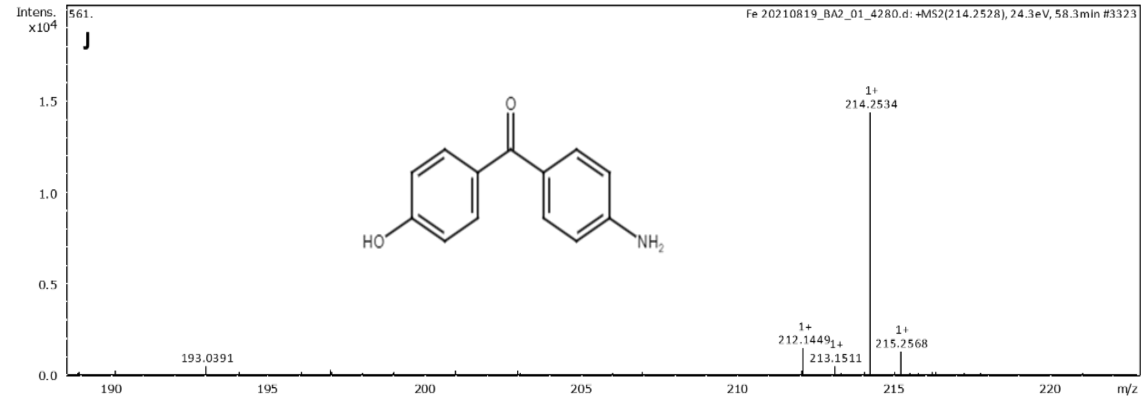
Intens. x10^4
561.
J
Fe 20210819_BA2_01_4280.d: +MS2(214.2528), 24.3eV, 58.3min #3323
O
HO
NH2
1+ 214.2534
1+ 212.1449
1+ 213.1511
1+ 215.2568
193.0391
0.0
0.5
1.0
1.5
190
195
200
205
210
215
220
m/z

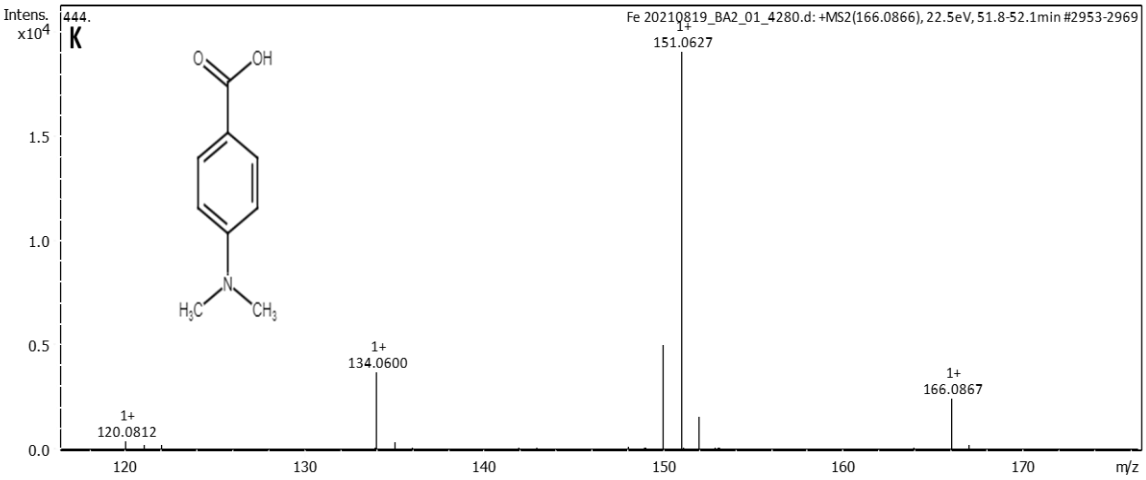

***Figure 3.16** Mass spectra of some MG degradation products identified by LC-MS/MS analysis. (A) [4-[[4-(dimethylamino)phenyl]-phenylmethylidene]cyclohexa-2,5-dien-1-ylidene]-dimethylazanium; (B) 4-[[4-(dimethylamino)phenyl]-phenylmethyl]-N,N-dimethylaniline; (C) [4-[(4-aminophenyl)-phenylmethylidene]cyclohexa-2,5-dien-1-ylidene] azanium; (D) 4-[[4-(methylamino)phenyl]-phenylmethyl]aniline; (E) benzhydrylbenzene ; (F) 4-[bis[4-(dimethylamino)phenyl]methyl]phenol; (G) [4-(dimethylamino)phenyl]-phenylmethanone; (H) [4-(methylamino)phenyl]-phenylmethanone; (I)* N,N-dimethyl aniline*;(J)* (4-aminophenyl)-(4-hydroxyphenyl)methanone*;(K) 4-(dimethylamino)benzoic acid*

Proposed mechanism for the degradation of MG using Fe nanoparticles

The degradation of MG involves both reductive and oxidative pathways along with the adsorption of the dye molecules. The reductive degradation of MG depends on the Fe^0 content and H$^+$ in the solution. During the reductive pathway, the MG molecules may adsorb onto the iron surface and degradation occurs through direct electron transfer or adsorbed H*. The two adsorbed atomic hydrogen can combine to form H$_2$[40]. These reactions in the reductive pathway are shown in equations 3.8-3.11.

$$Fe^0 \rightarrow Fe^{2+} + 2e^- \tag{3.8}$$

$$2Fe^0 + 2H^+ + 2e^- \rightarrow 2Fe - H^* \rightarrow 2Fe + H_2 \tag{3.9}$$

$$Dye + e^- \rightarrow Degradation\, products \tag{3.10}$$

$$Dye + 2Fe - H^* \rightarrow Degradation\, products \tag{3.11}$$

During the reductive degradation of MG dye, the MG was first reduced into leuco MG. After the initial stage of the degradation process, the degradation mechanism prevailed by oxidative pathway since the MG dye removal experiment did not take place in anaerobic system. In the presence of dissolved oxygen, the iron oxide layer formed quickly and decreased the probability of reductive degradation. The addition of second metal (Ni, Cu) changes the faith of Fe^0 nanoparticles upto an extent. Deposition with a second metal improves iron corrosion and hydrogen generation and prevents the blocking of the iron surface through the formation of oxide film[41]. The reductive removal of MG with bimetallic nanoparticles were shown in equation 3.12-3.14. The second metal (Ni or Cu) loses the electrons while reacting with the dye molecule. The formed nickel or copper ion was galvanically protected by electrons released from Fe/Fe^{2+} and Fe^{2+}/Fe^{3+} redox reactions and turned into metallic Ni or Cu again. This process will continue until there is an electronic bridge between the two metals. Along with the direct electron transfer, the hydride formation with deposited metal would also play an essential role in reductive dye degradation in bimetallic nanoparticles. Nickel hydride or copper hydride was formed by reacting with the atomic hydrogen. These hydride formations reductively degrade the MG molecules (as shown in equation 3.15-3.18) and during this time, a new hydride free surface formed in iron-based bimetals[41,42].

$$Fe^0 \rightarrow Fe^{2+} + 2e^- \tag{3.12}$$

$$Ni^{2+}/\,Cu^{2+} + 2e^- \rightarrow Ni^0/Cu^0 \tag{3.13}$$

$$Ni^0/Cu^0 + MG + H_2O \rightarrow Ni^{2+}/\,Cu^{2+} + MG_{reduced} + OH^- \tag{3.14}$$

$$2H_2O + 2e^- \rightarrow 2H^* + 2OH^- \tag{3.15}$$

$$Ni + H^* \rightarrow Ni - H^* \tag{3.16}$$

$$Cu + H^* \rightarrow Cu - H^* \tag{3.17}$$

$$Ni - H^*/\,Cu - H^* + MG \rightarrow Ni/Cu + MG\ degradation\,products \tag{3.18}$$

The oxidative removal of MG dye prevailed over time than reductive removal conditions. The iron nanoparticle acted as a heterogeneous Fenton-like catalysts since the iron nanoparticles react with dissolved oxygen in water and form reactive oxygen species like hydrogen peroxide, hydroxyl radical etc.[43–45] as shown in equations 3.19-3.23.

$$O_2 + 2e^- + 2H^+ \rightarrow 2\ \cdot OH \tag{3.19}$$

$$2Fe^0 + O_2 + 2H_2O \rightarrow 2Fe^{2+} + 2H_2O_2 \tag{3.20}$$

$$Fe^{2+} + H_2O_2 \rightarrow Fe^{3+} + \cdot OH + OH^- \tag{3.21}$$

$$Fe^{3+} + H_2O_2 \rightarrow Fe^{2+} + \cdot OOH + H^+ \tag{3.22}$$

$$Fe^{3+} + \cdot OOH \rightarrow Fe^{2+} + O_2 + H^+ \tag{3.23}$$

Hydroxyl radical formed by the reaction was reacted with the MG dye molecule and degraded them into smaller fragments. Bimetallic composition in the iron-based nanoparticles will improve the formation of hydroxyl radicals. For example, the formation of hydroxyl radical by Fe/Cu bimetallic nanoparticles[1] has been shown in equation 3.24.

$$Fe^{2+} + Cu^{2+} + 3H_2O_2 \rightarrow 3\ \cdot OH + HO_2 \cdot + H_2O + Fe^{3+} + Cu^{2+} \tag{3.24}$$

The MG and its degradation products are adsorbed onto the surface of Fe^0 and iron oxides as shown in equations 3.25 and 3.26.

$$Fe^0 + MG \rightarrow Fe^0 - MG \tag{3.25}$$

$$Fe_xO_y/FeOOH + MG\ degradation\ products \rightarrow Fe_xO_y/FeOOH - MG\ degradation\ products \tag{3.26}$$

The degradation pathway of MG by Fe^0 nanoparticles is shown in scheme 3.1. A few undetected degradation products are also depicted in scheme 3.1, including b2, b4, c4, d2, d8, e1, e2 and e4. Even though these degradation products were not detected in GC-MS/MS and LC-MS/MS analysis, the presence of some other compounds inferred the existence of these compounds.

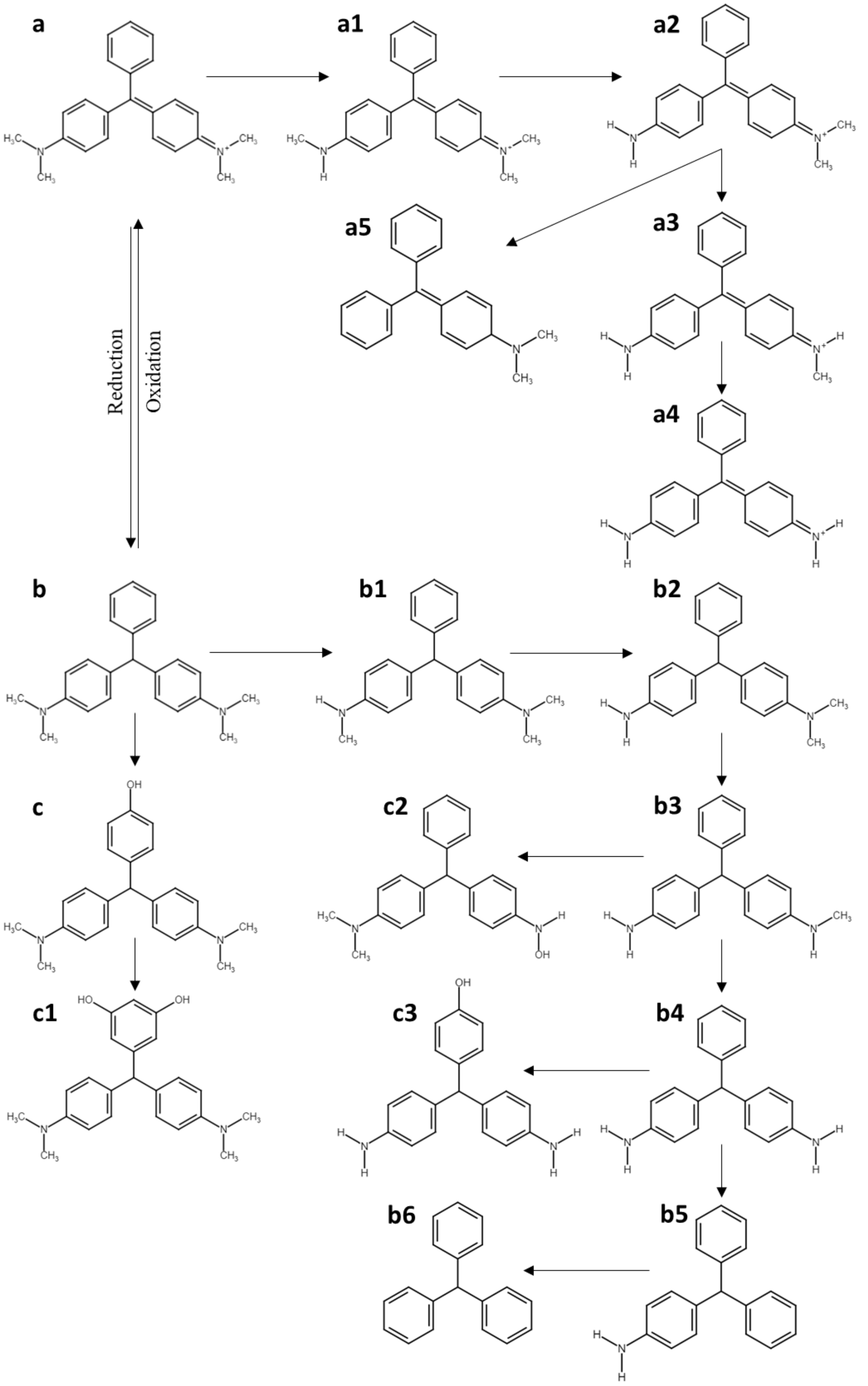
a
a1
a2
a5
a3
a4
Reduction
Oxidation
b
b1
b2
c
c2
b3
c1
c3
b4
b6
b5

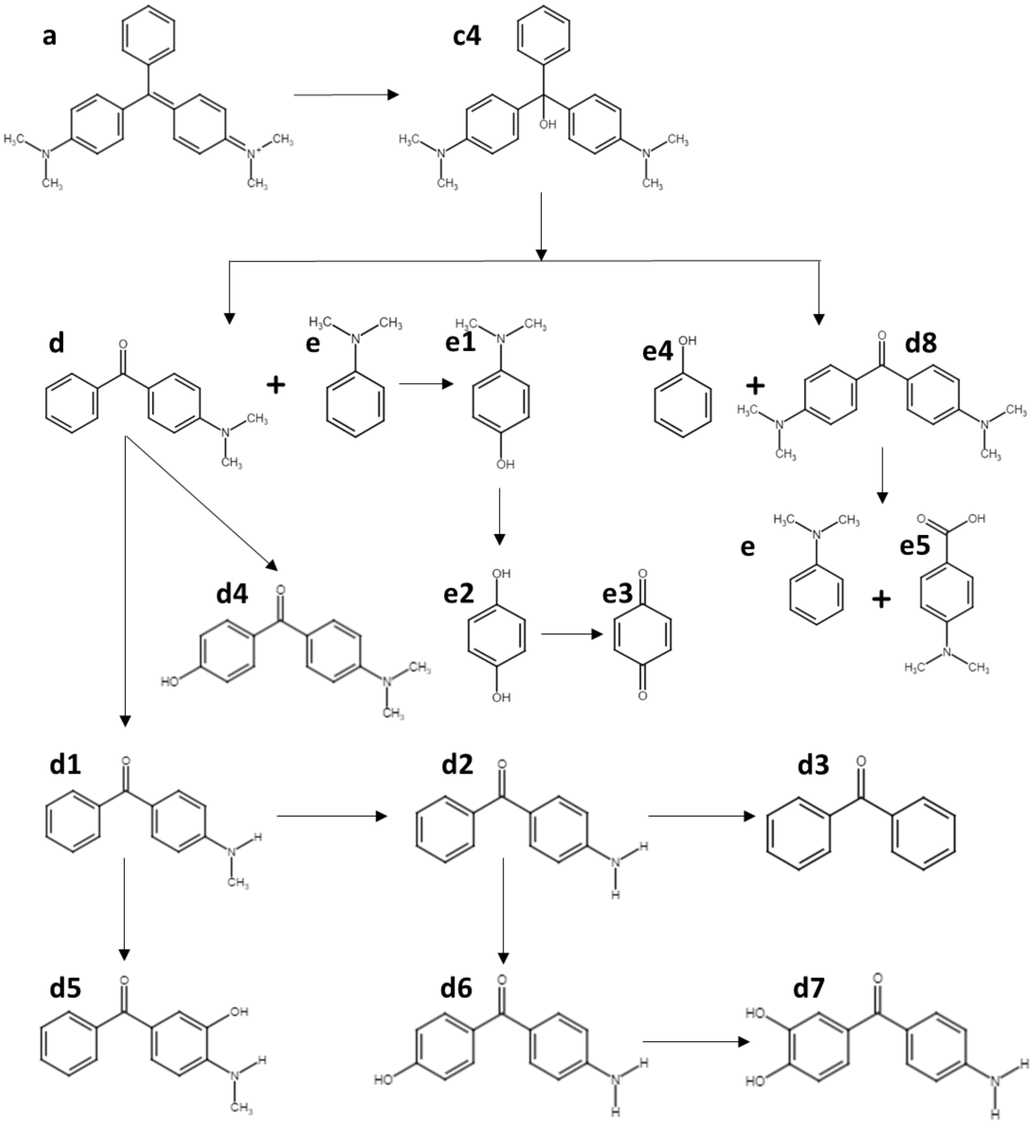

Scheme 3.1 *Degradation pathways of MG using Fe^0 nanoparticle*

MG degradation pathway shows that the attack by hydroxyl radical leads to the N-demethylation and deamination of MG and MG degradation products. N-demethylation has gradually occurred until the total elimination of the 4 methyl groups and deamination removes the amino group in the MG[18]. In the scheme, a1-a4, b1-b6 and d1-d3 represent the N-demethylation and deamination of MG and its degradation products. The next set of reactions that occurred in MG is hydroxyl addition reactions. The addition of hydroxyl radical happened in MG degradation products due to the non-selectivity of hydroxyl radical[46]. The products c-c4 and d4-d7 represent the results of hydroxyl addition reactions in MG and MG degradation products. The hydroxyl radical attacked the central carbon leading to the destruction of the conjugated structure. The c4 so formed gets degraded in two ways, (1) N,N-dimethylaniline (e) and [4-(dimethylamino)phenyl]-phenylmethanone (d), and (2) phenol (e4) and bis[4-(dimethylamino)phenyl]methanone (d8)[18,47]. N-demethylation, deamination and hydroxyl addition reactions occurred in N,N-dimethylaniline leading to hydroquinone formation. These formed hydroquinone molecules were suddenly transferred into cyclohexa-2,5-diene-1,4-dione in the presence of H_2O_2[48–50]. The bis[4-(dimethylamino)phenyl]methanone is further degraded into N,N-dimethylaniline and 4-(dimethylamino)benzoic acid (e5) by reacting with hydroxyl radical[18]. There will be a chance for further degradation and mineralisation of MG degraded products, but not detected by LC-MS/MS since below m/z 100 was not examined in this study.

3.4 Conclusions

In this study, zero valent iron nanoparticles and bimetallic iron-based nanoparticles were prepared through the liquid-phase reduction method using $NaBH_4$ as the reducing agent. The characterisation of the prepared nanoparticles has been done using XRD, HRTEM and EDAX and confirmed the formation of Fe^0, Fe/Ni, Fe/Zn and Fe/Cu nanoparticles. The reactivity of prepared nanoparticles was studied for Cr(VI) and dye removal and found that Fe/Cu and Fe/Ni bimetallic nanoparticles were more efficient than Fe^0 and Fe/Zn nanoparticles. The better efficiency of Fe/Cu and Fe/Ni bimetallic nanoparticles was due to their better direct electron transfer, hydride formation and formation of reactive oxygen species. The effect of various parameters such as initial concentration of the dye, nanoparticle dosage, initial pH of the solution, contact time and deposition of second metal has been examined in this study. Both MG dye and Cr(VI) removal preferred acidic pH and a second metal deposition of 10 %. Iron-based nanoparticles effectively removed the triphenylmethane dyes compared to azo and thiazine dyes. EDAX confirmed the reduction of Cr(VI) by prepared nanoparticles and the degradation of MG dye molecules was confirmed by GC-MS/MS and LC-MS/MS techniques. Thus, Fe/Ni and Fe/Cu bimetallic nanoparticles can be used as a cost-effective and practical material for Cr(VI) and MG dye removal.

3.5 References

[1] J. Scaria, P. V. Nidheesh, M.S. Kumar, Synthesis and applications of various bimetallic nanomaterials in water and wastewater treatment, J. Environ. Manage. 259 (2020) 110011. https://doi.org/10.1016/j.jenvman.2019.110011.

[2] D. O’Carroll, B. Sleep, M. Krol, H. Boparai, C. Kocur, Nanoscale zero valent iron and bimetallic particles for contaminated site remediation, Adv. Water Resour. 51 (2013) 104–122. https://doi.org/10.1016/j.advwatres.2012.02.005.

[3] N. Toshima, T. Yonezawa, Bimetallic nanoparticles - Novel materials for chemical and physical applications, New J. Chem. 22 (1998) 1179–1201. https://doi.org/10.1039/a805753b.

[4] T. Shubair, O. Eljamal, A.M.E. Khalil, A. Tahara, N. Matsunaga, Novel application of nanoscale zero valent iron and bimetallic nano-Fe/Cu particles for the treatment of cesium contaminated water, J. Environ. Chem. Eng. 6 (2018) 4253–4264. https://doi.org/10.1016/j.jece.2018.06.015.

[5] R. Wang, T. Tang, K. Huang, M. Zou, X. Tao, H. Yin, Z. Lin, Z. Dang, G. Lu, Debromination of polybrominated biphenyls (PBBs) by zero valent metals and iron-based bimetallic particles: Mechanisms, pathways and predicting descriptor, Chem. Eng. J. 351 (2018) 773–781. https://doi.org/10.1016/j.cej.2018.06.149.

[6] R. Wang, G. Lu, H. Lin, K. Huang, T. Tang, X. Xue, X. Yang, H. Yin, Z. Dang, Relative roles of H-atom transfer and electron transfer in the debromination of polybrominated diphenyl ethers by palladized nanoscale zerovalent iron, Environ. Pollut. 222 (2017) 331–337. https://doi.org/10.1016/j.envpol.2016.12.030.

[7] R. Wang, T. Tang, G. Lu, Z. Zheng, K. Huang, H. Li, X. Tao, H. Yin, Z. Shi, Z. Lin, F. Wu, Z. Dang, Mechanisms and pathways of debromination of polybrominated diphenyl ethers (PBDEs) in various nano-zerovalent iron-based bimetallic systems, Sci. Total Environ. 661 (2019) 18–26. https://doi.org/10.1016/j.scitotenv.2019.01.166.

[8] Z. Xiong, B. Lai, P. Yang, Y. Zhou, J. Wang, S. Fang, Comparative study on the reactivity of Fe/Cu bimetallic particles and zero valent iron (ZVI) under different conditions of N2, air or without aeration, J. Hazard. Mater. (2015). https://doi.org/10.1016/j.jhazmat.2015.05.006.

[9] K.K. Onchoke, S.A. Sasu, Determination of Hexavalent Chromium (Cr(VI)) Concentrations via Ion Chromatography and UV-Vis Spectrophotometry in Samples Collected from Nacogdoches Wastewater Treatment Plant, East Texas (USA), Adv. Environ. Chem. 2016 (2016) 1–10. https://doi.org/10.1155/2016/3468635.

[10] J.O. Ighere, K. Honjoya, R.C. Chawla, Using Ferrous Ion for the Reductive Degradation of Hexavalent Chromium, Adv. Chem. Eng. Sci. 05 (2015) 15–22. https://doi.org/10.4236/aces.2015.51002.

[11] F. Liu, Y. Lu, H. Chen, Y. Liu, Removal of Cr from groundwater using zero- valence iron in the laboratory Removal of Cr 6 + from groundwater using zero- valence iron in the laboratory, Chem. Speciat. Bioavailab. 2299 (2015) 2–5. https://doi.org/10.3184/095422902782775290.

[12] R.A. Anderson, Chromium as an Essential Nutrient for Humans, Regul. Toxicol. Pharmacol. 41 (1997). https://doi.org/10.1006/rtph.1997.1136.

[13] M.I.N. Ahamed, S. Rajeshkumar, V. Ragul, S. Anand, K. Kaviyarasu, Chromium remediation and toxicity assessment of nano zerovalent iron against contaminated lake water sample (Puliyanthangal Lake, Tamilnadu, India), South African J. Chem. Eng. 25 (2018) 128–132. https://doi.org/10.1016/j.sajce.2018.04.004.

[14] F. Liu, Y. Lu, H. Chen, Y. Liu, Removal of Cr 6+ from groundwater using zero-valence iron in the laboratory, Chem. Speciat. Bioavailab. 14 (2002) 75–77. https://doi.org/10.3184/095422902782775290.

[15] H. Oliveira, Chromium as an Environmental Pollutant: Insights on Induced Plant Toxicity, J. Bot. 2012 (2012) 1–8. https://doi.org/10.1155/2012/375843.

[16] A. Arunarani, P. Chandran, B. V. Ranganathan, N.S. Vasanthi, S. Sudheer Khan, Bioremoval of Basic Violet 3 and Acid Blue 93 by Pseudomonas putida and its adsorption isotherms and kinetics, Colloids Surfaces B Biointerfaces. 102 (2013) 379–384. https://doi.org/10.1016/j.colsurfb.2012.08.049.

[17] K.Z. Xu, H. Ma, Y.J. Wang, Y.J. Cai, X.R. Liao, Z.B. Guan, Extracellular expression of mutant CotA-laccase SF in Escherichia coli and its degradation of malachite green, Ecotoxicol. Environ. Saf. 193 (2020) 110335. https://doi.org/10.1016/j.ecoenv.2020.110335.

[18] L.N. Du, M. Zhao, G. Li, F.C. Xu, W.H. Chen, Y.H. Zhao, Biodegradation of malachite green by Micrococcus sp. strain BD15: Biodegradation pathway and enzyme analysis, Int. Biodeterior. Biodegrad. 78 (2013) 108–116. https://doi.org/10.1016/j.ibiod.2012.12.011.

[19] T. Bhagavathi Pushpa, J. Vijayaraghavan, S.J. Sardhar Basha, V. Sekaran, K. Vijayaraghavan, J. Jegan, Investigation on removal of malachite green using EM based compost as adsorbent, Ecotoxicol. Environ. Saf. 118 (2015) 177–182. https://doi.org/10.1016/j.ecoenv.2015.04.033.

[20] X. Hou, X. Tong, W. Dong, C. Dong, S. Shuang, Synchronous fluorescence determination of human serum albumin with methyl blue as a fluorescence probe, Spectrochim. Acta - Part A Mol. Biomol. Spectrosc. 66 (2007) 552–556. https://doi.org/10.1016/j.saa.2006.03.031.

[21] C. Sahoo, A.K. Gupta, Optimization of photocatalytic degradation of methyl blue using silver ion doped titanium dioxide by combination of experimental design and response surface approach, J. Hazard. Mater. 215–216 (2012) 302–310. https://doi.org/10.1016/j.jhazmat.2012.02.072.

[22] L. Han, S. Xue, S. Zhao, J. Yan, L. Qian, M. Chen, Biochar supported nanoscale iron particles for the efficient removal of methyl orange dye in aqueous solutions, PLoS One. 10 (2015) 1–15. https://doi.org/10.1371/journal.pone.0132067.

[23] D. Mirzaei, A. Zabardasti, Y. Mansourpanah, M. Sadeghi, S. Farhadi, Efficacy of Novel NaX/MgO–TiO2 Zeolite Nanocomposite for the Adsorption of Methyl Orange (MO) Dye: Isotherm, Kinetic and Thermodynamic Studies, J. Inorg. Organomet. Polym. Mater. 30 (2020) 2067–2080. https://doi.org/10.1007/s10904-019-01369-9.

[24] Z.X. Chen, X.Y. Jin, Z. Chen, M. Megharaj, R. Naidu, Removal of methyl orange from aqueous solution using bentonite-supported nanoscale zero-valent iron, J. Colloid Interface Sci. 363 (2011) 601–607. https://doi.org/10.1016/j.jcis.2011.07.057.

[25] E. Xingu-Contreras, G. García-Rosales, I. García-Sosa, A. Cabral-Prieto, Degradation of methyl orange using iron nanoparticles with/without support at different conditions, Microporous Mesoporous Mater. 292 (2020) 109782. https://doi.org/10.1016/j.micromeso.2019.109782.

[26] S. Arabi, M.R. Sohrabi, Removal of methylene blue, a basic dye, from aqueous solutions using nano-zerovalent iron, Water Sci. Technol. 70 (2014) 24–31. https://doi.org/10.2166/wst.2014.189.

[27] K. Badvi, V. Javanbakht, Enhanced photocatalytic degradation of dye contaminants with TiO2 immobilized on ZSM-5 zeolite modified with nickel nanoparticles, J. Clean. Prod. 280 (2021) 124518. https://doi.org/10.1016/j.jclepro.2020.124518.

[28] S. Zhu, X. Huang, D. Wang, L. Wang, F. Ma, Enhanced hexavalent chromium removal

performance and stabilization by magnetic iron nanoparticles assisted biochar in aqueous solution: Mechanisms and application potential, Chemosphere. 207 (2018) 50–59. https://doi.org/10.1016/j.chemosphere.2018.05.046.

[29] D. Fu, P.G. Keech, X. Sun, J.C. Wren, Iron oxyhydroxide nanoparticles formed by forced hydrolysis : dependence of phase composition on solution concentration, Phys. Chem. Chem. Phys. 13 (2011) 18523–18529. https://doi.org/10.1039/c1cp20188c.

[30] E. López-Fernández, C. Gómez-Sacedón, J. Gil-Rostra, J.P. Espinós, A.R. González-Elipe, F. Yubero, A. de Lucas-Consuegra, Ionomer-Free Nickel-Iron bimetallic electrodes for efficient anion exchange membrane water electrolysis, Chem. Eng. J. (2021) 133774. https://doi.org/10.1016/j.cej.2021.133774.

[31] Y. Yu, J. Peng, B. Liu, G. Chen, C. Srinivasakannan, Investigation on Preparation of Micro-Sized Hematite Powder from Hydrous Ferrous Sulfate Using Microwave and Conventional Heating, High Temp. Mater. Process. 32 (2013) 303–308. https://doi.org/10.1515/htmp-2012-0121.

[32] M. Rivero-Huguet, W.D. Marshall, Reduction of hexavalent chromium mediated by micro- and nano-sized mixed metallic particles, J. Hazard. Mater. 169 (2009) 1081–1087. https://doi.org/10.1016/j.jhazmat.2009.04.062.

[33] C. Jiao, Y. Cheng, W. Fan, J. Li, Synthesis of agar-stabilized nanoscale zero-valent iron particles and removal study of hexavalent chromium, Int. J. Environ. Sci. Technol. 12 (2015) 1603–1612. https://doi.org/10.1007/s13762-014-0524-0.

[34] B. Kakavandi, R.R. Kalantary, M. Farzadkia, A.H. Mahvi, A. Esrafili, A. Azari, A.R. Yari, A.B. Javid, Enhanced chromium (VI) removal using activated carbon modified by zero valent iron and silver bimetallic nanoparticles, J. Environ. Heal. Sci. Eng. 12 (2014) 1–10. https://doi.org/10.1186/s40201-014-0115-5.

[35] S. Li, T. You, Y. Guo, S. Yao, S. Zang, M. Xiao, Z. Zhang, Y. Shen, High dispersions of nano zero valent iron supported on biochar by one-step carbothermal synthesis and its application in chromate removal, RSC Adv. 9 (2019) 12428–12435. https://doi.org/10.1039/c9ra00304e.

[36] Y. He, J.F. Gao, F.Q. Feng, C. Liu, Y.Z. Peng, S.Y. Wang, The comparative study on the rapid decolorization of azo, anthraquinone and triphenylmethane dyes by zero-valent iron, Chem. Eng. J. 179 (2012) 8–18. https://doi.org/10.1016/j.cej.2011.05.107.

[37] P. Senthil Kumar, S.J. Varjani, S. Suganya, Treatment of dye wastewater using an ultrasonic aided nanoparticle stacked activated carbon: Kinetic and isotherm modelling, Bioresour. Technol. 250 (2018) 716–722. https://doi.org/10.1016/j.biortech.2017.11.097.

[38] P. Anju Rose Puthukkara, T. Sunil Jose, S. Dinoop lal, A.R. Puthukkara P, S. Jose T, D. lal S, Chitosan stabilized Fe/Ni bimetallic nanoparticles for the removal of cationic and anionic triphenylmethane dyes from water, Environ. Nanotechnology, Monit. Manag. 14 (2020) 100295. https://doi.org/10.1016/j.enmm.2020.100295.

[39] Y.H. Liou, S.L. Lo, C.J. Lin, W.H. Kuan, S.C. Weng, Chemical reduction of an unbuffered nitrate solution using catalyzed and uncatalyzed nanoscale iron particles, J. Hazard. Mater. 127 (2005) 102–110. https://doi.org/10.1016/j.jhazmat.2005.06.029.

[40] Y. Liu, G. V. Lowry, Effect of particle age (Fe0 content) and solution pH on NZVI reactivity: H2 evolution and TCE dechlorination, Environ. Sci. Technol. 40 (2006) 6085–6090. https://doi.org/10.1021/es060685o.

[41] A.D. Bokare, R.C. Chikate, C. V. Rode, K.M. Paknikar, Iron-nickel bimetallic nanoparticles for reductive degradation of azo dye Orange G in aqueous solution, Appl.

Catal. B Environ. 79 (2008) 270–278. https://doi.org/10.1016/j.apcatb.2007.10.033.

[42] Y.H. Liou, C.J. Lin, S.C. Weng, H.H. Ou, S.L. Lo, Selective decomposition of aqueous nitrate into nitrogen using iron deposited bimetals, Environ. Sci. Technol. 43 (2009) 2482–2488. https://doi.org/10.1021/es802498k.

[43] M.N. Morshed, N. Bouazizi, N. Behary, J. Guan, V. Nierstrasz, Stabilization of zero valent iron (Fe0) on plasma/dendrimer functionalized polyester fabrics for Fenton-like removal of hazardous water pollutants, Chem. Eng. J. 374 (2019) 658–673. https://doi.org/10.1016/j.cej.2019.05.162.

[44] A. Kumar, G. Sharma, M. Naushad, S. Thakur, SPION/β-cyclodextrin core-shell nanostructures for oil spill remediation and organic pollutant removal from waste water, Chem. Eng. J. 280 (2015) 175–187. https://doi.org/10.1016/j.cej.2015.05.126.

[45] Y. Ju, X. Liu, Z. Li, J. Kang, X. Wang, Y. Zhang, J. Fang, D.D. Dionysiou, Environmental application of millimetre-scale sponge iron (s-Fe0) particles (I): Pretreatment of cationic triphenylmethane dyes, J. Hazard. Mater. 283 (2015) 469–479. https://doi.org/10.1016/j.jhazmat.2014.09.051.

[46] L. Yong, G. Zhanqi, J. Yuefei, H. Xiaobin, S. Cheng, Y. Shaogui, W. Lianhong, W. Qingeng, F. Die, Photodegradation of malachite green under simulated and natural irradiation: Kinetics, products, and pathways, J. Hazard. Mater. 285 (2015) 127–136. https://doi.org/10.1016/j.jhazmat.2014.11.041.

[47] C. Berberidou, I. Poulios, N.P. Xekoukoulotakis, D. Mantzavinos, Sonolytic, photocatalytic and sonophotocatalytic degradation of malachite green in aqueous solutions, Appl. Catal. B Environ. 74 (2007) 63–72. https://doi.org/10.1016/j.apcatb.2007.01.013.

[48] G. Gao, A. Zhang, M. Zhang, J. Chen, Q. Zhang, Photocatalytic Degradation Mechanism of Malachite Green under Visible Light Irradiation over Novel Biomimetic Photocatalyst HMS-FePcs, Chinese J. Catal. 29 (2008) 426–430. https://doi.org/10.1016/S1872-2067(08)60043-1.

[49] G. Sharma, S. Bhogal, V.K. Gupta, S. Agarwal, A. Kumar, D. Pathania, G.T. Mola, F.J. Stadler, Algal biochar reinforced trimetallic nanocomposite as adsorptional/photocatalyst for remediation of malachite green from aqueous medium, J. Mol. Liq. 275 (2019) 499–509. https://doi.org/10.1016/j.molliq.2018.11.070.

[50] I. Owsik, B. Kolarz, The oxidation of hydroquinone to p-benzoquinone catalysed by Cu(II) ions immobilized on acrylic resins with aminoguanidyl groups: Part 1, J. Mol. Catal. A Chem. 178 (2002) 63–71. https://doi.org/10.1016/S1381-1169(01)00299-0.

CHAPTER 4

Synthesis of polymer stabilised Fe^0 and Fe/Ni bimetallic nanoparticles for the removal of Cr(VI) and triphenylmethane dyes from water

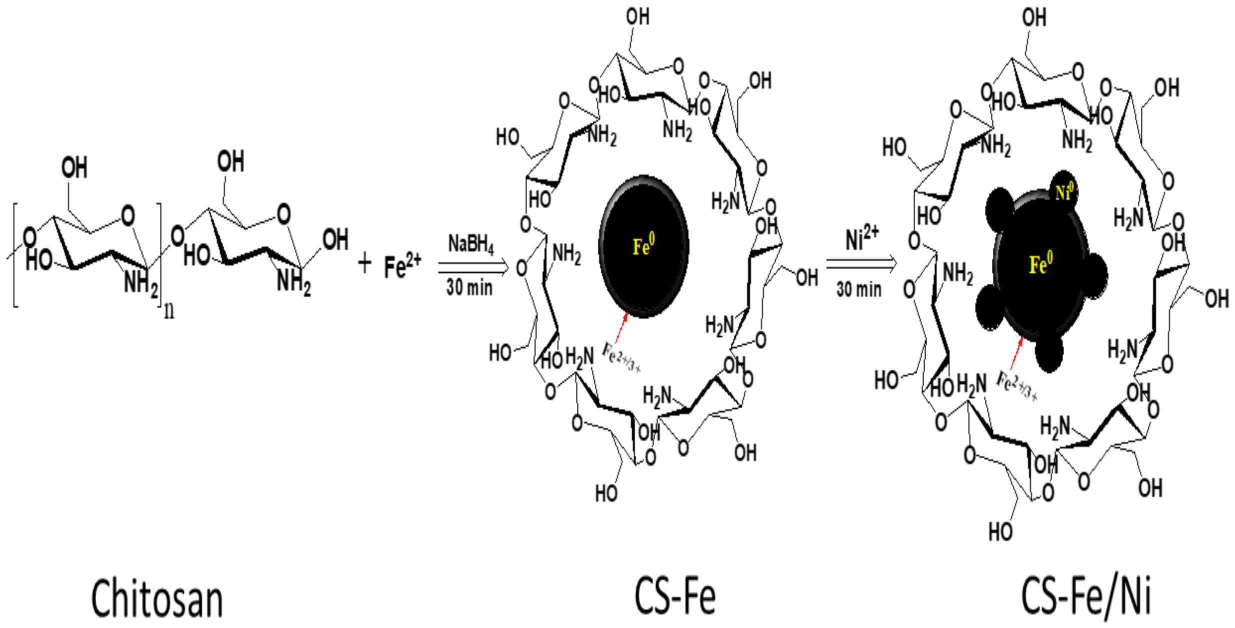

Chapter 4

Synthesis of polymer stabilised Fe^0 and Fe/Ni bimetallic nanoparticles for the removal of Cr(VI) and triphenylmethane dyes from water

4.1. Introduction

The zero valent iron (Fe^0) nanoparticles are considered a potential green material to remediate wastewater due to the availability of iron as recycled material and its capacity to degrade some contaminants completely. Even though Fe^0 nanoparticles show high reactivity towards pollutants, their major limitations are reactivity loss with time due to the precipitation of iron oxides on the surface of Fe^0 and their agglomeration tendency due to magnetic properties[1,2]. The addition of a second metal to the Fe^0 enhances the properties of zero valent iron through the synergetic effect of two distinct metals, which serves as a protective agent against corrosion of the iron surface. Till now, different iron-based bimetallic nanoparticles such as Fe/Al, Fe/Pd, Fe/Ni, Fe/Cu, Fe/Zn, Fe/Ag, Fe/Au, Fe/Co and Fe/Pt were synthesised and their catalytic elimination properties were studied in various pollutants[3,4]. Cost-effectiveness, efficiency, and toxic effect of second metal should be considered the three important criteria for selecting second metal regarding water pollution remediation. Among the synthesised bimetallic nanoparticles, Fe/Ni nanoparticles have special consideration because of their ability to enhance the formation of atomic hydrogen on the surface of Fe^0 and their ability to improve electron transfer between nanoparticles and pollutants. In addition, catalytic metal Ni is less toxic and economically feasible than other catalytic metals[5–8].

Although Fe^0 and Fe/Ni nanoparticles get considerable attention due to their high specific surface area and small size, the Fe^0 nanoparticles are highly reactive towards air and water. To develop the Fe^0 and Fe/Ni nanoparticles as an efficient remediating agent, they could be modified or combined with different methods. These methods are mostly immobilising Fe0 nanoparticles onto supports like zeolite, polymers, etc., and combining Fe^0 nanoparticles with other techniques like sonication and UV irradiation[9]. Even though the stabilisation of Fe^0 is extensively studied, further investigation is needed for the stabilisation of Fe^0 and Fe/Ni nanoparticles due to their potential capacity for water contaminant degradation and small footprint. This study incorporates chitosan, a biopolymer, with Fe^0 and Fe/Ni nanoparticles. Only limited studies have presently been reported on the stabilisation of Fe^0 nanoparticles by chitosan. Chitosan is a biopolymer produced by the deacetylation of chitin, derived from the exoskeleton of crustaceans and cartilages of molluscs. The presence of free amino and hydroxyl groups in chitosan makes them material with high adsorption potential and multipurpose materials in industrial applications. The other favourable characteristics of chitosan as an adsorbent are its macromolecular structure, non-toxicity, biocompatibility, biodegradability, low cost, etc.[10,11]. Previous studies of chitosan as a stabilising agent showed that it produces stabilised metallic (silver, gold, iron and platinum) nanoparticles with moderately average diameters[12,13].

In this work, we have synthesised chitosan-stabilised Fe^0 (CS-Fe) and chitosan-stabilised Fe/Ni (CS-Fe/Ni) nanoparticles by using chitosan as a stabilising agent for the removal of hexavalent chromium (Cr(VI)) and triphenylmethane dyes (malachite green and methyl blue). The properties of malachite green and methyl blue dyes have been discussed in chapter 3. We have investigated the influence of different parameters, such as the initial pollutant concentration, dosage of nanoparticles, contact time and pH of the solution in pollutant removal. We have also studied the effect of ionic strength of the solution in the removal of triphenylmethane dyes. Figure 4.1 represents malachite green (A) and methyl blue (B) chemical structure.

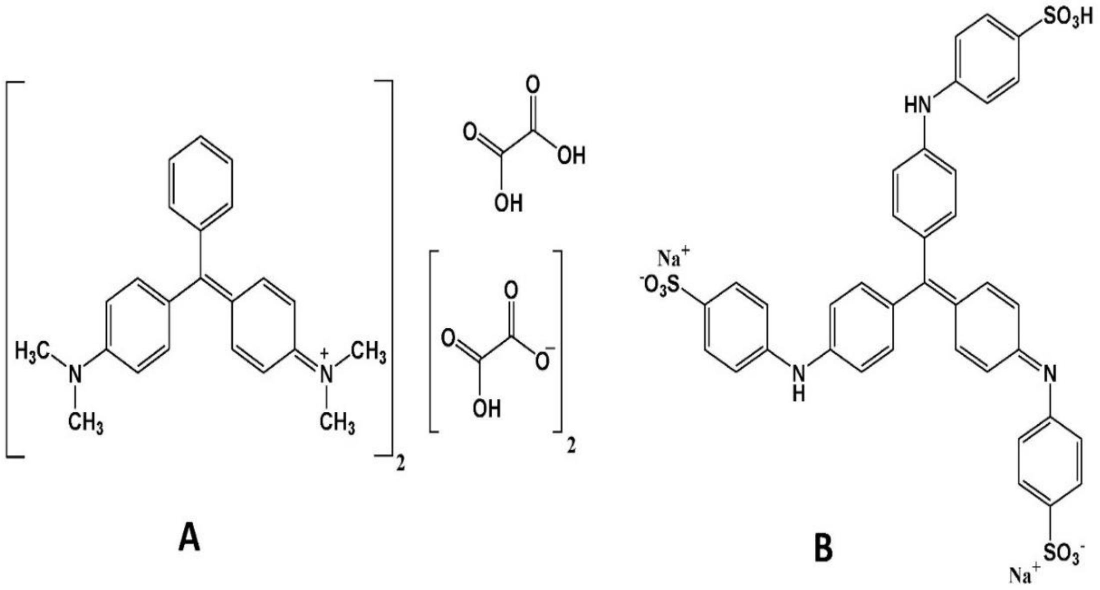

Figure 4.1 Chemical structure of Malachite Green (A) and Methyl Blue (B)

4.2. Experimental details

4.2.1 Synthesis of CS-Fe and CS-Fe/Ni nanoparticles

CS-Fe and CS-Fe/Ni nanoparticles were prepared using sodium borohydride as reducing agent[14,15]. Chitosan (0.5 %), the stabiliser used to synthesise CS-Fe and CS-Fe/Ni nanoparticles, was dissolved in dilute acetic acid using ultrasonication. $FeCl_3.6H_2O$ (0.973 g) was prepared in 50 mL deionised water to synthesise CS-Fe nanoparticles. The prepared $FeCl_3.6H_2O$ solution was incorporated with the dissolved chitosan solution in a round bottom flask under the nitrogen atmosphere. The mixture was stirred for 15 minutes using a magnetic stirrer and 50 mL of $NaBH_4$ (0.544 g) solution prepared in an ethanol-water system was added drop by drop into this mixture and stirred vigorously and continuously for 30 minutes. The formation of the black coloured precipitate indicates the presence of CS-Fe. The formation reaction of CS-Fe is represented in equation (4.1).

$$CS + Fe^{2+} + 2BH_4^- + 6H_2O \rightarrow CS - Fe^0 + 2B(OH)_3 + 7H_2O \qquad (4.1)$$

The method for synthesis of CS-Fe/Ni nanonoparticles was similar to that of chitosan stabilised Fe nanoparticles, except that the $NiSO_4.6H_2O$ solution was added to the prepared nanoparticles. $NiSO_4.6H_2O$ (0.089 g) solution was prepared in 10 mL deionised water added to freshly prepared CS-Fe solution and agitated for another 30 minutes. This would lead to the formation of CS-Fe/Ni nanoparticles depicted by equation (4.2). The prepared nanoparticles were collected through vacuum filtration and the nanoparticles were rinsed with deionised water, absolute ethanol and acetone successively. The prepared nanoparticles were lyophilised and stored in a sealed bottle.

$$CS - Fe_x^0 + yNi^{2+} \rightarrow CS - Fe_{x-y}^0 Ni^0 + Fe^{2+} \qquad (4.2)$$

4.2.2 Batch experiments

Cr(VI) removal studies

The details of batch experiments followed for Cr(VI) removal were discussed in chapter 2. Different parameters examined in this study for Cr(VI) removal were nanoparticle dosage (1-5 g/L), initial concentration of Cr(VI) (1-7 mg/L), initial pH of the solution (3-9) and contact time (15-60 min). The pH of the solution has been adjusted using 1.0 M NaOH and 1.0 M H_2SO_4. All experiments were performed with a duplicate.

Dye removal studies

The method followed for the batch experiments of dye removal were already given in chapter 3. Various parameters investigated in the present study are nanoparticle dosage (0.5-2 g/L), initial concentration of dye (50-150 mg/L), initial pH of the solution (4-12), contact time (60-180 min) and ionic strength of the solution (0.001-0.1 M). To study the influence of ionic strength, 20 mL of NaCl solution was added to 40 mL of 50 mg/L dye solution and the concentration of the NaCl was varied from 0.001 M to 0.1 M. The samples were analysed for the residual dye concentration using a UV-visible spectrophotometer and the experiments were performed with a duplicate.

4.2.3 Characterisation and analytical techniques used

The prepared nanoparticles were lyophilised using Operon FDU 7003 lyophiliser. The particle size and morphology of the CS-Fe and CS-Fe/Ni nanoparticles were analysed using HRTEM, XPS and FTIR. Details of characterisation techniques are discussed in chapter 2. In this case, the FTIR spectra of CS, CS-Fe and CS-Fe/Ni nanoparticles before and after the reaction with dyes were investigated through Fourier transform infrared spectrometer (SHIMADZU IR Affinity-1) in the wavelength range of 4000 – 600 cm^{-1}. Samples for FTIR analysis were prepared by mixing KBr with the samples and pressed into small thin pellets. The degradation products of MG dye using CS-Fe/Ni nanoparticles was analysed by GC-MS/MS and the procedure followed for GC-MS/MS analysis was discussed in chapter 3.

4.3. Results and discussion

4.3.1 Characterisation of CS, CS-Fe and CS-Fe/Ni nanoparticles

HRTEM

The transmission electron micrographs of the CS-Fe/Ni and CS-Fe, as shown in figure 4.2, revealed that a layer of grey material covered the spherical metallic nanoparticle. This indicates the core-shell structure of the nanoparticle. As chitosan was used as a stabiliser, it was concluded that the Fe^0 nanoparticle would have been coated with a layer of chitosan as the shell. By randomly counting around 50 nanoparticles in the HRTEM photograph, the CS-Fe and CS-Fe/Ni nanoparticles' average diameter was estimated as 14.87 nm and 9.2 nm respectively, with a metallic core of 9.73 nm and 5.57 nm. It is believed that the chitosan reduced the agglomeration tendency of nanoparticles that arose from the magnetic property of iron nanoparticles and protects the iron nanoparticle from oxidation by binding Fe^0 with hydroxyl and amine groups of the chitosan[16].

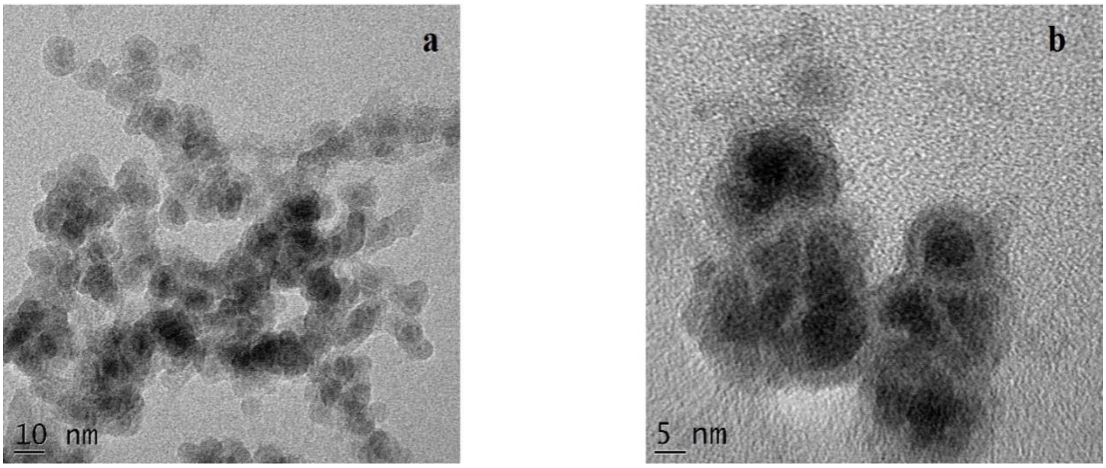

Figure 4.2 *HRTEM image of (a) CS-Fe/Ni and (b) CS-Fe nanoparticles*

XPS

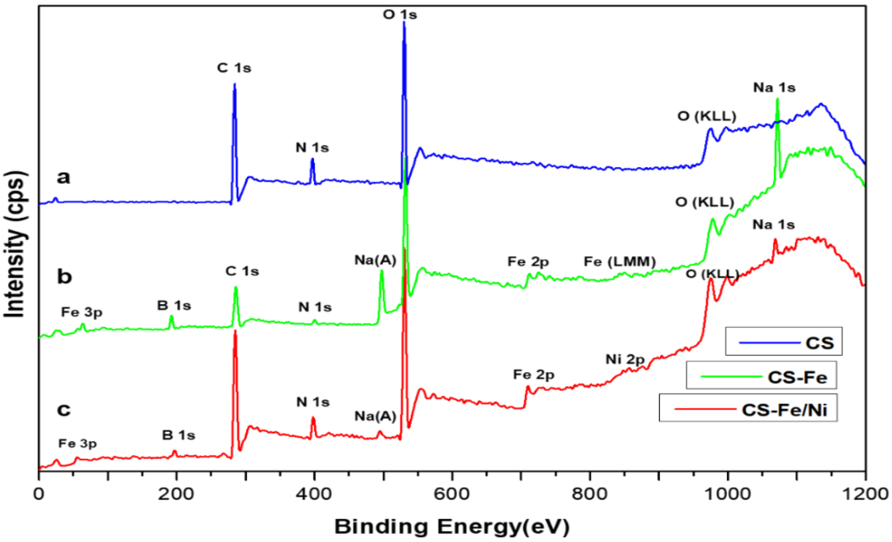

Figure 4.3 *XPS wide scan survey of (a) CS (b) CS-Fe and (c) CS-Fe/Ni nanoparticles*

The composition of the nanoparticles and oxidation states of elements in the nanoparticles were analysed by X-ray photoelectron spectroscopy (XPS). Being a surface analysing technique, XPS can investigate only up to 5-10 nm depth of the sample[17]. XPS wide scan spectra of CS, CS-Fe and CS-Fe/Ni are shown in Figure 4.3. From these spectra, it was evident that C, N, O, Fe and Ni were mainly present in CS-Fe/Ni nanoparticles. They also contained small amounts of elements B and Na, which were the reaction residues from the preparation of nanoparticles. Compared with the parent CS, the main difference between CS-Fe/Ni and CS-Fe were the emergence of peaks corresponding to the binding energy of Fe and Ni in CS-Fe/Ni and that of Fe in CS-Fe nanoparticles. Even though N 1s was more predominant in CS, a decrease in intensity of N 1s was observed for CS-Fe and CS-Fe/Ni and this may be due to the complexation of N 1s with iron nanoparticles.

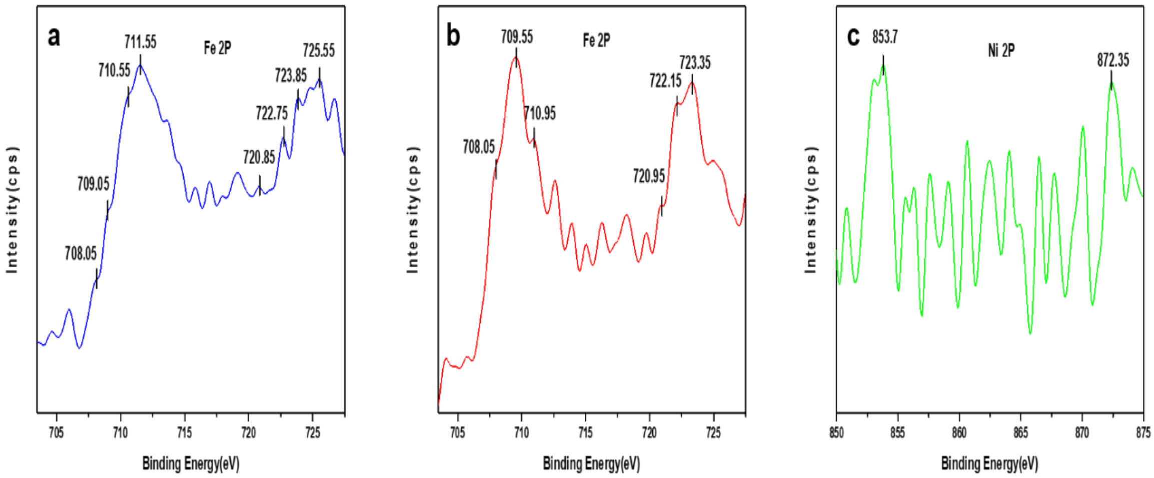

Figure 4.4 *Detailed XPS spectra of (a) Fe 2P in CS-Fe (b) Fe 2p and (c) Ni 2P in CS-Fe/Ni nanoparticles*

A comparison of Fe 2P spectra of CS-Fe and CS-Fe/Ni nanoparticles and Ni 2P spectra of CS-Fe/Ni nanoparticles are shown in figure 4.4. The existence of zero valent iron was confirmed by peaks at around 708.05 eV and 720.95 eV, which corresponds to the $2p^{3/2}$ and $2p^{1/2}$ binding energies of Fe^0 in CS-Fe/Ni nanoparticles[18,19]. The predominant photoelectron peak of CS-Fe/Ni at 709.55 eV and 722.15 eV matched with the binding energies of $2p^{3/2}$ and $2p^{1/2}$ of Fe^{2+} in FeO[20]. The results revealed that the CS-Fe/Ni nanoparticles were covered with a thin iron oxide shell, mainly FeO. The detailed Fe 2P spectrum on the CS-Fe nanoparticles mainly consists of Fe^{3+} species, indicated by the major peak around 711.55 eV and 725.55 eV, which belonged to the binding energies of $2p^{3/2}$ and $2p^{1/2}$ of Fe^{3+} respectively[16]. Compared with the CS-Fe/Ni, the intensity of peaks around 708.05 eV and 720.85 eV was less in CS-Fe, which indicated that more metallic iron was oxidised in CS-Fe. The Fe^{3+} species in samples may be due to the presence of FeO(OH), Fe_3O_4, Fe_2O_3 or Fe^{3+}–chitosan complex. The oxidation of iron that occurred during the detection process might have resulted in the high intensity of the Fe^{3+} peaks in the samples. The Ni 2P detailed spectra in CS-Fe/Ni was complex due to the interaction between iron and chitosan. The peak at 853.7 eV and 872.35 eV corresponds to the $2p^{3/2}$ and $2p^{1/2}$ binding energies of Ni^{2+} respectively in CS-Fe/Ni nanoparticles[21]. This may be due to the oxidation of Ni on the surface of Fe^0.

4.3.2 Cr(VI) removal studies

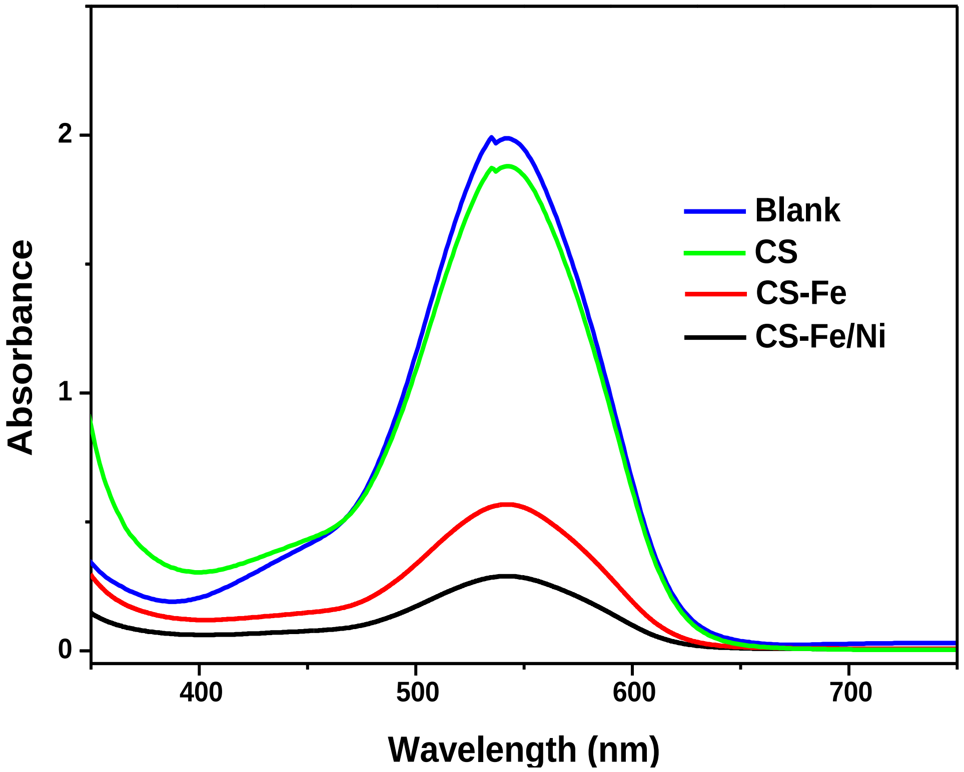

Figure 4.5 *UV-visible spectra of Cr(VI) after treating CS, CS-Fe and CS-Fe/Ni nanoparticles*

Figure 4.5 shows the UV-visible spectra of Cr(VI) treated using CS, CS-Fe and CS-Fe/Ni nanoparticles. The results show that the highest removal efficiency was exhibited by CS-Fe/Ni nanoparticles, followed by CS-Fe nanoparticles and the lowest by chitosan. The high removal efficiency could be due to the small particle size of the CS-Fe/Ni nanoparticles since chitosan on the surface of the nanoparticles causes the electrostatic or steric repulsion, thereby preventing the aggregation of the nanoparticles[22]. In addition to this, previous studies indicate that chitosan has a high tendency to chelate with Fe^{3+} using free amino groups and hydroxyl groups present in them, inhibiting the Fe^{3+}- Cr^{3+} precipitation on the surface of CS-Fe/Ni nanoparticles. It is important since the formation of Fe^{3+}- Cr^{3+} oxide/hydroxide precipitates can inhibit the electron transfer from Fe^0 to Cr(VI), thereby decreasing the Cr(VI) removal efficiency[23]. The better removal efficiency of CS-Fe/Ni nanoparticles compared to CS-Fe nanoparticles could be due to the galvanic effect of Ni. These results match with our previous assumption discussed in chapter 3. Bimetallisation of Fe^0 nanoparticles improves iron-based nanoparticles' reactivity through better electron transfer via catalytic metal Ni. In the same way, chitosan stabilised bimetallic Fe/Ni nanoparticles have superior removal efficiency than chitosan stabilised Fe nanoparticles. The amino and hydroxyl functional groups present in the chitosan itself show little Cr(VI) removal efficiency through adsorption via electrostatic attraction[24].

Effect of the nanoparticle dosage

Figure 4.6a shows the effect of nanoparticle dosage on the removal of Cr(VI) using CS, CS-Fe and CS-Fe/Ni nanoparticles by keeping the initial concentration of Cr(VI) (5 mg/L) and contact time (30 min) as constant. The nanoparticle dosage varies from 1 to 5 g/L. CS-Fe/Ni nanoparticles showed 95 % removal efficiency at a dosage of 5 g/L of the nanoparticle. However, CS-Fe and chitosan show only 81 % and 25 % removal efficiency at the same dosage. As the dosage of nanoparticles increases, the availability of active surface area and reactive sites also increases and more Cr(VI) removal occurs.

Effect of the initial concentration of Cr(VI)

As discussed previously, a fixed quantity of nanoparticles only removes a specific amount of Cr(VI). This study also shows a similar increase in Cr(VI) removal efficiency when the initial Cr(VI) concentration diminishes from 7 mg/L to 1 mg/L. The nanoparticle dosage (4 g/L) and contact time (30 minutes) were kept constant. Figure 4.6b shows the effect of the initial concentration of Cr(VI) in removing Cr(VI) using prepared nanoparticles, maintaining all other parameters as constant. The highest removal efficiency was observed in 1 mg/L Cr(VI) solution and the lowest removal efficiency in 7 mg/L Cr(VI) solution. The decreasing order of Cr(VI) removal efficiency by nanoparticle were CS-Fe/Ni > CS-Fe > CS. The formation of Fe^{3+}-Cr^{3+}precipitate on the surface of nanoparticles suppresses further reduction of Cr(VI). In higher Cr(VI) concentration, Fe^{3+}- Cr^{3+}precipitate was formed more fastly than lower Cr(VI) concentration.

Effect of contact time

Figure 4.6c displays the effect of contact time on the removal of Cr(VI) using prepared nanoparticles. CS does not show significant removal efficiency after 30 minutes. However, in the case of CS-Fe and CS-Fe/Ni nanoparticles, they are active upto 45 minutes and after that there is drastic reduction in the removal efficiency and reaches a plateau. Cr(VI) removal efficiency of CS, CS-Fe and CS-Fe/Ni nanoparticle were 17 %, 92 % and 93 %

respectively at 45 minutes. With the increase in contact time, the pH of the solution increases due to the reactive removal utilisation of H^+ ions during iron corrosion. This also causes a drop in the Cr(VI) removal.

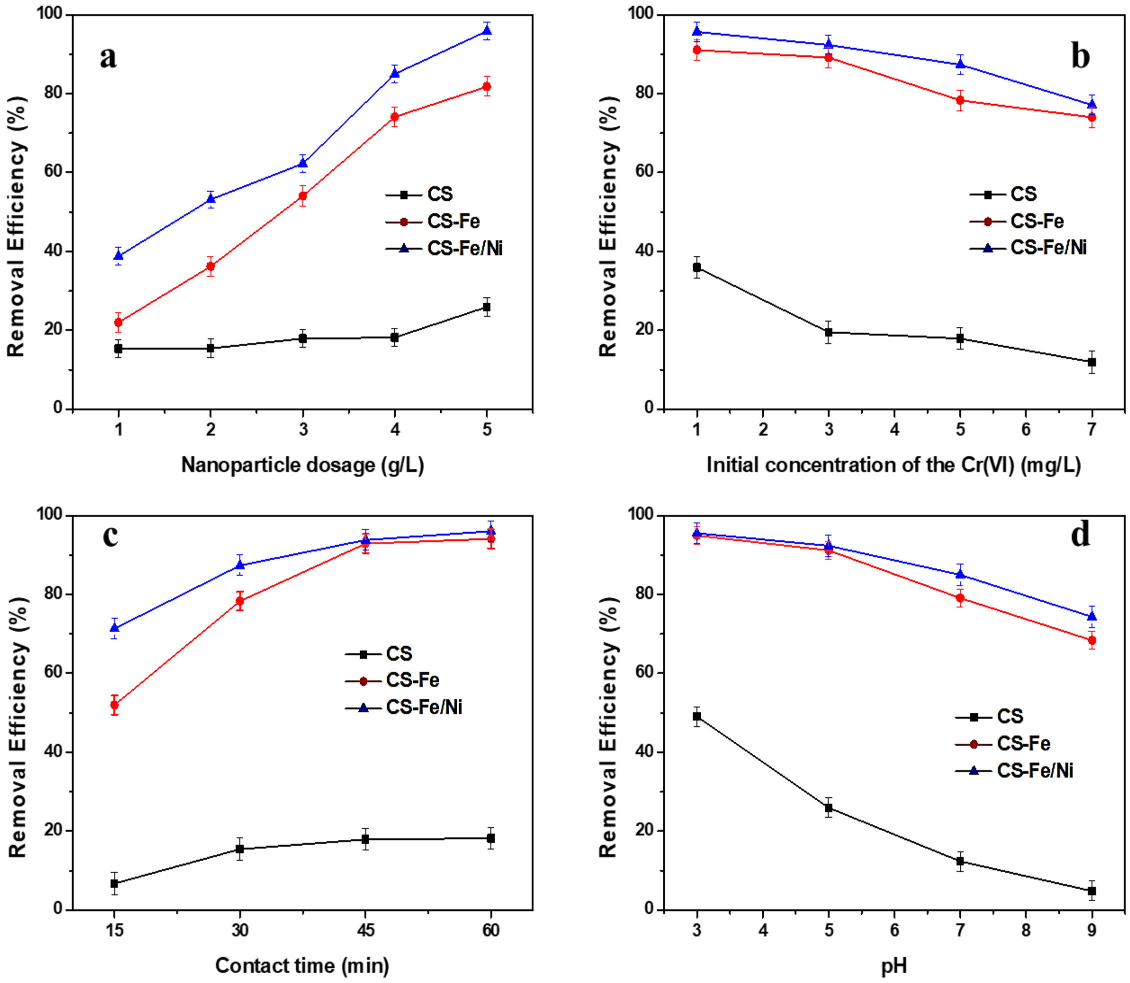

***Figure 4.6** (a) Effect of nanoparticle dosage,(b)Effect of initial concentration of Cr(VI), (c) Effect of contact time and (d) Effect of pH in Cr(VI) removal using CS, CS-Fe and CS-Fe/Ni nanoparticles*

Effect of pH

The effect of pH on removing Cr(VI) (figure 4.6d) was studied using prepared nanoparticles while keeping nanoparticle dosage (4 g/L), initial Cr(VI) concentration (5 mg/L) and contact time were kept constant. The results show that the lower pH of the solution has better removal efficiency than the higher pH. Interestingly, CS exhibits 49 % removal efficiency at pH 3, which may be due to the electrostatic attraction between positively charged chitosan (due to the protonation of amino groups) and Cr(VI) oxyanions. With the increase in pH of the solution, electrostatic repulsion occurs due to OH^- ions and decreases the Cr(VI) removal efficiency. In this case, CS-Fe/Ni nanoparticles obtained the highest removal efficiency compared to CS and CS-Fe nanoparticles. Even in CS-Fe and CS-Fe/Ni nanoparticles, more removal efficiency was obtained at lower solution pH. Coupled with adsorptive elimination by chitosan, the destruction of iron oxide shell at lower pH also played a critical role in Cr(VI) removal.

4.3.3 Dye removal studies

UV-visible spectroscopy

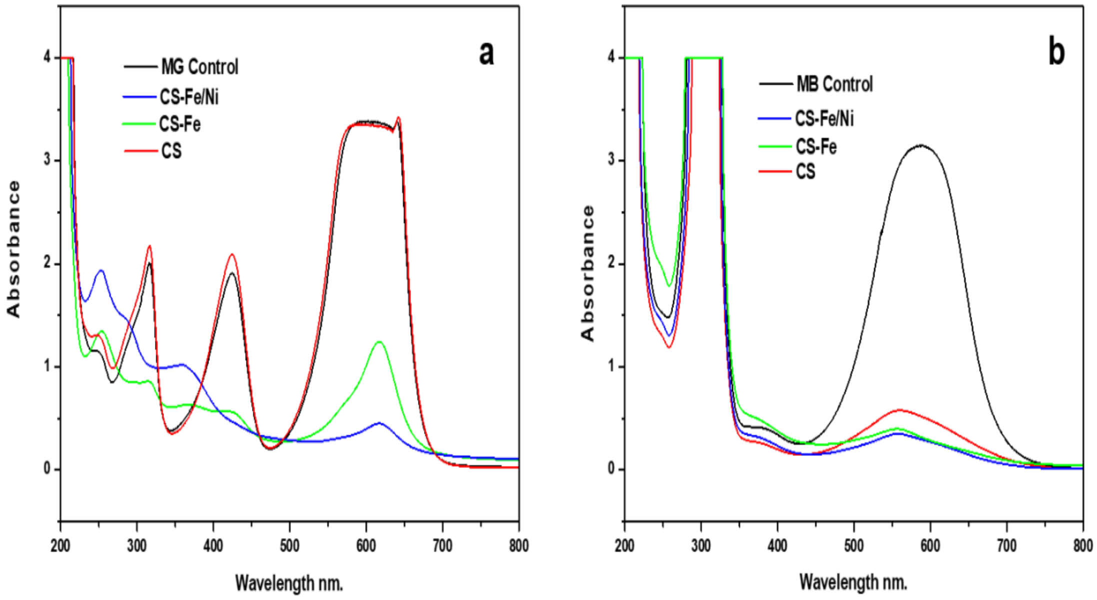

Figure 4.7 *UV-Visible spectra of (a) MG and (b) MB dye removal using CS, CS-Fe and CS-Fe/Ni nanoparticles*

The MG and MB dye removal efficiency were studied using CS, CS-Fe and CS-Fe/Ni nanoparticles through UV-visible spectroscopy as shown in figure 4.7. The disappearance of MG characteristic peaks and emergence of new peaks after adding CS-Fe and CS-Fe/Ni nanoparticles indicate that MG removal was through degradation and adsorption, which is matched with our previous assumption discussed in chapter 3. Dye solution containing CS-Fe and CS-Fe/Ni nanoparticles show high removal efficiency within 60 minutes and the chitosan does not significantly influence the degradation of MG[29]. For the removal of MB, the CS, CS-Fe and CS-Fe/Ni nanoparticles showed high dye decolourisation efficiency, which could be due to its better adsorptive capacity. The characteristic peak of MB observed at 595 nm[30] shifted towards a lower wavelength due to the change in the pH of the dye solution. No new peaks emerged as a consequence of MB dye removal using CS, CS-Fe and CS-Fe/Ni nanoparticles which indicated that the removal of MB occurred primarily through the adsorption process and even after degradation, the degraded products also adsorbed onto the prepared nanoparticles.

The dye removal mechanism of prepared nanoparticles and chitosan was through degradation catalysed by Fe^0 and adsorption caused by iron oxide shell and chitosan. The Fe^0 nanoparticles destroy the chromophoric conjugation of the dye molecule not only through direct electron transfer but also through the production of atomic hydrogen[29]. Ni on the surface of Fe^0 acted as a catalyst which facilitated atomic hydrogen production and enabled the electron transfer through the iron oxide shell. This stimulated the Fe/Ni nanoparticle for a greater dye removal efficiency[31]. In addition, oxidative removal also played an important role in dye removal when using iron-based nanoparticles. As a stabiliser, chitosan protects the iron nanoparticles and increases the interaction between Fe^0 and dye and shows a synergetic effect on the dye removal. In this study, CS-Fe/Ni nanoparticles showed a higher dye removal efficiency than the CS-Fe nanoparticles, consistent with the previous assumptions[15].

FTIR spectroscopy

The FTIR spectrum of CS, CS-Fe and CS-Fe/Ni nanoparticles is shown in figure 4.8. The FTIR measurements were carried out to determine the possible interactions between the metallic nanoparticle and chitosan. A broad overlapping band of OH stretching and N-H stretching of amine in chitosan was observed in the region centred at 3354 cm^{-1}. The absorption band at 2875 cm^{-1} is attributed to the C-H stretching vibrations. The absorption appeared at 1643 cm^{-1} corresponds to the C=O stretching of amide. The N-H bending vibration of the 1^0 amines was displayed by the absorption peak at 1539 cm^{-1}. The band at 1377 cm^{-1} corresponds to the bending vibrations of O-H and deformation of $-CH_3$ and $-CH_2$. The absorption peak observed at 1051 cm^{-1} could be due to the stretching vibrations of C-O in 1^0 alcohol/C-O-C/C-N of 1^0 amine. The peak at 893 cm^{-1} corresponds to the bending vibrations of =CH and $=CH_2$[15,16,32].

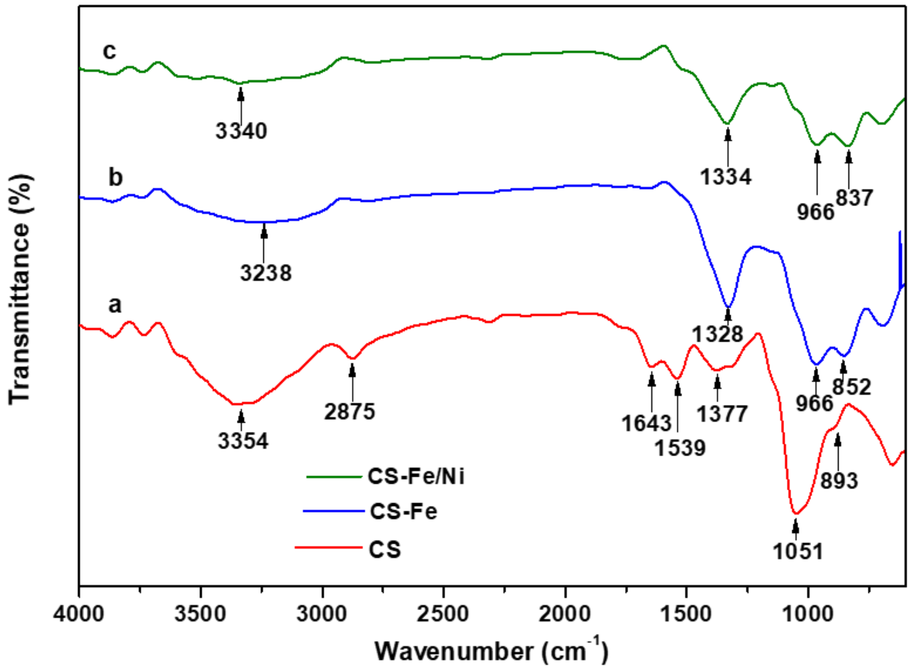

Figure 4.8 *FTIR spectra of (a) CS (b) CS-Fe and (c) CS-Fe/Ni nanoparticles*

The FTIR spectrum of CS-Fe and CS-Fe/Ni was different from that of the chitosan. The broad bands corresponding to O-H and N-H stretching of amine in chitosan was weakened and shifted to lower wavenumber in CS-Fe and CS-Fe/Ni. This may be due to the interaction of iron nanoparticles with these groups of chitosan. In addition to that, the intensity of peaks at 2875, 1643 and 1539 cm^{-1} decreased entirely and peaks at 1377, 1051 and 893 cm^{-1} shifted to lower wave number. From these results, it could be concluded that the iron interacted with amine and hydroxyl functional groups of chitosan, which proved to be a versatile stabiliser for zero valent iron. The addition of the second metal, Ni, possessed less significant changes in the FTIR spectra of CS-Fe/Ni compared with CS-Fe. This may be due to the low percentage of Ni in CS-Fe/Ni nanoparticles[15,32].

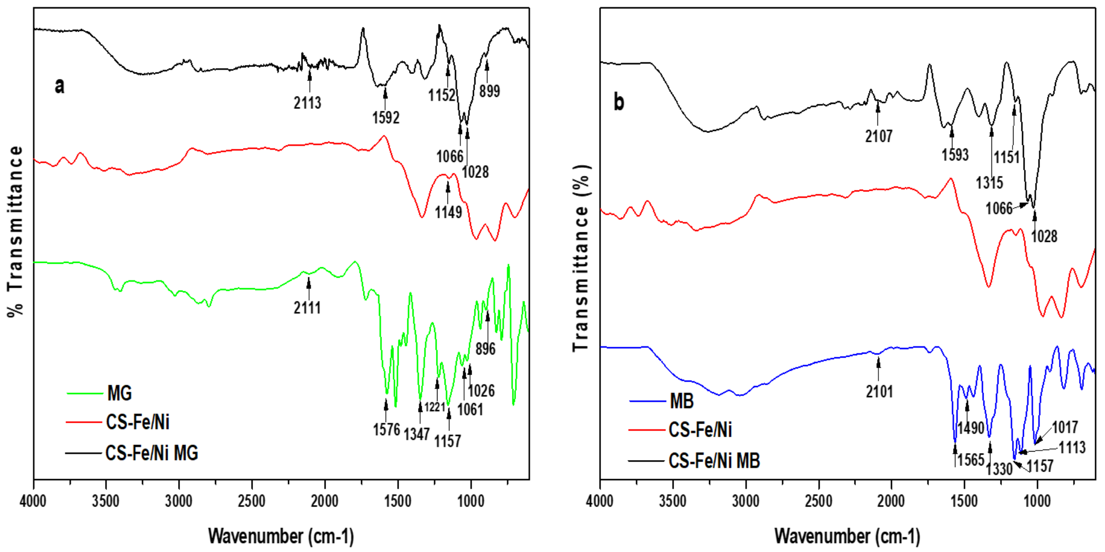

Figure 4.9 *FTIR spectra of CS-Fe/Ni nanoparticles after the removal of (a) MG and (b)MB*

FTIR spectra of CS, CS-Fe and CS-Fe/Ni nanoparticles showed remarkable changes after reacting with MB and MG dyes. The pattern of the fingerprint region changed due to the interaction between the prepared nanoparticles and dyes. Figure 4.9 (a,b) shows the FTIR spectra of CS-Fe/Ni nanoparticles after reacting with MG and MB dyes respectively. In the case of parent MG dye, the specific peaks in the fingerprint region (500-1500 cm^{-1}) match the mono-substituted and para-disubstituted benzene rings due to the C=C stretching of the benzene ring seen at 1576 cm^{-1}. MG also showed peaks at 1157 cm^{-1} and 1221 cm^{-1} corresponding to C-N stretching vibrations[33]. The peaks of parent MG dye are also seen in CS-Fe/Ni nanoparticles after reacting with MG. Some of the bands of MG get vanish, which indicates the destruction of the structure of MG in CS-Fe/Ni nanoparticles. The CS-Fe/Ni nanoparticles showed a similar peak of C=C stretching at 1592 cm^{-1}. The absence of peaks between 850–670 cm^{-1} supports the total disappearance of some aromatic rings of MG on reaction with the prepared nanoparticles. The peaks at 1221 cm^{-1} and 1347 cm^{-1} correspond to the C-N stretching whereas C-H bending was absent in the CS-Fe/Ni nanoparticles after the reaction[34].

In the case of parent MB, the peak at the 1565 cm^{-1} corresponds to N-H stretching vibration and the bands at 1113-1490 cm^{-1} belong to the framework vibration of benzene rings. The peak observed at 1017 cm^{-1} can be assigned to the S=O stretching vibrations[35]. FTIR spectra of CS-Fe/Ni nanoparticles after treating with MB showed similar peaks of parent MB dye, indicating that some of the MB molecules are adsorbed onto the CS-Fe/Ni nanoparticles. The MB peaks seen in CS-Fe/Ni nanoparticles exhibited a shift to lower wave number with the absence of few peaks. This suggests the destruction of the methyl blue structure by CS-Fe/Ni nanoparticles.

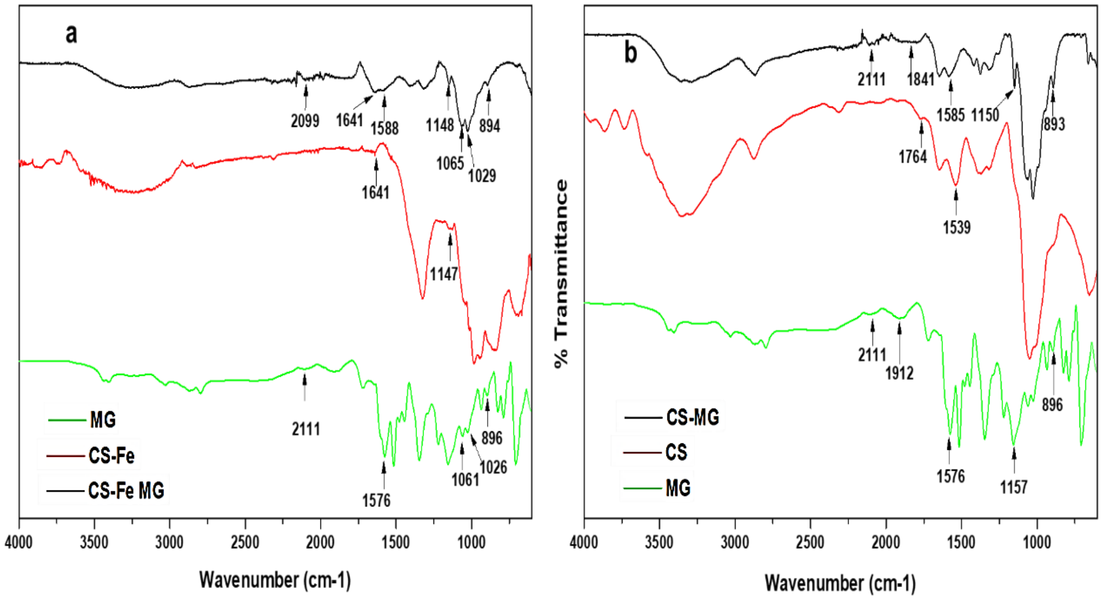

Figure 4.10 *FTIR spectra of CS-Fe (a) and CS (b) after treating with MG*

Figure 4.10 represents the FTIR spectra of CS-Fe (a) and CS (b) after MG dye removal and figure 4.11 corresponds to the FTIR spectra of CS-Fe (a) and CS (b) after MB dye removal. FTIR spectra of CS-Fe and CS nanoparticles after treating with MG/MB dyes showed a similar pattern of changes as CS-Fe/Ni nanoparticles. The spectra of CS, showed better similarity to parent MG/MB dye compared to that of CS-Fe and CS-Fe/Ni nanoparticles. This indicates that the removal of MG/MB by CS is mainly through adsorption.

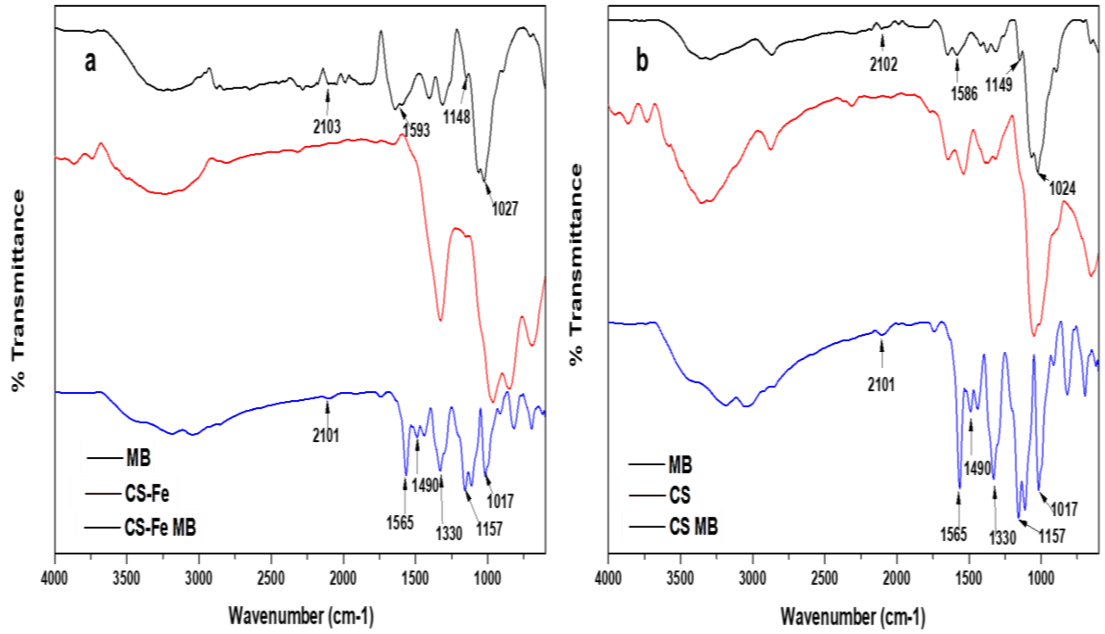

Figure 4.11 *FTIR spectra of CS-Fe (a) and CS (b) after treating with MB*

Effect of parameters on the removal of MG and MB

Effect of the initial concentration

The effect of the initial concentration of MG and MB dye was investigated in 20 mL of different dye concentrations ranging from 50 to 150 mg/L by using 2 g/L of CS, CS-Fe and CS-Fe/Ni nanoparticles, as shown in figure 4.12. The highest removal efficiencies of CS, CS-Fe and CS-Fe/Ni nanoparticles were 19 %, 88 % and 94 % respectively for MG and 74 %, 83 % and 85 % for MB at 50 mg/L of dye solution. The removal efficiencies seemed to be decreasing with an increase in the initial concentration of the dyes. The extensive percentage removal of MG by CS-Fe and CS-Fe/Ni is through a complex heterogeneous reaction greatly influenced by adsorptive and degradative pathways exhibited by Fe and chitosan. However, the removal of MB is primarily through the adsorption of prepared nanoparticles and chitosan. Degradation may take place on the adsorbed dye molecules. With the increase in dye concentration, the extent of adsorption also increases, but since the increase in dye molecules with concentration overwhelmed the percentage of dye molecules adsorbed, the overall effect is a decrease in dye removal efficiency with an increase in dye concentration.

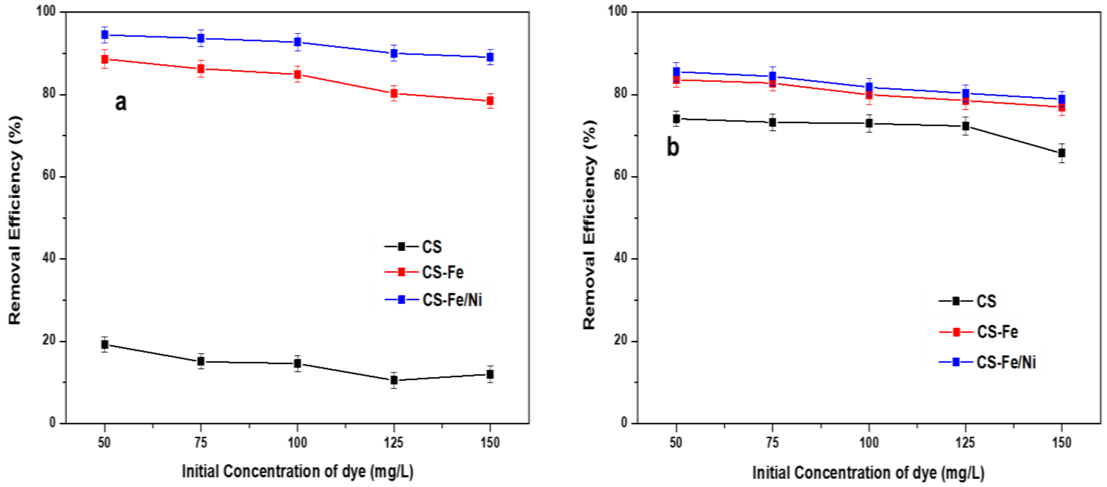

Figure 4.12 *Effect of initial dye concentration on dye removal (a) MG and (b) MB*

Effect of dosage of nanoparticles

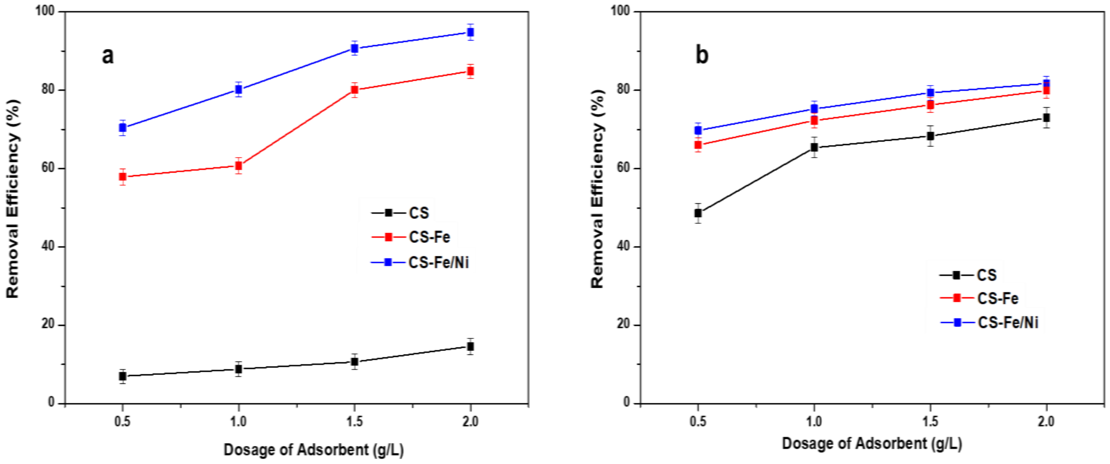

Figure 4.13 *Effect of dosage of nanoparticle in dye removal (a) MG and (b) MB*

The effect of nanoparticle dosage was studied in 4 different nanoparticle dosages, 0.5 g/L, 1 g/L, 1.5 g/L and 2 g/L of 50 mg/L of 40 mL dye solution as shown in figure 4.13. The highest removal efficiency, 94 % for MG and 82 % for MB, were seen in CS-Fe/Ni at 2 g/L. These results highlighted that the increase in dosage of CS-Fe and CS-Fe/Ni nanoparticles boosted the removal efficiency of MG and MB to a large extent. This was similar to the previous studies of dye removal using iron nanoparticles[36]. In the case of MB, chitosan also showed a high removal efficiency due to the adsorptive property of chitosan as a cationic polymer[37]. It is a well-known fact that the dye removal efficiency was greatly influenced by the concentration of available active reactive sites of Fe[30]. The increase in dosage of CS-Fe and CS-Fe/Ni nanoparticles with a small particles size would increase the total surface adsorptive sites available for dye degradation and adsorption, which eventually lead to a higher dye removal efficiency of MG and MB.

Effect of contact time

Figure 4.14 illustrates the effect of contact time on MG and MB dye removal at 50 mg/L of dye solution of 40 mL using 2 g/L of the nanoparticle. The removal efficiency of MG and MB dyes has been studied at 3 different time intervals of 60,120,180 minutes. 99 % and 88 % dye removal for MG and MB respectively were obtained by CS-Fe/Ni nanoparticles within 180 minutes. The results show that the first 60 minutes exhibit a greater removal efficiency for MG and MB dye in CS-Fe and CS-Fe/Ni nanoparticles. The chitosan showed 77 % dye removal for MB in 180 minutes. This may be primarily due to the presence of tremendous empty active sites on the surface of Fe and chitosan. As the dye molecules were adsorbed onto the Fe surface and chitosan, the availability of active adsorptive sites decreased gradually leading to decrease in the removal efficiency rate in MG and MB dye with contact time.

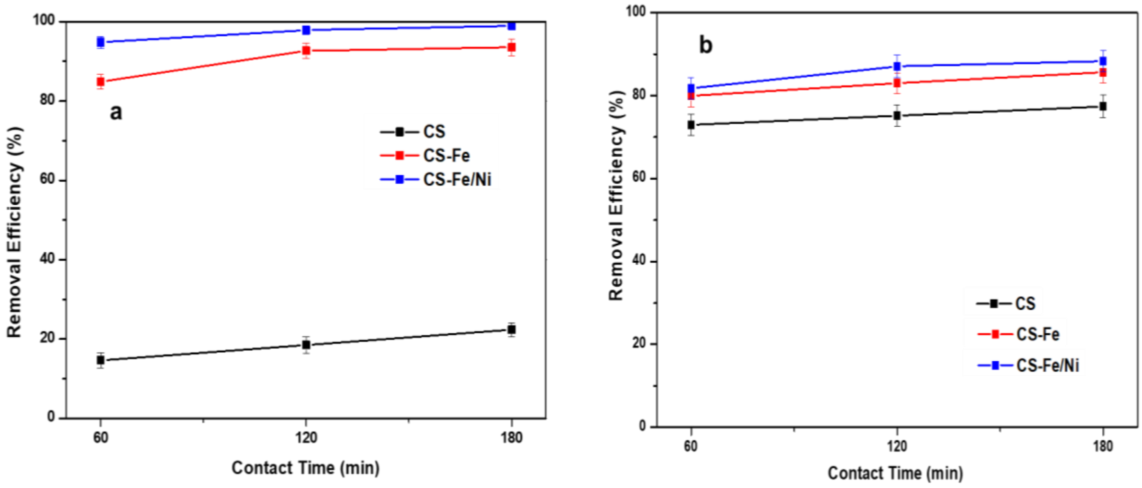

Figure 4.14 *Effect of contact time in (a) MG and (b) MB dye removal*

Effect of PH

The influence of pH on the MG and MB dye removal was studied at pH 4, pH 8 and pH 12 of 50 mg/L dye solution as shown in figure 4.15. The colour fading of triphenylmethane dyes with increased pH is due to the hydroxide ion attack on the central C atom of the planar ring system, thereby removing the conjugation[38]. The dye removal studies reveal that the highest removal efficiency for MG and MB occurred in acidic pH with 89 % dye removal for both MG and MB. The removal of MB and MG dye decreased with the increase in pH of the solution. This is attributed to the hydroxide precipitation at the surface of iron nanoparticles at alkaline pH[39] which eventually leads to a decrease in the reactivity of CS-Fe and CS-Fe/Ni nanoparticles. From the above observations, it could also be concluded that simple adsorption takes place at higher pH. As the pH decreases, the depletion of the iron oxide shell and solubilisation of chitosan take place, exposing the inner Fe^0 core. Due to this, degradation takes place in addition to adsorption[40]. This leads to the more availability of iron nanoparticles for adsorption and degradation.

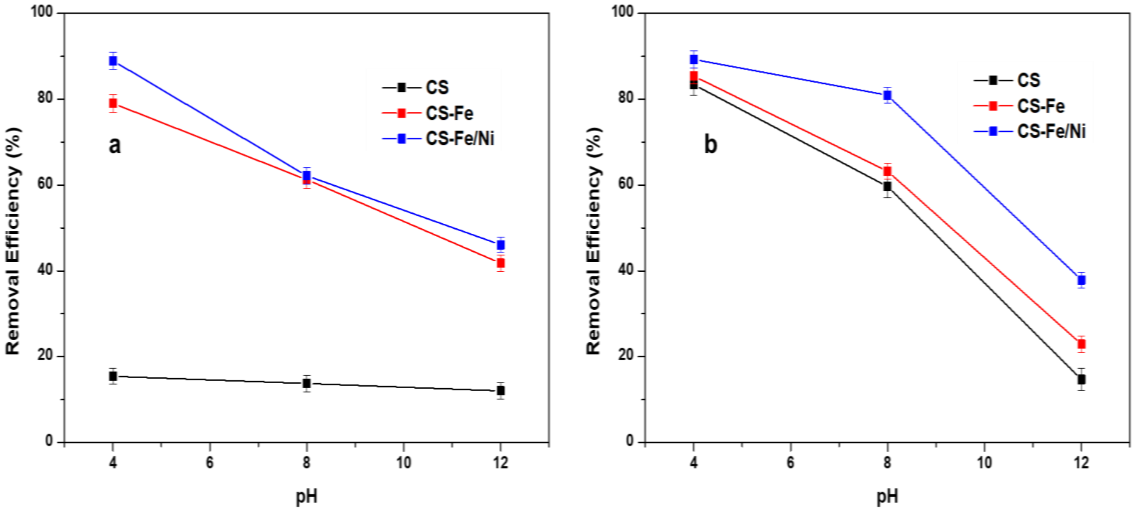

Figure 4.15 *Effect of pH in (a) MG and (b) MB dye removal*

Effect of Ionic Strength

The effect of ionic strength was studied by adding NaCl to the dye solution as shown in figure 4.16. The influence of ionic strength is studied in three different NaCl concentrations of 0.001 M, 0.01 M and 0.1 M. The introduction of the NaCl solution to the iron nanoparticles makes multiple effects on dye removal. When the NaCl concentration increases, the iron oxide shell drains away by reacting with the chloride ion. This will rejuvenate the Fe^0 surface and enhance dye degradation to a large extent. The results show that the introduction of NaCl has a negligible effect on MB adsorption with increasing ionic strength. These results indicate that the negatively charged Cl^- ions form a wall around the CS-Fe/Ni particles. Due to this, the methylene blue molecules cannot reach the nanoparticle surface, which eventually decreases its decolourisation[42]. In the case of MG, there is no significant decrease in dye removal with increasing ionic strength.

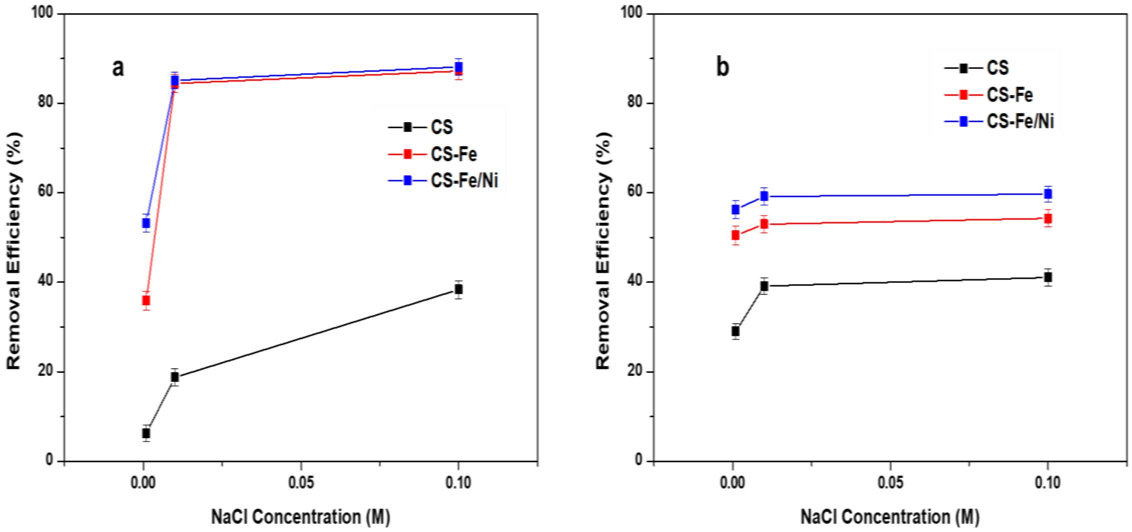

Figure 4.16 *Effect of ionic strength in (a) MG and (b) MB dye removal*

GC-MS/MS analysis

The GC-MS/MS analysis of MG dye after treating with CS-Fe/Ni nanoparticles has confirmed the degradation of MG dye molecules. GC-MS/MS analysis identified 4 degradation products such as (a) cyclohexa-2,5-diene-1,4-dione (MW 108), (b) diphenyl methanone (MW 182), (c) 4-nitrophenol (MW 139) and (d) 4-dimethylaminodiphenyl methane (MW 211) using the NIST library. Among the 4 identified degradation products, 4-nitrophenol and 4-dimethylaminodiphenylmethane were not detected in MG/Fe^0 system (chapter 3). The mass spectra of newly identified degradation products 4-nitrophenol (Rt 11.92) and 4-dimethylaminodiphenylmethane (Rt 22.91) are shown in figure 4.17(a & b) respectively. As displayed in scheme 4.1, the formation of 4-nitrophenol (a2) could result from the demethylation and OH addition reaction followed by oxidation of N,N-dimethylaniline (a) created during the degradation of MG dye molecules[45,46]. However, the formation of 4-dimethylaminodiphenylmethane (b2) could result from the hydrogenation of [4-(dimethylamino)phenyl]-phenylmethanone (b) in the presence of nickel as a catalyst since the deposition of CS-Fe with Ni improved the production of molecular hydrogen[47]. There were also some other chromatographic peaks in the spectrum which were not identified positively.

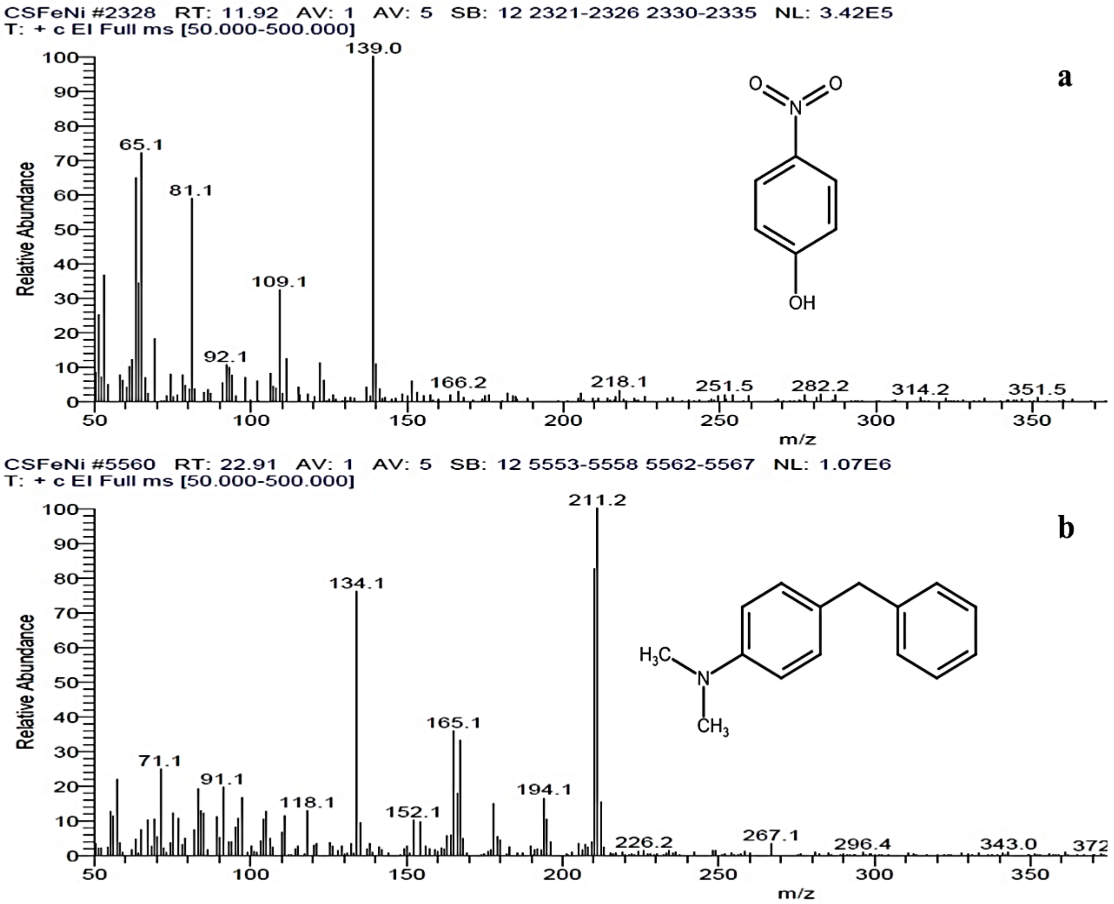

Figure 4.17 *Mass spectra of MG degradation products identified by GC-MS/MS analysis a) 4-nitrophenol and b) 4-dimethylaminodiphenylmethane*.

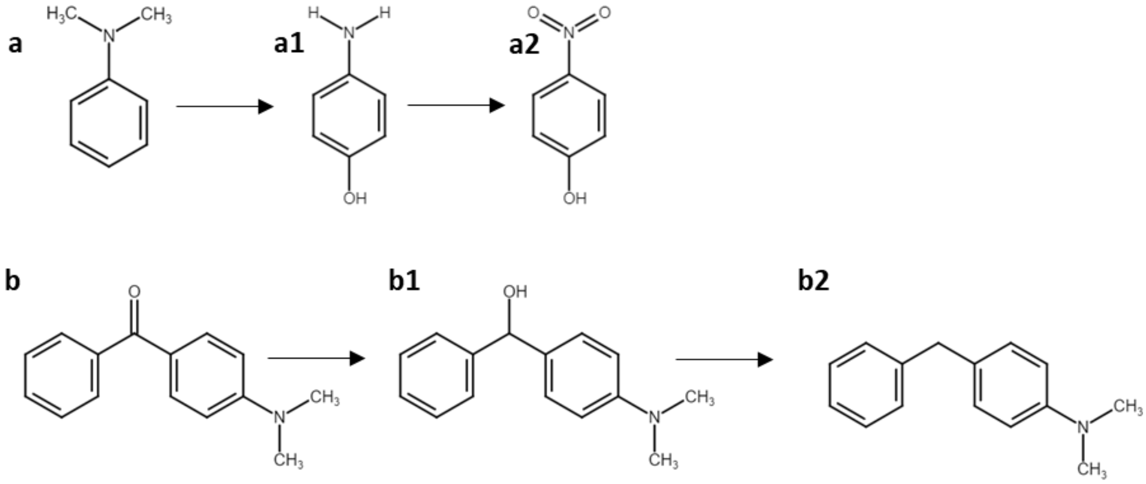

Scheme 4.1 *Degradation pathways of MG using CS-Fe/Ni nanoparticle*

4.4. Conclusions

The bimetallic Fe/Ni nanoparticles stabilised on the biopolymer chitosan (CS-Fe/Ni) established efficient Cr(VI) and dye removal compared with monometallic Fe stabilised on chitosan (CS-Fe) and the stabiliser chitosan (CS) alone. CS-Fe/Ni nanoparticles showed higher removal efficiency for hexavalent chromium. The cationic polymer, CS, also exhibited a high removal efficiency for anionic dye MB, which corresponded to the adsorptive property of the chitosan. The greater Cr(VI) and dye removal efficiency of CS-Fe/Ni nanoparticles were attributed to the small size of prepared nanoparticles and catalytic property of second metal Ni. The prepared nanoparticles displayed the effect of different parameters in the removal process of Cr(VI) and dye. The low pH of the solution was a favourable condition for the high pollutant removal efficiency of prepared nanoparticles. In general, the prepared CS-Fe/Ni nanoparticles were found more suitable for removing Cr(VI) and triphenylmethane dyes.

4.5. References

[1] T. Raychoudhury, T. Scheytt, Potential of Zerovalent iron nanoparticles for remediation of environmental organic contaminants in water: A review, Water Sci. Technol. 68 (2013) 1425–1439. https://doi.org/10.2166/wst.2013.358.

[2] B.D. Yirsaw, M. Megharaj, Z. Chen, R. Naidu, Environmental application and ecological significance of nano-zero valent iron, J. Environ. Sci. (China). 44 (2016) 88–98. https://doi.org/10.1016/j.jes.2015.07.016.

[3] W.J. Liu, T.T. Qian, H. Jiang, Bimetallic Fe nanoparticles: Recent advances in synthesis and application in catalytic elimination of environmental pollutants, Chem. Eng. J. 236 (2014) 448–463. https://doi.org/10.1016/j.cej.2013.10.062.

[4] G. Sharma, A. Kumar, S. Sharma, M. Naushad, R. Prakash Dwivedi, Z.A. ALOthman, G.T. Mola, Novel development of nanoparticles to bimetallic nanoparticles and their composites: A review, J. King Saud Univ. - Sci. 31 (2019) 257–269. https://doi.org/10.1016/j.jksus.2017.06.012.

[5] N. Ezzatahmadi, D.L. Marshall, K. Hou, G.A. Ayoko, G.J. Millar, Y. Xi, Simultaneous adsorption and degradation of 2,4-dichlorophenol on sepiolite-supported bimetallic Fe/Ni nanoparticles, J. Environ. Chem. Eng. 7 (2019) 102955. https://doi.org/10.1016/j.jece.2019.102955.

[6] S.L. Foster, K. Estoque, M. Voecks, N. Rentz, L.F. Greenlee, Removal of synthetic azo dye using bimetallic nickel-iron nanoparticles, J. Nanomater. 2019 (2019). https://doi.org/10.1155/2019/9807605.

[7] X. Weng, Z.Z. Chen, Z.Z. Chen, M. Megharaj, R. Naidu, Clay supported bimetallic Fe/Ni nanoparticles used for reductive degradation of amoxicillin in aqueous solution: Characterisation and kinetics, Colloids Surfaces A Physicochem. Eng. Asp. 443 (2014) 404–409. https://doi.org/10.1016/j.colsurfa.2013.11.047.

[8] Y. Gao, F. Wang, Y. Wu, R. Naidu, Z. Chen, Comparison of degradation mechanisms of microcystin-LR using nanoscale zero-valent iron (nZVI) and bimetallic Fe/Ni and Fe/Pd

nanoparticles, Chem. Eng. J. 285 (2016) 459–466. https://doi.org/10.1016/j.cej.2015.09.078.

[9] J. Adusei-Gyamfi, V. Acha, Carriers for nano zerovalent iron (nZVI): Synthesis, application and efficiency, RSC Adv. 6 (2016) 91025–91044. https://doi.org/10.1039/c6ra16657a.

[10] A. Pestov, S. Bratskaya, Chitosan and its derivatives as highly efficient polymer ligands, Molecules. 21 (2016). https://doi.org/10.3390/molecules21030330.

[11] S. Islam, M.A.R. Bhuiyan, M.N. Islam, Chitin and Chitosan: Structure, Properties and Applications in Biomedical Engineering, J. Polym. Environ. 25 (2017) 854–866. https://doi.org/10.1007/s10924-016-0865-5.

[12] H. Huang, Q. Yuan, X. Yang, Preparation and characterisation of metal-chitosan nanocomposites, Colloids Surfaces B Biointerfaces. 39 (2004) 31–37. https://doi.org/10.1016/j.colsurfb.2004.08.014.

[13] M. Ahmadi, M. Foladivanda, N. Jaafarzadeh, Z. Ramezani, B. Ramavandi, S. Jorfi, B. Kakavandi, Synthesis of chitosan zero-valent iron nanoparticles-supported for cadmium removal: Characterisation, optimisation and modeling approach, J. Water Supply Res. Technol. - AQUA. 66 (2017) 116–130. https://doi.org/10.2166/aqua.2017.027.

[14] A.A. Gonçalves, A.F. Araújo, M.J.M. Pires, R.M. Verly, D.V. Franco, L.M. Da Silva, Synthesis of chitosan-stabilised iron and nickel nanoparticles and the application in the reductive degradation of nimesulide, Eclet. Quim. 43 (2018) 10–25. https://doi.org/10.26850/1678-4618eqj.v43.1.10-25.

[15] X. Weng, S. Lin, Y. Zhong, Z. Chen, Chitosan stabilised bimetallic Fe/Ni nanoparticles used to remove mixed contaminants-amoxicillin and Cd (II) from aqueous solutions, Chem. Eng. J. 229 (2013) 27–34. https://doi.org/10.1016/j.cej.2013.05.096.

[16] B. Geng, Z. Jin, T. Li, X. Qi, Preparation of chitosan-stabilised Fe0 nanoparticles for removal of hexavalent chromium in water, Sci. Total Environ. 407 (2009) 4994–5000. https://doi.org/10.1016/j.scitotenv.2009.05.051.

[17] S.J. Gerber, E. Erasmus, Electronic effects of metal hexacyanoferrates: An XPS and FTIR study, Mater. Chem. Phys. 203 (2018) 73–81. https://doi.org/10.1016/j.matchemphys.2017.09.029.

[18] B. Desalegn, M. Megharaj, Z. Chen, R. Naidu, Green synthesis of zero valent iron nanoparticle using mango peel extract and surface characterisation using XPS and GC-MS, Heliyon. 5 (2019) e01750. https://doi.org/10.1016/j.heliyon.2019.e01750.

[19] Y. Momose, K. Tsuruya, T. Sakurai, K. Nakayama, Photoelectron emission and XPS studies of real iron surfaces subjected to scratching in air, water, and organic liquids, Surf. Interface Anal. 48 (2016) 202–211. https://doi.org/10.1002/sia.5942.

[20] Y. Xie, Y. Yi, Y. Qin, L. Wang, G. Liu, Y. Wu, Z. Diao, T. Zhou, M. Xu, Perchlorate degradation in aqueous solution using chitosan-stabilised zero-valent iron nanoparticles, Sep. Purif. Technol. 171 (2016) 164–173. https://doi.org/10.1016/j.seppur.2016.07.023.

[21] W. Huang, S. Ding, Y. Chen, W. Hao, X. Lai, J. Peng, J. Tu, Y. Cao, X. Li, 3D NiO hollow sphere/reduced graphene oxide composite for high-performance glucose biosensor, Sci. Rep. 7 (2017) 1–11. https://doi.org/10.1038/s41598-017-05528-1.

[22] G. Kurlyandskaya, L. Litvinova, A. Safronov, V. Schupletsova, I. Tyukova, O. Khaziakhmatova, G. Slepchenko, K. Yurova, E. Cherempey, N. Kulesh, R. Andrade, I. Beketov, I. Khlusov, Water-Based Suspensions of Iron Oxide Nanoparticles with Electrostatic or Steric Stabilisation by Chitosan: Fabrication, Characterisation and

Biocompatibility, Sensors. 17 (2017) 2605. https://doi.org/10.3390/s17112605.

[23] T. Liu, L. Zhao, D. Sun, X. Tan, Entrapment of nanoscale zero-valent iron in chitosan beads for hexavalent chromium removal from wastewater, J. Hazard. Mater. 184 (2010) 724–730. https://doi.org/10.1016/j.jhazmat.2010.08.099.

[24] P. Udaybhaskar, L. Iyengar, A.V.S.P. Rao, Hexavalent chromium interaction with chitosan, J. Appl. Polym. Sci. 39 (1990) 739–747. https://doi.org/10.1002/app.1990.070390322.

[25] C. Jiao, Y. Cheng, W. Fan, J. Li, Synthesis of agar-stabilised nanoscale zero-valent iron particles and removal study of hexavalent chromium, Int. J. Environ. Sci. Technol. 12 (2015) 1603–1612. https://doi.org/10.1007/s13762-014-0524-0.

[26] B. Kakavandi, R.R. Kalantary, M. Farzadkia, A.H. Mahvi, A. Esrafili, A. Azari, A.R. Yari, A.B. Javid, Enhanced chromium (VI) removal using activated carbon modified by zero valent iron and silver bimetallic nanoparticles, J. Environ. Heal. Sci. Eng. 12 (2014) 1–10. https://doi.org/10.1186/s40201-014-0115-5.

[27] S. Li, T. You, Y. Guo, S. Yao, S. Zang, M. Xiao, Z. Zhang, Y. Shen, High dispersions of nano zero valent iron supported on biochar by one-step carbothermal synthesis and its application in chromate removal, RSC Adv. 9 (2019) 12428–12435. https://doi.org/10.1039/c9ra00304e.

[28] M. Rivero-Huguet, W.D. Marshall, Reduction of hexavalent chromium mediated by micro- and nano-sized mixed metallic particles, J. Hazard. Mater. 169 (2009) 1081–1087. https://doi.org/10.1016/j.jhazmat.2009.04.062.

[29] Y. He, J.F. Gao, F.Q. Feng, C. Liu, Y.Z. Peng, S.Y. Wang, The comparative study on the rapid decolorisation of azo, anthraquinone and triphenylmethane dyes by zero-valent iron, Chem. Eng. J. 179 (2012) 8–18. https://doi.org/10.1016/j.cej.2011.05.107.

[30] X. Wang, P. Wang, J. Ma, H. Liu, P. Ning, Synthesis, characterisation, and reactivity of cellulose modified nano zero-valent iron for dye discoloration, Appl. Surf. Sci. 345 (2015) 57–66. https://doi.org/10.1016/j.apsusc.2015.03.131.

[31] A.D. Bokare, R.C. Chikate, C. V. Rode, K.M. Paknikar, Iron-nickel bimetallic nanoparticles for reductive degradation of azo dye Orange G in aqueous solution, Appl. Catal. B Environ. 79 (2008) 270–278. https://doi.org/10.1016/j.apcatb.2007.10.033.

[32] D. Jiang, D. Huang, C. Lai, P. Xu, G. Zeng, J. Wan, L. Tang, H. Dong, B. Huang, T. Hu, Difunctional chitosan-stabilized Fe/Cu bimetallic nanoparticles for removal of hexavalent chromium wastewater, Sci. Total Environ. 644 (2018) 1181–1189. https://doi.org/10.1016/j.scitotenv.2018.06.367.

[33] T. Bhagavathi Pushpa, J. Vijayaraghavan, S.J. Sardhar Basha, V. Sekaran, K. Vijayaraghavan, J. Jegan, Investigation on removal of malachite green using EM based compost as adsorbent, Ecotoxicol. Environ. Saf. 118 (2015) 177–182. https://doi.org/10.1016/j.ecoenv.2015.04.033.

[34] P. Raizada, P. Singh, A. Kumar, B. Pare, S.B. Jonnalagadda, Zero valent iron-brick grain nanocomposite for enhanced solar-Fenton removal of malachite green, Sep. Purif. Technol. 133 (2014) 429–437. https://doi.org/10.1016/j.seppur.2014.07.012.

[35] X. Yang, Z. Wang, M. Jing, R. Liu, F. Song, X. Shen, Magnetic nanocomposite Ba-ferrite/α-iron hollow microfiber: A multifunctional 1D space platform for dyes removal and microwave absorption, Ceram. Int. 40 (2014) 15585–15594. https://doi.org/10.1016/j.ceramint.2014.07.035.

[36] J. Guo, R. Wang, W.W. Tjiu, J. Pan, T. Liu, Synthesis of Fe nanoparticles@graphene composites for environmental applications, J. Hazard. Mater. 225–226 (2012) 63–73.

https://doi.org/10.1016/j.jhazmat.2012.04.065.

[37] S.-H. Lin, C.-P. Chang, J.-C. Chang, K. Mammel, Comparison of Dye Adsorption of Three Forms of Chitosan, Adv. Chem. Eng. Sci. 04 (2014) 319–326. https://doi.org/10.4236/aces.2014.43035.

[38] D.F. Latona, A.O. Dada, Kinetics of Reaction between Malachite Green and Hydroxyl Ion in the Presence of Reducing Sugars, J. Chem. Chem. Sci. 6 (2016) 1021–1028.

[39] L. Huang, F. Luo, Z. Chen, M. Megharaj, R. Naidu, Green synthesised conditions impacting on the reactivity of Fe NPs for the degradation of malachite green, Spectrochim. Acta - Part A Mol. Biomol. Spectrosc. 137 (2015) 154–159. https://doi.org/10.1016/j.saa.2014.08.116.

[40] F.S. Freyria, S. Esposito, M. Armandi, F. Deorsola, E. Garrone, B. Bonelli, Role of pH in the aqueous phase reactivity of zerovalent iron nanoparticles with acid orange 7, a model molecule of azo dyes, J. Nanomater. 2017 (2017). https://doi.org/10.1155/2017/2749575.

[41] T.S. Anirudhan, M. Ramachandran, Surfactant-modified bentonite as adsorbent for the removal of humic acid from wastewaters, Appl. Clay Sci. 35 (2007) 276–281. https://doi.org/10.1016/j.clay.2006.09.009.

[42] C. Sahoo, A.K. Gupta, Photocatalytic degradation of methyl blue by silver ion-doped titania: Identification of degradation products by GC-MS and IC analysis, J. Environ. Sci. Heal. - Part A Toxic/Hazardous Subst. Environ. Eng. 50 (2015) 1333–1341. https://doi.org/10.1080/10934529.2015.1059107.

[43] P. Yu, H. Yu, Q. Sun, B. Ma, Filter paper supported nZVI for continuous treatment of simulated dyeing wastewater, Sci. Rep. 9 (2019) 1–8. https://doi.org/10.1038/s41598-019-47863-5.

[44] N. Sleiman, V. Deluchat, M. Wazne, M. Mallet, A. Courtin-Nomade, V. Kazpard, M. Baudu, Phosphate removal from aqueous solutions using zero valent iron (ZVI): Influence of solution composition and ZVI aging, Colloids Surfaces A Physicochem. Eng. Asp. 514 (2017) 1–10. https://doi.org/10.1016/j.colsurfa.2016.11.014.

[45] C. Berberidou, I. Poulios, N.P. Xekoukoulotakis, D. Mantzavinos, Sonolytic, photocatalytic and sonophotocatalytic degradation of malachite green in aqueous solutions, Appl. Catal. B Environ. 74 (2007) 63–72. https://doi.org/10.1016/j.apcatb.2007.01.013.

[46] S. Singh, S.L. Lo, V.C. Srivastava, A.D. Hiwarkar, Comparative study of electrochemical oxidation for dye degradation: Parametric optimisation and mechanism identification, J. Environ. Chem. Eng. 4 (2016) 2911–2921. https://doi.org/10.1016/j.jece.2016.05.036.

[47] G. Bai, L. Niu, Z. Zhao, N. Li, F. Li, M. Qiu, F. He, G. Chen, Z. Ma, Ni–La–B amorphous alloys supported on SiO2 and γ-Al2O3 for selective hydrogenation of benzophenone, J. Mol. Catal. A Chem. 363–364 (2012) 411–416. https://doi.org/10.1016/j.molcata.2012.07.018.

CHAPTER 5

TiO_2-zeolite composite modified Fe^0 nanoparticles for the removal of Cr(VI) and malachite green dye from water

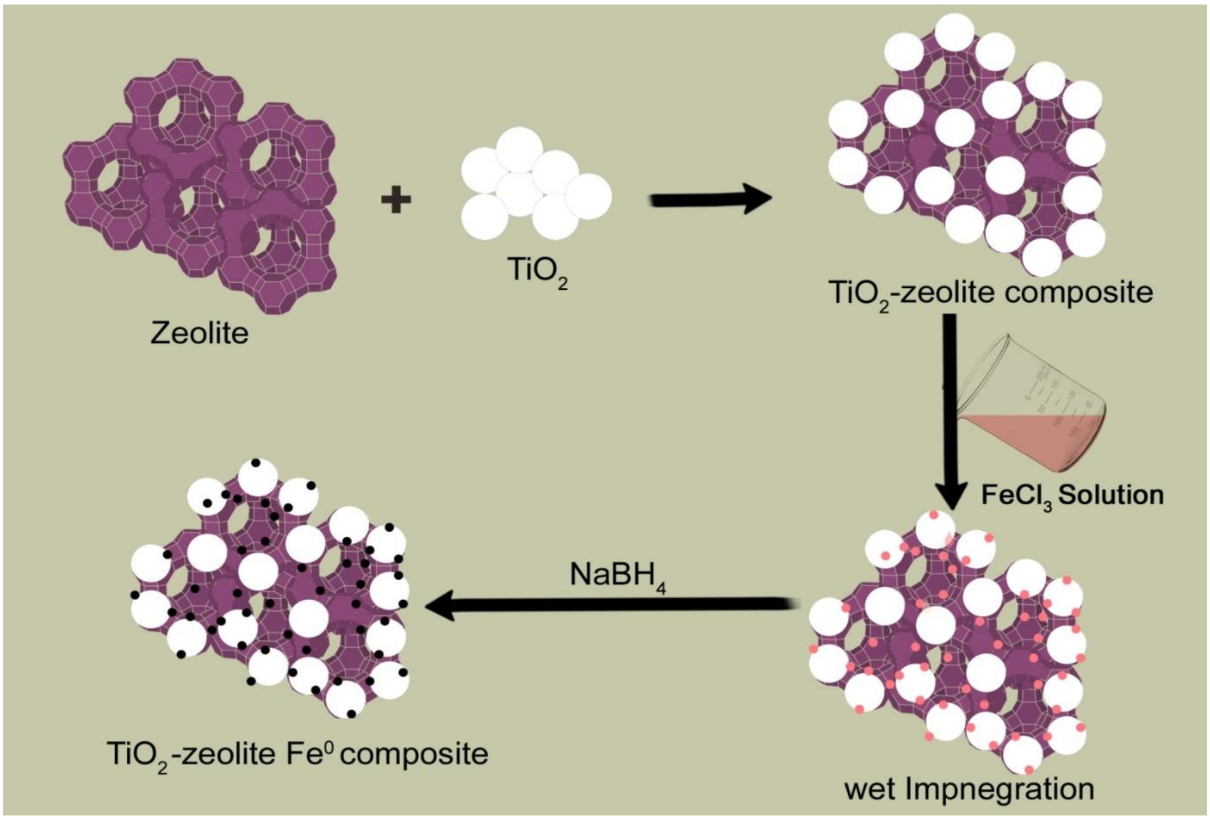

Chapter 5

TiO_2-zeolite composite modified Fe^0 nanoparticles for the removal of Cr(VI) and malachite green dye from water

5.1. Introduction

The search for the most suitable material for the remediation of water pollutants is a never-ending process. As discussed in previous chapters, zero valent iron (Fe^0) nanoparticle is an appropriate material for water remediation. However, the stability of Fe^0 nanoparticles is still a complicated issue. The rapid oxidation of the Fe^0 nanoparticles by reacting with air, moisture and non-targeted pollutants make them hard to handle. As per literature, TiO_2 can be used to retard the corrosion of metals and metal alloys[1]. In addition to this, TiO_2 is used for the adsorption of heavy metals[2], dyes[3] etc. and it is also used as a photocatalyst in various studies due to its chemical and photochemical stability, quantum confinement effect, strong resistance to acids and alkalis, large surface area to volume ratio along with low cost and low toxicity[4,5]. Efraim et al. used TiO_2 as a photocatalyst to degrade the antibiotic oxacillin through hydroxyl radicals created in the valence band of the former through photogenerated holes. In their study, around 90 % of the total organic carbon was removed by TiO_2 based photocatalysis[6]. Former studies show that Fe^{3+} doping of TiO_2 reduces the TiO_2 band gap since the Ti^{4+} ions in the crystal lattice are substituted by Fe^{3+} ions. The doping can shift the absorption of TiO_2 from the UV region to the visible region.

The charge carrier recombination rate gets reduced and the hydroxyl radical production has improved in Fe^{3+} doped TiO_2 photocatalyst. This leads to the enhanced photocatalytic degradation of the organic pollutant under UV and visible light illumination[7]. The presence of metal ions/metal nanoparticles in the TiO_2 surface improves photocatalytic activity and can act as electron scavengers to catch the photogenerated electrons[8]. This property will be helpful for the stabilization of Fe^0 nanoparticles for more extended periods. Even though the TiO_2 nanoparticles can be used for water treatment, they show high colloidal stability in water and are difficult to separate and recover after use[9].

The disadvantages of TiO_2 nanoparticles can be overcome by immobilizing them on a suitable support, which helps easy removal and separation after use. One of the inexpensive and non-toxic supports for metal/metal oxide nanoparticles are zeolites (Z). Zeolites are three-dimensional aluminosilicate frameworks that show high surface area, abundant surface active sites for adsorption and excellent ion exchange capacity. More than that, it is resistant to the attack of hydroxyl radicals and effective even after recycling many times. It is important to note that the negative surface charges of the zeolites help them to show a high affinity towards cationic species[10]. The modification of zeolite by TiO_2 has been studied over the years. Different methods were used to establish TiO_2 nanoparticles on the surface of the zeolite. The most common method is growing TiO_2 nanoparticles on the zeolite matrix. Qing et al. produced TiO_2 nanoparticles supported on natural zeolite by the hydrolysis of $TiCl_4$[11]. Yan-Huei et al. prepared TiO_2-zeolite composite by wetness impregnation method in which the components are mixed, sonicated and finely sprayed on the hot glass plate[12]. In another study, Daryoush et al. synthesized NaX zeolite stabilized MgO–TiO_2 nanocomposite using the ultrasound-assisted dispersion method. The MgO and TiO_2 nanoparticles were mixed with NaX zeolite in water followed by sonication, stirring, drying, and calcination, giving NaX/MgO–TiO_2 nanocomposite [13].

In the present study, TiO_2-zeolite composite was prepared by the hydrothermal method and these composites were used to stabilize Fe^0 nanoparticles. The major objectives of the study are (1) preparation of TiO_2-zeolite composite (T-Z) with varying TiO_2 dosage, (2) synthesis of Fe^0 nanoparticles supported on TiO_2 nanoparticles, natural zeolite and TiO_2-zeolite composites, (3) characterization of the prepared composites and nanoparticles and (4) malachite green dye and Cr(VI) removal studies by prepared nanoparticles.

5.2. Experimental details

5.2.1 Preparation TiO_2-zeolite stabilized Fe nanoparticles

Preparation of TiO_2-zeolite Composites

The TiO_2-zeolite composite was prepared by depositing TiO_2 nanoparticles on the zeolite surface. At first, clean the purchased natural zeolite to remove organic impurities present in it. This is attained through sonication of zeolite in water followed by calcination at 600°C for 6 hours in a muffle furnace. The subsequent cooling at room temperature and powdering using pestle and mortar provide refined zeolite particles. The TiO_2-zeolite composite was prepared by mixing specific weight percentages of purchased TiO_2 nanoparticles with clean zeolite powder in a 10 % ethanolic aqueous medium. This solution was sonicated using a probe sonicator for 30 minutes and kept at 120°C for 6 hours in a teflon-lined stainless steel autoclave. After that, the autoclave was cooled down at room temperature and washed with demineralised water. The TiO_2-zeolite composite was further calcinated at 600°C for 6 hours and powdered using pestle and mortar. The 25 % TiO_2 nanoparticles loaded zeolite (25-T-Z) and 50 % TiO_2 nanoparticles loaded zeolite (50-T-Z) were prepared by maintaining the TiO_2 and zeolite particles ratio at 25:75 and 50:50 respectively.

Synthesis of stabilized Fe nanoparticles

The TiO_2-zeolite-Fe composite was prepared by the wet impregnation followed by liquid phase reduction method. For this, $FeCl_3.6H_2O$ (1 g) was dissolved in 10 mL of water and added 0.5 g of T-Z into it. The solution was stirred for 30 minutes and evaporated the solvent using a hot plate. The obtained material was powdered, weighed and redispersed in 10 mL of water and stirred 30 minutes under the nitrogen atmosphere. $NaBH_4$ solution was prepared by dissolving 0.5 g in 50 L of water and added dropwise to the solution. The appearance of a black precipitate indicates the formation of Fe^0 nanoparticles in the TiO_2-zeolite matrix. The precipitate was collected by vacuum filtration, washed with acetone, lyophilized and stored in airtight vials. In the synthesis of 25-T-Z-Fe, the 25-T-Z composite was used and for 50-T-Z-Fe preparation, the composite 50-T-Z was used. A similar procedure was followed to prepare T-Fe and Z-Fe nanoparticles in which TiO_2 nanoparticles and zeolite were used as stabilizing agents.

5.2.2 Batch experiments

Cr(VI) removal studies

The details of batch experiments followed for Cr(VI) removal were discussed in chapter 2. Different parameters examined in this study for Cr(VI) removal were nanoparticle dosage (0.4-1 g/L), initial concentration of Cr(VI) (1-7 mg/L), initial pH of the solution (4-10) and contact time (10-40 min). The pH of the solution has been adjusted using 1.0 M NaOH and 1.0 M H_2SO_4. All the experiments were performed with a duplicate.

Dye removal studies

The method followed for the MG dye removal batch experiment was already mentioned in chapter 3. The parameter studied in the present study were nanoparticle dosage (0.16-0.4 g/L), initial concentration of dye (10-50 mg/L), initial pH of the solution (5-9) and contact time (15-60 min). The volume of dye solution taken was 25 mL and all the experiments were performed with a duplicate. The residual dye concentration was evaluated by UV-visible spectroscopy.

5.2.3 Characterisation and analytical techniques used

The prepared nanoparticles were lyophilised using Operon FDU 7003 lyophiliser. The characteristics of TiO_2 nanoparticles, zeolite and TiO_2–zeolite composites and corresponding iron nanoparticles were examined by HRTEM, UV-visible spectroscopy, EDAX, XRD and FTIR. Details of characterisation techniques were discussed in chapter 2. UV-visible spectrometer UV-2600, Shimadzu, Japan, was used to study the absorbance of TiO_2 nanoparticles, zeolite and TiO_2–zeolite composites and corresponding iron nanoparticles. Fourier transform infrared spectra of the prepared composite and corresponding Fe nanoparticles were investigated through Spectrum Two Fourier transform infrared spectrometer (FTIR, Perkin Elmer, USA). Jeol 6390LA/OXFORD XMX N was used for the elemental analysis of T-Fe, Z-Fe, 50-T-Z and 50-T-Z-Fe nanoparticles. GC-MS/MS analysed the degradation products of MG dye using 25-T-Z-Fe nanoparticles. The procedure followed for the GC-MS/MS analysis was discussed in chapter 3.

5.3. Results and discussion

5.3.1 Characterisation of the prepared materials

XRD

X-ray diffractogram of TiO_2 nanoparticles, zeolite powder, 25 % TiO_2 loaded zeolite composite and 50 % TiO_2 loaded zeolite composite was shown in figure 5.1. The powder XRD pattern of TiO_2 exhibited strong diffraction peaks at $2\theta = 25.7^o$ (101), 38.3º (004), 48.49º (200), 54.49º (105) and 55.44º (211) corresponding to the anatase phase of TiO_2[14]. The diffraction peaks observed at $2\theta = 69.31^o$ (031) and 70.5 (112) indicated the presence of the rutile phase of TiO_2 in lower percentages (JCPDS no 98-018-6186). Anatase TiO_2 nanoparticles show superior photocatalytic property compared to rutile TiO_2. In the XRD spectrum of zeolite, the peaks shown at 30.3º, 27.4º, 24.3º, 22.0º and 10.5º corresponds to the clinoptilolite zeolite[15,16]. The XRD peaks of 25-T-Z and 50-T-Z have a similar pattern of TiO_2 and zeolite, with a slight shift in the XRD peaks. With the increase in TiO_2 dosage, the peaks of zeolite were decreased drastically. This indicates that zeolites are covered with TiO_2 nanoparticles completely. Figure 5.2 shows the XRD pattern of Fe nanoparticles stabilised on the TiO_2 nanoparticles, zeolite, 25-T-Z and 50-T-Z composites. XRD peak at 45.4° indicates (110) plane of the zero valent iron, which is present in all the four Fe nanoparticles[17]. The intense peak at 31.7° corresponds to the (104) plane of α-Fe_2O_3[18]. The other peaks in the T-Fe, Z-Fe, 25-T-Z-Fe and 50-T-Z-Fe nanoparticles were that of the corresponding stabilising agent, TiO_2 and zeolite, with a slight shift in their peak position.

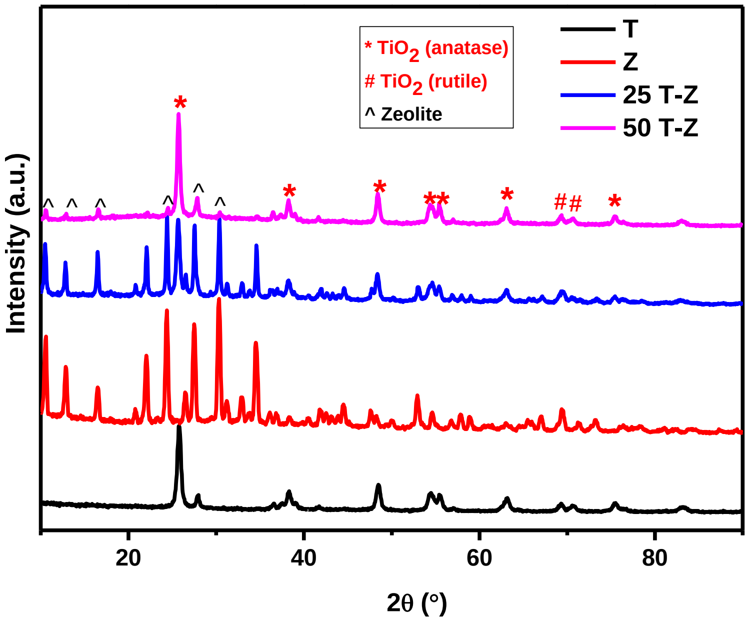

Figure 5.1 *XRD pattern of TiO_2 nanoparticles, zeolite, 25-T-Z and 50-T-Z composite*

The high peak intensity of Fe^0 in 50-T-Z-Fe and T-Fe nanoparticles indicates the efficient stabilization of Fe^0 in these matrices. This is mainly due to the involvement of TiO_2 nanoparticles. Typically, TiO_2 nanoparticles are photocatalytically active in the UV region. However, its activity can be shifted to the visible region through the doping of Fe[19]. Electrons get excited to the conduction band of TiO_2 from its valence band when exposed to UV radiation. This leads to the formation of electron-hole pairs within the system. The lifetime of these excited electron-hole pair determines the photochemistry of TiO_2. Photocatalytic activity of TiO_2 is minimized as the excited electrons in the conduction band recombines with the holes in the valence band. This charge recombination could be minimized by coupling TiO_2 with materials that can accept the electrons from the conduction band. According to Eleni et al., the iron oxide shell of the Fe^0 nanoparticles can act as electron trappers that accept the photoexcited electron from the conduction band of TiO_2, thereby reducing Fe^{3+} to Fe^{2+}. The interaction between TiO_2 and Fe retard the thicker iron oxide layer formation and gives longer reactivity of Fe^0 nanoparticles in TiO_2 matrices[8]. The incorporation of zeolite enhanced the efficiency of TiO_2 nanoparticles, which may be due to the more dispersibility of TiO_2 nanoparticles in the zeolite matrix. Previous studies show that the photocatalytic activity of TiO_2 can be enhanced using zeolite as a supporting agent. Guangxin et al. synthesized TiO_2-zeolite composite and applied it to degrade gaseous and aqueous organic pollutants. They detected high efficiency for the degradation of organic pollutants which is attributed to high surface area of TiO_2-zeolite composite[20]. In the case of 50-T-Z-Fe, the TiO_2 nanoparticles were more dispersed in zeolite matrix and may show high surface area. This leads to the improved stabilization Fe^0 in 50-T-Z-Fe nanoparticles.

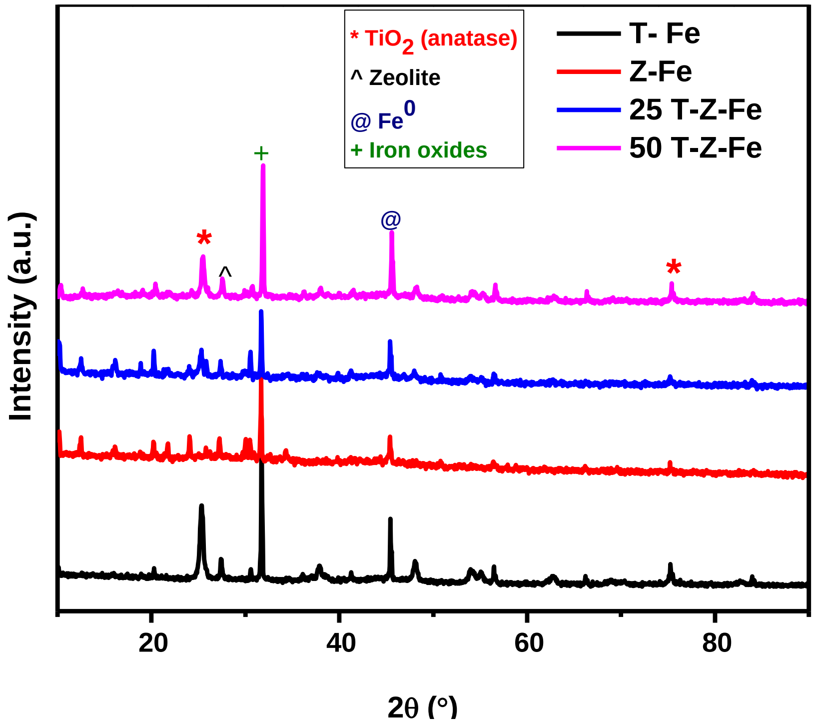

Figure 5.2 XRD pattern of T-Fe, Z-Fe, 25-T-Z-Fe and 50-T-Z-Fe nanoparticles

HRTEM

Figure 5.3 represents the HRTEM image and SAED pattern of 50-T-Z and 50-T-Z-Fe respectively. As shown in figure 5.3a, the TiO_2 nanoparticles were deposited on the surface of the zeolite. The particle size of TiO_2 ranges between 20-35 nm with an average particle size of 25 nm and the size of zeolite particles is around 150 nm. The 50-T-Z materials show the crystalline property, which is evident from the SAED pattern. Figure 5.3b envisages that the Fe^0 nanoparticles with particle size below 20 nm were deposited on the surface of TiO_2 nanoparticles. The Fe nanoparticles exhibit a shell of iron oxide which may arise due to the oxidation of nanoparticles. The SAED pattern of 50-T-Z-Fe shows that the nanoparticles display crystalline properties similar to the 50-T-Z.

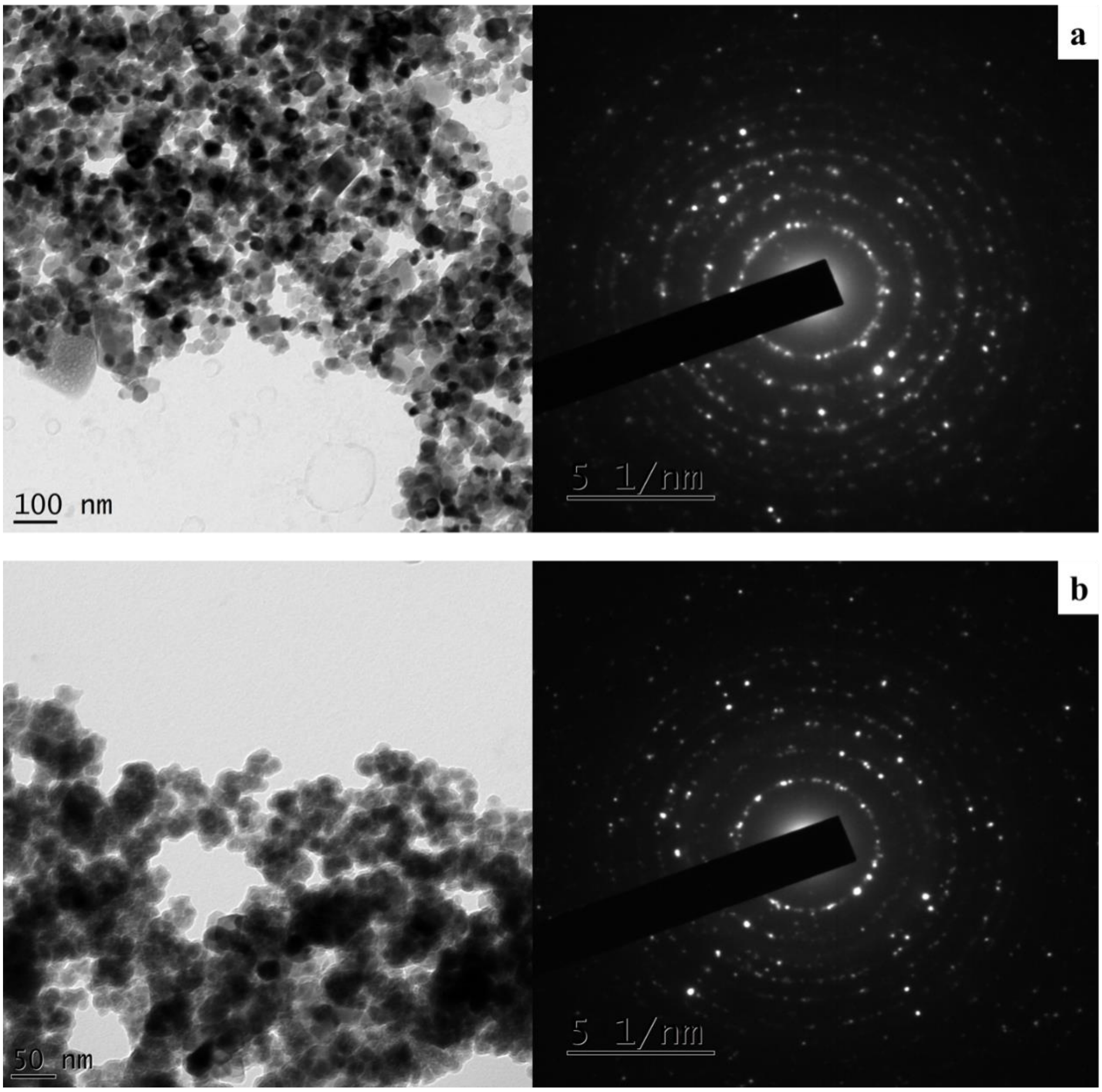

***Figure 5.3** HRTEM image SAED pattern of 50-T-Z (a) and 50-T-Z-Fe nanoparticles*

EDAX

EDAX spectra and mapping of T-Fe, Z-Fe, 50-T-Z and 50-T-Z-Fe nanoparticles were shown in figure 5.4 (a, b, c & d) and figure 5.5 (a, b, c & d) respectively. EDAX spectra confirm the presence of respective elements in prepared nanoparticles; for example, T-Fe contains Ti, O and Fe, Z-Fe contains Al, Si, O and Fe, 50-T-Z contains Al, Si, O and Ti, and 50-T-Z-Fe contains Al, Si, O, Ti and Fe elements. As shown in figure 5.4, the percentage of oxygen is less in 50-T-Z-Fe compared to T-Fe and Z-Fe, which shows that 50-T-Z protects Fe^0 more efficiently than TiO_2 and zeolite. In accordance with the EDAX spectra, the atomic weight percentage of Fe in T-Fe, Z-Fe and 50-T-Z-Fe nanoparticles were 15 %, 16 % and 20 % respectively. The EDAX mapping of prepared nanoparticles gives information about the distribution of Fe nanoparticles in TiO_2, zeolite, 25-T-Z and 50-T-Z matrices. The iron nanoparticles were uniformly distributed in TiO_2 and 50-T-Z surfaces. In the case of Z-Fe, the Fe nanoparticles were more present in zeolite channel/cavities than surfaces as indicated by the reduced intensity of Fe in Z-Fe nanoparticles (figure 5.5b).

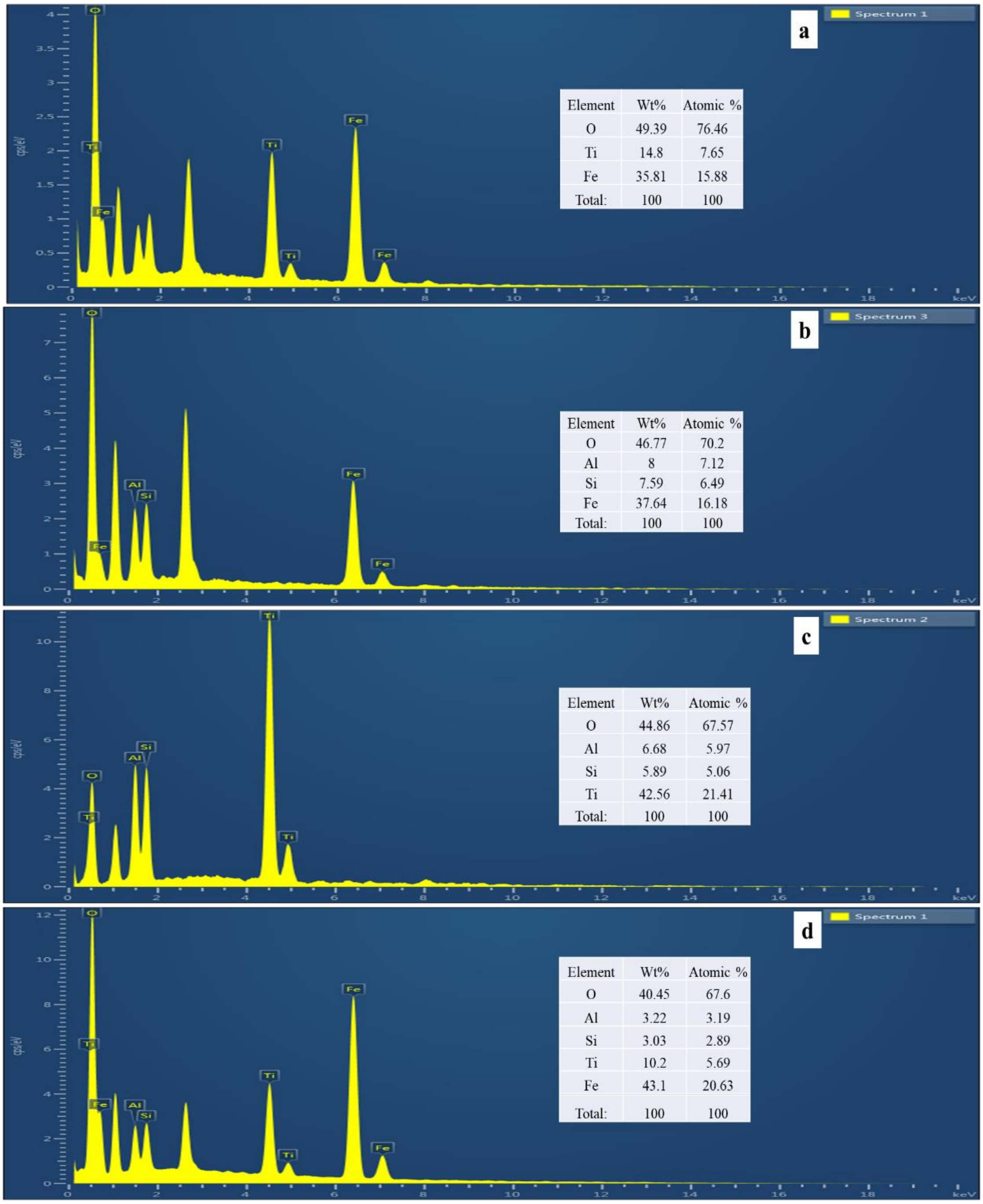

Element	Wt%	Atomic %
O	49.39	76.46
Ti	14.8	7.65
Fe	35.81	15.88
Total:	100	100

Element	Wt%	Atomic %
O	46.77	70.2
Al	8	7.12
Si	7.59	6.49
Fe	37.64	16.18
Total:	100	100

Element	Wt%	Atomic %
O	44.86	67.57
Al	6.68	5.97
Si	5.89	5.06
Ti	42.56	21.41
Total:	100	100

Element	Wt%	Atomic %
O	40.45	67.6
Al	3.22	3.19
Si	3.03	2.89
Ti	10.2	5.69
Fe	43.1	20.63
Total:	100	100

Figure 5.4 *EDAX spectra of (a) T-Fe, (b) Z-Fe, (c) 50-T-Z and (d) 50-T-Z-Fe*

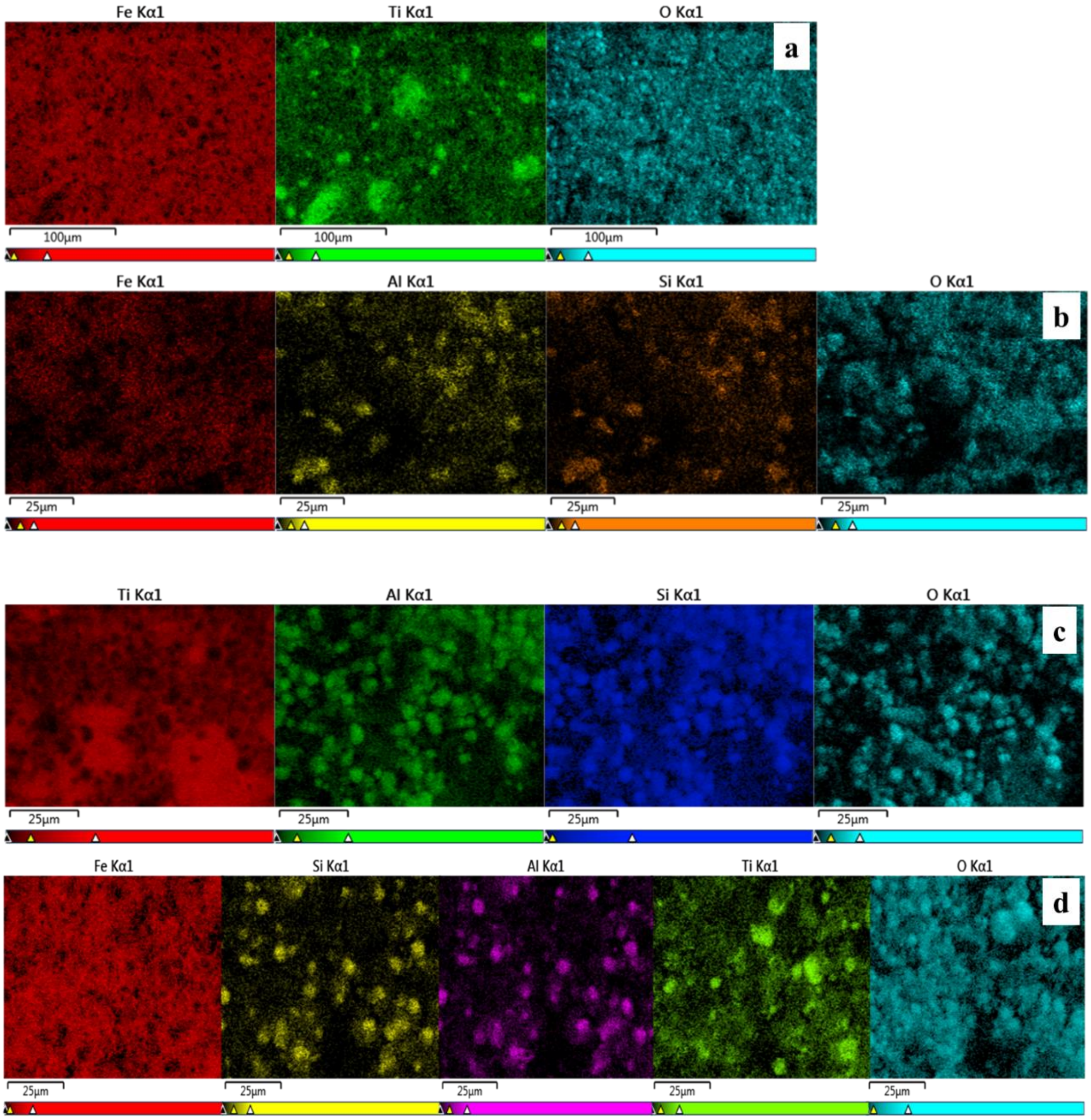

Figure 5.5 *EDAX mapping of (a) T-Fe, (b) Z-Fe, (c) 50-T-Z and (d) 50-T-Z-Fe*

FTIR

Figure 5.6 represents the FTIR spectra of T-Fe, Z-Fe, 25-T-Z-Fe and 50-T-Z-Fe nanoparticles and their corresponding stabilizing materials. The interaction between Fe^0 and stabilizing materials were established using FTIR measurements. Figure 5.6a represents the FTIR spectra of TiO_2 and T-Fe nanoparticles. The peak centred at 3479 cm^{-1}, belonging to the stretching vibration of the -OH group due to the absorption of moisture from the atmosphere. The peak at 730 cm^{-1} corresponding to the O–Ti–O bonding of TiO_2 anatase nanoparticles shifted to 694 cm^{-1} in T-Fe nanoparticles[21]. This confirms the incorporation of Fe in TiO_2 lattice since the red shift is a sign of structural defect in TiO_2 lattice. In figure 5.6b, the existence of zeolite can be confirmed by the peaks between

400-850 cm^{-1}[22]. The shift in peak position from 1365 cm^{-1} to 1350 cm^{-1} suggests the interaction of Fe nanoparticles with zeolite. The peak centred around 980 cm^{-1} is due to the vibration of Si-O or Al-O of the zeolite is split into two peaks due to the replacement of Si with Fe during the Fe deposition. The zeolite peaks at 663 cm^{-1} were blue-shifted to 696 cm^{-1} in Z-Fe nanoparticles. This also supports the interaction of zeolite with Fe^0 nanoparticles. A similar trend has also been seen in 25-T-Z-Fe and 50-T-Z-Fe nanoparticles too. The FTIR spectra of 25-T-Z and 50-T-Z exhibit the peaks of TiO_2 and zeolite. The introduction of Fe shifted the peaks to higher/lower wavenumber.

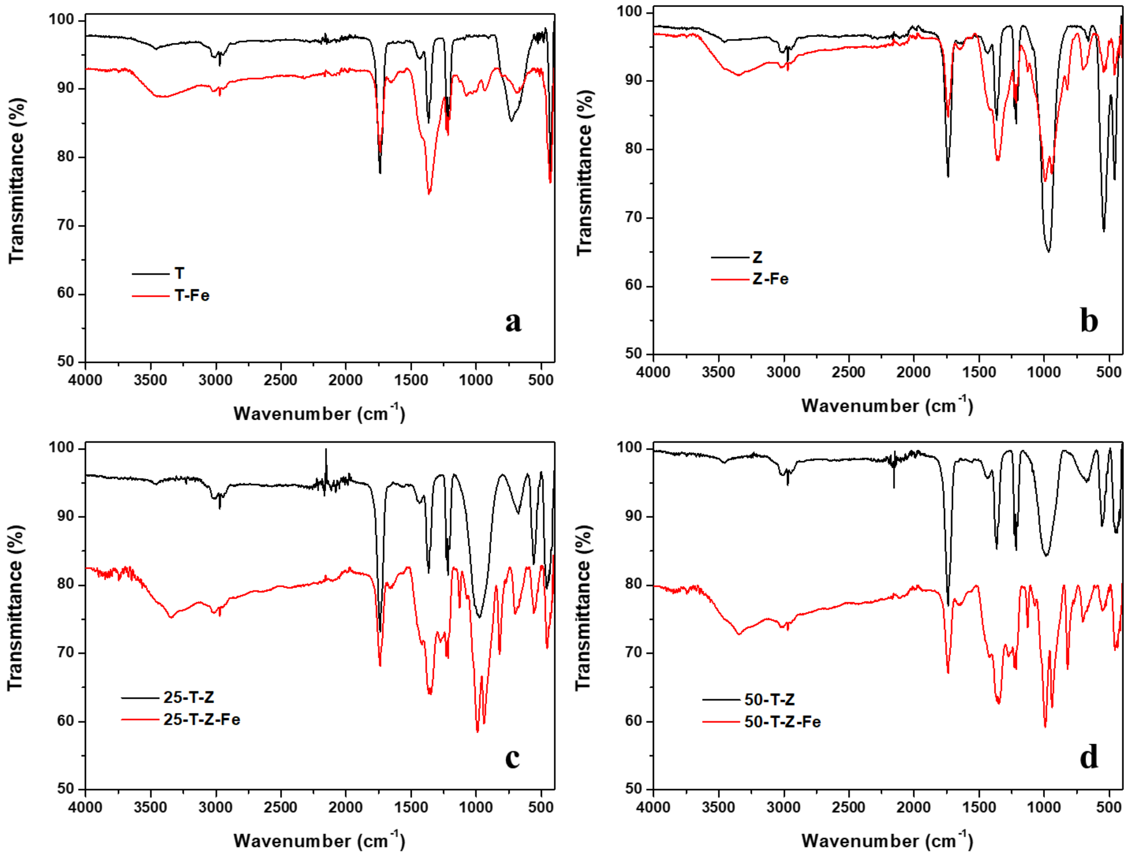

Figure 5.6 *FTIR spectra of (a) TiO_2 and T-Fe nanoparticles, (b) zeolite and Z-Fe nanoparticles, (c) 25-T-Z and 25-T-Z-Fe nanoparticles and (d) 50-T-Z and 50-T-Z-Fe nanoparticles*

UV-visible spectroscopy

TiO_2 exhibited its characteristic absorption maxima in the UV region as observed by UV-visible spectroscopy (figure 5.7). The absorbance spectrum of zeolite also reveals its characteristic absorbance in the UV region of spectra. A considerable shift in peak intensity and position occurred in the absorption spectra of TiO_2 and zeolite with the incorporation of Fe. The presence of Fe in TiO_2, decreased the intensity of absorption of the latter in the UV region and enhanced the absorption of TiO_2 in the visible region. This red shift in the peak position of TiO_2 in T-Fe is depicted in figure 5.7a. On the other hand, the spectra of Z-Fe composite displayed enhanced absorption intensity in UV and the visible region compared to that of pristine zeolite. All these observations support the existence of molecular interaction between TiO_2 as well as zeolite with Fe. The presence of Fe extended the absorption of TiO_2 and zeolite to the visible region. Similar reconstructions were observed in the absorption bands of T-Z composites (25 T-Z-Fe and 50 T-Z-Fe) with the association of Fe. The extension of absorption of TiO_2, Zeolite and T-Z to visible region in the presence of Fe also suggests the possibility of these composites to exhibit their photocatalytic activity in the visible region too.

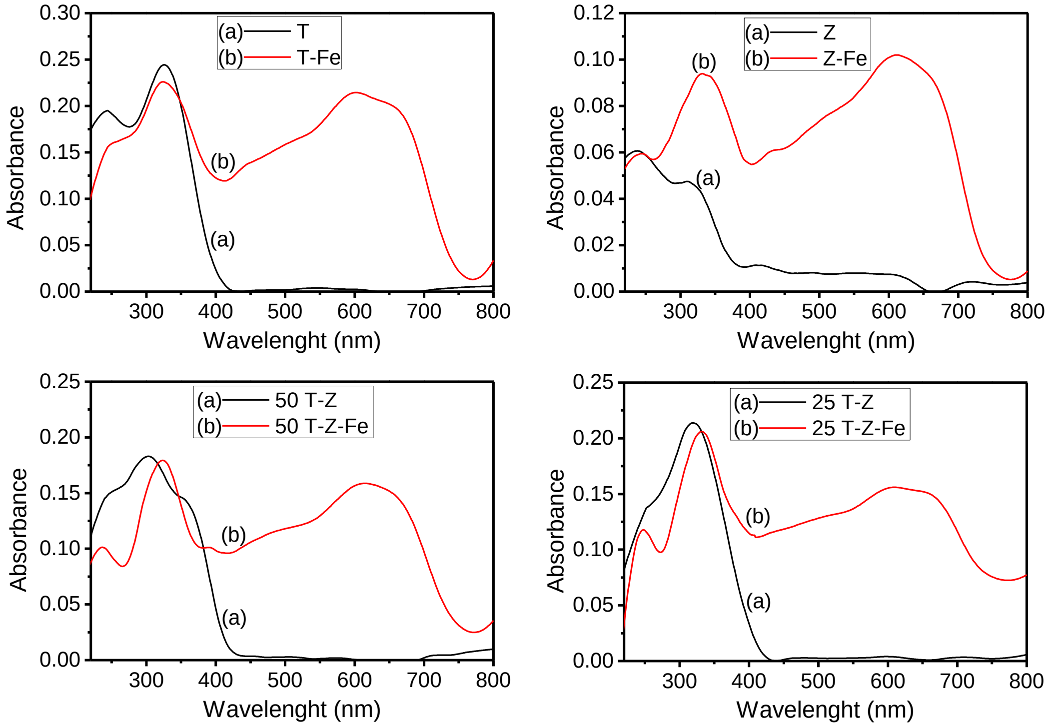

Figure 5.7 *UV-visible spectra of T-Fe, Z-Fe, 25-T-Z-Fe and 50-T-Z-Fe nanoparticles in comparison with TiO_2 and zeolite*

5.3.2 Cr(VI) removal studies

Cr(VI) removal studies have been done using T-Fe, Z-Fe, 25-T-Z-Fe and 50-T-Z-Fe nanoparticles and are shown in figure 5.7. The results show that 25-T-Z-Fe and 50-T-Z-Fe nanoparticles exhibit the highest removal efficiency compared to T-Fe and Z-Fe nanoparticles. This indicates the presence of more Fe^0 in 25-T-Z-Fe and 50-T-Z-Fe than

T-Fe and Z-Fe nanoparticles. The improved efficiency of Z-Fe over T-Fe may be due to the adsorption of Cr(VI) ions onto the empty cavities/channels of zeolite. The synergetic activity of zeolite and TiO_2 significantly reduced the oxidation probability of Fe^0 nanoparticles and enhanced the adsorption properties of 25-T-Z-Fe and 50-T-Z-Fe nanoparticles. The existence of TiO_2 nanoparticles also added some effect on Cr(VI) removal. TiO_2 nanoparticles exhibit photocatalytic activity in the visible region along with the UV region due to the doping of Fe[19]. So the absorption of visible light followed by the generation of electrons and holes also influenced the reduction of Cr(VI). The photogenerated electrons reduce the Cr(VI) to Cr(III) through redox reactions to some extent[23]. Some of the photogenerated electrons were trapped by the iron oxide shell and regenerated after the Cr(VI) reduction[8]. The synergetic photocatalytic effect of TiO_2 and zeolite adsorption significantly improved the Cr(VI) removal in 25-T-Z-Fe and 50-T-Z-Fe systems.

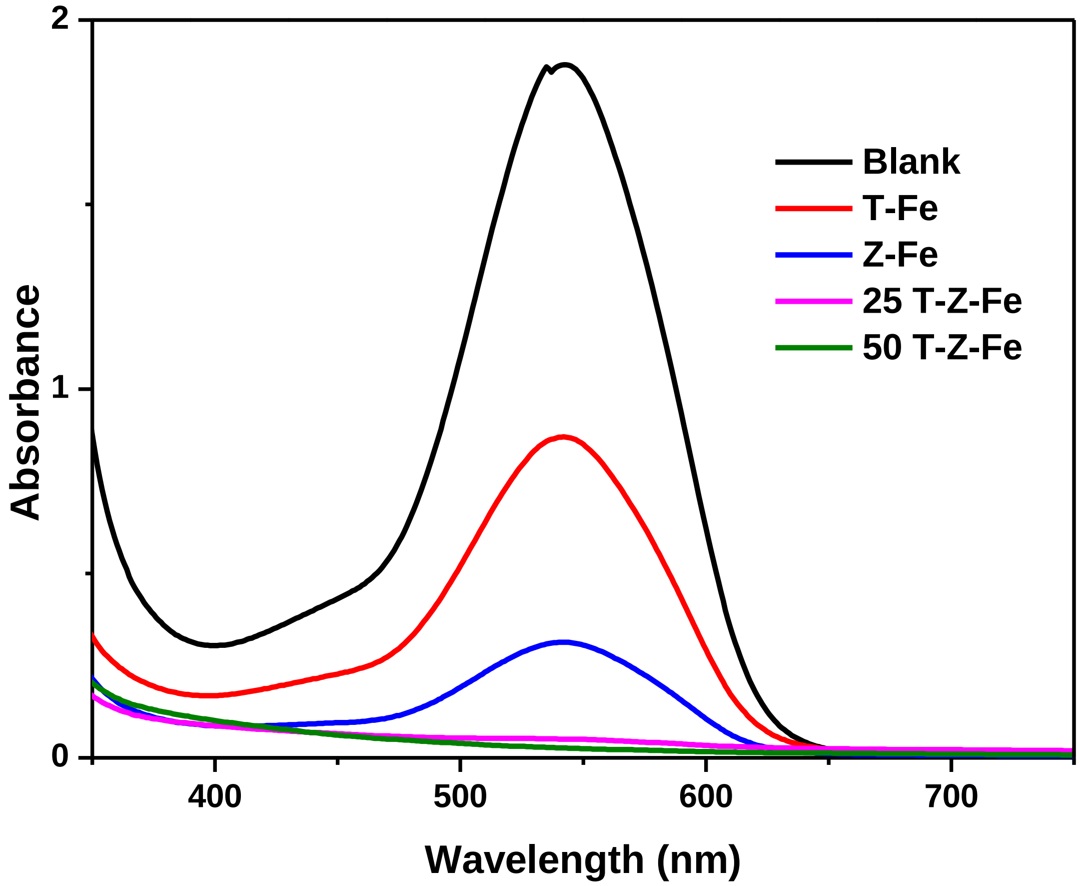

***Figure** 5.7 UV-visible spectra of Cr(VI) after treating with T-Fe, Z-Fe, 25-T-Z-Fe and 50-T-Z-Fe nanoparticles*

Effect of nanoparticle dosage

Figure 5.8a represents the effect of nanoparticles dosage on the Cr(VI) removal using T-Fe, Z-Fe, 25-T-Z-Fe and 50-T-Z-Fe nanoparticles. The nanoparticles dosage varied between 0.4 g/L to 1 g/L maintaining the initial Cr(VI) concentration at 5 mg/L and with a 15 minute contact time. The results show the highest removal efficiency in 25-T-Z-Fe nanoparticles along with 50-T-Z-Fe nanoparticles and the lowest Cr(VI) removal efficiency exhibited by T-Fe nanoparticles. While using 0.8 g/L of nanoparticles, the T-Fe, Z-Fe, 25-T-Z-Fe and 50-T-Z-Fe nanoparticles show 78 %, 89 %, 95 % and 93 % of Cr(VI) removal efficiency respectively. The removal efficiency increased with the increase in nanoparticles dosage which is attributed to the high surface area and high surface active sites of prepared nanoparticles along with the rise in nanoparticles dosage. After the dosage of 0.8 g/L, the removal efficiency does not improve significantly. This may be due to the aggregation of nanoparticles.

Effect of the initial concentration of the Cr(VI) solution

The effect of the initial concentration of nanoparticles on the removal of Cr(VI) from water is shown in figure 5.8b. The nanoparticles dosage and contact time during the study were kept constant at 0.6 g/L and 15 minutes respectively. The results show that the removal efficiency decreased drastically with an increase in Cr(VI) concentration. The highest removal efficiency was exhibited in 1 mg/L Cr(VI) solution and the lowest by 7 mg/L Cr(VI) solution. In 1 mg/L solution, the T-Fe, Z-Fe, 25-T-Z-Fe and 50-T-Z-Fe nanoparticles show 81%, 93 %, 95 % and 95 % removal efficiency which is reduced to 49 %, 63 %, 78 % and 76 % at 7 mg/L solutions. This is due to the increase in the ratio between pollutant molecules and nanoparticle dosage, which leads to the decrease in the availability of surface active sites for the reduction of Cr(VI) ions.

Effect of contact time

As shown in figure 5.8c, the effect of contact time on Cr(VI) removal has been studied by keeping nanoparticles dosage (0.6 g/L) and initial Cr(VI) concentration (5 mg/L) constant. The results show that the 25-T-Z-Fe and 50-T-Z-Fe nanoparticles attained the maximum removal efficiency within 20 minutes of reaction time. However, in the case of T-Fe and Z-Fe nanoparticles, 30 minutes is needed to attain the maximum removal efficiency. This indicates that 25-T-Z-Fe and 50-T-Z-Fe nanoparticles reacted more actively with Cr(VI) ions than T-Fe and Z-Fe nanoparticles. At 40 minutes of contact time the T-Fe, Z-Fe, 25-

T-Z-Fe and 50-T-Z-Fe nanoparticles display 77 %, 87 %, 93 % and 92 % Cr(VI) removal efficiency.

Effect of pH

The effect of pH on Cr(VI) removal was studied and depicted in figure 5.8c. The results demonstrate that the pH has little effect on Cr(VI) removal for Z-Fe, 25-T-Z-Fe and 50-T-Z-Fe nanoparticles. However, the removal efficiency reduced significantly in T-Fe nanoparticles from acidic to basic pH. The high removal efficiency in low pH may be due to the high degree of protonation of prepared nanoparticles and the shredding of iron oxide shell in the prepared Fe^0 nanoparticles.

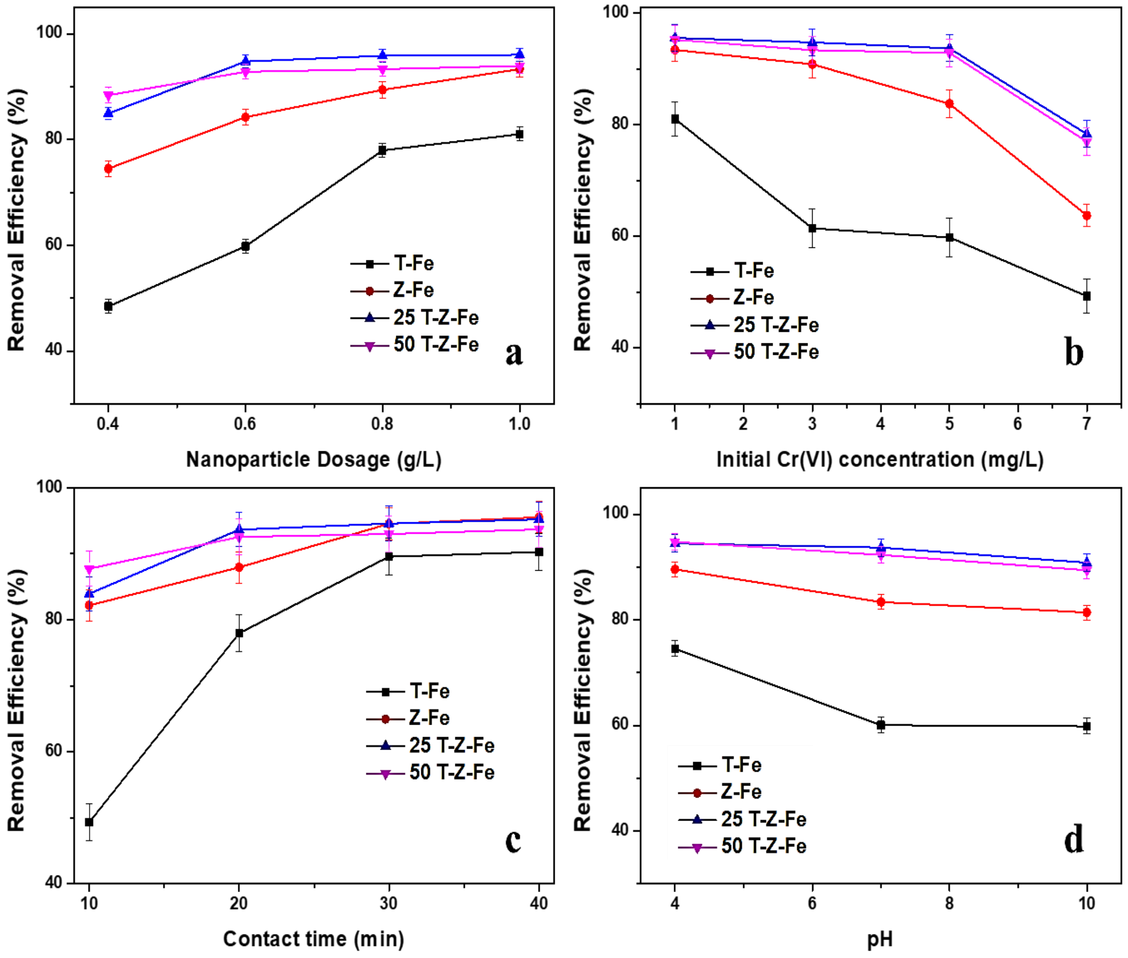

Figure 5.8 *(a) Effect of nanoparticle dosage, (b) Effect of initial concentration of Cr(VI), (c) Effect of contact time and (d) Effect of pH on Cr(VI) removal using T-Fe, Z-Fe, 25-T-Z-Fe and 50-T-Z-Fe nanoparticles*

5.3.3 MG dye removal studies

Malachite green dye removal studies have been done using T-Fe, Z-Fe, 25-T-Z-Fe and 50-T-Z-Fe nanoparticles and are depicted in figure 5.9. The highest removal efficiency was exhibited by 25-T-Z-Fe nanoparticles followed by 50-T-Z-Fe, T-Fe and Z-Fe nanoparticles. This is due to the enhanced electron transfer, production of reactive oxygen species and adsorption onto zeolite.

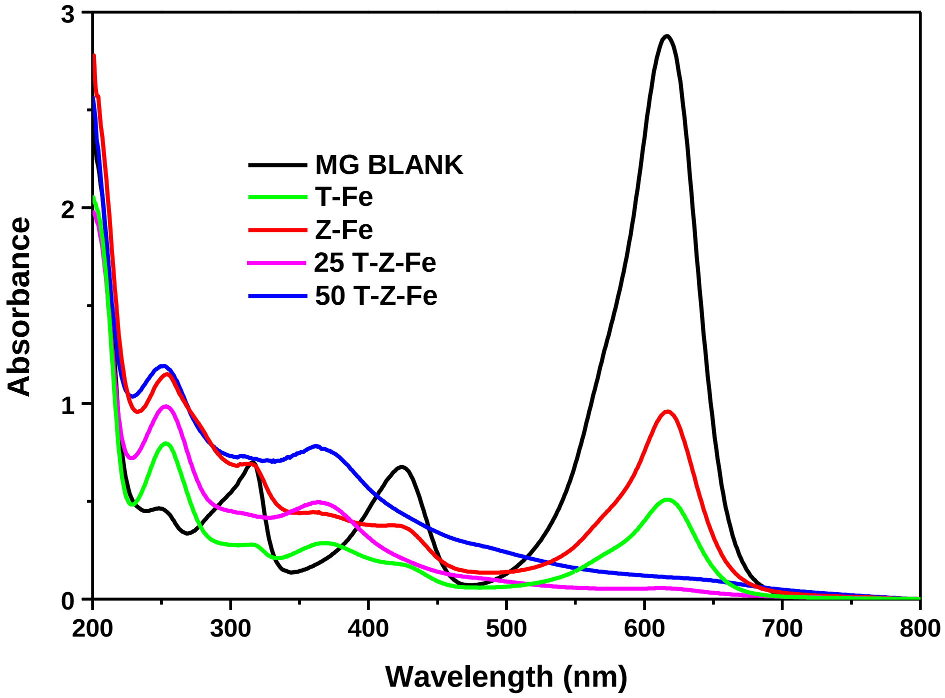

***Figure 5.9** UV-visible spectra of MG dye after treating with T-Fe, Z-Fe, 25-T-Z-Fe and 50-T-Z-Fe nanoparticles*

As discussed in chapter 3, Fe^0 nanoparticles degrade the malachite green dye molecules through reduction by direct electron transfer and atomic hydrogen and oxidation by reactive oxygen species such as hydroxyl radical. Along with the property of Fe^0, the stabilizing material is also involved in the removal of malachite green in T-Fe, Z-Fe, 25-T-Z-Fe and 50-T-Z-Fe nanoparticles. Previous studies show that malachite green was effectively adsorbed by zeolite through single layer adsorption and the intraparticle diffusion affected the adsorption rate of malachite green[24]. In addition to the adsorptive properties of zeolite, TiO_2 nanoparticles also played an important role in removing malachite green. Zulakha et al. effectively removed congo red dye using Fe_2O_3-titanium dioxide nanotubes under visible light[25]. This agrees with the previous assumption that Fe doped TiO_2 is an excellent photocatalyst compared to TiO_2 nanoparticles. The photogenerated electrons can act as reducing agents and holes created by TiO_2 nanoparticles react with OH^- ions and form hydroxyl radicals. These hydroxyl radicals can act as excellent oxidizing agents for dye degradation[8]. Earlier, Meng et al. treated industrial dye wastewater using TiO_2–zeolite nanocomposites and they found that TiO_2–Zeolite nanocomposites were more effective than pristine TiO_2 particles. This is due to the adsorption-oriented photocatalytic degradation of dye molecules when using TiO_2–zeolite nanocomposites[26]. The synergetic effect of Fe^0 with TiO_2-zeolite in T-Z-Fe composite significantly enhances the dye removal.

Effect of nanoparticle dosage

The effect of nanoparticles dosage on dye removal has given in figure 5.10a. The quantity of nanoparticles added was varied from 0.16 g/L to 0.4 g/L with a constant initial concentration of dye (50 mg/L) and contact time (30 min). 90 % removal of dye molecules was attained by 25-T-Z-Fe nanoparticles followed by 50-T-Z-Fe (89 %), T-Fe (83 %) and Z-Fe (78 %) using 4 g/L of nanoparticles. With the increase in nanoparticles dosage, the MG removal efficiency increases due to the more direct electron transfer, formation of reactive oxygen species and increase in adsorption sites.

Effect of the initial concentration of the MG

The effect of the initial concentration of the MG dye was studied and shown in 5.10b. During the study, the nanoparticle dosage was taken as 0.32 g/L and contact time was kept as 30 minutes. The results show a decrease in MG removal efficiency with an increase in the initial concentration of dye molecules except in the case of 10 mg/L dye solution. This indicates that adsorption also played an important role in MG dye removal using prepared nanoparticles along with degradation. As expected, the dye removal efficiency decreased with the increased initial concentration of the dye, which may be due to the insufficient availability of surface active sites in a finite nanoparticle dosage.

Effect of contact time

The effect of contact time on the removal of MG dye molecules was studied (figure 5.10c.) by keeping nanoparticles dosage and initial concentration of the dye constant. The effect of contact time was studied in 15 minute time intervals and the results show that the 25-T-Z-Fe and 50-T-Z-Fe nanoparticles attained maximum removal efficiency within 15 minutes and the T-Fe and Z-Fe nanoparticles accomplished maximum removal efficiency within 30 minutes. With the increase in contact time, the vacant adsorptive sites get occupied and the formation of reactive species gets reduced. This eventually reduced the removal efficiency of T-Fe, Z-Fe, 25-T-Z-Fe and 50-T-Z-Fe nanoparticles. The maximum removal efficiency attained by the prepared nanoparticles was 85 %, 74 %, 90 % and 89 % respectively, for T-Fe, Z-Fe, 25-T-Z-Fe and 50-T-Z-Fe nanoparticles.

Effect of pH

Figure 5.10d represents the effect of pH on the removal of MG dye using T-Fe, Z-Fe, 25-T-Z-Fe and 50-T-Z-Fe nanoparticles. The significant decrease in removal efficiency can be seen when the solution pH changes from acidic to basic. In acidic pH, the nanoparticles show 82 %, 81 %, 89 % and 89 % removal efficiency respectively for T-Fe, Z-Fe, 25-T-Z-Fe and 50-T-Z-Fe nanoparticles, which decreased to 63 %, 58 %, 79 % and 80 % in basic medium. This is due to the formation of the iron oxide layer, which reduces the reactivity of Fe^0 nanoparticles at higher pH.

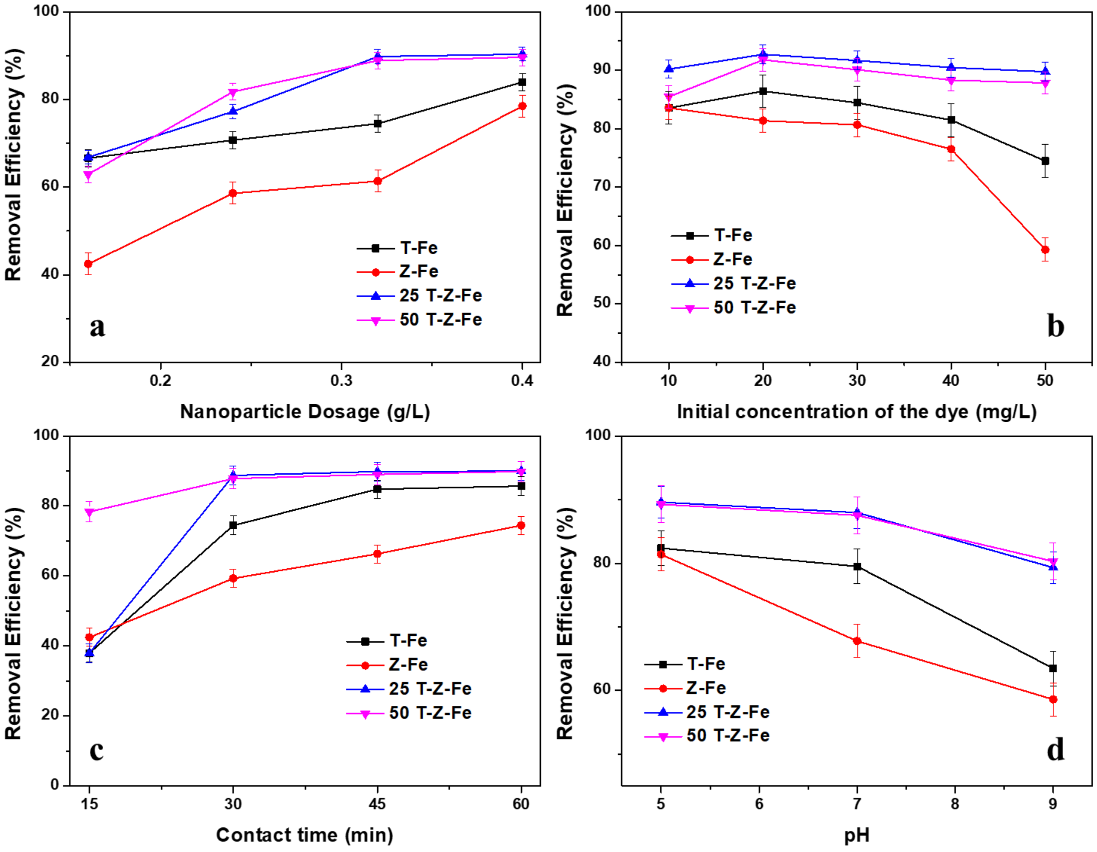

Figure 5.10 *(a) Effect of nanoparticle dosage, (b) Effect of initial concentration of MG, (c) Effect of contact time and (d) Effect of pH on MG dye removal using T-Fe, Z-Fe, 25-T-Z-Fe and 50-T-Z-Fe nanoparticles*

GC-MS/MS analysis

The GC-MS/MS analysis has been done on MG dye's degradation product, which is treated with the 25-T-Z-Fe nanoparticles. The GC-MS/MS analysis identified four degradation products of MG as (a) cyclohexa-2,5-diene-1,4-dione (MW 108), (b) diphenylmethanone (MW 182), (c) 3-(dimethylamino)phenol (MW 137) and (d) [4-(dimethylamino)phenyl]-phenylmethanone (MW 225) using the NIST library. The degradation products cyclohexa-2,5-diene-1,4-dione and diphenylmethanone were already reported in MG/Fe^0 system (chapter 3). However, the 3-(dimethylamino)phenol (R_t 15.81) and [4-(dimethylamino) phenyl]-phenylmethanone (R_t 21.27) were not reported by GC-MS/MS analysis in the previous chapters and figure 5.11 a & b represents the mass spectra of respective degradation products. The hydroxyl radical attack causes the degradation of MG into [4-(dimethylamino)phenyl]-phenylmethanone and N,N-dimethylaniline. The N,N-dimethyl aniline further transformed into 3-(dimethylamino)phenol through hydroxyl addition reaction[28]. Scheme 5.1 represents the formation of 3-(dimethylamino)phenol from N,N-dimethylaniline.

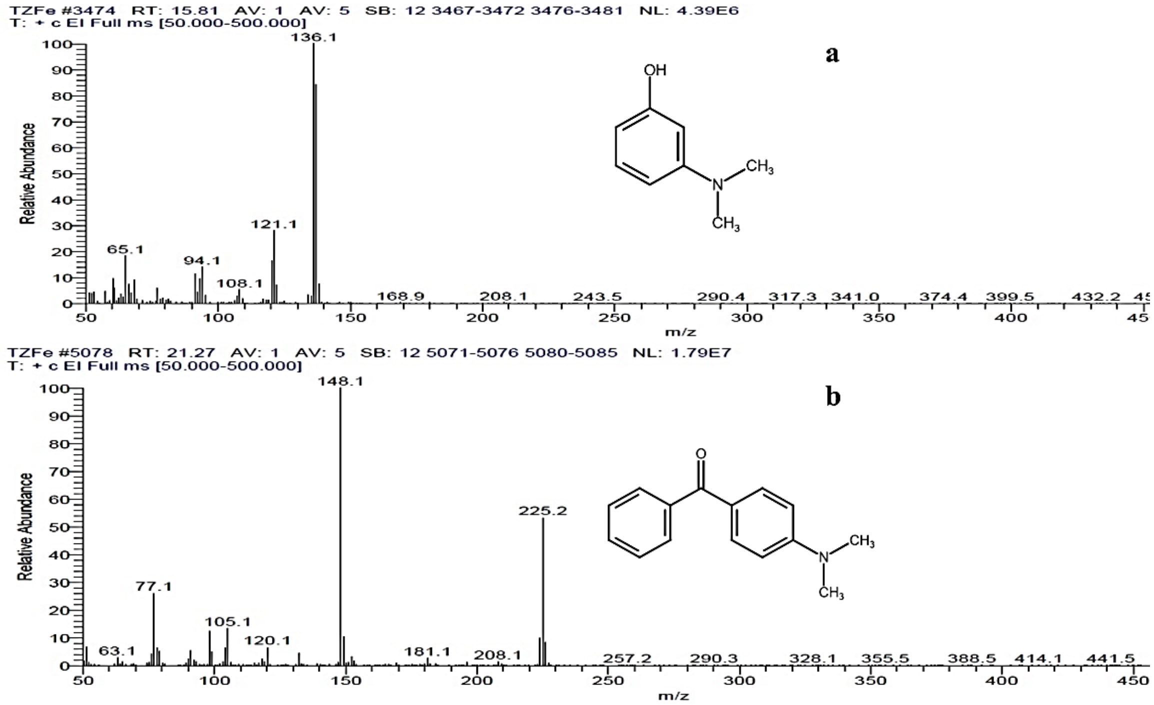

Figure 5.11 Mass spectra of MG degradation products identified by GC-MS/MS analysis a) 3-(dimethylamino)phenol and b) [4-(dimethylamino)phenyl]-phenylmethanone

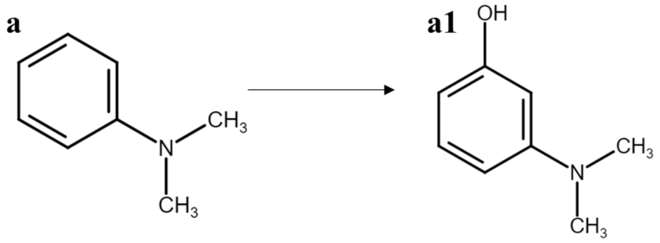

Scheme 5.1 *Degradation pathways of MG using 25-T-Z-Fe nanoparticles*

5.4. Conclusion

In this study, TiO_2-zeolite composite was used to stabilize Fe^0 nanoparticles. The TiO_2-zeolite composite was prepared by sonication followed by the hydrothermal method. The Fe^{3+} was incorporated in TiO_2-zeolite composite by wet impregnation and synthesized Fe^0 nanoparticles by liquid-phase reduction. The characterization of TiO_2-zeolite composite and T-Z-Fe nanoparticles have been done by XRD, FTIR, UV-visible spectroscopy, EDAX and HRTEM. In the prepared nanoparticles, 25-T-Z-Fe and 50-T-Z-Fe nanoparticles show more removal efficiency for Cr(VI) and MG dye compared to T-Fe and Z-Fe nanoparticles. The removal efficiency increases with increasing nanoparticle dosage and contact time and decreasing the initial concentration of the pollutant and pH of the solution. The study envisages that among the iron nanoparticles prepared in TiO_2/zeolite composites, 25-T-Z-Fe is the most efficient material for the removal of environmental pollutants.

5.5. References

[1] A. Shanaghi, A.R. Sabour, T. Shahrabi, M. Aliofkhazraee, Corrosion protection of mild steel by applying TiO_2 nanoparticle coating via sol-gel method, Prot. Met. Phys. Chem. Surfaces. 45 (2009) 305–311. https://doi.org/10.1134/S2070205109030071.

[2] W. Zhang, L. Zou, L. Wang, Photocatalytic TiO_2/adsorbent nanocomposites prepared via wet chemical impregnation for wastewater treatment: A review, Appl. Catal. A Gen. 371 (2009) 1–9. https://doi.org/10.1016/j.apcata.2009.09.038.

[3] M. Abbas, Experimental investigation of titanium dioxide as an adsorbent for removal of Congo red from aqueous solution, equilibrium and kinetics modeling, J. Water Reuse Desalin. 10 (2020) 251–266. https://doi.org/10.2166/wrd.2020.038.

[4] S.-Y. Lee, S.-J. Park, TiO_2 photocatalyst for water treatment applications, J. Ind. Eng. Chem. 19 (2013) 1761–1769. https://doi.org/10.1016/j.jiec.2013.07.012.

[5] S. Riaz, S.-J. Park, An overview of TiO_2-based photocatalytic membrane reactors for water and wastewater treatments, J. Ind. Eng. Chem. 84 (2020) 23–41. https://doi.org/10.1016/j.jiec.2019.12.021.

[6] E.A. Serna-Galvis, J. Silva-Agredo, A.L. Giraldo, O.A. Flórez, R.A. Torres-Palma,

Comparison of route, mechanism and extent of treatment for the degradation of a β-lactam antibiotic by TiO 2 photocatalysis, sonochemistry, electrochemistry and the photo-Fenton system, Chem. Eng. J. 284 (2016) 953–962. https://doi.org/10.1016/j.cej.2015.08.154.

[7] H. Khan, I.K. Swati, Fe^{3+} -doped Anatase TiO 2 with d–d Transition, Oxygen Vacancies and Ti^{3+} Centers: Synthesis, Characterization, UV–vis Photocatalytic and Mechanistic Studies, Ind. Eng. Chem. Res. 55 (2016) 6619–6633. https://doi.org/10.1021/acs.iecr.6b01104.

[8] E. Petala, M. Baikousi, M.A. Karakassides, G. Zoppellaro, J. Filip, J. Tuček, K.C. Vasilopoulos, J. Pechoušek, R. Zbořil, Synthesis, physical properties and application of the zero-valent iron/titanium dioxide heterocomposite having high activity for the sustainable photocatalytic removal of hexavalent chromium in water, Phys. Chem. Chem. Phys. 18 (2016) 10637–10646. https://doi.org/10.1039/c6cp01013j.

[9] S. Mustapha, M.M. Ndamitso, A.S. Abdulkareem, J.O. Tijani, D.T. Shuaib, A.O. Ajala, A.K. Mohammed, Application of TiO_2 and ZnO nanoparticles immobilized on clay in wastewater treatment: a review, Appl. Water Sci. 10 (2020) 49. https://doi.org/10.1007/s13201-019-1138-y.

[10] J. Huang, S. Yi, C. Zheng, I.M.C. Lo, Persulfate activation by natural zeolite supported nanoscale zero-valent iron for trichloroethylene degradation in groundwater, Sci. Total Environ. 684 (2019) 351–359. https://doi.org/10.1016/j.scitotenv.2019.05.331.

[11] Q. Sun, X. Hu, S. Zheng, Z. Sun, S. Liu, H. Li, Influence of calcination temperature on the structural, adsorption and photocatalytic properties of TiO_2 nanoparticles supported on natural zeolite, Powder Technol. 274 (2015) 88–97. https://doi.org/10.1016/j.powtec.2014.12.052.

[12] Y.H. Jan, L.Y. Lin, M. Karthik, H. Bai, Titanium dioxide/zeolite catalytic adsorbent for the removal of NO and acetone vapors, J. Air Waste Manag. Assoc. 59 (2009) 1186–1193. https://doi.org/10.3155/1047-3289.59.10.1186.

[13] D. Mirzaei, A. Zabardasti, Y. Mansourpanah, M. Sadeghi, S. Farhadi, Efficacy of Novel NaX/MgO–TiO_2 Zeolite Nanocomposite for the Adsorption of Methyl Orange (MO) Dye: Isotherm, Kinetic and Thermodynamic Studies, J. Inorg. Organomet. Polym. Mater. 30 (2020) 2067–2080. https://doi.org/10.1007/s10904-019-01369-9.

[14] K. Kusdianto, M. Hudandini, D. Jiang, M. Kubo, M. Shimada, Effect of Heating Rate on the Photocatalytic Activity of Ag–TiO_2 Nanocomposites by One-Step Process via Aerosol Routes, Catalysts. 12 (2021) 17. https://doi.org/10.3390/catal12010017.

[15] S.M. Baghbanian, Synthesis, characterization, and application of Cu 2 O and NiO nanoparticles supported on natural nanozeolite clinoptilolite as a heterogeneous catalyst for the synthesis of pyrano[3,2-b]pyrans and pyrano[3,2-c]pyridones, RSC Adv. 4 (2014) 59397–59404. https://doi.org/10.1039/C4RA10537K.

[16] A. Kalantarifard, J.G. Gon, G.S. Yang, Formaldehyde Adsorption into Clinoptilolite Zeolite Modified with the Addition of Rich Materials and Desorption Performance Using Microwave Heating, Terr. Atmos. Ocean. Sci. 27 (2016) 865–875. https://doi.org/10.3319/TAO.2016.05.28.01(TT).

[17] W. Gao, D. Zhong, Y. Xu, H. Luo, S. Zeng, Nano zero-valent iron supported by macroporous styrene ion exchange resin for enhanced Cr(VI) removal from aqueous solution, J. Dispers. Sci. Technol. (2020) 1–11. https://doi.org/10.1080/01932691.2020.1848583.

[18] Y. Sun, B. Yang, Y. Tian, G. Guo, W. Cai, M. He, Y. Liu, Facile synthesis of Ag–Fe_2O_3 core–shell composite nanoparticles by an in situ method, Micro Nano Lett. 6 (2011) 82–

85. https://doi.org/10.1049/mnl.2010.0149.

[19] S. Sood, A. Umar, S.K. Mehta, S.K. Kansal, Highly effective Fe-doped TiO 2 nanoparticles photocatalysts for visible-light driven photocatalytic degradation of toxic organic compounds, J. Colloid Interface Sci. 450 (2015) 213–223. https://doi.org/10.1016/j.jcis.2015.03.018.

[20] G. Zhang, A. Song, Y. Duan, S. Zheng, Enhanced photocatalytic activity of TiO_2/zeolite composite for abatement of pollutants, Microporous Mesoporous Mater. 255 (2018) 61–68. https://doi.org/10.1016/j.micromeso.2017.07.028.

[21] S. Bagheri, K. Shameli, S.B. Abd Hamid, Synthesis and Characterization of Anatase Titanium Dioxide Nanoparticles Using Egg White Solution via Sol-Gel Method, J. Chem. 2013 (2013) 1–5. https://doi.org/10.1155/2013/848205.

[22] Y. Rashtbari, J.H.P. Américo-Pinheiro, S. Bahrami, M. Fazlzadeh, H. Arfaeinia, Y. Poureshgh, Efficiency of Zeolite Coated with Zero-Valent Iron Nanoparticles for Removal of Humic Acid from Aqueous Solutions, Water. Air. Soil Pollut. 231 (2020). https://doi.org/10.1007/s11270-020-04872-9.

[23] Y. Song, X. Lu, Z. Liu, W. Liu, L. Gai, X. Gao, H. Ma, Efficient Removal of Cr(VI) by TiO_2 Based Micro-Nano Reactor via the Synergy of Adsorption and Photocatalysis, Nanomaterials. 12 (2022) 291. https://doi.org/10.3390/nano12020291.

[24] M. Tanyol, Rapid malachite green removal from aqueous solution by natural zeolite: process optimization by response surface methodology, Desalin. WATER Treat. 65 (2017) 294–303. https://doi.org/10.5004/dwt.2017.20185.

[25] Z. Zafar, R. Fatima, J.-O. Kim, Effect of HCl treatment on physico-chemical properties and photocatalytic performance of Fe–TiO_2 nanotubes for hexavalent chromium reduction and dye degradation under visible light, Chemosphere. 284 (2021) 131247. https://doi.org/10.1016/j.chemosphere.2021.131247.

[26] M.N. Chong, Z.Y. Tneu, P.E. Poh, B. Jin, R. Aryal, Synthesis, characterisation and application of TiO_2-zeolite nanocomposites for the advanced treatment of industrial dye wastewater, J. Taiwan Inst. Chem. Eng. 50 (2015) 288–296. https://doi.org/10.1016/j.jtice.2014.12.013.

[27] S. Banerjee, M.C. Chattopadhyaya, Adsorption characteristics for the removal of a toxic dye, tartrazine from aqueous solutions by a low cost agricultural by-product, Arab. J. Chem. 10 (2017) S1629–S1638. https://doi.org/10.1016/j.arabjc.2013.06.005.

[28] V. Chaturvedi, P. Verma, Biodegradation of malachite green by a novel copper-tolerant Ochrobactrum pseudogrignonense strain GGUPV1 isolated from copper mine waste water, Bioresour. Bioprocess. 2 (2015). https://doi.org/10.1186/s40643-015-0070-8.

CHAPTER 6

Green synthesis of iron nanoparticles using plant extracts of *Abrus precatorius* and *Strychnos nux-vomica* for the removal of Cr(VI) and malachite green dye from water

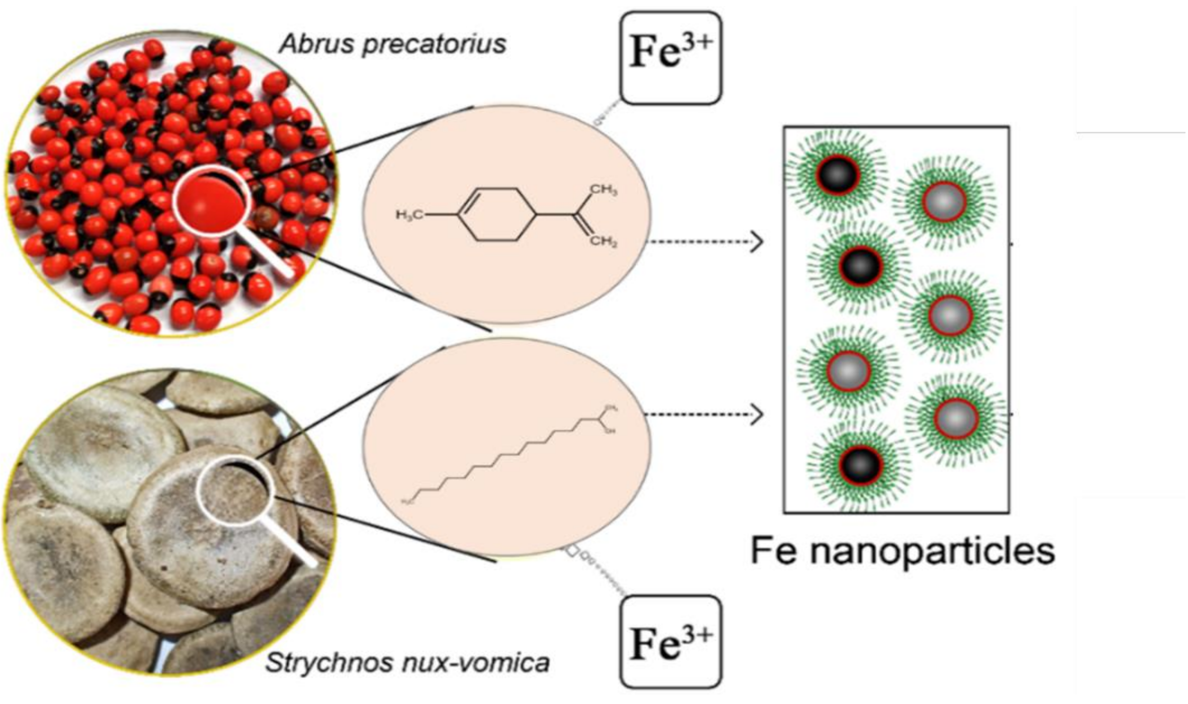

Chapter 6

Green synthesis of iron nanoparticles using plant extracts of Abrus precatorius and Strychnos nux-vomica for the removal of Cr(VI) and malachite green dye from water

6.1. Introduction

Different synthesis routes were developed for Fe nanoparticles including physical, chemical and biological methods. Chemically synthesised Fe nanoparticles get easily oxidised in aerobic conditions and agglomerated due to the magnetic property of Fe nanoparticles. Researchers introduced supporting material and stabilising agents for iron nanoparticles to overcome this problem. Even though these materials decrease the agglomeration and oxidation tendency of the Fe nanoparticles, they may adversely affect the efficiency of Fe nanoparticles due to the competition for the active sites with target pollutants. The high production cost and water pollution due to residual toxic reductants are also the downsides of chemically synthesised Fe nanoparticles[1].

Green synthesis of Fe nanoparticles is a suitable alternative for chemically synthesised nanoparticles. Although plants, microorganisms and enzymes were used in green synthesis, plant extracts are the most investigated green reducing agents for Fe nanoparticles. In green synthesis, Fe nanoparticles were prepared by the simple mixing of Fe precursor solution with plant extract at room temperature. High activity, small particle size, high dispersibility, high stability, nontoxicity, cost-effectiveness and environmental friendliness are the attractive features of green Fe nanoparticles. Also, it does not require any additional supporting, stabilising or capping agents. So far, various plant extracts such as *Eucalyptus globules*, *Amaranthus dubius*, *Emblica Officinalis*, *Citrus limetta*, *Moringa oleifera*, green tea, Aloe vera and Clove have been reported for the synthesis of Fe nanoparticles. Most plant extracts are derived from plant leaves and water as the extracing solvent. The critical active components present in the plant extract for reducing Fe^{3+} ions are polyphenols, flavonoids, amino acids, terpenoids, reducing sugars, steroids, saponins, vitamins, alkaloids and organic acids. Diverse plant species and their complex bioactive components are still unknown to the world. It makes the booster on the search of the most appropriate and strong reducing agent for Fe nanoparticles, even though some plant extracts have succeeded in the effective production of Fe nanoparticles[2].

In this study, two novel plant extracts, ethanolic seed coat extracts of *Abrus precatorius* (AP) and *Strychnos nux-vomica* (SN) were selected for the effective production of Fe nanoparticles. Photographs of seeds of AP and SN are shown in figure 6.1. AP, commonly known as rosary pea, is a leguminous plant native to India and seen in other tropical and subtropical areas. Traditionally, the leaves, seeds and roots were used for medicinal purposes[3]. Recently, zinc sulfide nanoparticles were produced from AP leaf extract and tested for toxicity using *Eudrilus eugeniae*[4]. Silver nanoparticles produced from the leaf extract of AP showed antibacterial activity against gram-positive and gram-negative bacteria[5]. The AP seeds are usually tiny and have a red and black seed coat. Campesterol, cholesterol, palmitic acid, lignoceric acid, linoleic acid, oleic acid, β-sitosterol, stigmasterol, trigonelline and brassicasterol are the significant components contained in AP seed[3]. *Strychnos nux-vomica* is a deciduous tree native to southeast Asia and belonging to the *Loganiaceae* family[6]. Its dried seeds are used to treat cancer, rheumatic pain, arthritis, inflammation and central nervous system disorders in traditional medicine[7]. Alkaloids, flavonoids, tannins, saponins and glycosides are the phytochemicals present in the SN and are responsible for its antioxidant, antidiabetic, antidiarrhoeal, antiviral, analgesic and anti-inflammatory properties[6]. SN contains two major alkaloids (strychnine and brucine) and a significant amount of glucoside (loganic acid)[8]. Other phytochemicals present in SN are α-colubrine, β-colubrine, 3-methoxyicajine, protostrychnine, novacine, n-oxystrychnine, pseudostrychnine, isostrychnine, chlorogenic acid, vomicine and igasurine[9]. In 2018, ZnO phytonano composites were prepared from aqueous leaf extract of *Strychnos nux-vomica,* exhibiting potential antimicrobial activity[10]. Rectified ethanol is used as the extracting solvent since it dissolves the majority of the plant bioactive components and prevents the growth of microbes during storage.

This work adopts a simple, eco-friendly method for synthesising Fe nanoparticles using AP and SN plant extracts to remove Cr(VI) and malachite green dye from water. In the presence of hydrogen peroxide, Fe nanoparticles act as Fenton-like catalyst and produce more hydroxyl radicals. These hydroxyl radicals can cause the degradation of the dye molecules[2,11]. The specific objectives are to 1) synthesise Fe nanoparticles using AP and SN plant extract, 2) examine the chemical reactivity of AP-Fe and SN-Fe for the removal of Cr(VI) and malachite green dye from water, 3) investigate the influence of different parameters such as initial pollutant concentration, pH, the dosage of adsorbent and contact time during the removal of pollutant.

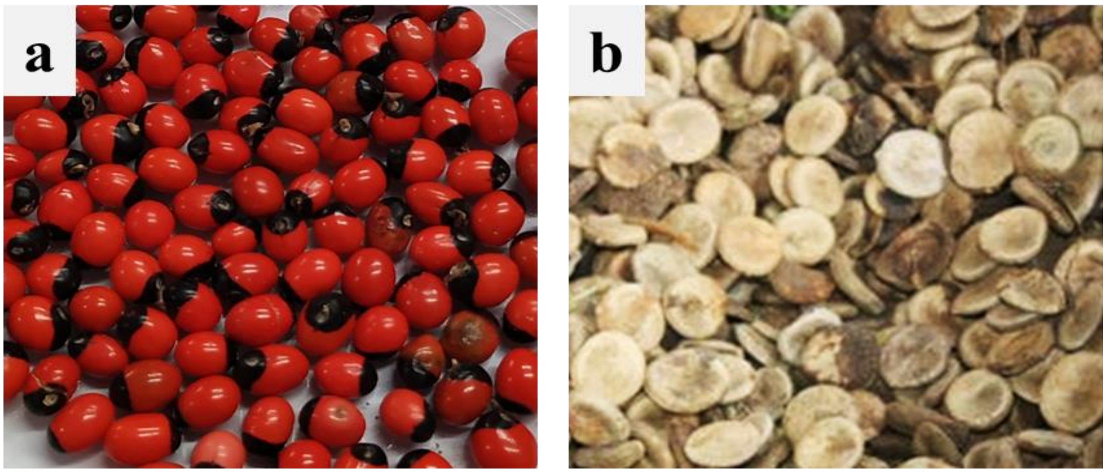

Figure 6.1 *Photographs of seeds of Abrus precatorius (a) and Strychnos nux-vomica (b)*

6.2. Experimental details

6.2.1 Preparation of plant extracts and phytogenic Fe nanoparticles

Preparation of AP and SN extract

The dried seeds of *Abrus precatorius* and *Strychnos nux-vomica* collected from the local market were washed and dried to remove impurities and moisture. AP seeds were crushed into small pieces using a pestle and mortar and seed coats were separated manually. SN seeds were cut into small pieces, ground using a mixer and feathery seed coats were collected manually. The plant extract was prepared by refluxing 4g of plant seed coat in 100 mL ethanol at a temperature of 90ºC for 2 hours. The extract was then cooled, filtered using Whatman number 41 filter paper and stored at 4ºC for further use.

Synthesis of phytogenic Fe nanoparticles

Fe nanoparticles were synthesised by mixing the prepared plant extracts with 0.01 M ferric chloride ethanol solution at a 1:1 volume ratio at room temperature. The rapid development of black colour suspension indicates the formation of Fe nanoparticles. This suspension was centrifuged and the collected nanoparticles were lyophilised and then stored in airtight vials for characterisation studies.

6.2.2 Batch experiments

Cr(VI) removal studies

To simplify the removal studies procedure and evade the loss of Fe nanoparticles during the centrifugation and drying process, the phytogenic Fe nanoparticles were added in liquid form. For this, 10 mL of 5 mg/L Cr(VI) solution was treated with freshly prepared 0.2 mL of phytogenic nanoparticles. Effect of different parameters such as nanoparticle dosage (0.1-0.5 mL), initial concentration of Cr(VI) (1-7 mg/L), initial pH of the solution (4-10) and contact time (10-40 min) was also examined. NaOH (1.0 M) and H_2SO_4 1.0 M) were used for the pH adjustment and all the experiments were performed with a duplicate.

Malachite green dye removal studies

MG dye removal experiments were carried out in a 30 mL vial in which the freshly prepared 1mL of phytogenic nanoparticles was treated with 10 mL 50 mg/L dye solution and added 1 mL of H_2O_2 into it. After agitating the solution for 15 minutes using a bath sonicator, the samples were centrifuged to remove the nanoparticles and the residual dye concentration was measured using a UV-visible spectrophotometer. Samples without nanoparticles were also investigated. To study the effect of various parameters, different nanoparticle dosage (1-5 mL), initial concentration of MG dye (10-50 mg/L), pH of the solution (5-9) and contact time (10-40 min) were also investigated.

6.2.3 Characterisation and analytical techniques used

The properties of plant extract were examined by UV-visible spectrophotometer and FTIR. The phytogenic iron nanoparticles were lyophilised using Operon FDU 7003 lyophiliser. The characterisation of prepared nanoparticles was done by HRTEM, EDAX, FTIR and UV-visible spectrophotometer. The details of characterisation techniques were discussed in chapter 2. Fourier transform infrared spectra of the AP and SN plant extracts and AP-Fe and SN-Fe nanoparticles were investigated through Spectrum Two Fourier transform infrared spectrometer (FTIR, Perkin Elmer, USA). Jeol 6390LA/OXFORD XMX N was used to analyse AP-Fe and SN-Fe nanoparticles elemental analysis. GC-MS/MS was used to determine the plant extract components and malachite green degradation products in the solution. The method used in GC-MS/MS analysis has conversed in chapter 3.

6.3. Results and discussion

6.3.1 Characterisation of AP and SN plant extracts

The phytochemical composition of plant extracts has been analysed through GC-MS/MS. Alcohols, phenols, flavonoids, terpenoids, aldehydes, amines and alkanes are the major compounds present in the AP and SN seed coat extracts[8,12]. The mass spectra of identified compounds of AP and SN seed coat extracts by GC-MS/MS are shown in figure 6.2(a1-a8) and figure 6.3(b1-b5) respectively. Biomolecules identified by GC-MS/MS in the AP and SN extracts and their properties were listed in table 6.1. The -OH, -CHO and C=O functional groups in the biomolecules get oxidised into –COOH simultaneously reducing Fe^{3+} ions to Fe nanoparticles. The biomolecules like limonene and 2-hexadecanol act as reducing and stabilising/capping agents, preventing the overgrowth and aggregation of nanoparticles and supporting the reduction of Fe^{3+} ions[13]. Some other biomolecules act as antioxidants that prevent the oxidation of formed nanoparticles and impart more stability.

No.	Retention time (t)	Name of the compound	Molecular weight	Action	Reference
Abrus precautious					
a1.	6.27	furan-2-carbaldehyde	96	Stabilizing agent	[14]
a2.	8.55	1-methyl-4-prop-1-en-2-ylcyclohexene	136	Reducing and capping agent	[15]
a3.	10.21	2,6,6-trimethylbicyclo[3.1.1]hept-2-ene	136	Antioxidant	[16]
a4.	17.25	2,2,4-trimethyl-1H-quinoline	173	Antioxidant	[17]
a5.	23.86	ethyl 3,4,5-trihydroxybenzoate	198	Antioxidant	[18,19]
a6.	12.10	3,5-dihydroxy-6-methyl-2,3-dihydropyran-4-one	144	Antioxidant	[20]
a7.	13.59	5-(hydroxymethyl)furan-2-carbaldehyde	126	Reducing agent	[21]
a8.	20.42	3H-1,3-benzothiazol-2-one	151	Antioxidant	[22]

Strychnos nux-vomica					
b1.	12.01	1,2-dimethoxybenzene	138	Antioxidant	[23,24]
b2.	12.89	3-methoxy-2-methylpyran-4-one	140	Antioxidant	[25]
b3.	17.23	2,2,4-trimethyl-1H-quinoline	173	Antioxidant	[17]
b4.	18.36	4-methoxy-6-prop-2-enyl-1,3-benzodioxole	192	Antioxidant	[26]
b5.	21.73	hexadecan-2-ol	242	Reducing and stabilising agent	[27]

Table 6.1 *Biomolecules identified in AP and SN extract by GC-MS/MS*

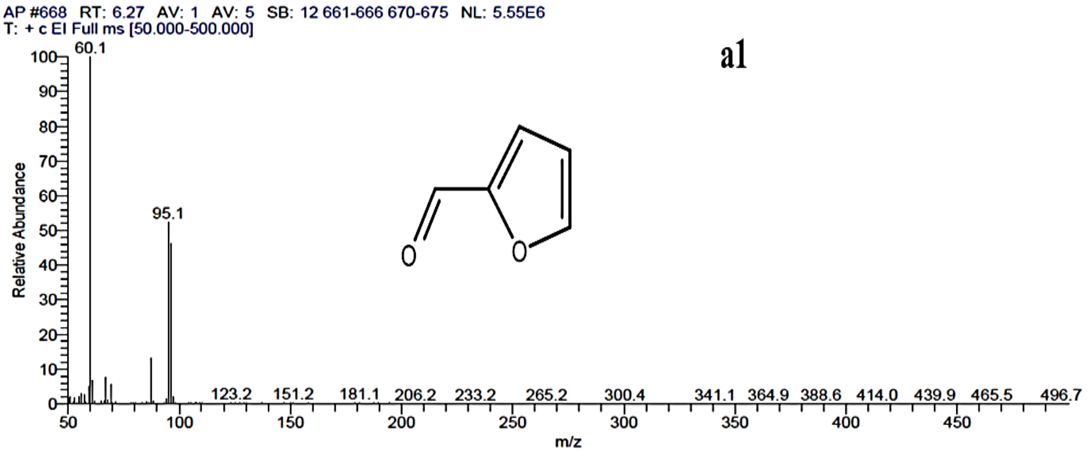

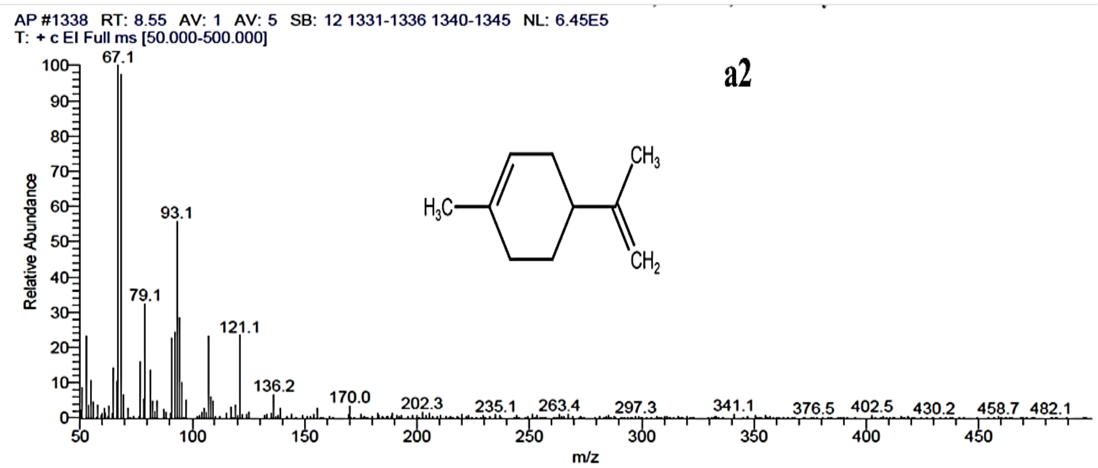

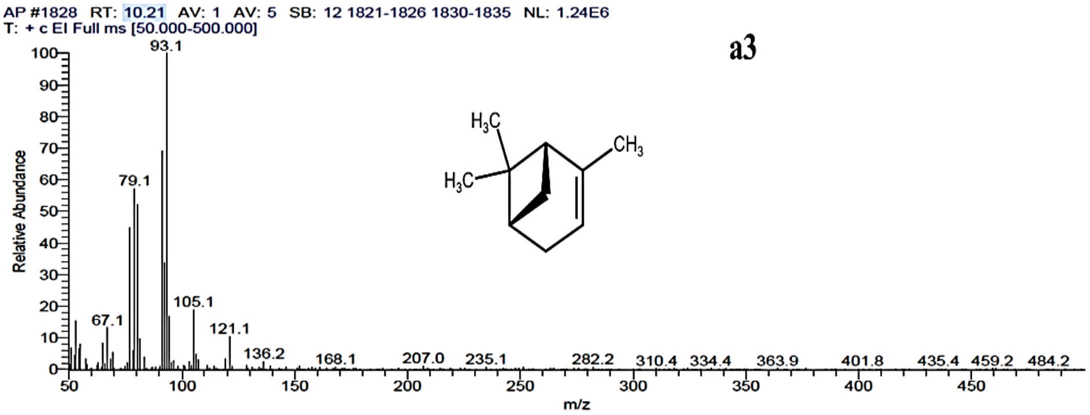
AP #1828 RT: 10.21 AV: 1 AV: 5 SB: 12 1821-1826 1830-1835 NL: 1.24E6
T: + c EI Full ms [50.000-500.000]
a3
Relative Abundance
m/z
93.1
79.1
67.1
105.1
121.1
136.2
168.1
207.0
235.1
282.2
310.4
334.4
363.9
401.8
435.4
459.2
484.2
H_3C
H_3C
CH_3

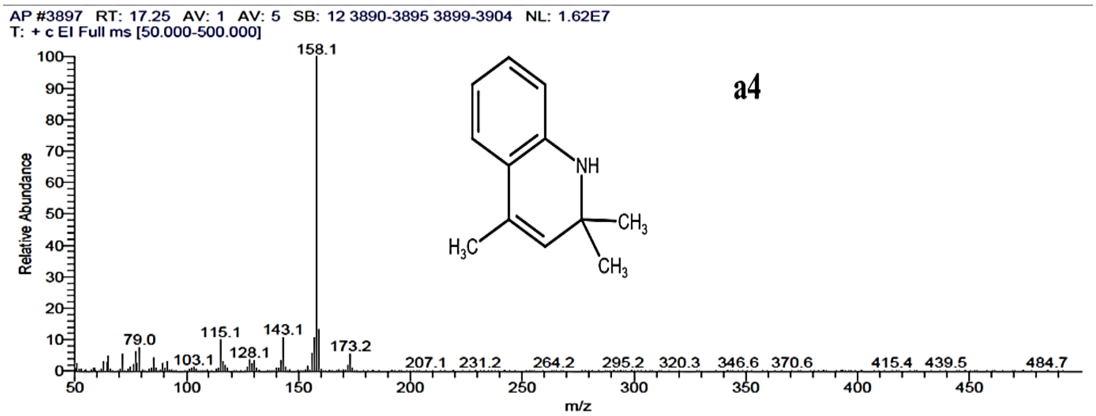
AP #3897 RT: 17.25 AV: 1 AV: 5 SB: 12 3890-3895 3899-3904 NL: 1.62E7
T: + c EI Full ms [50.000-500.000]
a4
Relative Abundance
m/z
158.1
79.0
103.1
115.1
128.1
143.1
173.2
207.1
231.2
264.2
295.2
320.3
346.6
370.6
415.4
439.5
484.7
NH
CH_3
CH_3
H_3C

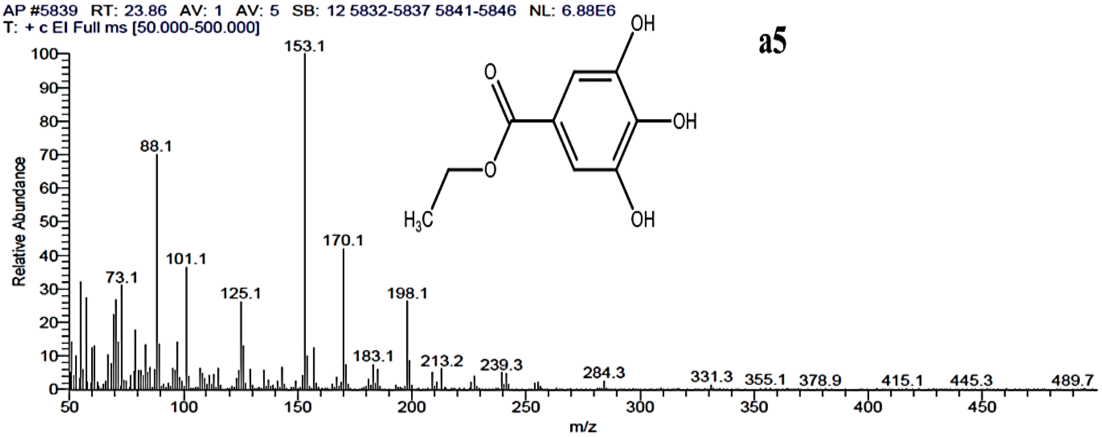
AP #5839 RT: 23.86 AV: 1 AV: 5 SB: 12 5832-5837 5841-5846 NL: 6.88E6
T: + c EI Full ms [50.000-500.000]
a5
Relative Abundance
m/z
153.1
88.1
73.1
101.1
125.1
170.1
198.1
183.1
213.2
239.3
284.3
331.3
355.1
378.9
415.1
445.3
489.7
OH
O
OH
O
H_3C
OH

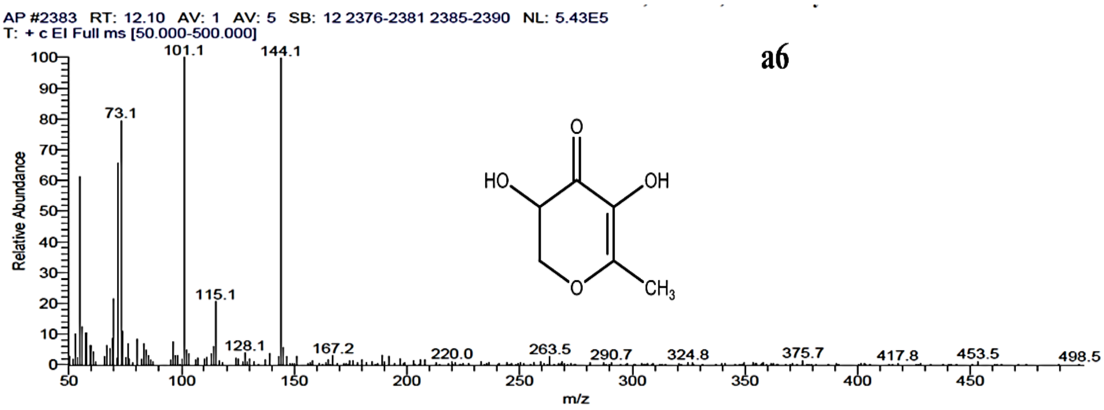
AP #2383 RT: 12.10 AV: 1 AV: 5 SB: 12 2376-2381 2385-2390 NL: 5.43E5
T: + c EI Full ms [50.000-500.000]
a6
Relative Abundance
m/z
101.1
144.1
73.1
115.1
128.1
167.2
220.0
263.5
290.7
324.8
375.7
417.8
453.5
498.5
O
HO
OH
O
CH_3

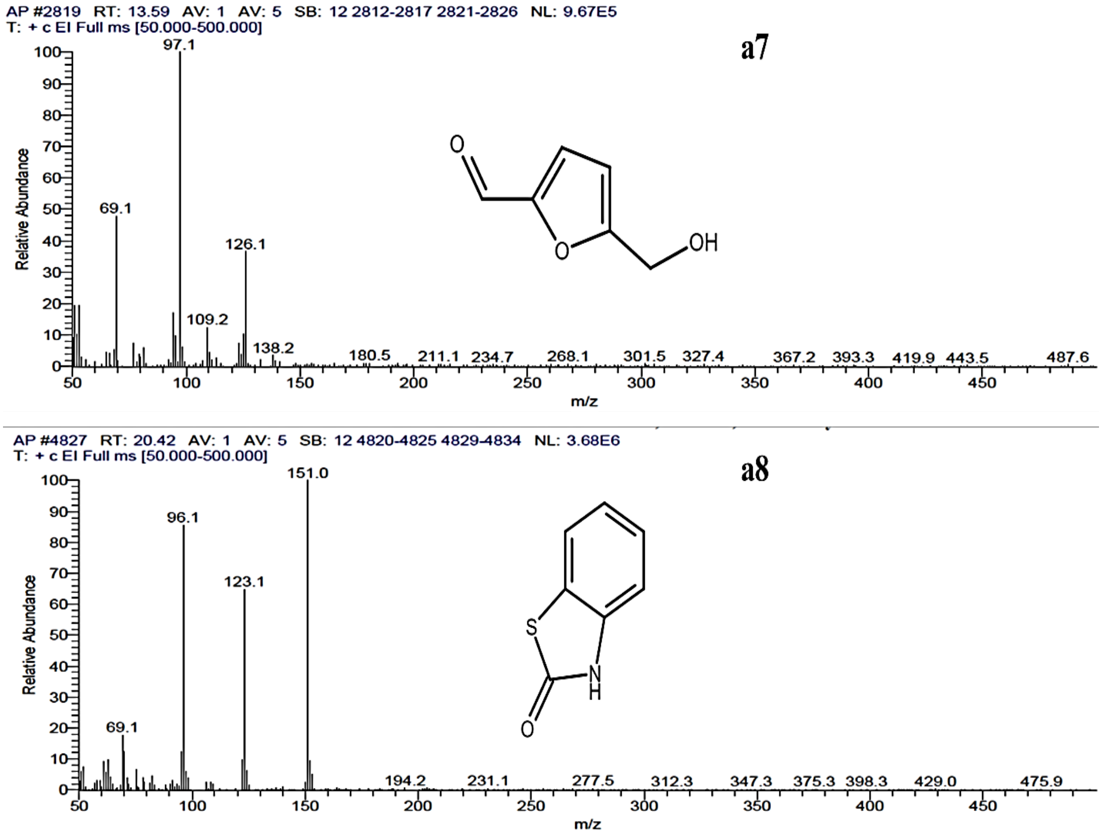

Figure 6.2 *Mass spectra of compounds identified in AP extract by GC-MS/MS. (a1) furan-2-carbaldehyde; (a2) 1-methyl-4-prop-1-en-2-ylcyclohexene; (a3) 2,6,6-trimethylbicyclo [3.1.1]hept-2-ene; (a4) 2,2,4-trimethyl-1H-quinoline; (a5) ethyl 3,4,5-trihydroxybenzoate ; (a6) 3,5-dihydroxy-6-methyl-2,3-dihydropyran-4-one; (a7) 5-(hydroxymethyl)furan-2-carbaldehyde; (a8) 3H-1,3-benzothiazol-2-one*

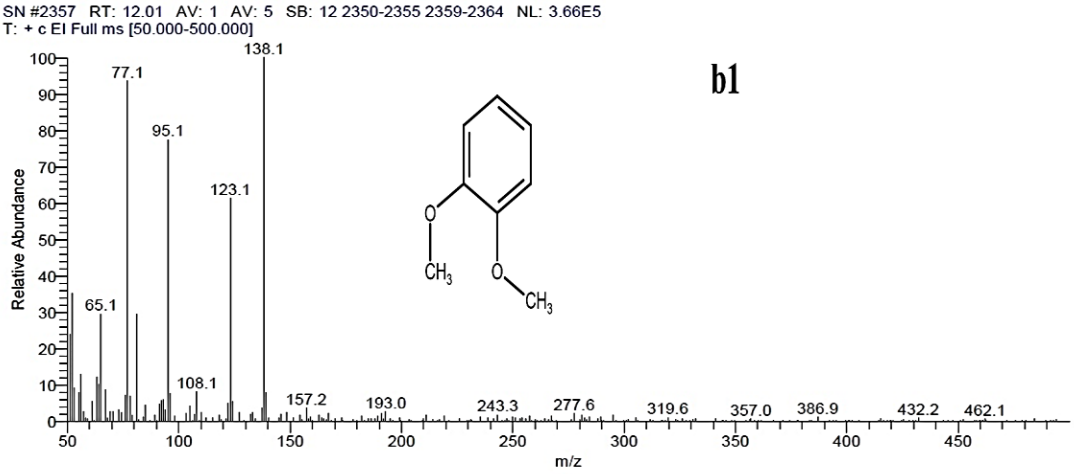

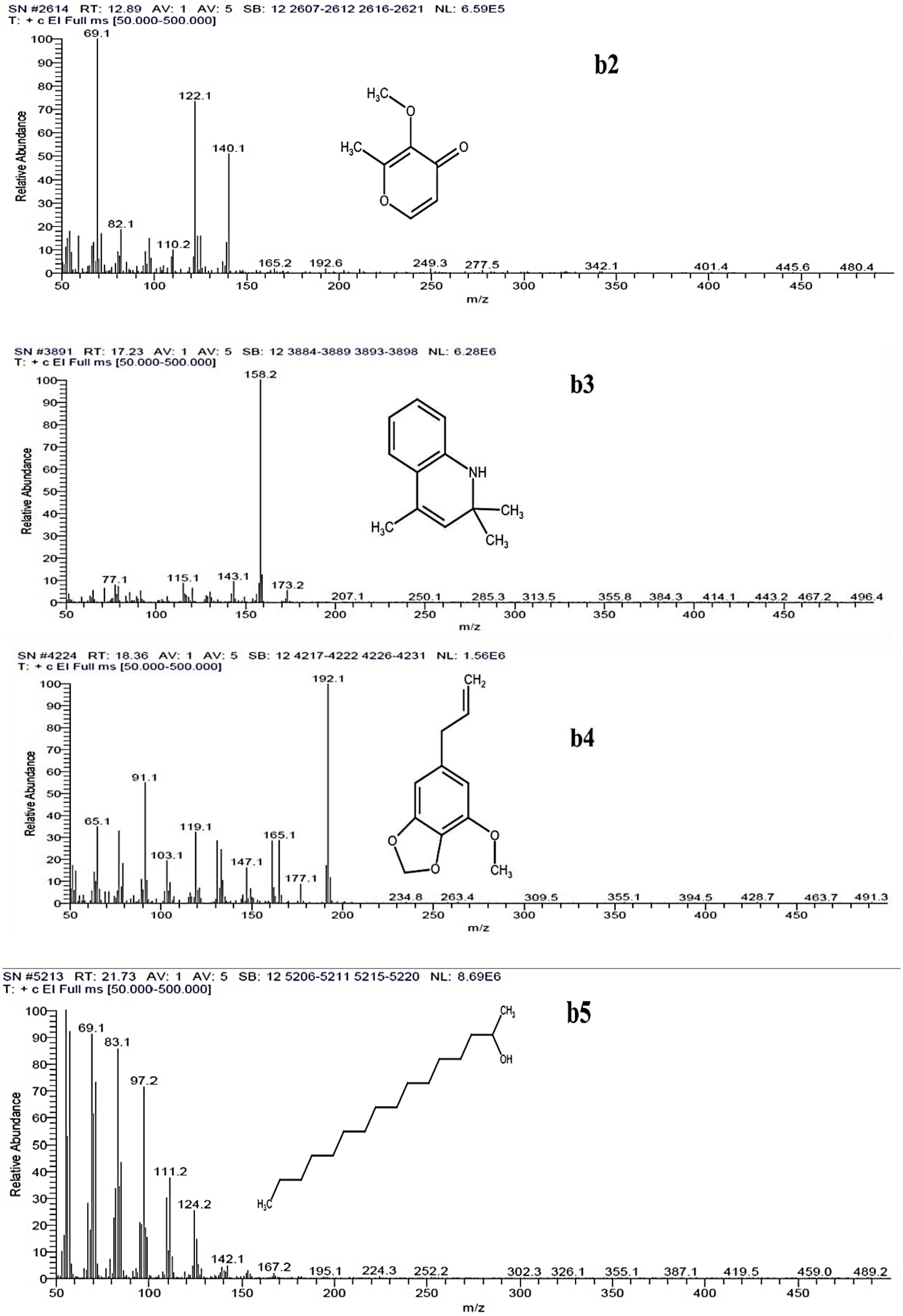

Figure 6.3 Mass spectra of compounds identified in SN extract by GC-MS/MS. (b1) 1,2-dimethoxybenzene; (b2) 3-methoxy-2-methylpyran-4-one; (b3) 2,2,4-trimethyl-1H-quinoline; (b4) 4-methoxy-6-prop-2-enyl-1,3-benzodioxole; (b5) hexadecan-2-ol

6.3.2 Characterisation of AP-Fe and SN-Fe nanoparticles

UV-visible spectroscopy

A dark black solution was formed immediately when the plant extracts were mixed with $FeCl_3$ solution, indicating the formation of Fe nanoparticles[28]. The black precipitates in the solution were visually observable; however, the formation of iron nanoparticles was further confirmed by a UV-visible spectrophotometer. The UV-visible spectra of AP and SN extract, $FeCl_3$ solution and phytogenic iron nanoparticles are shown in figure 6.4. The $FeCl_3$ solution and plant extracts did not show any characteristic peak in UV-visible spectra between 450-750 nm. Nevertheless, the AP-Fe and SN-Fe nanoparticles showed broad adsorption around this region, indicating the formation of Fe nanoparticles[29].

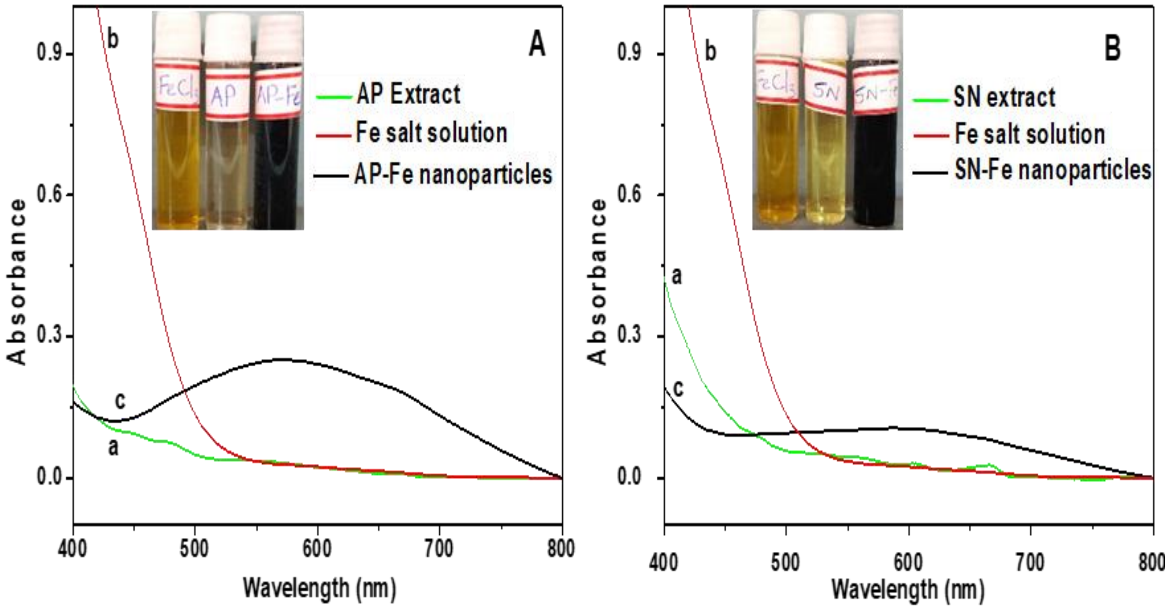

Figure 6.4 *Photographs and UV-visible spectra of A) a. AP extract, b. $FeCl_3$ solution and c. AP-Fe nanoparticles, B) a. SN extract, b. $FeCl_3$ solution and c. SN-Fe nanoparticles*

HRTEM

HRTEM photographs of AP-Fe and SN-Fe nanoparticles are shown in figure 6.5. The spherical SN-Fe nanoparticles are non-agglomerated and monodispersed. It can be due to the stabilisation by the major components of SN, such as strychnine and brucine. The particle size of SN-Fe nanoparticles ranged from 2.1 to 5 nm, having a mean diameter of 3.3 nm. SAED analysis of SN-Fe nanoparticles shows faded spots and diffused rings, which indicate the nanoparticles amorphous nature. The d-spacing values 2.73 Å and 2.14 Å calculated from the SAED pattern match with the (220) and (311) planes of the

Fe_3O_4[30]. AP-Fe nanoparticles were irregularly shaped with size ranging from 3 nm to 32 nm. SAED pattern comprised of spot patterns with diffused rings indicates the presence of dispersed crystalline particles over the amorphous phase of AP-Fe. AP extract contains plant components with different reducing and complexing capacities, leading to the formation of different Fe nanoparticles such as Fe^0 and Fe_3O_4. SAED pattern displays d-spacing values 2.0 Å and 2.89 Å corresponding to (311) and (213) plane of Fe^0[31]. The d- spacing values of 2.7 Å corresponds to the planes of Fe_3O_4[32].

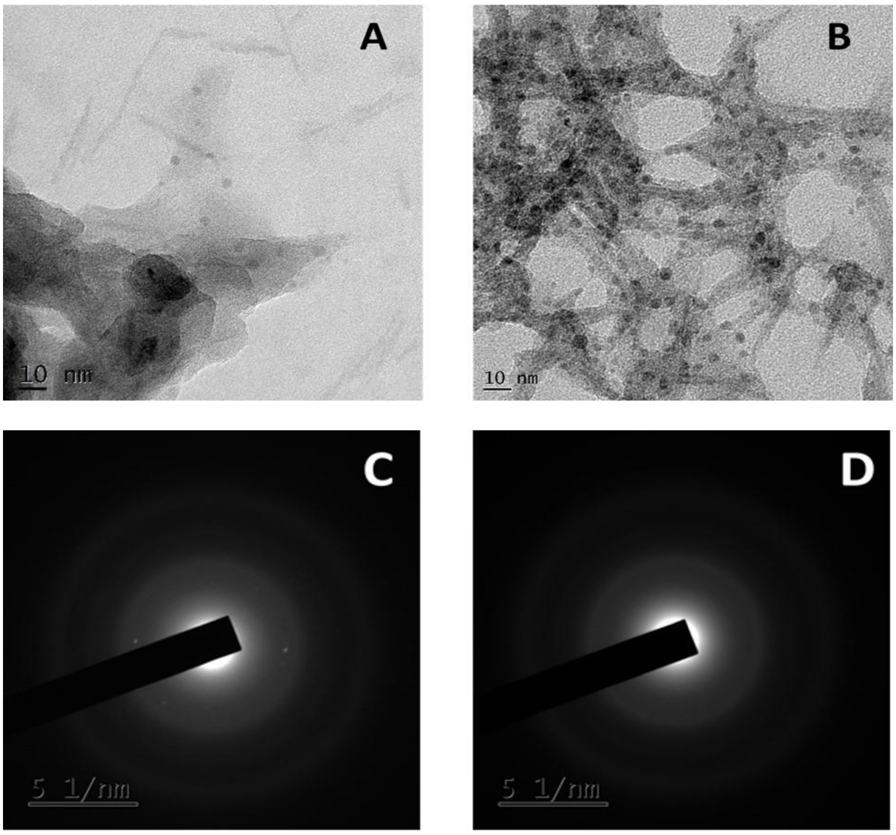

Figure 6.5 *TEM image of the synthesised A) AP-Fe nanoparticles and B) SN-Fe nanoparticles and SAED pattern of C) AP-Fe nanoparticles and D) SN-Fe nanoparticles*

EDAX

The qualitative and quantitative information of nanoparticles and the elements involved in the formation of nanoparticles has been studied through EDAX analysis. As shown in figure 6.6, the AP-Fe and SN-Fe nanoparticles depict intense peaks of Fe, C and O. The results reveal that the atomic percentages of iron in AP-Fe and SN-Fe nanoparticles were 7.57 and 7.15 respectively. The presence of C, O, Ca and K may be from the organic coating on the iron nanoparticles and the presence of chlorine from the ferric chloride which is used as the iron precursor during the synthesis of nanoparticles.

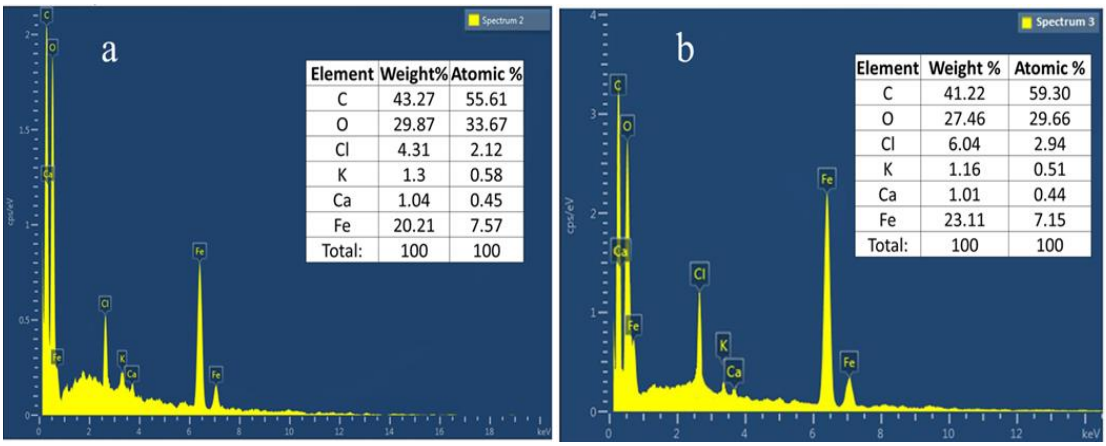

Element	Weight%	Atomic %
C	43.27	55.61
O	29.87	33.67
Cl	4.31	2.12
K	1.3	0.58
Ca	1.04	0.45
Fe	20.21	7.57
Total:	100	100

Element	Weight %	Atomic %
C	41.22	59.30
O	27.46	29.66
Cl	6.04	2.94
K	1.16	0.51
Ca	1.01	0.44
Fe	23.11	7.15
Total:	100	100

***Figure 6.6** EDAX spectra of a) AP-Fe nanoparticles and b) SN-Fe nanoparticles*

FTIR spectroscopy

The FTIR spectra of the AP-Fe and SN-Fe nanoparticles are shown in figure 6.7. It envisages the functional groups in bioactive components responsible for the formation and stabilisation of iron nanoparticles. The phytogenic nanoparticles showed a broad peak between 3700-3000 cm^{-1}, corresponding to O-H stretching and N-H stretching bands of polyphenols and amines respectively[33]. The peaks at 1725 cm^{-1} (AP-Fe) and 1719 cm^{-1} (SN-Fe) corresponds to the C=O stretching vibrations and the peaks at 1425 cm^{-1} (AP-Fe) and 1416 cm^{-1} (SN-Fe) corresponds to the O-H bending vibrations of -COOH group present in the phytogenic Fe nanoparticles. The peaks found at 1195 cm^{-1} for AP-Fe and 1192 cm^{-1} and 1035 cm^{-1} for SN-Fe is related to the C-N stretching vibrations and the peaks at 1579 cm^{-1} (AP-Fe) and 1581 cm^{-1} (SN-Fe) corresponds to the N-H bending vibrations of amines present in the plant component. The presence of aromatic amine was confirmed through C-N stretching vibrations which shows the peak at 1334 cm^{-1} for AP-Fe and 1328 cm^{-1} for SN-Fe nanoparticles. The peaks that appeared at 2925 cm^{-1} and 2856 cm^{-1} for AP-Fe and 2921 cm^{-1} and 2850 cm^{-1} for SN-Fe were associated with the C-H stretching vibrations. The stretching vibrations of C=C peaks at 1615 cm^{-1} and 1620 cm^{-1} correspond to AP-Fe and SN-Fe nanoparticles. The peaks observed at 1069 cm^{-1} (AP-Fe) and 1072 cm^{-1} (SN-Fe) indicates the O-H stretching vibrations of alcohol. The low intense peaks at 671 cm^{-1} (AP-Fe) and 679 cm^{-1} (SN-Fe) corresponds to the iron-carbonyl complexes (Fe–C=O), which confirmed the iron interaction with the plant components[34]. The peaks at 446 cm^{-1} and 467 cm^{-1} confirm the Fe-O stretching vibration of iron oxide present in the AP-Fe and SN-Fe nanoparticles[35]. The results envisage that plant components cling on the surface of Fe nanoparticles as capping agents and are part of the Fe nanoparticles. This organic moiety increases the stability of the Fe nanoparticles.

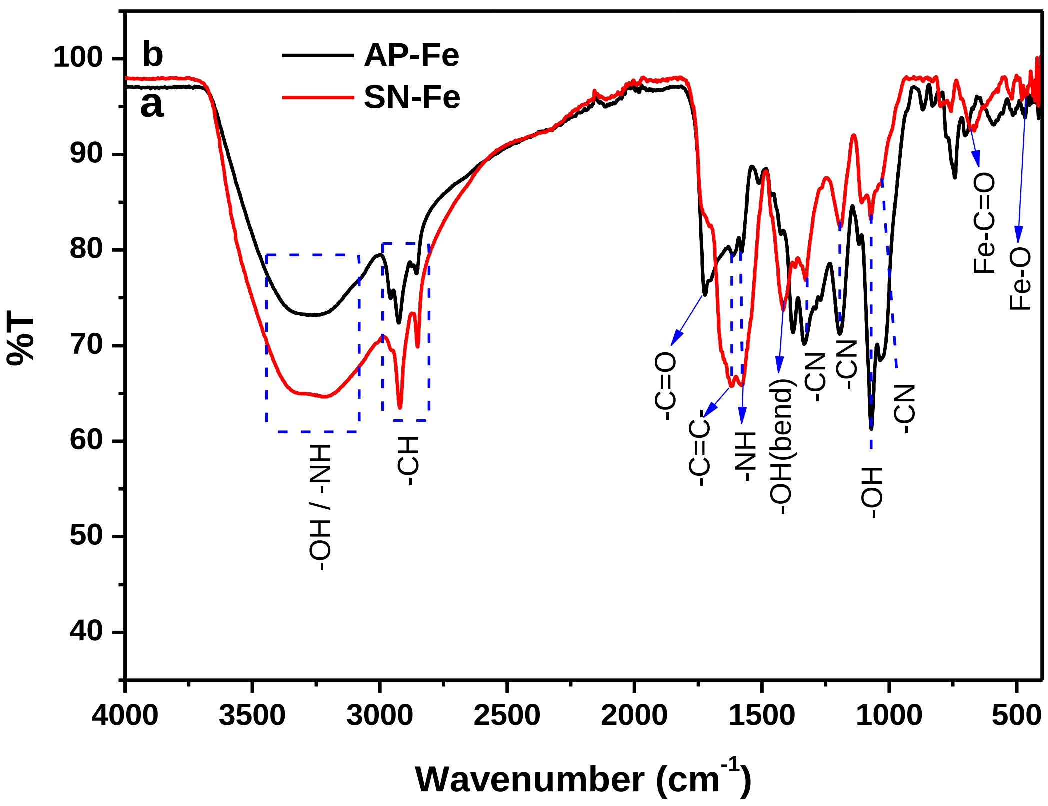

Figure 6.7 *FTIR spectra of a) AP-Fe nanoparticles and b) SN-Fe nanoparticles*

6.3.3 Cr(VI) removal studies

The Cr(VI) removal efficiency of AP-Fe and SN-Fe nanoparticles was evaluated using 0.2 mL phytogenic nanoparticles in 10 mL, 5 mg/L Cr(VI) solution for 15 minutes, as shown in figure 6.8. The AP-Fe and SN-Fe nanoparticles showed 73 % and 69 % removal efficiency which indicate that AP-Fe nanoparticles exhibit more Cr(VI) removal efficiency than SN-Fe nanoparticles. This is attributed to the composition of AP-Fe nanoparticles since they contain zero valent iron and iron oxide nanoparticles. Zero valent iron nanoparticles have shown more Cr(VI) reduction capacity than iron oxide nanoparticles[36]. The removal of Cr(VI) using phytogenic Fe nanoparticles displays reduction, precipitation and adsorption of chromium species[37,38]. The possible Cr(VI) removal mechanism of AP-Fe and SN-Fe nanoparticles was proposed in equations 6.1-6.6.

1. Adsorption process

$$Cr(VI) + AP - Fe \longrightarrow Cr(VI)/AP - Fe \tag{6.1}$$

$$Cr(VI) + (AP/SN) - Fe_2O_3 \longrightarrow Cr(VI)/(AP/SN) - Fe_3O_4 \tag{6.2}$$

$$Fe^{2+}/Fe^{3+} + H_2O \longrightarrow FeOOH \tag{6.3}$$

$$Cr(VI) + FeOOH \longrightarrow Cr(VI) - FeOOH \tag{6.4}$$

2. Reduction and precipitation process

$$2Fe^0 + Cr_2O_7^{2-} + 8H^+ \longrightarrow 3Fe^{2+} + 2Cr(OH)_3 + H_2O \tag{6.5}$$

$$6Fe^{2+} + Cr_2O_7^{2-} + 8H^+ \longrightarrow 6Fe^{3+} + 2Cr(OH)_3 + H_2O \tag{6.6}$$

In addition to this, plant components present in the solution also have an important role in removing Cr(VI). Plant extracts have different bioactive components which help to form Fe nanoparticles by acting as reducing and stabilising agents. These plant components may also have the capacity to remove Cr(VI) from water[36]. Overall, the phytogenic Fe nanoparticles display good Cr(VI) removal efficiency.

As per previous reports, different parameters influence Cr(VI) removal using phytogenic Fe nanoparticles. The influence of these parameters such as nanoparticle dosage, initial concentration of Cr(VI), initial pH of the Cr(VI) solution and contact time were investigated for Cr(VI) removal.

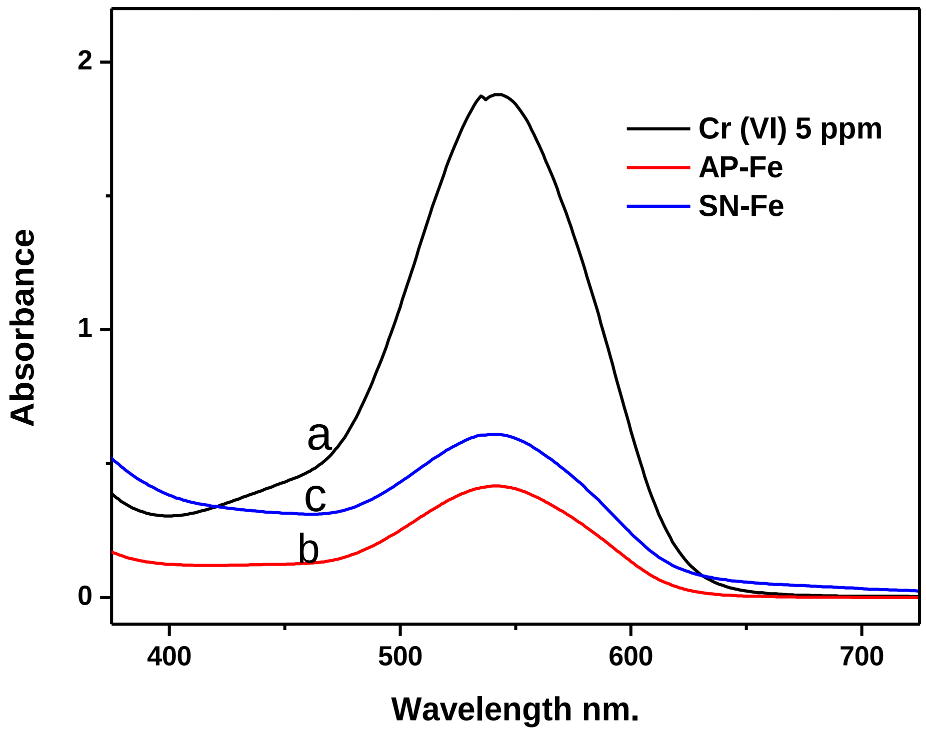

Figure 6.8 *UV-visible spectra of Cr(VI) solution after treating 15 minutes a) blank Cr(VI) 5 mg/L, b) AP-Fe nanoparticles and c) SN-Fe nanoparticles*

Effect of nanoparticle dosage

The effect of nanoparticle dosage was studied by varying the nanoparticles dosage from 0.1 mL to 0.5 mL, maintaining 5 mg/L as the initial concentration of Cr(VI) and 15 minutes as the contact time. Figure 6.9a indicates that the increased nanoparticle dosage enhances the extent of Cr(VI) removal. AP-Fe nanoparticles exhibit 100 % Cr(VI) removal using a dosage of 0.4 mL, while using the same quantity, SN-Fe nanoparticles exhibit only 76 % removal. The maximum removal attained by SN-Fe nanoparticles was 80 % using 0.5 mL nanoparticles. With the increase in nanoparticle dosage, the reactive sites for reduction and adsorption were also increased, leading to the higher removal of Cr(VI) ions. In short, AP-Fe nanoparticles show more potential to reduce Cr(VI) than SN-Fe nanoparticles.

Effect of the initial concentration of the Cr(VI) solution

As shown in figure 6.9b, the effect of initial Cr(VI) concentration on Cr(VI) removal was investigated while keeping all other parameters constant. In this study, 0.2 mL nanoparticle solution was added into different Cr(VI) concentrations, varied from 1 mg/L to 7 mg/L and the absorbance was measured after 15 minutes. When the chromium concentration was 1 mg/L, 100 % Cr(VI) removal occurred in AP-Fe nanoparticles and 89 % Cr(VI) removal occurred in SN-Fe nanoparticles. However, in 7 mg/L Cr(VI) solution, the removal percentage decreases to 71 % by AP-Fe nanoparticles and 58 % by SN-Fe nanoparticles. So with the increase in Cr(VI) concentration, naturally there occurs a decrease in the availability of sufficient reactive sites, for Cr(VI) ions, which eventually leads to the decrease in Cr(VI) removal efficiency.

Effect of contact time

The effect of contact time was studied by adding 0.2 mL phytogenic nanoparticles into 5 mg/L Cr(VI) solution and the samples were collected at regular time intervals of 10, 20, 30 and 40 minutes. As shown in figure 6.9c, Cr(VI) removal efficiency increases with increasing contact time, even though the increase in rate is not high. 67 % and 60 % of removal were observed for the first 10 minutes of contact time by AP-Fe and SN-Fe nanoparticles respectively. However, for 40 minutes of contact time, the Cr(VI) removal efficiency was 80 % and 71 % for AP-Fe and SN-Fe nanoparticles. This may be due to the fact that with the increase in contact time, the Cr(VI) molecules have more time to interact with the AP-Fe and SN-Fe nanoparticles and the removal efficiency increases. As time proceeds, iron gets exceedingly oxidised and the adsorption sites become blocked by precipitation leading to decreased Cr(VI) removal rate.

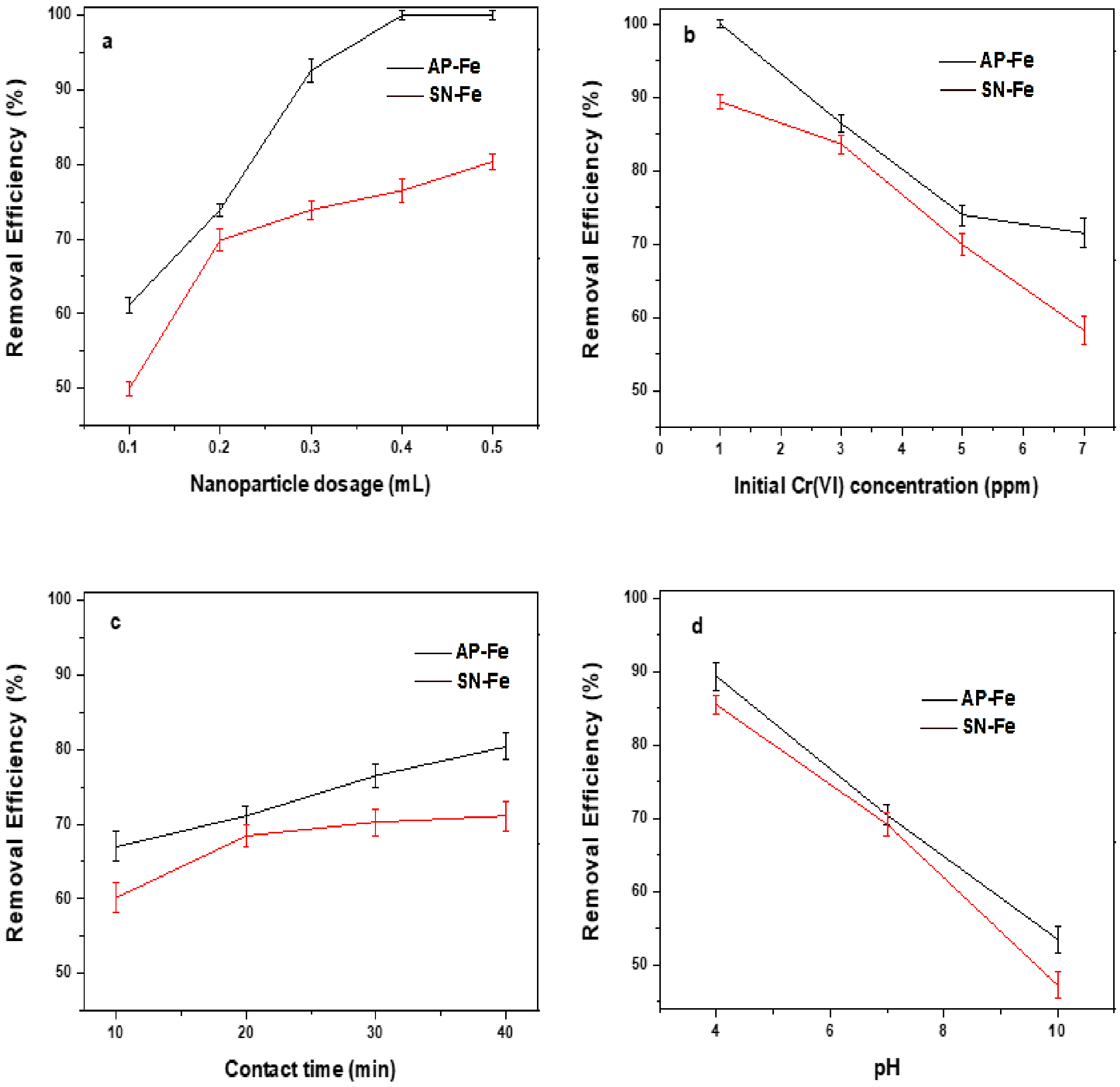

Figure 6.9 *Effects of various factors on Cr(VI) removal: (a) nanoparticle dosage, (b) initial Cr(VI) concentration, (c) contact time and (d) initial solution pH .*

Effect of pH

The initial pH of the solution greatly influences the efficiency of Cr(VI) removal. With 0.2 mL nanoparticles in 5 mg/L Cr(VI) solution, the effect of initial pH was evaluated at three pH values viz 4, 7 and 10. As shown in figure 6.9d, the Cr(VI) removal efficiency decreases with the increase of the initial solution pH. At pH 4, the AP-Fe and SN-Fe nanoparticles remove 89 % and 85 % of Cr(VI) respectively, which gradually reduces to 53 % and 47 % at pH 10. The initial pH of the solution influences the surface charge and distribution of reactive sites in the phytogenic Fe nanoparticles and the speciation of Cr(VI) ions in the aqueous solution[39]. At lower pH, the dominant form of Cr(VI) was $HCrO_4^-$, the hydrolysis product of $Cr_2O_7^{2-}$[29]. This Cr(VI) form get reduced in the presence of H^+ ions in acidic solution as follows

$$2HCrO_4^- + 3Fe^0 + 14H^+ \longrightarrow 3Fe^{2+} + 2Cr^{3+} + 8H_2O \qquad (6.7)$$

$$2HCrO_4^- + 6Fe^{2+} + 14H^+ \longrightarrow 6Fe^{3+} + 2Cr^{3+} + 8H_2O \qquad (6.8)$$

In addition to this, the electrostatic attraction between negatively charged $HCrO_4^-$ and positively charged Fe nanoparticles surface is intense in acidic conditions, which leads to the more adsorption of Cr(VI) species[29,39].

At pH value > 6, the dominant Cr(VI) species was $Cr_2O_4^{2-}$ which compete with the OH^- ions for adsorptive sites of phytogenic Fe nanoparticles, leading to decreased removal efficiency. Furthermore, in basic pH, the formation of the oxide passive layer in the Fe nanoparticles hinders the Fe nanoparticle's extent of corrosion and leads to the decline of Cr(VI) removal efficiency[39,40].

6.3.4 MG dye removal studies

Fenton's reaction is extensively studied to degrade toxic dyes due to its high efficiency and low cost. In this catalytic process, an iron catalyst produces hydroxyl radicals (·OH) from hydrogen peroxide (H_2O_2). The formed ·OH radicals interact with the dye molecules and form new oxidised low molecular weight intermediates which are finally converted to CO_2 and H_2O by the continued action of ·OH radicals[41]. MG dye removal studies were conducted in the presence of H_2O_2 to evaluate the reactivity of the synthesised Fe nanoparticles. In dye removal, the influence of initial dye concentration, pH, contact time and nanoparticle dosage were also examined. Generally, MG exhibits three absorbance peaks in the UV-visible spectrum. The characteristic peak is seen at 617 nm (-C-N- bond) and absorbance due to associated aromatic rings are seen at 424 and 316 nm[42]. As shown in figure 6.10, the best results occurred when the phytogenic Fe nanoparticles were used, while negligible MG removal was observed using H_2O_2 only. AP-Fe nanoparticles removed approximately 98 % of MG within 15 minutes, higher than SN-Fe (91 %) nanoparticles. While reacting with phytogenic Fe nanoparticles, the intensity of the MG characteristic peak decreased, two minor peaks disappeared and a new peak formed around

360 nm. It may be due to the cleavage of the -C=C- bond and destruction of MG conjugated structures[43]. The high intensity below 275 nm could be due to the polyphenols present in the phytogenic Fe nanoparticles and the degraded products of MG[44]. The possible mechanism of MG dye removal using phytogenic Fe nanoparticles are 1) Adsorption of MG and its degraded products into Fe/Fe_3O_4 capped with plant component and 2) degradation of MG molecule due to the ·OH radicals produced through reaction with H_2O_2[42]. The high activity of AP-Fe nanoparticles was owing to the formation of more ·OH radicals compared to SN-Fe nanoparticles since Fe^0 have more zero valent iron. The MG removal process can be explained as equation 6.9-6.17.

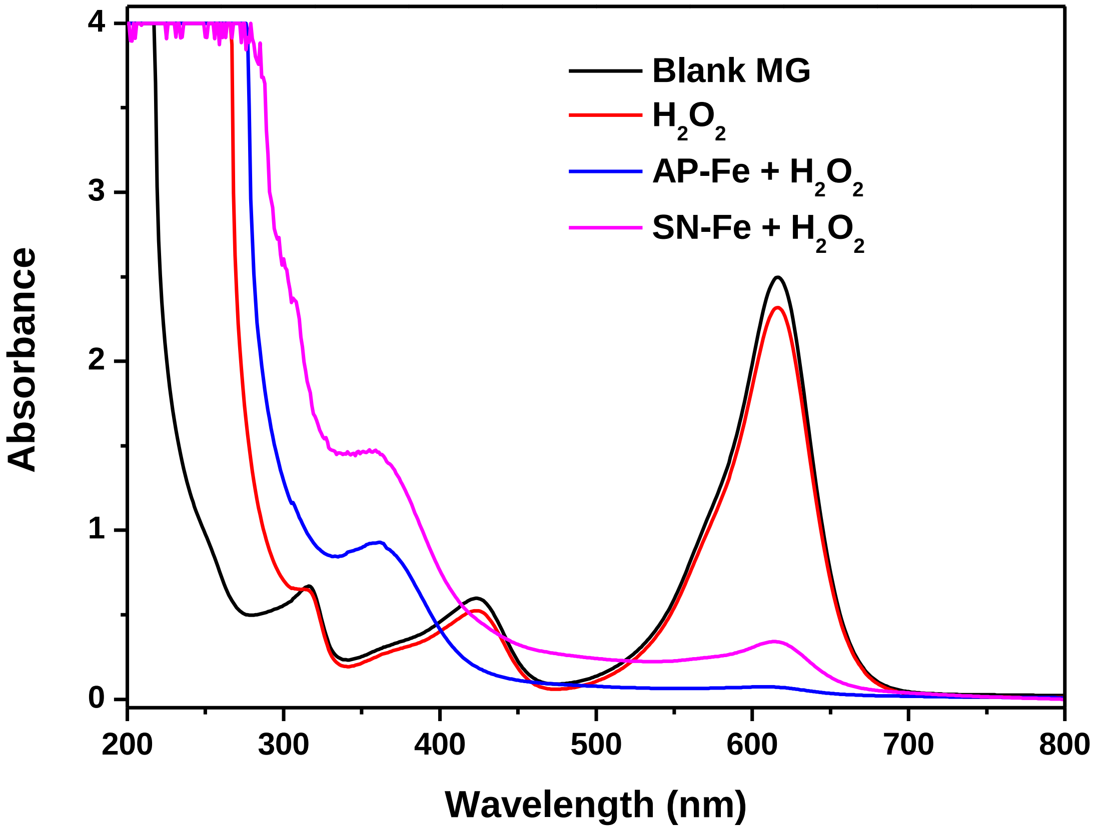

Figure 6.10 *UV-visible spectra of MG dye solution after treating 15 minutes a) blank MG 50 mg/L, b) AP-Fe nanoparticles and c) SN-Fe nanoparticles*

1. Adsorption process:

$$MG + AP - Fe \longrightarrow MG/AP - Fe \qquad (6.9)$$

$$MG + (AP/SN) - Fe_3O_4 \longrightarrow MG/(AP/SN) - Fe_3O_4 \qquad (6.10)$$

2. Degradation of MG dye through the attack of the ·OH radicals:

$$Fe^0 + H_2O_2 \longrightarrow Fe^{2+} + 2OH^- \tag{6.11}$$

$$Fe^{2+} + H_2O_2 \longrightarrow Fe^{3+} + OH^- + {}^{\cdot}OH \tag{6.12}$$

$$Fe^{3+} + H_2O_2 \longrightarrow Fe^{2+} + H^+ + HO_2{}^{\cdot} \tag{6.13}$$

$$Fe^{2+}/Fe^{3+} + H_2O \longrightarrow FeOOH \tag{6.14}$$

$$MG + Fe_3O_4/FeOOH \longrightarrow MG - (Fe_3O_4\ /\ FeOOH) \tag{6.15}$$

$$MG - (Fe_3O_4/FeOOH) + {}^{\cdot}OH \longrightarrow MG\ degradation\ products \tag{6.16}$$

$$MG\ degradation\ products + {}^{\cdot}OH \longrightarrow CO_2 + H_2O \tag{6.17}$$

Effect of nanoparticle dosage

Dosage of phytogenic Fe nanoparticles significantly influences the MG dye removal. As shown in figure 6.11a, the MG dye removal efficiency increased from 98 % to 100 % in AP-Fe nanoparticles and 91 % to 96 % in SN-Fe nanoparticles as the nanoparticle dosage increased from 1 to 2.5 mL. The MG dye concentration and contact time were kept constant at 50 mg/L and 15 min. MG removal is attributed to increased Fe^{2+} availability for the hydroxyl radical formation with nanoparticle dosage. With the increase in hydroxyl radicals formation, more dye molecules get degraded. In addition, total adsorption sites were increased with an increase in phytogenic Fe nanoparticles, which eventually led to the adsorption of more dye molecules and their degraded products.

Effect of the initial concentration of the MG

The effect of the initial concentration of MG on the removal of MG dye is shown in figure 6.11b. The dosage of nanoparticles and contact time were kept constant as 1 mL and 15 minutes respectively. The AP-Fe nanoparticles show 98 to 100 % removal and SN-Fe nanoparticles shows 91 % to 97 % removal when the MG concentration decreases from 50 mg/L to 10 mg/L. The efficiency for the removal of MG decreased with the increasing initial concentration of MG. The decrease in MG removal efficiency with increased concentration is attributed to the insufficiency of hydroxyl radicals and adsorption sites required for dye degradation.

Effect of contact time

Contact time is another crucial parameter influencing the removal efficiency of MG dye. The effect on the removal of MG having 50 mg/L concentration was studied at different time intervals using 1 mL of AP-Fe nanoparticles and SN-Fe nanoparticles, as shown in figure 6.11c. The percentage of removal efficiency increases with an increase in contact time from 10 minutes to 40 minutes. AP-Fe nanoparticles attained 100 % removal efficiency within 30 minutes. At the same time, SN-Fe nanoparticles only attained 94 % removal efficiency. The interaction between hydroxyl radical and dye molecule increases with increasing contact time leading to more dye removal.

Effect of pH

The degradation of MG by AP-Fe nanoparticles and SN-Fe nanoparticles were studied at initial pH values of 5, 7 and 9 as shown in figure 6.11d. The removal efficiency of the AP-Fe nanoparticles and SN-Fe nanoparticles was decreased with an increase in pH value. At pH 5, the AP-Fe nanoparticles attained 100 % and SN-Fe nanoparticles exhibited 96 % removal efficiency. As the pH increases, iron hydroxide precipitation decreases the MG removal efficiency.

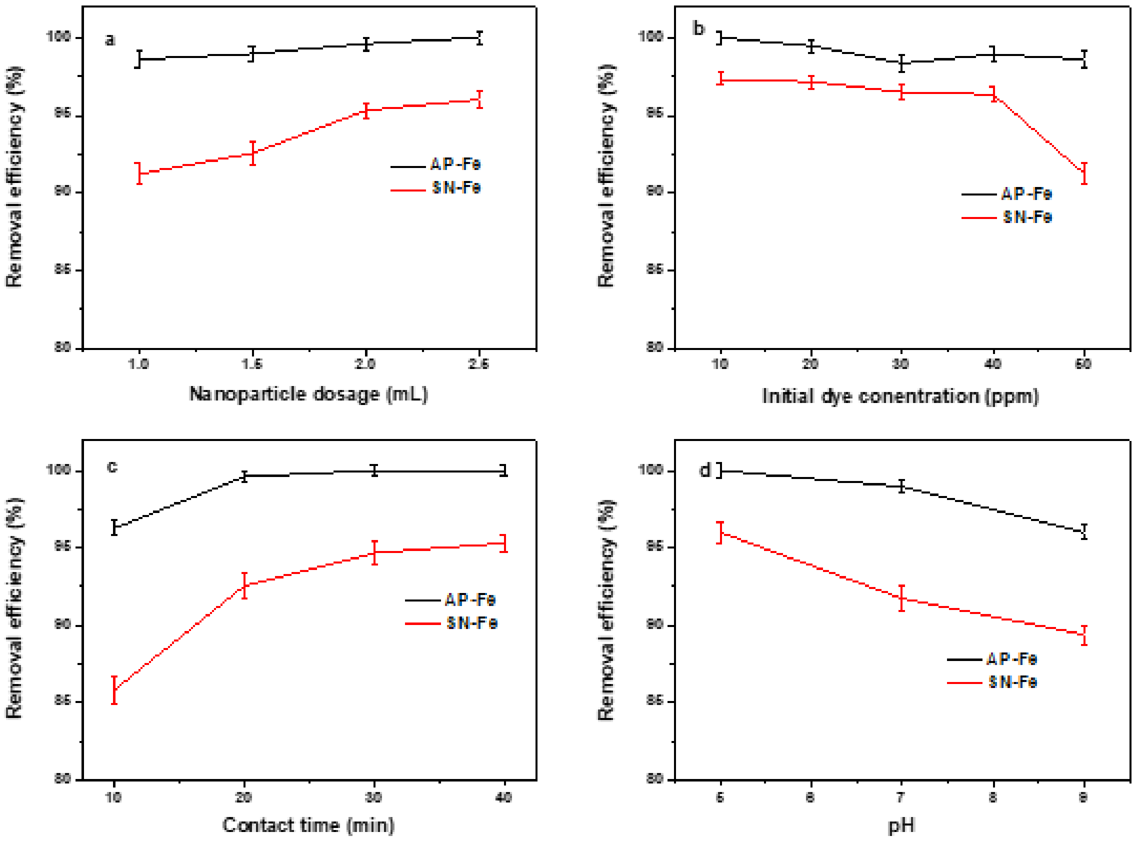

Figure 6.11 *Effects of various factors on MG removal (a) nanoparticle dosage, (b) initial MG concentration, (c) contact time and (d) initial solution pH.*

GC-MS/MS analysis

The GC-MS/MS analysis of malachite green after treating with AP-Fe nanoparticles confirmed the degradation of MG dye molecules. The GC-MS/MS analysis shows the presence of [4-(dimethylamino)phenyl]-phenylmethanone (Rt 21.28, MW 225), benzoic acid (Rt 12.23, MW 122) and diphenylmethanone (Rt 19.91, MW 182) in the solution. Among the three degradation products, benzoic acid is not detected in our previous studies. The MS spectra and structure of benzoic acid are shown in figure 6.12. Hydroxyl radical attack on the [3-hydroxy-4-(methylamino)phenyl]-phenylmethanone causes the formation of benzoic acid[45] as shown in scheme 6.1. The creation of [3-hydroxy-4-(methylamino)phenyl]-phenylmethanone, a degradation product of malachite green dye is discussed in chapter 3. The results show that the addition of H_2O_2 into the reaction medium enhances the oxidation of malachite green degradation products into smaller molecules like benzoic acid.

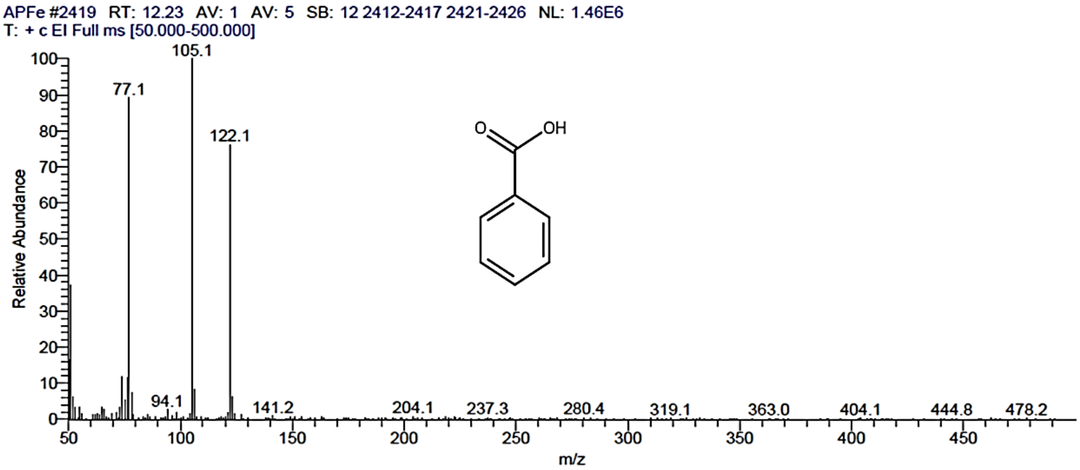

__Figure 6.12__ Mass spectra of benzoic acid identified by GC-MS/MS analysis

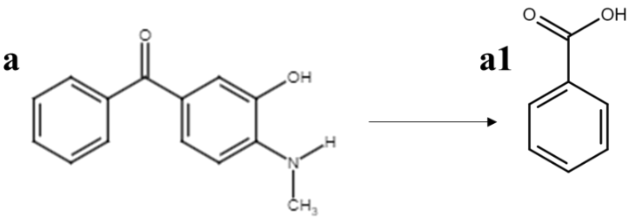

Scheme 6.1 *Degradation pathway of MG using AP-Fe nanoparticles*

6.4. Conclusions

The green synthesis of Fe nanoparticles using seed coat extracts of *Strychnos nux-vomica* and *Abrus precatorius* and their efficiency for removing malachite green dye and Cr(VI) has been investigated. GC-MS/MS analysis identified the bioactive components present in the AP and SN plant extracts. UV-visible spectral analysis confirms the formation of Fe nanoparticles and FTIR spectra provide the probable functional groups present in the plant component which reduces Fe^{3+} and stabilise Fe nanoparticles. AP-Fe nanoparticles have dispersed crystalline particles over an amorphous phase with particle size ranging from 3-32 nm and SN-Fe nanoparticles are amorphous with particle size ranging between 2.1-5 nm, as confirmed through HRTEM analysis. SAED pattern of the synthesised Fe nanoparticles suggests that SN-Fe nanoparticles have Fe_3O_4 composition and AP-Fe nanoparticles have a mixture of Fe^0 and Fe_3O_4 nanoparticles which is attributed to the major bioactive components present in the plant extract. Additionally, the study also envisaged that AP-Fe nanoparticles and SN-Fe nanoparticles have a high potential for the removal of Cr(VI) and MG dye. The result shows that AP-Fe nanoparticles and SN-Fe nanoparticles removed 73 % and 69 % Cr(VI) using 0.2 mL nanoparticles dosage within 15 minutes through adsorption, reduction to Cr(III) and precipitation. In the presence of H_2O_2, the prepared nanoparticles acted as Fenton-like catalyst and degraded the MG dye through oxidation. The AP-Fe and SN-Fe nanoparticles were removed 98 % and 91 % MG using 1 mL nanoparticles and H_2O_2 within 15 minutes. The parameters such as nanoparticle dosage, initial pollutant concentration, initial pH of the solution and contact time were also investigated. The study established that plant extracts can be used for the effective production of stable Fe nanoparticles, which can act as a promising source for contaminant removal.

6.5. References

[1] Z. Xiao, M. Yuan, B. Yang, Z. Liu, J. Huang, D. Sun, Plant-mediated synthesis of highly active iron nanoparticles for Cr (VI) removal: Investigation of the leading biomolecules, Chemosphere. 150 (2016) 357–364. https://doi.org/10.1016/j.chemosphere.2016.02.056.

[2] P.A.R. Puthukkara, T. Sunil Jose, S. Dinoop lal, Plant mediated synthesis of zero valent iron nanoparticles and its application in water treatment, J. Environ. Chem. Eng. (2020) 104569. https://doi.org/10.1016/j.jece.2020.104569.

[3] S. Upadhyay, V.K. Dixit, A.K. Ghosh, V. Singh, Effect of petroleum ether and ethanol fractions of seeds of Abrus precatorius on androgenic alopecia, Rev. Bras. Farmacogn. 22 (2012) 359–363. https://doi.org/10.1590/S0102-695X2011005000221.

[4] M. Biruntha, J. Archana, K. Kavitha, B. Karunai Selvi, J.A. John Paul, R. Balachandar, M. Saravanan, N. Karmegam, Green Synthesis of Zinc Sulfide Nanoparticles Using Abrus precatorius and Its Effect on Coelomic Fluid Protein Profile and Enzymatic Activity of the Earthworm, Eudrilus eugeniae, Bionanoscience. 10 (2020) 149–156. https://doi.org/10.1007/s12668-019-00694-0.

[5] B. Gaddala, S. Nataru, Synthesis, characterization and evaluation of silver nanoparticles through leaves of Abrus precatorius L.: an important medicinal plant, Appl. Nanosci. 5 (2015) 99–104. https://doi.org/10.1007/s13204-014-0295-4.

[6] K. Steffy, G. Shanthi, A.S. Maroky, S. Selvakumar, Potential bactericidal activity of S. nux-vomica–ZnO nanocomposite against multidrug-resistant bacterial pathogens and wound-healing properties, J. Trace Elem. Med. Biol. 50 (2018) 229–239. https://doi.org/10.1016/j.jtemb.2018.07.009.

[7] K. Patel, D. Laloo, G.K. Singh, M. Gadewar, D.K. Patel, A review on medicinal uses, analytical techniques and pharmacological activities of Strychnos nux-vomica Linn.: A concise report, Chin. J. Integr. Med. (2017) 1–13. https://doi.org/10.1007/s11655-016-2514-1.

[8] Q. Bin Han, S.L. Li, C.F. Qiao, J.Z. Song, Z.W. Cai, P.P.H. But, P.C. Shaw, H.X. Xu, A simple method to identify the unprocessed Strychnos seeds used in herbal medicinal products, Planta Med. 74 (2008) 458–463. https://doi.org/10.1055/s-2008-1034359.

[9] R. Bhati, A. Singh, V. Saharan, V.A. Ram, A. Bhandari, Strychnos nux-vomica seeds: Pharmacognostical standardization, extraction, and antidiabetic activity, J. Ayurveda Integr. Med. 3 (2012) 80–84. https://doi.org/10.4103/0975-9476.96523.

[10] K. Steffy, G. Shanthi, A.S. Maroky, S. Selvakumar, Synthesis and characterization of ZnO phytonanocomposite using Strychnos nux-vomica L. (Loganiaceae) and antimicrobial activity against multidrug-resistant bacterial strains from diabetic foot ulcer, J. Adv. Res. 9 (2018) 69–77. https://doi.org/10.1016/j.jare.2017.11.001.

[11] T. Shahwan, S. Abu Sirriah, M. Nairat, E. Boyaci, A.E. Eroĝlu, T.B. Scott, K.R. Hallam, Green synthesis of iron nanoparticles and their application as a Fenton-like catalyst for the degradation of aqueous cationic and anionic dyes, Chem. Eng. J. 172 (2011) 258–266. https://doi.org/10.1016/j.cej.2011.05.103.

[12] N. Garaniya, A. Bapodra, Ethno botanical and Phytophrmacological potential of Abrus precatorius L.: A review, Asian Pac. J. Trop. Biomed. 4 (2014) S27–S34. https://doi.org/10.12980/APJTB.4.2014C1069.

[13] R. Javed, M. Zia, S. Naz, S.O. Aisida, N. ul Ain, Q. Ao, Role of capping agents in the application of nanoparticles in biomedicine and environmental remediation: recent trends and future prospects, J. Nanobiotechnology. 18 (2020) 172. https://doi.org/10.1186/s12951-020-00704-4.

[14] R. Lakra, M.S. Kiran, P.S. Korrapati, Furfural mediated synthesis of silver nanoparticles for photocatalytic reduction of hexavalent chromium, Environ. Technol. Innov. 21 (2021) 101348. https://doi.org/10.1016/j.eti.2020.101348.

[15] P.V. Kumar, S.M. Jelastin Kala, K.S. Prakash, Green synthesis derived Pt-nanoparticles using Xanthium strumarium leaf extract and their biological studies, J. Environ. Chem. Eng. 7 (2019) 103146. https://doi.org/10.1016/j.jece.2019.103146.

[16] Anderson Thesing, José E. R. do Nascimento, Raquel G. Jacob, Jacqueline F. L. Santos, Eucalyptus Oil-Mediated Synthesis of Gold Nanoparticles, J. Chem. Chem. Eng. 12 (2018). https://doi.org/10.17265/1934-7375/2018.02.002.

[17] B. Ibrahim, A. Wiranata, A. Malik, The Effect of Addition of Antioxidant 1,2-dihydro-2,2,4-trimethyl-quinoline on Characteristics of Crepe Rubber Modified Asphalt in Short Term Aging and Long Term Aging Conditions, Appl. Sci. 10 (2020) 7236. https://doi.org/10.3390/app10207236.

[18] T. Kalaivani, C. Rajasekaran, M. Shalini, V. Vijayakumar, D.P. Pandey, L. Mathew, Structural Elucidation and Antioxidant Activity of Ethyl Gallate Isolated from Acacia nilotica (L.) Wild. ex. Delile subsp. indica (Benth.) Brenan, Natl. Acad. Sci. Lett. 41 (2018) 355–359. https://doi.org/10.1007/s40009-018-0725-z.

[19] M. Tiwari, P. Kumar, K.K. Tejavath, V. Tiwari, Assessment of Molecular Mechanism of Gallate-Polyvinylpyrrolidone-Capped Hybrid Silver Nanoparticles against Carbapenem-Resistant Acinetobacter baumannii, ACS Omega. 5 (2020) 1206–1213. https://doi.org/10.1021/acsomega.9b03644.

[20] A. R, R. Naika, Anti-inflammatory properties of Pavetta Crassicaulis Bremek. Leaf and flower crude extracts and its pure compounds collected from Western ghats, Karnataka, India, Asian J. Pharm. Clin. Res. 11 (2018) 72. https://doi.org/10.22159/ajpcr.2018.v11i9.21885.

[21] W. Liang, R. Zhu, X. Li, J. Deng, Y. Fu, Heterogeneous photocatalyzed acceptorless dehydrogenation of 5-hydroxymethylfurfural upon visible-light illumination, Green Chem. 23 (2021) 6604–6613. https://doi.org/10.1039/D1GC01286J.

[22] H. Chabane, M. Messarah, M. Liacha, Comparative study for the synthesis of new generation of2(3H)-benzothiazolones as antioxidant agents, Der Pharma Chem. 8 (2016) 20–26.

[23] A. Suvitha, S. Periandy, P. Gayathri, NBO, HOMO–LUMO, UV, NLO, NMR and vibrational analysis of veratrole using FT-IR, FT-Raman, FT-NMR spectra and HF–DFT computational methods, Spectrochim. Acta Part A Mol. Biomol. Spectrosc. 138 (2015) 357–369. https://doi.org/10.1016/j.saa.2014.11.011.

[24] S.J.S. Flora, Structural, Chemical and Biological Aspects of Antioxidants for Strategies Against Metal and Metalloid Exposure, Oxid. Med. Cell. Longev. 2 (2009) 191–206. https://doi.org/10.4161/oxim.2.4.9112.

[25] M.-B. Hu, W. Peng, Y.-J. Liu, D. Yan, X. Chen, C.-J. Wu, Maillard reaction induces changes in saccharides and amino acids during stir-baking of areca nuts, Trop. J. Pharm. Res. 15 (2016) 2107. https://doi.org/10.4314/tjpr.v15i10.8.

[26] E.F. Seneme, D.C. dos Santos, E.M.R. Silva, Y.E.M. Franco, G.B. Longato, Pharmacological and Therapeutic Potential of Myristicin: A Literature Review, Molecules. 26 (2021) 5914. https://doi.org/10.3390/molecules26195914.

[27] K. Abdulwahab, M.A. Malik, P. O'Brien, K. Govender, C.A. Muryn, G.A. Timco, F. Tuna, R.E.P. Winpenny, Synthesis of monodispersed magnetite nanoparticles from iron pivalate clusters, Dalt. Trans. 42 (2013) 196–206. https://doi.org/10.1039/C2DT32478D.

[28] A. Rana, N. Kumari, M. Tyagi, S. Jagadevan, Leaf-extract mediated zero-valent iron for oxidation of Arsenic (III): Preparation, characterization and kinetics, Chem. Eng. J. 347 (2018) 91–100. https://doi.org/10.1016/j.cej.2018.04.075.

[29] Z. Xiao, H. Zhang, Y. Xu, M. Yuan, X. Jing, J. Huang, Q. Li, D. Sun, Ultra-efficient removal of chromium from aqueous medium by biogenic iron based nanoparticles, Sep. Purif. Technol. 174 (2017) 466–473. https://doi.org/10.1016/j.seppur.2016.10.047.

[30] D. Patiño-Ruiz, L. Sánchez-Botero, L. Tejeda-Benitez, J. Hinestroza, A. Herrera, Green synthesis of iron oxide nanoparticles using Cymbopogon citratus extract and sodium

carbonate salt: Nanotoxicological considerations for potential environmental applications, Environ. Nanotechnology, Monit. Manag. 14 (2020) 100377. https://doi.org/10.1016/j.enmm.2020.100377.

[31] P. Prema, S. Thangapandian, M. Selvarani, S. Subharanjani, C. Amutha, Color removal efficiency of dyes using nanozerovalent iron treatment, Toxicol. Environ. Chem. 93 (2011) 1908–1917. https://doi.org/10.1080/02772248.2011.606613.

[32] C. Prasad, K. Sreenivasulu, S. Gangadhara, P. Venkateswarlu, Bio inspired green synthesis of Ni/Fe3O4 magnetic nanoparticles using Moringa oleifera leaves extract: A magnetically recoverable catalyst for organic dye degradation in aqueous solution, J. Alloys Compd. 700 (2017) 252–258. https://doi.org/10.1016/j.jallcom.2016.12.363.

[33] K.V.G. Ravikumar, S.V. Sudakaran, K. Ravichandran, M. Pulimi, C. Natarajan, A. Mukherjee, Green synthesis of NiFe nano particles using Punica granatum peel extract for tetracycline removal, J. Clean. Prod. 210 (2019) 767–776. https://doi.org/10.1016/j.jclepro.2018.11.108.

[34] E.S. Madivoli, P.G. Kareru, A.N. Gachanja, S.M. Mugo, D.S. Makhanu, Phytofabrication of iron nanoparticles and their catalytic activity, SN Appl. Sci. 1 (2019). https://doi.org/10.1007/s42452-019-0951-0.

[35] S. Eslami, M.A. Ebrahimzadeh, P. Biparva, Green synthesis of safe zero valent iron nanoparticles by: Myrtus communis leaf extract as an effective agent for reducing excessive iron in iron-overloaded mice, a thalassemia model, RSC Adv. 8 (2018) 26144–26155. https://doi.org/10.1039/c8ra04451a.

[36] Y. Wei, Z. Fang, L. Zheng, E.P. Tsang, Biosynthesized iron nanoparticles in aqueous extracts of Eichhornia crassipes and its mechanism in the hexavalent chromium removal, Appl. Surf. Sci. 399 (2017) 322–329. https://doi.org/10.1016/j.apsusc.2016.12.090.

[37] F. Zhu, S. He, T. Liu, Effect of pH, temperature and co-existing anions on the Removal of Cr(VI) in groundwater by green synthesized nZVI/Ni, Ecotoxicol. Environ. Saf. 163 (2018) 544–550. https://doi.org/10.1016/j.ecoenv.2018.07.082.

[38] F. Zhu, S. Ma, T. Liu, X. Deng, Green synthesis of nano zero-valent iron/Cu by green tea to remove hexavalent chromium from groundwater, J. Clean. Prod. 174 (2018) 184–190. https://doi.org/10.1016/j.jclepro.2017.10.302.

[39] A. Soliemanzadeh, M. Fekri, The application of green tea extract to prepare bentonite-supported nanoscale zero-valent iron and its performance on removal of Cr(VI): Effect of relative parameters and soil experiments, Microporous Mesoporous Mater. 239 (2017) 60–69. https://doi.org/10.1016/j.micromeso.2016.09.050.

[40] X. Jin, Y. Liu, J. Tan, G. Owens, Z. Chen, Removal of Cr(VI) from aqueous solutions via reduction and absorption by green synthesized iron nanoparticles, J. Clean. Prod. 176 (2018) 929–936. https://doi.org/10.1016/j.jclepro.2017.12.026.

[41] P.V. Nidheesh, R. Gandhimathi, S.T. Ramesh, Degradation of dyes from aqueous solution by Fenton processes: A review, Environ. Sci. Pollut. Res. 20 (2013) 2099–2132. https://doi.org/10.1007/s11356-012-1385-z.

[42] X. Wang, A. Wang, J. Ma, M. Fu, Facile green synthesis of functional nanoscale zero-valent iron and studies of its activity toward ultrasound-enhanced decolorization of cationic dyes, Chemosphere. 166 (2017) 80–88. https://doi.org/10.1016/j.chemosphere.2016.09.056.

[43] P. Anju Rose Puthukkara, T. Sunil Jose, S. Dinoop lal, A.R. Puthukkara P, S. Jose T, D. lal S, Chitosan stabilized Fe/Ni bimetallic nanoparticles for the removal of cationic and anionic

triphenylmethane dyes from water, Environ. Nanotechnology, Monit. Manag. 14 (2020) 100295. https://doi.org/10.1016/j.enmm.2020.100295.

[44] L. Huang, X. Weng, Z. Chen, M. Megharaj, R. Naidu, Green synthesis of iron nanoparticles by various tea extracts: Comparative study of the reactivity, Spectrochim. Acta - Part A Mol. Biomol. Spectrosc. 130 (2014) 295–301. https://doi.org/10.1016/j.saa.2014.04.037.

[45] G. Sharma, S. Bhogal, V.K. Gupta, S. Agarwal, A. Kumar, D. Pathania, G.T. Mola, F.J. Stadler, Algal biochar reinforced trimetallic nanocomposite as adsorptional/photocatalyst for remediation of malachite green from aqueous medium, J. Mol. Liq. 275 (2019) 499–509. https://doi.org/10.1016/j.molliq.2018.11.070.

CHAPTER 7

Green synthesis of iron nanoparticles using ayurvedic composition *Triphala* and its constituents for the removal of Cr(VI) and malachite green dye from water

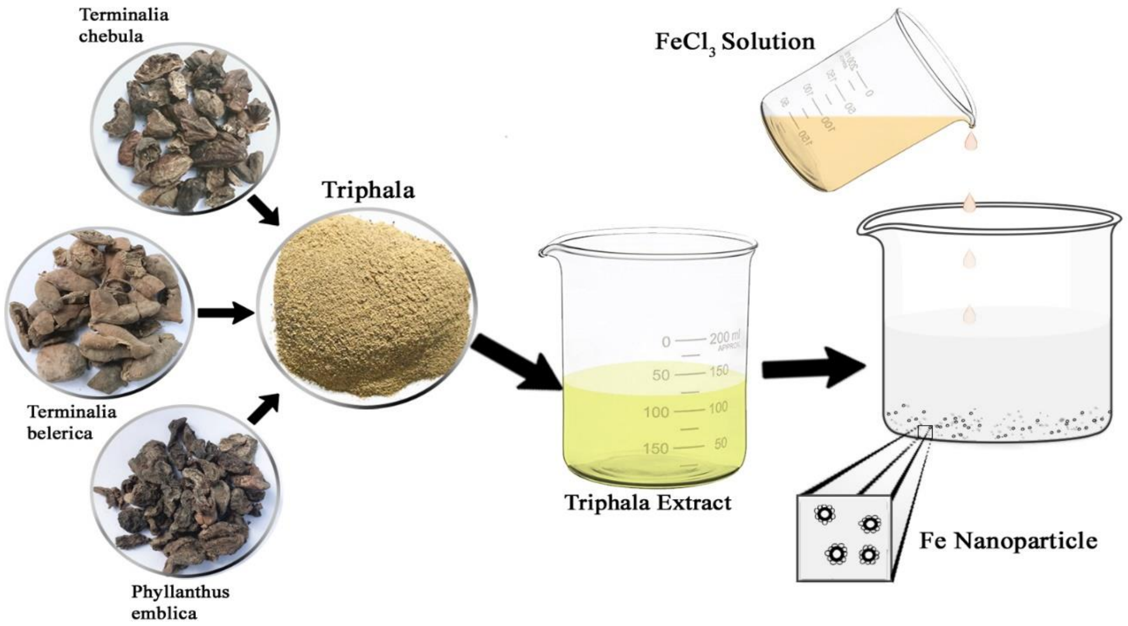

Chapter 7

Green synthesis of iron nanoparticles using ayurvedic composition *Triphala* and its constituents for the removal of Cr(VI) and malachite green dye from water

7.1. Introduction

As discussed in chapter 6, the green synthesis of Fe nanoparticles and their application in water treatment is a vast area of research. The tremendous availability of plant materials always opens up doors for a new horizon. In this study, ayurvedic composition *Triphala* (TP) and its constituents such as *Terminalia chebula* (TC), *Terminalia belerica* (TB) and *Phyllanthus emblica* (PE) have been studied for the preparation of iron nanoparticles. *Triphala* is a powdered preparation of dried fruits of TC, TB and PE in equal proportion. Dried fruit extract of TC contains chebulic acid, theophylline, stigmasterol, brassicasterol[1], gallic acid, protocatechuic acid, catechin, quinic acid, orientin, chlorogenic acid, epicatechin, mangiferin, ferulic acid, sinapic acid, isoorientin, vitexin, chebulinic acid, isovitexin, rutin, ellagic acid, naringin, kaempferol-3-o-rutinoside, eriodictyol, scutellarein, quercetin, genistein, kaempferol, apigenin, betulinic acid, arjunetin, amentoflavone, arjungenin, chrysin and arjunolic acid[2]. Mohan et al. synthesised gold and silver nanoparticles using an aqueous extract of TC seed powder since the phytochemicals present in the TC have the potential to act as reducing and stabilizing agents [3,4]. Similar to TC, the major phytochemicals present in the TB seed extract are gallic acid, protocatechuic acid, catechin, quinic acid, epicatechin, mangiferin, ferulic acid, sinapic acid, isoorientin, chebulinic acid, ellagic acid, naringin, kaempferol-3-o-rutinoside, eriodictyol, scutellarein, genistein, kaempferol, apigenin, arjunetin, arjungenin and vanillic acid[2]. Silver nanoparticles were prepared by Rama et al. using ethanolic TB extract and their photocatalytic and antimicrobial activity were examined. The results show good efficiency for photocatalytic degradation of methylene blue[5]. Another plant material used in this study is the dried fruit of PE, also known as Indian gooseberry. The major active components in PE extract are quinic acid, caffeic acid, gallic acid, gentisic acid-o-hexoside, catechin, brecifolin, ellagic acid, chrysin, methyl gallate, coumaric acid, betulinic acid, oleanolic acid, quercetin, rutin and kaempferol[6]. Recently renuka et al. synthesised silver nanoparticles using PE extract and tested for antimicrobial activity[7]. Previous studies show that these plant extracts can be used for the synthesis of metal nanoparticles as reductant, antioxidant, capping and stabilizing agent.

As already stated, *Triphala* is a combination of TC, TB and PE plant fruit powders. Figure 7.1 shows the photographs of *Triphala* and its components. In Ayurveda, *Triphala* possesses more activity than its components. The increased activity of TP belongs to the synergetic effect of plant components. The therapeutic use of *Triphala* and its components includes antimicrobial and anti-inflammatory activities, blood purification, remedy for leucorrhea, headache, pneumonia and tuberculosis[8]. To date, there is no report about the synthesis of Fe nanoparticles using *Triphala* as a reducing and stabilizing agent. In this study, Fe nanoparticles have been prepared using *Triphala* and its constituents and a comparative study has been done on the removal of malachite green (MG) dye and Cr(VI) removal using the prepared nanoparticles. MG removal studies have taken place in the presence of H_2O_2 with prepared nanoparticles. The parameters influencing the removal of pollutants such as nanoparticles dosage, initial concentration of the dye, contact time and solution pH were also examined.

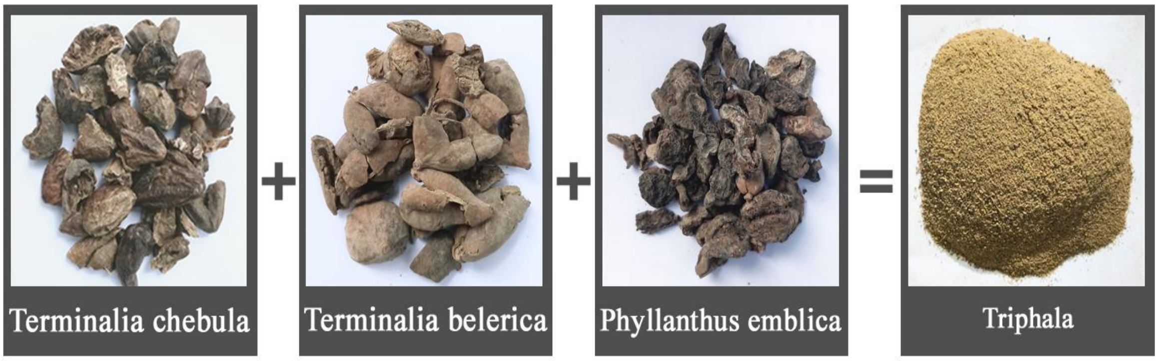

***Figure 7.1** Photographs of Terminalia chebula, Terminalia belerica, Phyllanthus emblica and Triphala*

7.2. Experimental details

7.2.1 Preparation of plant extracts and phytogenic Fe nanoparticles

Preparation of TC, TB, PE and TP extract

To prepare *Triphala* powder, equal amounts of the dried pericarp of three fruits, *Terminalia chebula, Terminalia belerica* and *Phyllanthus emblica* were weighed separately and ground to powder. The *Triphala* extracts (20 g/L) were prepared by refluxing 2 g of *Triphala* powder in 100 mL ethanol at a temperature of 90 ºC for 2 hours.

The extract was then cooled, filtered using Whatman number 40 filter paper and stored at 4 °C for further use.

A similar procedure was followed for the preparation of TC, TB and PE plant extracts. These plant extracts with 20 mg/L concentration were prepared by refluxing 2 g of plant powder in 100 mL ethanol followed by cooling and filtration.

Synthesis of phytogenic Fe nanoparticles

The procedure for synthesising phytogenic Fe nanoparticles was already discussed in chapter 6, except plant extracts used in this study were TP, TC, TB and PE. After the synthesis, the lyophilised nanoparticles were stored for characterisation studies.

7.2.2 Batch experiments

Cr(VI) removal studies

In Cr(VI) removal studies, prepared nanoparticles were used in liquid form. In the optimised condition, 10 mL of 5 mg/L Cr(VI) solution were treated with 0.2 mL of freshly prepared nanoparticles. Different parameters examined in this study were nanoparticle dosage (0.1-0.5 mL), initial concentration of Cr(VI) (1-7 mg/L), initial pH of the solution (4-10) and contact time (10-40 min). NaOH (1.0 M) and H_2SO_4 (1.0 M) were used for the pH adjustment and all the experiments were performed with a duplicate.

Malachite green dye removal studies

The procedure followed for the MG removal studies by phytogenic Fe nanoparticles were also discussed in chapter 6. The different parameters studied to check the efficiency of prepared nanoparticles were nanoparticle dosage (1-5 mL), initial concentration of MG dye (10 - 50 mg/L), pH of the solution (5 - 9) and contact time (10-40 min).

7.2.3 Characterisation and analytical techniques used

The prepared plant extracts were characterised by UV-visible spectrophotometer and GC-MS/MS. The procedure for GC-MS/MS analysis was discussed in chapter 3. The characterisation of nanoparticles have been done using HRTEM, EDAX, FTIR and UV-visible spectrophotometer and the details of characterisation techniques are discussed in chapter 2. Fourier transform infrared spectra of the prepared plant extracts and corresponding Fe nanoparticles were investigated through Spectrum Two Fourier transform infrared spectrometer (FTIR, Perkin Elmer, USA). Jeol 6390LA/OXFORD XMX N was used for the elemental analysis of TC-Fe, TB-Fe, PE-Fe and TP-Fe nanoparticles.

7.3. Results and discussion

7.3.1 Characterisation of TP plant extract

No.	Retention time (t)	Name of the compound	Molecular weight	Action	Reference
a.	13.47	5-(hydroxymethyl)furan-2-carbaldehyde	126	Reducing agent	[9]
b.	16.37	benzene-1,3,5-triol	126	Reducing and capping agent	[10]
c.	16.57	benzene-1,2,3-triol	126	Reducing and capping agent	[10]
d.	17.25	2,2,4-trimethyl-1H-quinoline	173	Antioxidant	[11]
e.	18.09	2,6-ditert-butyl-4-methylphenol	220	Reducing agent and antioxidant	[12]
f.	19.71	4,7-dimethoxy-5-prop-2-enyl-1,3-benzodioxole	222	Antioxidant	[13]
g.	20.42	3H-1,3-benzothiazol-2-one	151	Antioxidant	[14]
h.	23.16	methyl hexadecanoate	270	Antioxidant	[15]
i.	23.49	hexadecanoic acid	256	Antioxidant and stabilizing agent	[16,17]
j.	23.85	ethyl hexadecanoate	284	Antioxidant	[15]

Table 7.1 *Biomolecules identified in TP extract by GC-MS/MS*

The phytochemical analysis of ethanolic TP plant extract was done using GC-MS/MS and identified ten bioactive compounds. The results show that TP extract contains reducing, stabilizing and antioxidizing agents. Retention time, molecular weight and mode of action of the bioactive compounds are presented in table 7.1. In the extract, the presence of methyl hexadecanoate/ethyl hexadecanoate may be due to the esterification of hexadecenoic acid with ethanol, which is used as a solvent for the extraction of plant components. Recently Hao et al. synthesised Fe nanoparticles from green tea aqueous extract and confirmed that the presence of bioactive components like benzene-1,3,5-triol and benzene-1,2,3-triol acted as reducing and capping agents during Fe nanoparticles formation[10]. Mass spectra of the identified bioactive components have been shown in figure 7.2.

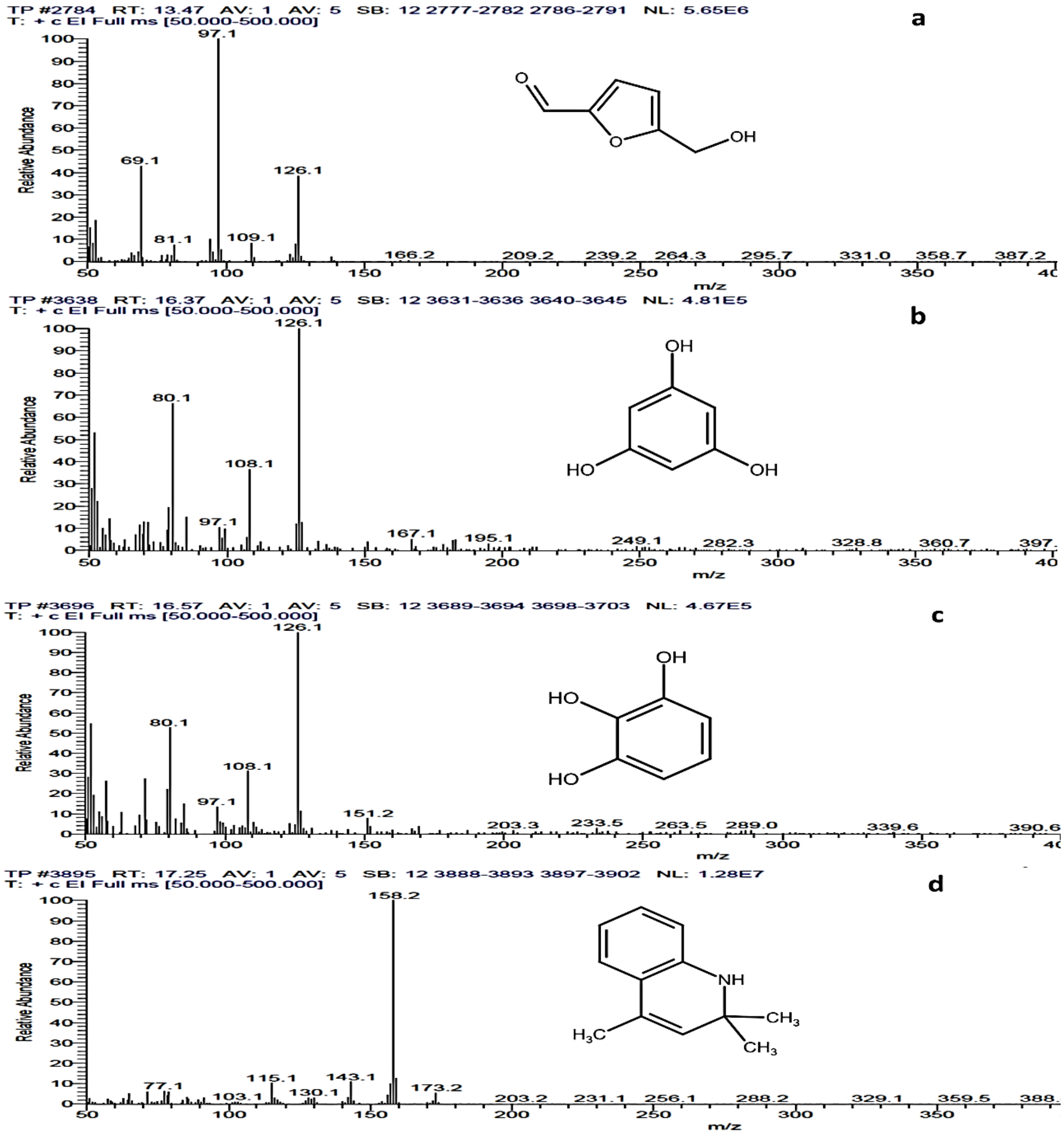

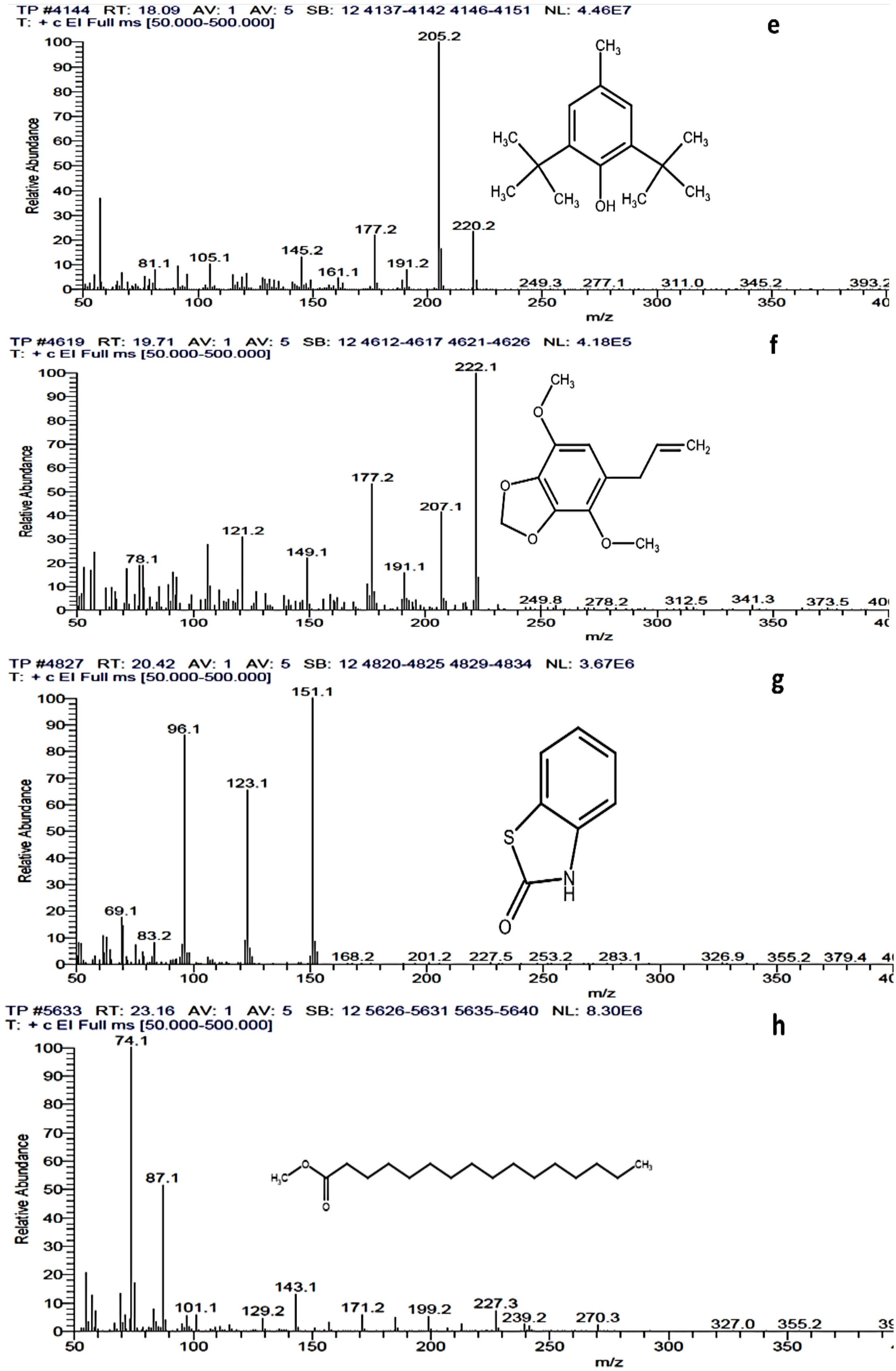
TP #4144 RT: 18.09 AV: 1 AV: 5 SB: 12 4137-4142 4146-4151 NL: 4.46E7
T: + c EI Full ms [50.000-500.000]
e
Relative Abundance
m/z
205.2
220.2
177.2
145.2
105.1
81.1
161.1
191.2
249.3
277.1
311.0
345.2
393.2
CH3
H3C
CH3
H3C
CH3
OH
H3C
CH3
TP #4619 RT: 19.71 AV: 1 AV: 5 SB: 12 4612-4617 4621-4626 NL: 4.18E5
T: + c EI Full ms [50.000-500.000]
f
Relative Abundance
m/z
222.1
177.2
207.1
121.2
149.1
78.1
191.1
249.8
278.2
312.5
341.3
373.5
CH3
O
CH2
O
O
O—CH3
TP #4827 RT: 20.42 AV: 1 AV: 5 SB: 12 4820-4825 4829-4834 NL: 3.67E6
T: + c EI Full ms [50.000-500.000]
g
Relative Abundance
m/z
151.1
96.1
123.1
69.1
83.2
168.2
201.2
227.5
253.2
283.1
326.9
355.2
379.4
S
NH
O
TP #5633 RT: 23.16 AV: 1 AV: 5 SB: 12 5626-5631 5635-5640 NL: 8.30E6
T: + c EI Full ms [50.000-500.000]
h
Relative Abundance
m/z
74.1
87.1
143.1
101.1
129.2
171.2
199.2
227.3
239.2
270.3
327.0
355.2
H3C
O
O
CH3

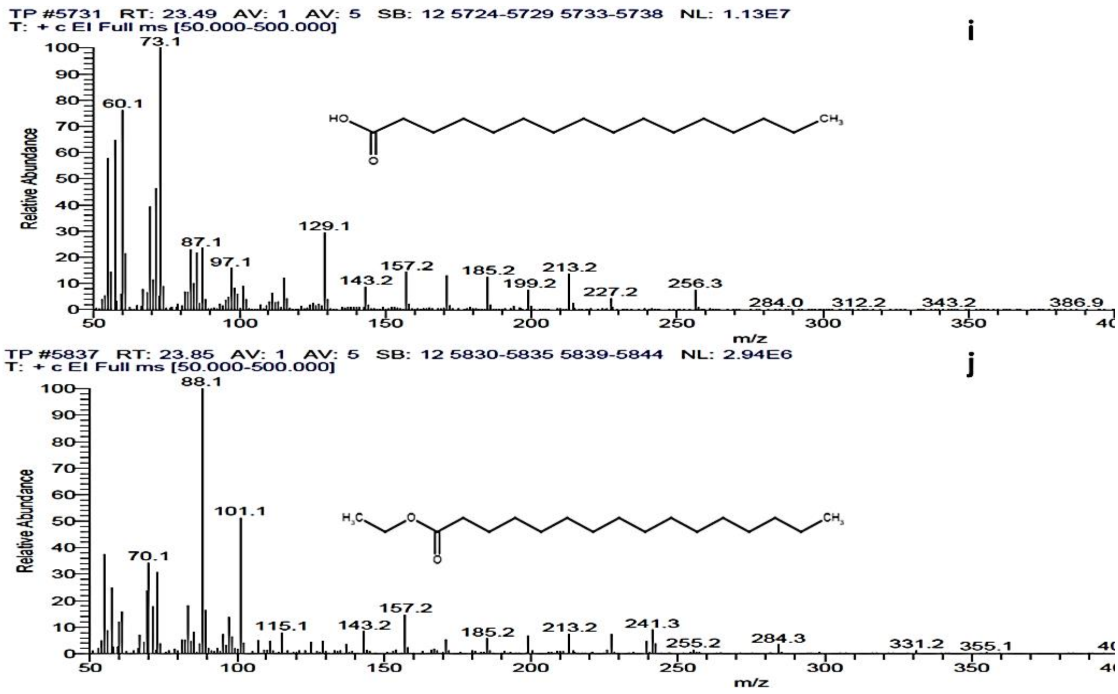

Figure 7.2 *Mass spectra of compounds identified in TP extract by GC-MS/MS. (a) 5-(hydroxymethyl)furan-2-carbaldehyde; (b) benzene-1,3,5-triol; (c) benzene-1,2,3-triol; (d) 2,2,4-trimethyl-1H-quinoline; (e) 2,6-ditert-butyl-4-methylphenol; (f) 4,7-dimethoxy-5-prop-2-enyl-1,3-benzodioxole; (g) 3H-1,3-benzothiazol-2-one; (h) methyl hexadecanoate; (i) hexadecanoic acid; (j) ethyl hexadecanoate*

7.3.2 Characterisation of TC-Fe, TB-Fe, PE-Fe and TP-Fe nanoparticles

UV-visible spectroscopy

As discussed in chapter 6, the development of black precipitate during the mixing of iron salt solution and plant extract indicates the formation of Fe nanoparticles[18]. Figure 7.3 shows the photographs and UV-visible spectra of plant extracts before and after reaction with the iron salt solution. The broad peak centred around 600 nm indicates the formation of Fe nanoparticles. However, the plant extracts and Fe salt solution does not exhibit any transition in this region[19].

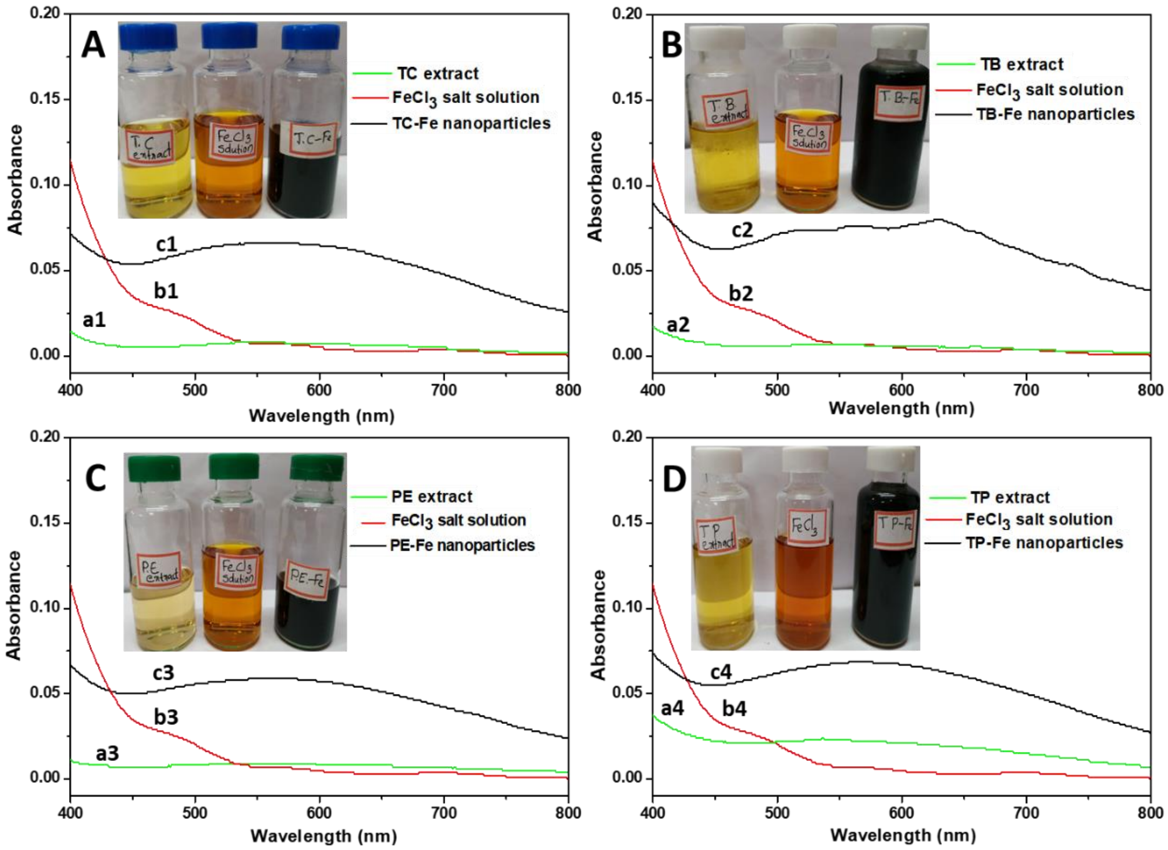

Figure 7.3 *Photographs and UV-visible spectra of A) a1. TC extract, b1. $FeCl_3$ solution and c1. TC-Fe nanoparticles, B) a2. TB extract, b2. $FeCl_3$ solution and c2. TB-Fe nanoparticles, C) a3. PE extract, b3. $FeCl_3$ solution and c3. PE-Fe nanoparticles, D) a4. TP extract, b4. $FeCl_3$ solution and c4. TP-Fe nanoparticles*

HRTEM

Figure 7.4 shows the HRTEM images and SAED pattern of TC-Fe, TB-Fe and PE-Fe nanoparticles. Figure 7.4 (a, b, & c) envisages that the formed Fe nanoparticles are covered with plant materials and agglomerated as a chain/needle-like structure. The formation of nanoparticles is more evident from figure 7.4 (a1, b1 & c1) and it indicates that the formed nanoparticles have a particle size below 6 nm. The TC-Fe, TB-Fe and PE-Fe nanoparticles have an average particle size of 5.2, 2.4 and 3 nm respectively and the d-spacing of the Fe nanoparticles is observable. TC-Fe nanoparticles show a d-spacing of 2.7 Å, which corresponds to the (220) plane of Fe_3O_4[20]. However, TB-Fe and PE-Fe nanoparticles showed a d-spacing of 2.6 Å and this corresponds to the (311) plane of Fe_3O_4[21]. SAED pattern of all the three iron oxide nanoparticles (figure 7.4) show only diffused rings and no bright spots which indicates the amorphous nature of the TC-Fe, TB-Fe and PE-Fe nanoparticles.

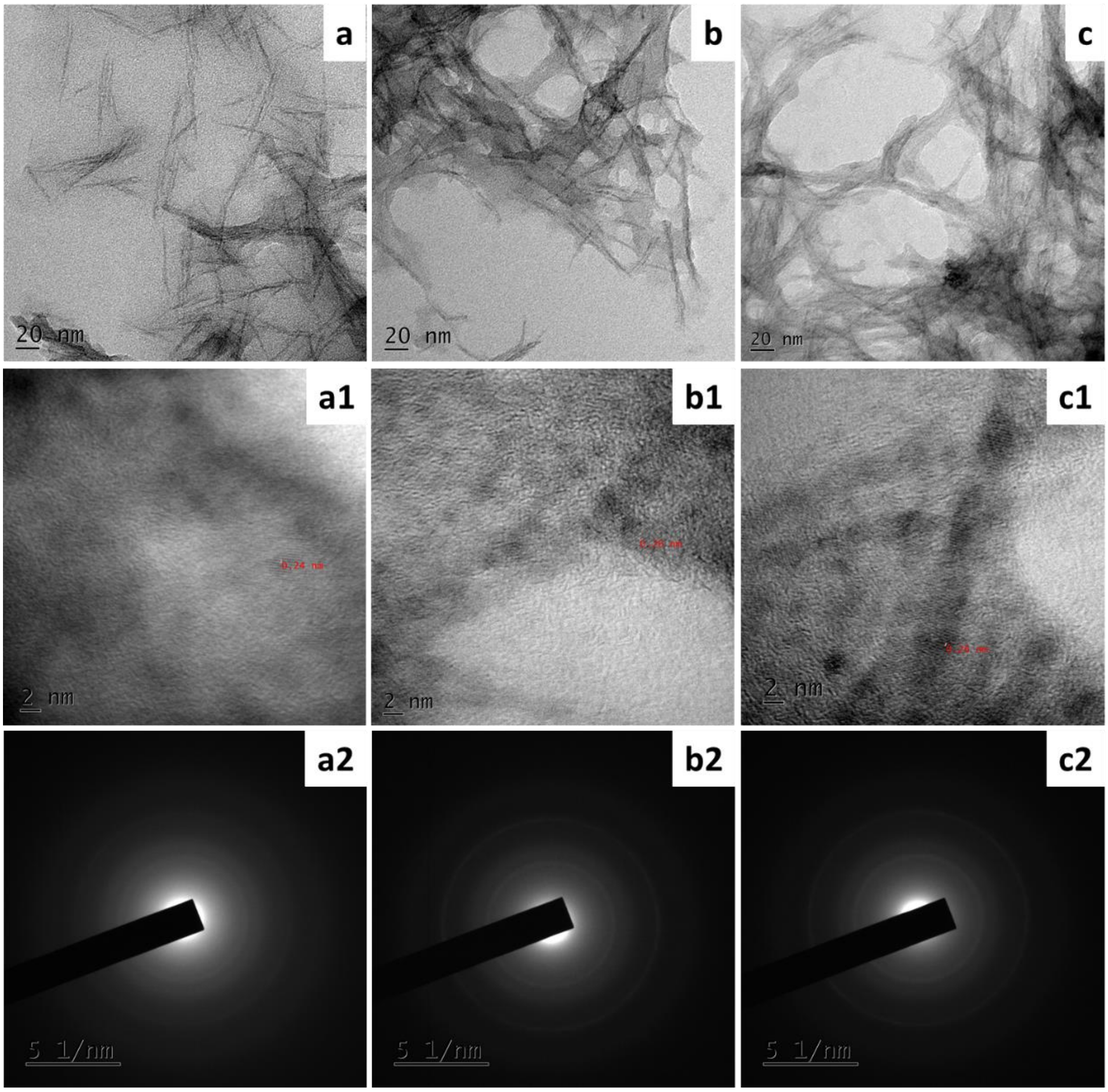

Figure 7.4 *HRTEM image of the (a-a1) TC-Fe, (b-b1) TB-Fe and (c-c1) PE-Fe nanoparticles and SAED pattern of (a2) TC-Fe, (b2) TB-Fe and (c2) PE-Fe nanoparticles*

Figure 7.5 (a & a1) displays the HRTEM image and SAED pattern of the TP-Fe nanoparticles. As shown in figure 7.5a, irregularly shaped nanoparticles were agglomerated and unevenly dispersed in the plant extract. The size of the TP-Fe nanoparticles was varied from 7-14 nm with an average diameter of 11 nm. SAED pattern displays faded spots with diffused rings, indicating the presence of crystalline and amorphous Fe particles in TP-Fe. The d-spacing values calculated from the SAED pattern of TP-Fe are 2.01 Å and 1.29 Å which corresponds to the (110) plane of Fe^0[22] and (311) plane of FeO (JCPDS No 00-006-0615). The formation of and Fe^0 and FeO nanoparticles suggest that the synergetic effect of three plant components improved the reduction and stabilization potential of TP extract and the growth of the nanoparticles was also enhanced significantly.

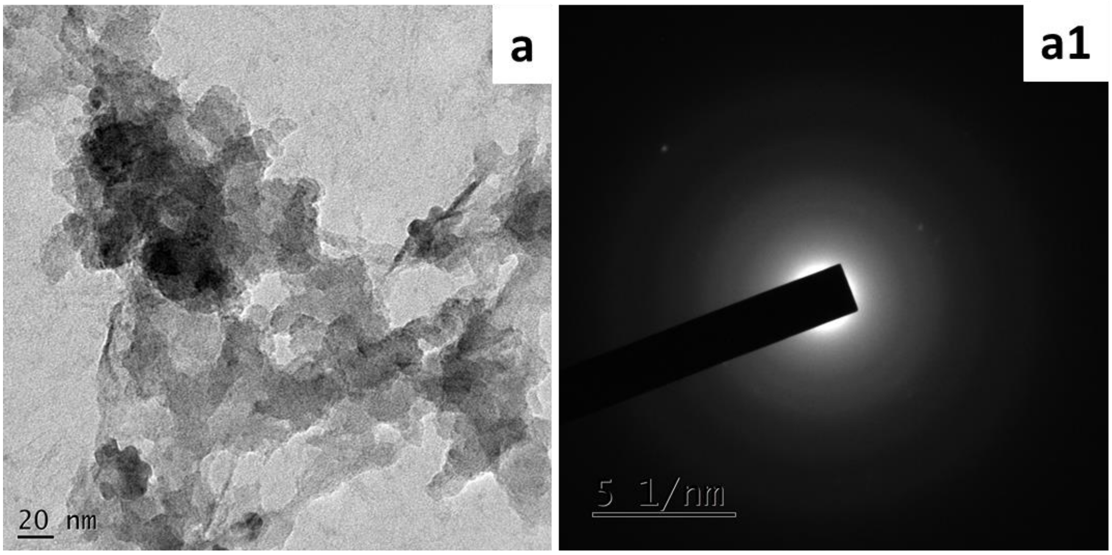

Figure 7.5 *(a) HRTEM image and (a1) SAED pattern of the TP-Fe nanoparticles*

EDAX

Figure 7.6 demonstrates the EDAX spectra of the TC-Fe, TB-Fe, PE-Fe and TP-Fe nanoparticles. The results reveal that the atomic percentage of Fe in TC-Fe, TB-Fe, PE-Fe and TP-Fe nanoparticles were 6.33, 8.01, 8.60 and 6.62 % respectively. The other elements such as C from plant components, Cl from $FeCl_3$ and O by air oxidation were also present in the prepared nanoparticles.

Figure 7.7 shows the EDAX mapping (Fe and O mapping images) of TC-Fe, TB-Fe, PE-Fe and TP-Fe nanoparticles. EDAX mapping of the prepared nanoparticles inferred that Fe is uniformly and finely distributed in TC-Fe, TB-Fe and PE-Fe nanoparticles however in the case of TP-Fe nanoparticles, more aggregation of Fe can be seen in the Fe mapping image. This agrees with the HRTEM results in which more coarse particles were identified. The presence of oxygen in the prepared nanoparticles may be from the iron oxide and the plant components adsorbed on the nanoparticles.

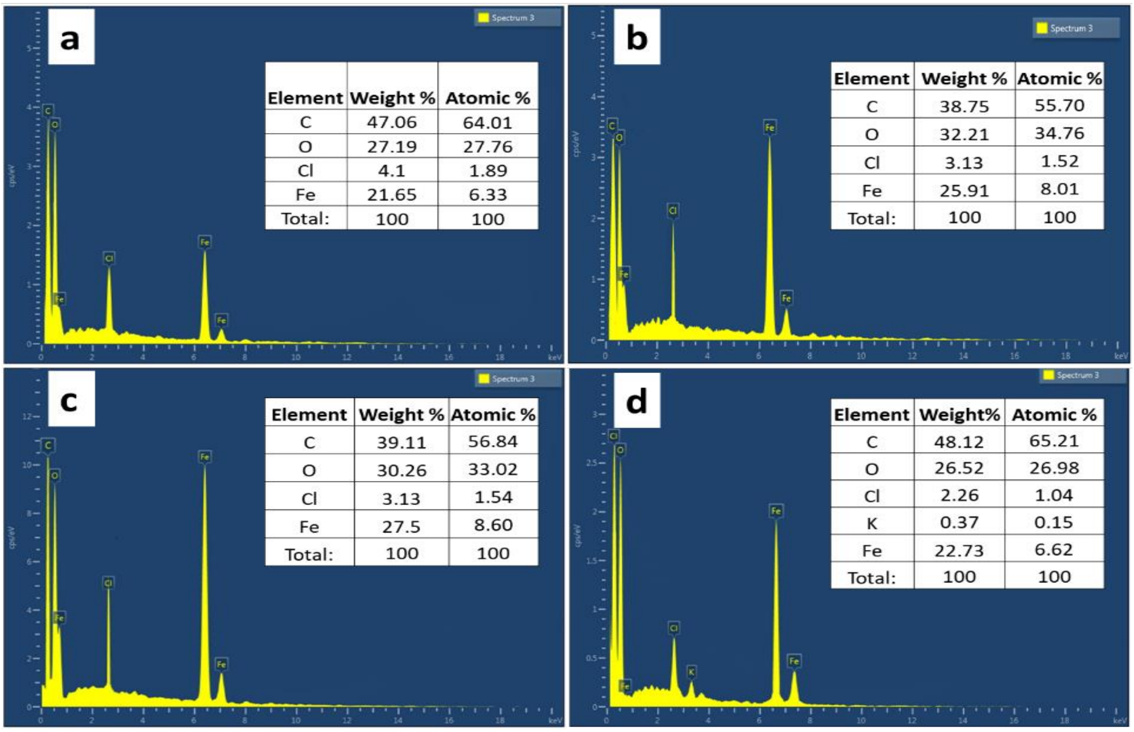

a

Element	Weight %	Atomic %
C	47.06	64.01
O	27.19	27.76
Cl	4.1	1.89
Fe	21.65	6.33
Total:	100	100

b

Element	Weight %	Atomic %
C	38.75	55.70
O	32.21	34.76
Cl	3.13	1.52
Fe	25.91	8.01
Total:	100	100

c

Element	Weight %	Atomic %
C	39.11	56.84
O	30.26	33.02
Cl	3.13	1.54
Fe	27.5	8.60
Total:	100	100

d

Element	Weight%	Atomic %
C	48.12	65.21
O	26.52	26.98
Cl	2.26	1.04
K	0.37	0.15
Fe	22.73	6.62
Total:	100	100

Figure 7.6 *EDAX spectra of a) TC-Fe, b) TB-Fe, c) PE-Fe and d) TP-Fe nanoparticles*

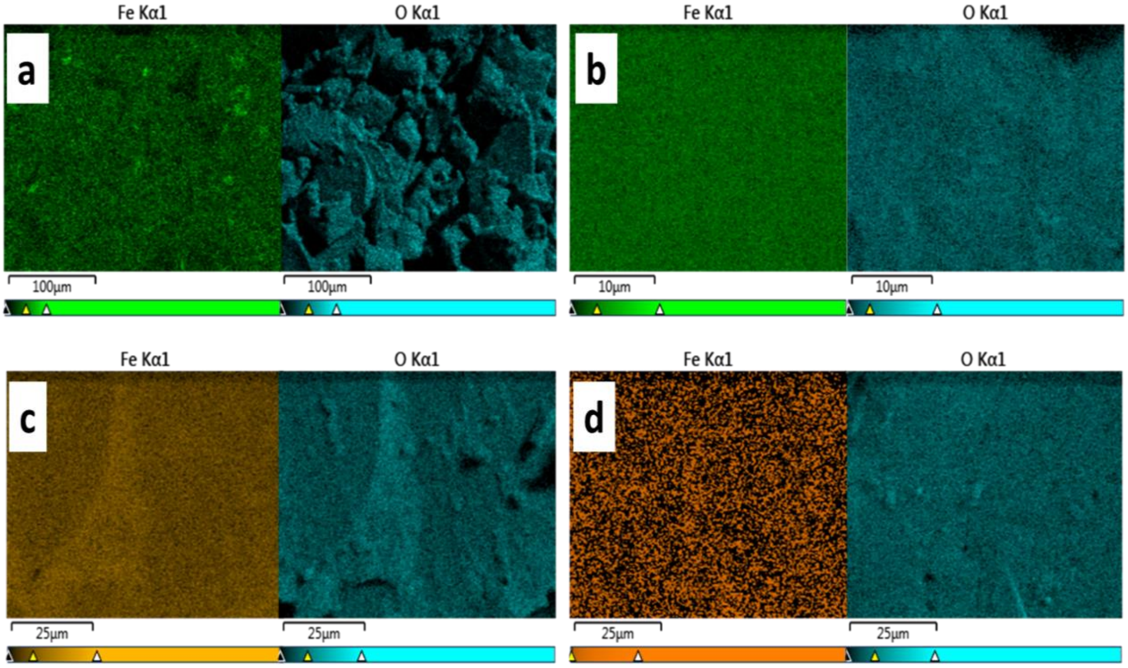

Figure 7.7 *EDAX mapping of a) TC-Fe, b) TB-Fe, c) PE-Fe and d) TP-Fe nanoparticles*

FTIR spectroscopy

The FTIR spectra of TC, TB, PE and TP plant extracts and their corresponding Fe nanoparticles are shown in figure 7.8(a, b, c & d). All the plant extracts show characteristic peaks of almost similar functional groups. Similar to AP-Fe and SN-Fe nanoparticles discussed in chapter 6, a broad peak is seen between 3700-3000 cm^{-1} in all the plant extracts and in Fe nanoparticles which corresponds to the O-H and N-H stretching vibrations of the polyphenols and amines present[23]. The groups present in the prepared plant extracts based on the FTIR results were O-H, N-H, C-H, C=O, C=C, C-N, C-Br and C-I, which is due to the presence of polyphenols, carboxylic acids, amino acids and alkaloids in them. Most of the functional groups can also be seen in the corresponding Fe nanoparticles. This indicates that biomolecules in the plant extract are adsorbed on the surface of Fe nanoparticles as a capping/stabilizing agent. However, the FTIR spectra of prepared nanoparticles show some changes in the characteristic peaks. The intensity of certain peaks was increased/decreased whereas some were shifted to higher/lower wavenumbers.

In TP-Fe nanoparticles, the O-H, N-H, C=O, C-N and C-O vibrations were shifted to lower wavenumbers compared to plant extract. For example, 1737 cm^{-1}, 1645 cm^{-1} and 1217 cm^{-1} peaks in TP extract shifted to 1703 cm^{-1}, 1621 cm^{-1} and 1190 cm^{-1}. This may be due to the decreased bond strength of functional groups due to the enhanced interaction with Fe nanoparticles. The peak at 458 cm^{-1} indicates the stretching vibration of Fe-O in the TP-Fe nanoparticles[24]. TC-Fe, TB-Fe and PE-Fe nanoparticles exhibit a different pattern of changes than TP-Fe nanoparticles. In TC-Fe nanoparticles, stretching vibrations of C-N and C=O correspondingly shifted to higher wavenumbers, from 1705 cm^{-1} to 1738 cm^{-1} and 1323 cm^{-1} to 1365 cm^{-1} respectively and vibrations corresponding to C-O changes to lower wavenumber compared to TC extract. Peak shift indicates that these functional groups are involved in the binding mechanism of Fe nanoparticles[25]. In TB-Fe nanoparticles, O-H, N-H, C=O, C-N and C=C characteristic peaks were shifted to higher wavenumbers, whereas in PE-Fe nanoparticles, C=C, O-H and N-H peaks were shifted to higher wavenumber compared to respective plant extracts. Changes in FTIR spectra indicate that reduction and stabilization of these Fe nanoparticles proceeded via these functional groups. The FTIR spectra of the prepared plant extracts and the respective Fe nanoparticles confirmed that the plant biocomponents synergistically employ reducing and capping/stabilizing properties during the synthesis of Fe nanoparticles.

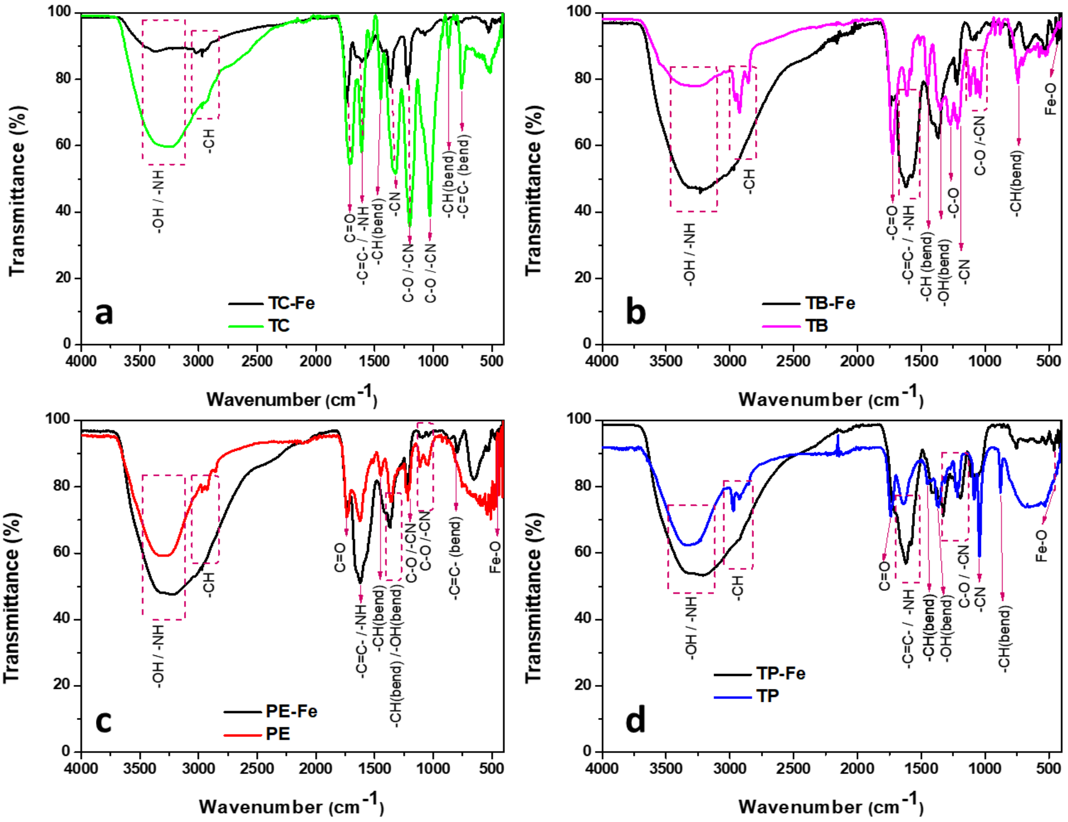

Figure 7.8 *FTIR spectra of a) TC-Fe, b) TB-Fe, c) PE-Fe and d) TP-Fe nanoparticles*

7.3.3 Cr(VI) removal studies

Figure 7.9 shows the Cr(VI) removal efficiency of TC-Fe, TB-Fe, PE-Fe and TP-Fe nanoparticles studied using 0.2 mL phytogenic nanoparticles added to 10 mL Cr(VI) solution having 5 mg/L concentration for 15 minutes. TP-Fe nanoparticles show the highest Cr(VI) removal efficiency in the prepared nanoparticles followed by TC-Fe, PE-Fe and TB-Fe nanoparticles. This may be due to the compositional difference of the Fe nanoparticles since TP-Fe contains Fe^0 and FeO nanoparticles whereas TC-Fe, PE-Fe and TB-Fe have Fe_3O_4 composition[26]. As discussed in chapter 6 the reduction, precipitation and adsorption are the pathway mechanisms followed for removing Cr(VI) using phytogenic Fe nanoparticles[27,28]. Along with the Fe nanoparticles, the capped plant components also have some ability to remove Cr(VI) from water. For example, Gajanan et al. removed Cr(VI) from water using *Terminalia chebula*[29]. The synergistic effect of plant components and Fe nanoparticles drastically improved the Cr(VI) removal efficiency. The effect of different parameters such as nanoparticle dosage, initial concentration of Cr(VI), initial pH of the Cr(VI) solution and contact time were investigated for Cr(VI) removal.

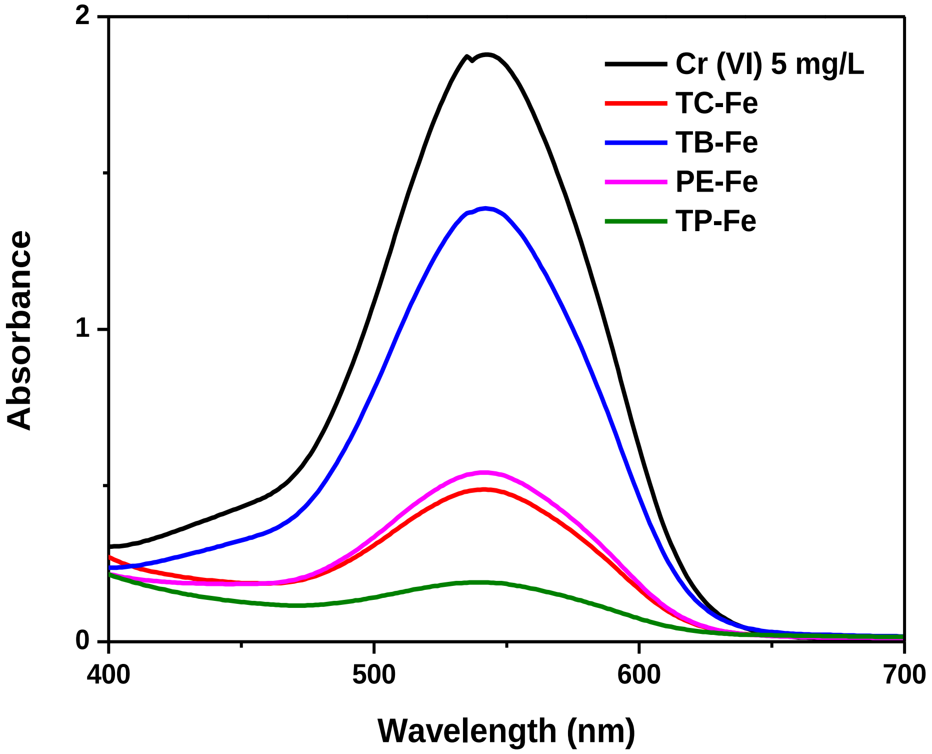

Figure 7.9 *UV-visible spectra of Cr(VI) solution after treating with nanoparticles*

Effect of nanoparticle dosage

As expected, the Cr(VI) removal efficiency increased with increasing nanoparticles dosage from 0.1 mL to 0.5 mL maintaining the initial Cr(VI) concentration (5 mg/L) and contact time (15 min) kept constant. This is simply because of increased effective active sites in the system with nanoparticle dosage. As shown in figure 7.10a, the highest removal efficiency has been shown by TP-Fe nanoparticles. PE-Fe and TC-Fe nanoparticles have almost similar removal efficiency and the lowest removal efficiency has been shown by TB-Fe nanoparticles. At 0.4 mL nanoparticles dosage, all the prepared nanoparticles except TB-Fe showed almost 100 % removal efficiency.

Effect of the initial concentration of the Cr(VI) solution

The effect of initial Cr(VI) concentration on the Cr(VI) removal was documented in figure 7.10b. The nanoparticles dosage (0.2 mL) and contact time (15 minutes) were kept constant throughout the study. As the concentration increases from 1 to 7 mg/L, the percentage of Cr(VI) removal efficiency decreases in all the prepared Fe nanoparticles. This is due to the unvarying available surface active sites at constant nanoparticle dosage required for complete Cr(VI) removal at higher concentrations. In 3 mg/L Cr(VI) solution, the TC-Fe, TB-Fe, PE-Fe and TP-Fe nanoparticles show 88.9 %, 37.6 %, 89.2 % and 100 % of Cr(VI) removal efficiency respectively.

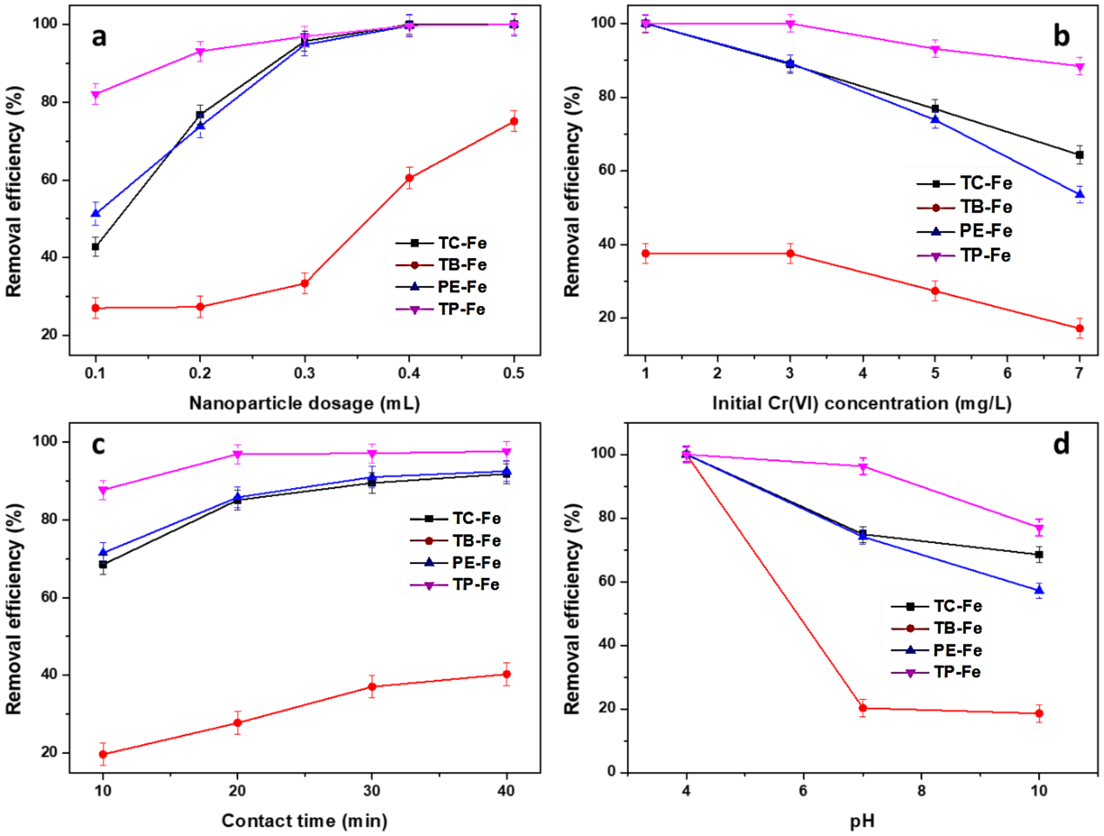

Figure 7.10 *Effects of various factors on Cr(VI) removal: (a) nanoparticle dosage, (b) initial Cr(VI) concentration, (c) contact time and (d) initial solution pH .*

Effect of contact time

Figure 7.10c represents the study of the effect of contact time in TC-Fe, TB-Fe, PE-Fe and TP-Fe nanoparticles while keeping all other parameters constant. As expected, Cr(VI) removal efficiency increases with increasing contact time since more contact time results more interaction between Fe nanoparticles and Cr(VI) in solution. In TP-Fe nanoparticles, there is no significant changes in Cr(VI) removal after 10 minutes which indicates that the removal process by TP-Fe nanoparticles appears very fast. On the other hand, nanoparticles such as TC-Fe, TB-Fe and PE-Fe attained plateau in Cr(VI) removal after 30 minutes only.

Effect of pH

As discussed in chapter 3, the pH of the solution significantly influences the Cr(VI) removal efficiency. Figure 7.10d represents the effect of solution pH in Cr(VI) removal keeping all other parameters constant. At pH 4, all the nanoparticles show 100 % removal efficiency, which is drastically reduced into 68 %, 18 %, 57 % and 77 % in TC-Fe, TB-Fe, PE-Fe and TP-Fe nanoparticles respectively, at pH 10. This may be due to the fact that in acidic pH, the positively charged surface of Fe nanoparticles attracts the negatively charged Cr(VI) ions, improving the removal efficiency[19].

7.3.4 MG dye removal studies

The prepared TC-Fe, TB-Fe, PE-Fe and TP-Fe nanoparticles were evaluated by examining their ability to remove MG dye. The prepared nanoparticles were used as heterogeneous Fenton-like catalysts in the presence of H_2O_2. Applying a heterogeneous Fenton-like system in dye removal is attractive since it causes the complete mineralisation of dye molecules and retard the formation of slurry, which is usually seen in a homogeneous Fenton system[30]. Figure 7.11 represents the MG removal using prepared nanoparticles and H_2O_2. The results show that TP-Fe nanoparticles have the highest removal efficiency, followed by PE-Fe, TB-Fe and TC-Fe nanoparticles. H_2O_2 alone does not show significant removal efficiency compared to Fe nanoparticles. The mechanism for MG removal was similar to AP-Fe and SN-Fe nanoparticles discussed in chapter 6. Adsorption of MG into iron oxide and degradation through the $^{\cdot}OH$ radicals results in the removal of MG dye molecules[31]. TP-Fe nanoparticles show the highest removal efficiency since they are mainly composed of Fe^0 and FeO compared to other nanoparticles composed of Fe_3O_4 and Fe_3O_4.

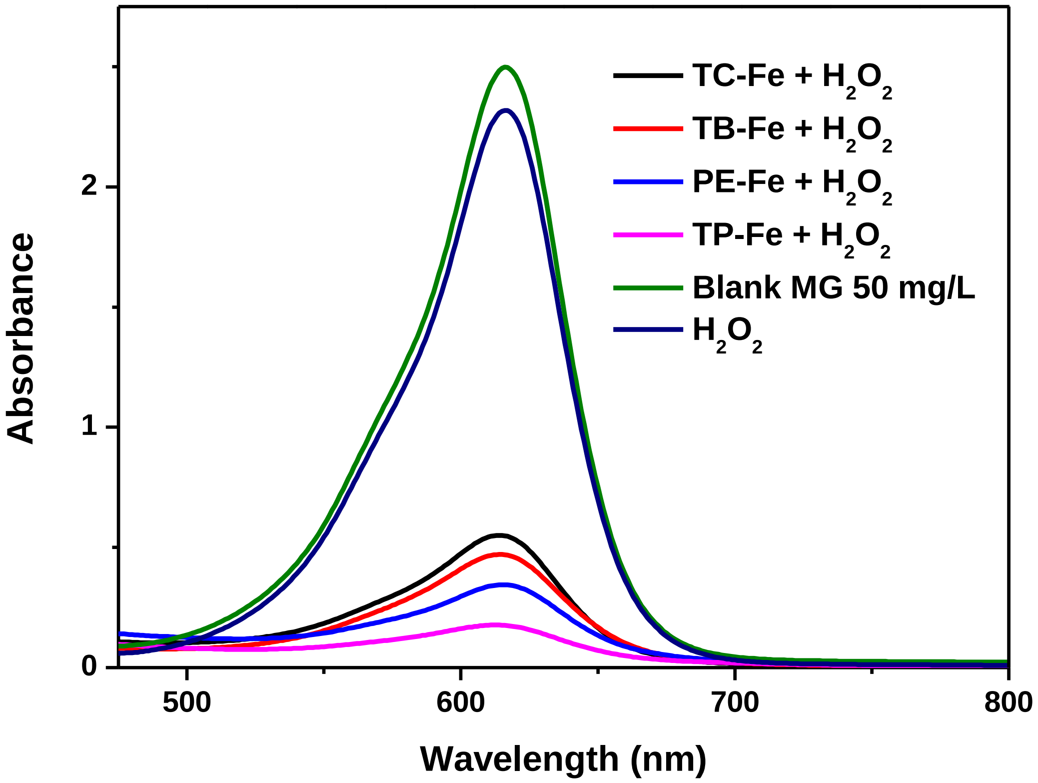

Figure 7.11 *UV-visible spectra of MG dye solution after treating with nanoparticles*

Effect of nanoparticle dosage

It is not surprising that MG dye removal increases with increasing nanoparticles dosage. The availability of more Fe nanoparticles for adsorption and Fenton reaction results in improved MG dye removal at higher nanoparticles dosage. Figure 7.12a represents the MG removal by phytogenic nanoparticles with varying nanoparticle dosages from 0.5 mL to 2.5 mL while keeping the initial dye concentration (50 mg/L) and contact time (15 min) constant. At 1 mL nanoparticle dosage, 76 %, 82 %, 86 % and 93 % removal efficiency were shown by TC-Fe, TB-Fe, PE-Fe and TP-Fe nanoparticles respectively. As expected, the removal efficiency increases with increasing nanoparticle dosage.

Effect of initial concentration of the MG

Figure 7.12b represents the effect of the initial concentration of MG on the removal of MG dye molecules, keeping nanoparticle dosage (1 mL) and contact time (15 min) constant. The removal efficiency decreases slightly with an increase in the initial concentration of the MG dye. This is because of the insufficient availability of Fe nanoparticles corresponding to the increased concentration of MG dye. The highest removal efficiency was seen in the solution of 10 mg/L and the increasing order of removal efficiency was 89 %, 92 %, 94 % and 98 % for TC-Fe, TB-Fe, PE-Fe and TP-Fe nanoparticles.

Effect of contact time

The effect of contact time on MG removal efficiency was studied and represented in figure 7.12c. The nanoparticle dosage (1 mL) and initial concentration of MG dye (50 mg/L) were kept constant during the study. In the first 10 minutes, TC-Fe, TB-Fe, PE-Fe and TP-Fe nanoparticles showed 71 %, 84 %, 90 % and 90 % removal efficiency, respectively. When it was increased to 40 minutes, the removal efficiency was 75 %, 87 %, 95 % and 95 %. The results show that the removal efficiency increases with increasing contact time; however, the rate of increase is not much significant.

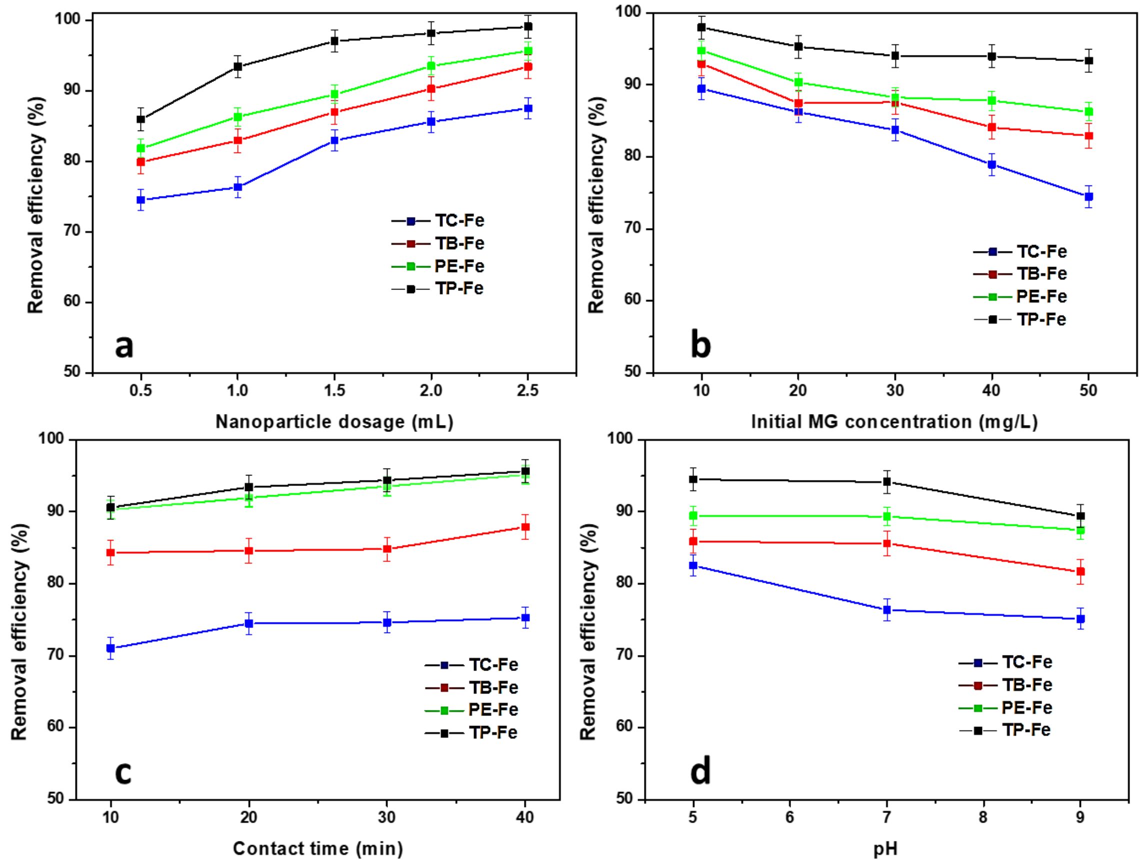

__Figure 7.12__ Effects of various factors on MG removal (a) nanoparticle dosage, (b) initial MG concentration, (c) contact time and (d) initial solution pH.

Effect of pH

The effect of pH on the removal of MG dye was illustrated in figure 7.12d. The TC-Fe, TB-Fe, PE-Fe and TP-Fe nanoparticles show 76 %, 85 %, 89 % and 94 % removal efficiency at neutral pH. However, the removal efficiency decreases slightly when it shifts to basic pH. This is due to the formation of ferric/ferrous hydroxide complexes. Acidic pH improves the removal efficiency of the prepared nanoparticles.

7.4. Conclusions

In summary, phytogenic Fe nanoparticles were synthesised using ayurvedic composition *Triphala* and its constituents such as *Terminalia chebula*, *Terminalia belerica* and *Phyllanthus emblica*. The characterization of nanoparticles was done by UV-visible spectroscopy, HRTEM, EDAX and FTIR. The appearance of the broad band around 600 nm suggests the formation of Fe nanoparticles in the solution. HRTEM results suggest that the nanoparticles have a particle size less than 6 nm when using plant extracts. However, the particles size of *Triphala* based Fe nanoparticles was around 11 nm. The SAED pattern indicates that the composition of prepared nanoparticles mainly consists of iron oxides. FTIR confirmed the presence of organic components in the prepared nanoparticles that might induce stability to the prepared nanoparticles. The application of prepared nanoparticles for Cr(VI) removal studies clearly indicates that TP-Fe nanoparticles have the highest removal efficiency, followed by TC-Fe, PE-Fe and TB-Fe nanoparticles. However, in the case of MG dye removal, again the TP-Fe nanoparticles have the highest removal efficiency followed by PE-Fe, TB-Fe and TC-Fe nanoparticles.

7.5. References

[1] G. Subramanian, D. Shanmugamprema, R. Subramani, K. Muthuswamy, V. Ponnusamy, K. Tankay, T. Velusamy, V. Krishnan, S. Subramaniam, Anti-Obesity Effect of T. Chebula Fruit Extract on High Fat Diet Induced Obese Mice: A Possible Alternative Therapy, Mol. Nutr. Food Res. 65 (2021) 2001224. https://doi.org/10.1002/mnfr.202001224.

[2] A. Singh, V. Bajpai, S. Kumar, B. Kumar, M. Srivastava, K.B. Rameshkumar, Comparative profiling of phenolic compounds from different plant parts of six Terminalia species by liquid chromatography–tandem mass spectrometry with chemometric analysis, Ind. Crops Prod. 87 (2016) 236–246. https://doi.org/10.1016/j.indcrop.2016.04.048.

[3] K. Mohan Kumar, B.K. Mandal, M. Sinha, V. Krishnakumar, Terminalia chebula mediated green and rapid synthesis of gold nanoparticles, Spectrochim. Acta Part A Mol. Biomol. Spectrosc. 86 (2012) 490–494. https://doi.org/10.1016/j.saa.2011.11.001.

[4] K. Mohan Kumar, M. Sinha, B.K. Mandal, A.R. Ghosh, K. Siva Kumar, P. Sreedhara Reddy, Green synthesis of silver nanoparticles using Terminalia chebula extract at room

temperature and their antimicrobial studies, Spectrochim. Acta Part A Mol. Biomol. Spectrosc. 91 (2012) 228–233. https://doi.org/10.1016/j.saa.2012.02.001.

[5] R. Sharma, Synthesis of Terminalia bellirica fruit extract mediated silver nanoparticles and application in photocatalytic degradation of wastewater from textile industries, Mater. Today Proc. 44 (2021) 1995–1998. https://doi.org/10.1016/j.matpr.2020.12.118.

[6] S. Kumar, A. Singh, B. Kumar, Identification and characterization of phenolics and terpenoids from ethanolic extracts of Phyllanthus species by HPLC-ESI-QTOF-MS/MS, J. Pharm. Anal. 7 (2017) 214–222. https://doi.org/10.1016/j.jpha.2017.01.005.

[7] R. Renuka, K.R. Devi, M. Sivakami, T. Thilagavathi, R. Uthrakumar, K. Kaviyarasu, Biosynthesis of silver nanoparticles using phyllanthus emblica fruit extract for antimicrobial application, Biocatal. Agric. Biotechnol. 24 (2020) 101567. https://doi.org/10.1016/j.bcab.2020.101567.

[8] S. Ranjani, K. Tamanna, S. Hemalatha, Triphala green nano colloids: synthesis, characterization and screening biomarkers, Appl. Nanosci. 10 (2020) 1269–1279. https://doi.org/10.1007/s13204-019-01208-w.

[9] W. Liang, R. Zhu, X. Li, J. Deng, Y. Fu, Heterogeneous photocatalyzed acceptorless dehydrogenation of 5-hydroxymethylfurfural upon visible-light illumination, Green Chem. 23 (2021) 6604–6613. https://doi.org/10.1039/D1GC01286J.

[10] R. Hao, D. Li, J. Zhang, T. Jiao, Green Synthesis of Iron Nanoparticles Using Green Tea and Its Removal of Hexavalent Chromium, Nanomaterials. 11 (2021) 650. https://doi.org/10.3390/nano11030650.

[11] B. Ibrahim, A. Wiranata, A. Malik, The Effect of Addition of Antioxidant 1,2-dihydro-2,2,4-trimethyl-quinoline on Characteristics of Crepe Rubber Modified Asphalt in Short Term Aging and Long Term Aging Conditions, Appl. Sci. 10 (2020) 7236. https://doi.org/10.3390/app10207236.

[12] M.Z. Kassaee, M. Mohammadkhani, A. Akhavan, R. Mohammadi, In situ formation of silver nanoparticles in PMMA via reduction of silver ions by butylated hydroxytoluene, Struct. Chem. 22 (2011) 11–15. https://doi.org/10.1007/s11224-010-9671-1.

[13] M.M. Saleh-e-In, N. Sultana, M.M. Rahim, M.A. Ahsan, M.N.H. Bhuiyan, M.N. Hossain, M.M. Rahman, S. Kumar Roy, M.R. Islam, Chemical composition and pharmacological significance of Anethum Sowa L. Root, BMC Complement. Altern. Med. 17 (2017) 127. https://doi.org/10.1186/s12906-017-1601-y.

[14] H. Chabane, M. Messarah, M. Liacha, Comparative study for the synthesis of new generation of2(3H)-benzothiazolones as antioxidant agents, Der Pharma Chem. 8 (2016) 20–26.

[15] T. Sudha, S. Chidambarampillai, V.. Mohan, GC-MS analysis of bioactive components of aerial parts of fluggea leucopyrus willd. (Euphorbiaceae), J. Appl. Pharm. Sci. 3 (2013) 126–130. https://doi.org/10.7324/JAPS.2013.3524.

[16] P. Bhuyar, M.H.A. Rahim, S. Sundararaju, R. Ramaraj, G.P. Maniam, N. Govindan, Synthesis of silver nanoparticles using marine macroalgae Padina sp. and its antibacterial activity towards pathogenic bacteria, Beni-Suef Univ. J. Basic Appl. Sci. 9 (2020) 3. https://doi.org/10.1186/s43088-019-0031-y.

[17] S. Siswadi, G.S. Saragih, Phytochemical analysis of bioactive compounds in ethanolic extract of Sterculia quadrifida R.Br., in: 2021: p. 030098. https://doi.org/10.1063/5.0053057.

[18] A. Rana, N. Kumari, M. Tyagi, S. Jagadevan, Leaf-extract mediated zero-valent iron for oxidation of Arsenic (III): Preparation, characterization and kinetics, Chem. Eng. J. 347 (2018) 91–100. https://doi.org/10.1016/j.cej.2018.04.075.

[19] Z. Xiao, H. Zhang, Y. Xu, M. Yuan, X. Jing, J. Huang, Q. Li, D. Sun, Ultra-efficient removal of chromium from aqueous medium by biogenic iron based nanoparticles, Sep. Purif. Technol. 174 (2017) 466–473. https://doi.org/10.1016/j.seppur.2016.10.047.

[20] D. Patiño-Ruiz, L. Sánchez-Botero, L. Tejeda-Benitez, J. Hinestroza, A. Herrera, Green synthesis of iron oxide nanoparticles using Cymbopogon citratus extract and sodium carbonate salt: Nanotoxicological considerations for potential environmental applications, Environ. Nanotechnology, Monit. Manag. 14 (2020) 100377. https://doi.org/10.1016/j.enmm.2020.100377.

[21] T. Sarkar, T.K. Dhiman, R.K. Sajwan, S. Sri, P.R. Solanki, Studies on carbon-quantum-dot-embedded iron oxide nanoparticles and their electrochemical response, Nanotechnology. 31 (2020) 355502. https://doi.org/10.1088/1361-6528/ab925e.

[22] W. Teng, J. Fan, W. Wang, N. Bai, R. Liu, Y. Liu, Y. Deng, B. Kong, J. Yang, D. Zhao, W. Zhang, Nanoscale zero-valent iron in mesoporous carbon (nZVI@C): stable nanoparticles for metal extraction and catalysis, J. Mater. Chem. A. 5 (2017) 4478–4485. https://doi.org/10.1039/C6TA10007D.

[23] K.V.G. Ravikumar, S.V. Sudakaran, K. Ravichandran, M. Pulimi, C. Natarajan, A. Mukherjee, Green synthesis of NiFe nano particles using Punica granatum peel extract for tetracycline removal, J. Clean. Prod. 210 (2019) 767–776. https://doi.org/10.1016/j.jclepro.2018.11.108.

[24] S. Eslami, M.A. Ebrahimzadeh, P. Biparva, Green synthesis of safe zero valent iron nanoparticles by: Myrtus communis leaf extract as an effective agent for reducing excessive iron in iron-overloaded mice, a thalassemia model, RSC Adv. 8 (2018) 26144–26155. https://doi.org/10.1039/c8ra04451a.

[25] W.K.A. Wan Mat Khalir, K. Shameli, S.D. Jazayeri, N.A. Othman, N.W. Che Jusoh, N.M. Hassan, Biosynthesized Silver Nanoparticles by Aqueous Stem Extract of Entada spiralis and Screening of Their Biomedical Activity, Front. Chem. 8 (2020). https://doi.org/10.3389/fchem.2020.00620.

[26] Y. Wei, Z. Fang, L. Zheng, E.P. Tsang, Biosynthesized iron nanoparticles in aqueous extracts of Eichhornia crassipes and its mechanism in the hexavalent chromium removal, Appl. Surf. Sci. 399 (2017) 322–329. https://doi.org/10.1016/j.apsusc.2016.12.090.

[27] F. Zhu, S. He, T. Liu, Effect of pH, temperature and co-existing anions on the Removal of Cr(VI) in groundwater by green synthesized nZVI/Ni, Ecotoxicol. Environ. Saf. 163 (2018) 544–550. https://doi.org/10.1016/j.ecoenv.2018.07.082.

[28] F. Zhu, S. Ma, T. Liu, X. Deng, Green synthesis of nano zero-valent iron/Cu by green tea to remove hexavalent chromium from groundwater, J. Clean. Prod. 174 (2018) 184–190. https://doi.org/10.1016/j.jclepro.2017.10.302.

[29] G. Kapure, S. Mohan Rao, Application of Terminalia chebula for Removal of Hexavalent Chromium in Chromite Concentrates, ISIJ Int. 48 (2008) 868–874. https://doi.org/10.2355/isijinternational.48.868.

[30] S.S.F. Carvalho, N.M.F. Carvalho, Dye degradation by green heterogeneous Fenton catalysts prepared in presence of Camellia sinensis, J. Environ. Manage. 187 (2017) 82–88. https://doi.org/https://doi.org/10.1016/j.jenvman.2016.11.032.

[31] X. Wang, A. Wang, J. Ma, M. Fu, Facile green synthesis of functional nanoscale zero-valent iron and studies of its activity toward ultrasound-enhanced decolorization of cationic dyes, Chemosphere. 166 (2017) 80–88. https://doi.org/10.1016/j.chemosphere.2016.09.056.

CHAPTER 8

Summary and Conclusion

Chapter 8

Summary and Conclusion

The effective handling of water pollutants is a thrust area of research since only one percent of the water on earth is fit for use. Conventional water treatment methods like filtration, coagulation, chemical methods, aerobic and anaerobic treatments require high operational cost, less efficient and reliable, pretreatment requirements and formation of potentially toxic by-products. The application of nanotechnology contributes significantly to environmental and climate protection by saving raw materials, energy and water and reducing greenhouse gases and hazardous wastes. The nanomaterials have high reactivity and strong sorption properties due to their unique size-dependent properties, such as incredibly large surface area and quantum confinement effect.

For the past few years, iron-based nanoparticles have been considered a cost-effective solution for environmental clean-up problems. Iron-based nanoparticles typically include zero valent iron, iron oxides and iron oxy-hydroxides. They are considered practicable and environmentally friendly materials, owing to their easy availability, relatively cheap, low toxicity and simple preparation methods. Zero valent iron (Fe^0) has a unique position among iron nanoparticles due to its high reactivity and large surface area. The successful field application of Fe^0 nanoparticles makes them an attractive area for researchers. However, the rapid oxidation and agglomeration of Fe^0 nanoparticles and toxic effects of chemicals used during the synthesis act as barriers in the development of Fe^0 based environmental remediation. Developing stable and efficient Fe^0 based nanoparticles with low secondary pollution is the key objective of all the lab-scale studies. To achieve these goals, this thesis emphasises different methods to enhance the reactivity, stability and dispersibility of the Fe^0 nanoparticles. The study also reports green synthesis methods for the preparation of Fe^0 nanoparticles.

A review of various types of nanomaterials used for the remediation of water pollutants and iron-based nanomaterials is discussed in chapter 1. The properties, synthesis and modification methods and application of Fe^0 nanoparticles are also discussed in this chapter. Chapter 2 discusses the materials used in this work and the methods followed for the batch experiments of hexavalent chromium and dye removal studies.

The enhancement of reactivity of Fe^0 nanoparticles by bimetallisation is examined in chapter 3. Fe^0 nanoparticles and catalytic metal (Cu, Ni and Zn) loaded Fe^0 nanoparticles were prepared using the liquid-phase reduction method and applied to remove toxic hexavalent chromium and organic dyes. XRD and HRTEM confirm the formation of Fe^0 and bimetallic Fe nanoparticles. Fe/Cu and Fe/Ni nanoparticles show high reactivity for the Cr(VI) and malachite green dye removal among the prepared nanoparticles. The better efficiency of Fe/Cu and Fe/Ni bimetallic nanoparticles was assumed due to the direct electron transfer, hydride formation and formation of reactive oxygen species. The reduction and precipitation of Cr(VI) were established through EDAX. The degradation mechanism for malachite green was confirmed through GC-MS/MS and LC-MS/MS analysis.

In chapter 4, Fe^0 and bimetallic Fe/Ni nanoparticles were prepared using a biopolymer, chitosan, as a stabilising agent. Chitosan reduces the particle size and agglomeration of the Fe^0 and Fe/Ni nanoparticles and provides more stability. The formation of chitosan stabilised iron-based nanoparticles were confirmed by HRTEM and XPS. The deposition of Ni on Fe^0 makes CS-Fe/Ni nanomaterials more efficient in Cr(VI) and triphenylmethane dye removal than CS-Fe nanoparticles.

Chapter 5 discussed the preparation of TiO_2-zeolite-Fe^0 composites with different percentages of TiO_2. The TiO_2-zeolite composite was prepared by sonication of ingredients followed by the hydrothermal method. The incorporation of Fe nanoparticles into TiO_2-zeolite composite was done using wet impregnation followed by the liquid-phase reduction method. The characterisation of prepared nanoparticles was done by XRD, HRTEM, FTIR, UV-visible spectroscopy and EDAX. The photocatalytic nature of TiO_2-zeolite composite reduced the oxidation tendency of Fe^0 nanoparticles and made Fe^0 active for more extended periods. Due to the synergetic effect of TiO_2, Fe^0 and zeolite, the TiO_2-zeolite-Fe composite exhibits high efficiency for Cr(VI) and malachite green removal.

Chapters 6 and 7 emphasise the reducing and stabilising property of plant extracts to prepare the Fe^0 nanoparticles. In chapter 6, two novel plant extracts from *Abrus precatorius (AP)* and *Strychnos nux-vomica (SN)* were used to prepare Fe^0 nanoparticles. Different plant components reduce the Fe^{3+} ions differently and produce Fe nanoparticles. GC-MS/MS analysis identified the volatile bioactive components present in the prepared plant extracts. The formation of iron nanoparticles was confirmed by UV-visible spectroscopy and HRTEM, and the presence of plant components in prepared nanoparticles were confirmed through FTIR. The results from the SAED pattern suggest that AP-Fe nanoparticles have a mixture of Fe^0 and Fe_2O_3 nanoparticles and the SN-Fe nanoparticles mainly have Fe_3O_4 nanoparticles. In the presence of H_2O_2, the Fe nanoparticles act as a Fenton-like catalyst to degrade malachite green dye molecules. The high efficiency of AP-Fe nanoparticles over SN-Fe nanoparticles in the removal of Cr(VI) and malachite green dye is attributed to the composition of AP-Fe.

In chapter 7, the preparation of extracts from an ayurvedic composition *Triphala* (TP) and its components such as *Terminalia chebula*, *Terminalia belerica* and *Phyllanthus emblica* was discussed. The Fe nanoparticles prepared by these plant extracts were mainly iron oxides. The SAED pattern shows that TP-Fe is mainly composed of Fe^0 and FeO and the iron nanoparticles prepared from *Triphala* components individually consist of Fe^0 and Fe_3O_4. The formation of FeO is due to the improved antioxidation property of *Triphala* composition. The prepared nanoparticles act as an excellent Fenton-like catalyst for malachite green dye removal and it also exhibits high efficiency for Cr(VI) removal.

8.1. The practical significance of our work

- We have synthesised bimetallic Fe nanoparticles to determine the most efficient bimetallic Fe composition for the Cr(VI) and dye removal. Observed that the characteristics of the incoporated second metal influence the removal efficiency of water pollutants. Fe/Ni and Fe/Cu are the most efficient bimetal combinations for Cr(VI) and dye removal. The optimum percentage of second metal loading was also verified through the batch experiment study.
- The malachite green degradation mechanism by Fe^0 nanoparticles is not studied in detail before. We have found that at the early stage, the dye degradation occurs through reduction and later the oxidative degradation mechanism has prevailed.
- The thesis also gives more information on the application of biopolymer chitosan for the stabilisation of bimetallic nanoparticles. Our synthesis method gives the smallest chitosan stabilised iron/bimetallic and iron nanoparticles compared to previous studies.
- The synthesis of different percentages of TiO_2 loaded zeolite stabilized iron nanoparticles provides a significantly efficient material for Cr(VI) removal and dye

degradation. The reason for the improved efficiency of TiO_2-zeolite-Fe composite was also discussed.

- The thesis also identified two novel plant extracts for the preparation of Fe nanoparticles and their properties were examined. The Fenton-like degradation of malachite green using phytogenic Fe nanoparticles was studied in detail.
- The preparation of novel iron nanoparticles using ayurvedic composition *Triphala* and the comparative study of iron nanoparticles prepared by *Triphala* constituents give light to the synergistic effect of plant extracts for the preparation of iron nanoparticles.

8.2. Future scope of our investigation

Different modifications have been done on the Fe nanoparticles to improve their properties. However, the selection of modified materials/methods to be carefully considered for the field application of the Fe nanoparticles. In the natural environment, different parameters such as humic acid and different inorganic solutes significantly influence the reactivity of nanoparticles. The storage stability, transportation and toxicity of the nanoparticles are also important parameters in the natural environment. Our plan is to discover the most appropriate, non-toxic, cost-effective material/method for natural environmental applications.

LIST OF PUBLICATIONS

i. **Anju Rose Puthukkara P**, Sunil Jose T and Dinooplal S., “Chitosan-stabilized Fe/Ni bimetallic nanoparticles for the removal of cationic and anionic triphenylmethane dyes from water”, Environmental Nanotechnology, Monitoring and Management, 2020, Volume 14, https://doi.org/10.1016/j.enmm.2020.100295.

ii. **Anju Rose Puthukkara P**, Sunil Jose T, and Dinooplal S., “Plant mediated synthesis of zero valent iron nanoparticles and its application in water treatment”, Journal of Environmental Chemical Engineering, 2020, https://doi.org/10.1016/j.jece.2020.104569.

iii. Dinoop lal S, Sunil Jose T, Rajesh C, **Anju Rose Puthukkara P**, Savitha Unnikrishnan K, Arun K J., “Accelerated photodegradation of polystyrene by TiO_2-polyaniline photocatalyst under UV radiation”, European Polymer Journal, 2021, https://doi.org/10.1016/j.eurpolymj.2021.110493.

LIST OF CONFERENCE PRESENTATIONS

i. **Anju Rose Puthukkara P** and Sunil Jose T, “Removal of malachite green dye using chitosan stabilised bimetallic nanoparticles” in International Conference on Chemistry and Physics of Materials 2018 (ICCPM 2018) held at St.Thomas College (Autonomous) Thrissur, 19-21st December 2018.

ii. **Anju Rose Puthukkara P** and Sunil Jose T, “Removal of cationic and anionic triphenylmethane dyes using zero valent iron and bimetallic Fe/Ni nanoparticles stabilised by chitosan” in International Conference on Energy and Environment 2019 (ICEE 2019) held at TKM College of Arts and Sciences, Kollam, 12-14th December 2019.

iii. **Anju Rose Puthukkara P** and Sunil Jose T, “Synthesis of chitosan stabilised Fe/Ni nanoparticles for the removal of hexavalent chromium in water” in the International Conference on Advances in Polymer Technology, organised jointly by the Department of Polymer Science and Rubber Technology, CUSAT & Indian Rubber Institute, 27-29th May 2021.

iv. **Anju Rose Puthukkara P** and Sunil Jose T, “Synthesis of bimetallic Fe particles and application in dye removal” in 32nd Kerala Science Congress held at Yuvakshetra Institute of Management Studies, Mundur, Palakkad, 25-27th January 2020.

PAPERS COMMUNICATED

i. Environmental Technology - Taylor & Francis

Anju Rose Puthukkara P, Sunil Jose T*, Dinoop lal S, Savitha Unnikrishnan K, Martin Francis P, “Phytogenic synthesis of iron nanoparticles and their application for the removal of Cr (VI) and malachite green dye from water”

(Communicated)

ii. Science of The Total Environment – Elsevier

Anju Rose Puthukkara P, Sunil Jose T*, Dinoop lal S, “Removal of malachite green dye from aqueous solution by zero valent iron stabilised on TiO_2-zeolite composite”

(Communicated)